

30MW Multi-Rotor Turbine Block Design

Final report

Group 21

Luka Distelbrink	5274400	Mihai Fetecau	5236789
Lorenzo Gonzalez	5242231	Bartosz Jemioł	5275830
Michael Kamal Rizk	5008883	Marco Peralta Tapia	5098955
Ionut Porcescu	5274508	Jānis Pudāns	5307910
Jan Roth	5262054	Mustafa Tuğtekin	5210925

30MW Multi-Rotor Turbine Block Design

Final report

by

Group 21

Luka Distelbrink	5274400	Mihai Fetecau	5236789
Lorenzo Gonzalez	5242231	Bartosz Jemioł	5275830
Michael Kamal Rizk	5008883	Marco Peralta Tapia	5098955
Ionut Porcescu	5274508	Jānis Pudāns	5307910
Jan Roth	5262054	Mustafa Tuğtekin	5210925



Report duration: May 25, 2023 – June 21, 2023

Project tutor: Dr.ir. Carlos Simao Ferreira

Project coaches: Dr. Morgan Li, Stratos Koufis

Course: AE3200 Design Synthesis

Executive Overview

The goal of the report is to present a design of an offshore wind turbine that, in comparison to conventional horizontal axis wind turbines: has a lower impact on the environment, produces energy at a lower cost and is easier to design and manufacture. Increasing performance in all categories required a drastic change to the design of wind turbines. This executive overview will give an summary how that new wind turbine concept was designed. Each section describes the processes and the final decision taken for every aspect of the design. First a description of the fiances is given. Second a summary of trade-off is presented. Thirdly, a review of all the in depth analysis performed on the design.

Budgeting and Cost Analysis

The budgeting and the cost analysis are based on the leveledized cost of electricity. The reason for choosing the LCoE as the financial indicator was the fact it incorporates all the performance figures, energy production, power density, and ongoing and upfront costs, in one easy-to-compare number. The budget for MR-TBD has been set to an LCoE of 30€/MWh, which is a 45% reduction compared to the projected cost by WindEurope [1]. There also the possibility of using the design to replace old farms beyond 2050, which would set the LCoE target at 36€/MWh. The initial budgeting showed that with the anticipated changes in costs, the proposed design is unlikely to achieve the set target for current deployment (with an LCoE of 36€/MWh), but would hit targets for future contractions. The initial data also showed the break-even point at 13 years.

After the design had been completed, a more in depth cost analysis was performed. By comparing the cost of different components to a reference 10MW wind turbine, a better estimation of the LCoE can be given. After the analysis, value of LCoE went from 36€/MWh to 38€/MWh. Additional financial indicators were also computed. The expected time to break-even was computed to drop from 13 to 9 years and the weight average cost of capital at which the turbine is profitable has rose from 3% to 6.7% (with energy sale price of 54€/MWh).

Design Trade-Off

A total of eight trade-offs were performed concerning the possible options for the design. The first trade-off was performed between the usage of horizontal axis wind turbines (HAWTs) and vertical axis wind turbines (VAWTs). An additional option with grouped rotors and with non-grouped rotors was differentiated. The trade-off indicated that grouped-rotor VAWTs were the best design option, mainly due to drastically reducing generator costs and the number of generators reducing maintenance costs.

The trade-off for the yaw control system was performed after that. The choice was made between using aerodynamic, electric, hydraulic yaw control, or a combination of these. The main advantage of aerodynamic control is large torques it can achieve without additional components which is the reason it was selected. The aerodynamic yaw system does not work during a storm or very low wind speeds so an electric system is needed for those conditions.

The next trade-off which was performed was between the choice of a fixed foundation (monopile or jacket) and a floating foundation (using a pontoon/floater). The choice of using a fixed foundation was made mainly due to the shallow depth for which the system was designed, making this option lighter and simpler. Should the design need to be installed in much deeper water, this decision may need to be revised. Subsequently, the choice for a monopile was made over the jacket structure, due to maintenance and manufacturing concerns.

Drive train trade-off was performed next, to choose between four different generator types: a DD-PMS generator, an EES generator, a DFI generator, and a geared PMS generator. Due to its low use of rare-earth metals, the trade-off ended in favour of a three-stage geared double-fed induction generator over a permanent magnet option. This was one of the most important trade-offs when it comes to maintenance and sustainability, as generators account for a large part of maintenance costs and rare-earth usage.

The trade-off of the structure cell had two options: a triangle-based cell and a rectangle-based cell. The rectangle-based cell was chosen because a triangle-based cell would increase the generator count by a factor of 2.

Shaft position trade-off chose between mounting the shaft in front of the structure cell or in the middle of the structure cell. The choice was made in favour of mounting the shaft in front of the structure because the position is less constraining on the structure and makes the assembly easier.

Rotor selection trade-off considered 5 different rotor types: Drag-based Savonius, Darrieus Troposkien type, H-type, Gorlov helical type, and V-type. V-type and Darrieus Troposkien types were discounted due to not fitting well a square shape. Drag-based Savonius was discounted due to low performance. Helix shape was the hardest to manufacture so it was not considered. H-shape was selected, as it performed well in all categories.

For the structure buckling was identified as critical. When Euler buckling was removed from structural simulations, the weight of the system decreased drastically. Euler buckling is determined by the moment of inertia of a cross-section with mass away from its centre is advantageous. Individual element selection was done to select the most buckling-resistant cross-section of an individual element. The main two choices were between a hollow cylinder and a truss element. The choice for the hollow cylinder was made because of its simplicity to manufacture and simulate.

Tower design

The tower structure consists of a large rectangular truss structure. It was designed using a truss simulation tool that optimises the mass of the structure based on its shape and the applied loads, by varying the profiles of the hollow cylindrical truss elements. A set of 20 different profiles with associated radii and thicknesses was used.

The considered loads were the mass of the structure, drivetrain, rotors, shafts, high-lift devices, the thrust of the rotors, the drag on the structure, the torque of the electric yaw system, and the downforce and drag on the high-lift devices.

The truss consists of smaller rectangular tillable cells. Seven different cell shapes with different numbers of braces and brace locations were examined. A full structure was generated for each. The masses of the resulting structures were then compared, and the lightest cell shape was selected.

With the cell shape set, the actual size of the individual cells was picked. For the same total structural width and height 4x4, 6x4, 6x6, 6x10, 6x12, and 8x8 cells were considered. The lightest configuration was 6x6 cells, so this configuration was chosen.

Then the depth of the structure was selected. A sensitivity analysis was done for the structural mass depending on the depth-to-width ratio of the structure. The ratio associated with the lightest overall structure was 12 %. This leads to a structural depth of 33.6 m.

After the depth, the thickness-to-radius ratio of the hollow cylindrical truss elements was selected. Because a lower thickness ratio leads to higher moments of inertia, elements with a lower thickness ratio are more resistant to Euler buckling. This leads to lower structural masses, as most elements loaded in compression will fail in Euler buckling. However, sheet buckling is not modelled, and once elements become too thin they may become too flexible. In addition to this, a lower thickness ratio leads to higher radii, leading to a higher drag on the structure. As this is a limiting load case, the radii of the elements should not become too large. To balance these factors a thickness-to-radius ratio of 0.01 was chosen.

To select a material, the mass of an optimised design and raw material cost were compared for a few different types of steel. The two most promising options were high-carbon steel and medium-carbon steel, with high-carbon steel leading to a slightly lighter design. However, medium-carbon steel is easier to man-

ufacture parts from as it is softer. It is also more ductile, and resistant to corrosion [2]. For these reasons, medium-carbon steel was chosen. In addition to this, multiple layers of white organic solvent-based paint will be applied to the truss structure. This is done to protect the structure from the harsh environment and reduce its capability of absorbing heat from the sun. This process is done for all the above water elements exposed to air.

To account for the additional mass of connections between the truss elements, a 20 % margin was added to the structural mass, leading to a total of 2455 t. Adding an estimated mass of 312 tonne for the generator bedplates, the final mass of the truss tower is 2767 tn.

Finally, the natural frequencies of the structure were analysed, assuming masses of elements were lumped at their nodes. The lowest natural frequency of the structure turned out to be slightly higher than the rotor frequency. As they are very close this requires special consideration during a more detailed analysis. If the rotor frequency indeed turns out to be a problem, the structure can be made stiffer by increasing the size of the elements. However, this is not a mass-efficient solution. Another solution would be to design dampers and insert them at the clamps that attach the rotor shafts to the structure, to damp out and remove the problematic excitation frequencies.

Wake control subsystem design

The wake control system of the MR-TBD is comprised of four wings (one per each row of the structure) with a total effective span of 280 m and a chord of 20 m. Each of them is divided into six equal sections. The wings themselves have a maximum lift coefficient of $C_L = 3$ when fully deployed. This gives them a drag coefficient of $C_D = 0.256$ and a moment coefficient of at most $C_M = 0.2$.

To determine these values and wake recovery characteristics, an analysis of the effects of lift-generating airfoils was performed by assuming the potential flow and effects of each of the wings could be modelled as a pair of circulation regions. These circulation regions cause upwash, which clears the wake regime of slower-moving air and removes losses due to proximity to other turbines. To find the needed circulation by each wing, along with the number of wings needed, energy density was computed based on the distance covered by the undisturbed flow. This was done before all the points which started in the region bound by the wind turbine left that wake boundary.

For the power production of a single turbine, the width was varied with even multiples of rotor diameter, while the height was fixed at 280 m. For each wing present, three meters were taken from the height used to compute power per turbine. Results for this analysis can be seen in Figure 1. The figure shows energy densities achieved for designs with different power ratings (corresponding to different widths). The horizontal dashed line shows the minimum value dictated by requirement **UR-02**.

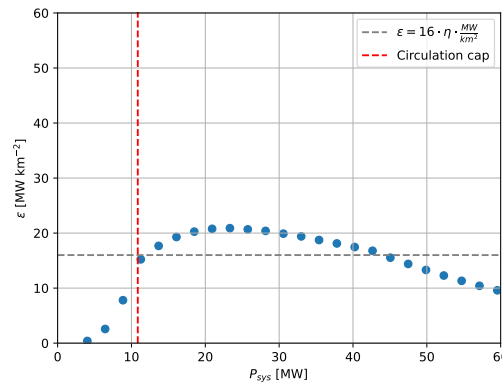


Figure 1: Results of analysis for WCT-CFG-02, which was the name of the chosen configuration

After examining the results of the analysis, a configuration with the circulation of $330 \text{ m}^2 \text{s}^{-1}$ was selected. Since this was examined at speed of 11 m s^{-1} , this gave that $c \cdot C_L = 60 \text{ m}$. Originally, design with $c = 12 \text{ m}$ and $C_L = 5$ was considered, but in order to make it easier to improve storm survivability (with winds of up to 70 m s^{-1}), it was changed to $c = 20 \text{ m}$ and $C_L = 3$.

The design for each wing is to have a two-element cambered airfoil, with both Kruger and triple flaps, which dramatically increase its C_L to the required value. These would retract and need to bring the lift to as low as $C_L \leq 0.074$ in order to survive storms. The wing sections would be integrated with the structural elements, with the diagonal elements on the bottom of each cell as the base supporting the first and biggest part of the multi-element airfoil. The combined mass of the four wings is estimated at 648 t, having the mass split halfway between the HLDs and the steel spars, all made from medium carbon steel.

Rotors

The design of the rotor began by choosing an airfoil and the shape. The airfoil was chosen to be the same as the one used by [Jamieson et al.](#), since the performance characteristics of said airfoil were favourable [3]. The choice of the shape required a trade-off, which included V, H, Spiral, Darrieus and Savonius type as possible candidates. Ultimately the H-type rotor was chosen, due to its high packing ratio, aerodynamic performance, and easy manufacturability.

The next step in the design process was choosing a strategy for power production. The power production strategy influenced both the sizing of the drive train and the sizing of the structural components. The goal of designing a power production strategy is to maximise energy production while keeping the wear and tear on the turbine minimal. It was decided that for the MR-TBD it is best to use a simple power control scheme, keeping the power production uncapped until the rated wind speed and capping the production at 30 MW for wind speeds above the rated wind speed. This is a good scheme for energy production, but might cause some large loading. However, it has been calculated that the impact on the structural components was minimal and the benefits of extra energy production (higher revenue) outweigh the extra cost of a stronger structure. From the power production strategy the loading of the shafts was established.

The main shaft was sized during the detail design phased. Considering the requirements to withstand the torque of the rotors during the entire operational envelop while also being loaded in compression by its own weight and the weight of the blades and struts, the shaft was sized using fatigue and yielding failure modes. Buckling was not considered as the height of the shaft is segmented by seven equidistant deep groove ball bearings, which were treated as pin supports. Using the standard of infinite life for the constituent material, low carbon steel, the shaft was designed to have a hollow cylindrical profile, with a diameter of 1.62 m and a thickness of 24.3 mm, spanning 270 m and yielding an individual mass of 260 t. The deflection of the shaft in the most extreme load case considered was evaluated at 3.84 mm at the midway point between each pair of bearings. This was determined to not create connection conflicts with the bearings, which were evaluated based on their reaction loads to weigh 1 t each.

Drive train

The architecture of the drive train will be presented along with a few design decisions taken. In the main, the direct train is a conventional one, including generator, gearbox, brake and multiple couplings.

The trade-off that has been made in the previous work concluded that the best generator architecture to use was DFIG. Furthermore, it was also decided to use brushless DFIGs since they are made of more sustainable materials and their maintenance is easier. Even if they are slightly more expensive than their brushed alternatives, for instance, permanent magnet synchronous or electrically excited synchronous generators, they are more reliable. One particular company that would be able to develop such elements with the specified characteristics, around 5 MW, is ABB. However, the largest ever built brushless generator can produce a maximal power of 500 kW [4]. The generators will be placed horizontally, at the bottom part

of the truss structure, in order to allow easy maintenance. In case of failure, they could be disconnected and immediately replaced. The broken item would be sent onshore to be fixed.

The calculated torque needed to stop one shaft spinning at a rate of 24 RPM is roughly 6.61 MNm. This torsion is the one that has to be applied immediately on the main shaft. This is not achievable with modern technology on the market. Such a high torque imposes to place the brake after the gearbox, where the torsion will be much lower. Normally, it would have been convenient to have the brake before the gearbox since when stopping the mechanism, the gearbox does need to be operating. After being reduced, the required moment for stopping the one main shaft of wind turbine is about 131 kNm.

According to the rated RPM of the generator, which should be similar to the high-speed shaft of the transmission unit, the conversion ratio of the gearbox should be 43. What is unique about the required product is that it needs to be right-angled. Since the main shafts connecting the rotors have a vertical rotational axis and the generator's one is horizontal, a bevel gear is necessary. Having the gearboxes, which have the highest probability of failures, and longest downtime, located at the bottom of the truss structure is helpful since they can be replaced easily in case of failure, as well as generators.

Yaw bearings

The yaw control subsystem design consisted of sizing the yaw bearing arrangement to withstand structural and operational loads. It was decided to go with two yaw bearings, a bottom bearing located at the base of the tower and a top bearing at the top of the monopile, located at 140 m height in the tower, to reduce tilting moments. The bearings were sized to withstand axial forces due to weight and radial forces due to maximum produced thrust at the rated windspeed. The dynamic rating C_{dyn} for the bearings is established from the conservative assumption that the tower will have to yaw 180° every 30 minutes to align with the wind. The resulting specifications for both bearings are presented in Table 1.

Table 1: Top and bottom bearing specifications

Parameter	Top bearing	Bottom bearing
Inner diameter [m]	10	15
F_a [kN]	68800	11700
F_r [kN]	17200	2920
C_{stat} [kN]	171353.3	29123.8
Lifetime revolution req.	219000	219000
C_{dyn} [kN]	54139.9	9204.8
Estimated mass [kg]	19000	35000

Furthermore, the bearings will need to include outward facing gears in order to be driven by the electrical yaw drives. They will also need corrosion protection to level C5-M (level of corrosion protection required for offshore environments)¹ to prevent the salinity of the water from reducing their service life.

Foundation

The foundation subsystem is required to transfer all loads from the tower to the seabed, while also being subjected to aerodynamic and tidal forces. At the early stages of the design concept three concepts were considered for the foundation, namely a floater, an XL monopile and a jacket configuration. Using trade-off criteria such as structural mass, maintainability, lifetime operations, ecological impact and usable depth, it was decided that the monopile represented the best option. During preliminary design the monopile was evaluated at rated wind speed conditions against Euler column buckling and yielding and

¹ URL: <https://www.liebherr.com/shared/media/components/documents/grosswaelzlager/liebherr-slewing-bearings-product-catalogue-en-metric-web.pdf> [cited: 18 June 2023]

was sized to have a constant diameter of 15 m and thickness of 160 mm, leading to a mass of 7141 t. It is important to note that at this point in the design only yaw bearing was used, leading to the foundation to be only 60 m high from the mudline.

During the detailed design phase the yaw subsystem evolved to incorporate two slewed bearing at heights 30 m and 170 m above sea level respectively. This forced the monopile design to change to a total height of 200 m from mudline and aided the gradual transfer of topside loads onto the foundation. At this time more accurate estimates and models were used to determine the aerodynamic and tidal loading of the system. The monopile was iterated to consider yielding von Mises stress and to avoid both local and global buckling. Additionally, this enabled the designer to vary both the diameter and the thickness of the subsystem. This yielded a geometry that varies from a diameter of 17.8 m with a thickness of 100 mm to a diameter of 11 m with a thickness of 60 mm. Due to corrosion and plastic deformation concerns S355J manganese steel alloy graded for marine conditions was used, leading to a monopile mass of 6200 t.

The possibility of foundation's collapse as a consequence of vibrations due to tidal loads is small, but not impossible. Results show that resonance is not expected during storms or normal conditions when the wind speed varies from 1 m/s to 25 m/s. The problematic scenario is when very exceptional conditions such as hurricanes, cyclones, typhoons, or tornadoes are experienced. Nevertheless, it is desired to equip the monopile with multiple dampers to reduce the risk of failure.

Reliability, Availability, Maintenance, and Safety

Preliminary RAMS analysis was performed, based primarily on research by [Carroll et al.](#), who investigated unexpected failures of offshore wind turbines. Assumptions were made based on the changes from the traditional HAWT to the design presented in this report [5]. These were accounted for by changing reliability and material costs for individual components.

The results of these assumptions and scaling factors are shown in Table 2, which shows relative costs of maintenance based on what assumptions are applied; first none, then only the faults are adjusted, next only the material costs, and lastly both. This does not include reductions in costs due to lower downtime and ease of access. Assuming this also mostly to scheduled maintenance, this would mean that the assumptions made by the cost model are correct.

Table 2: Summary of effects of assumptions on relative maintenance costs

Assumptions Made	Baseline	Adjusted Faults	Adjusted Costs	Adjusted Both
Relative Costs [-]	100.00 %	61.68 %	65.05 %	40.67 %

Based on the adjusted failure rates, the lowered repair time needed for unscheduled maintenance was also found, which was reduced by 18 %. Assuming the same reduction applies to scheduled maintenance, the availability of the system would increase to a total of 91.8 % based on [6].

In terms of safety, the system needs no special considerations, given that the system can be operated from a remote control room, only needing visits for maintenance, for safety during maintenance, safety rails and guards are installed. For ease of access, the frame structure has integrated lifts, catwalks, and stairs, all with safety guards to protect against strong winds.

Control, operations and logistics

The designed wind turbine will be equipped with over fifteen types of sensors that will continuously measure the atmospheric conditions, the temperature of components, moments and loads experienced. Furthermore, cameras and microphones will be used for visual and audio inspection.

On the topic of maintenance and logistics, installation, decommissioning and storing and fixing parts need to be taken into account. First off the manufacturing of the components is to be done mainly in Rotterdam. Multiple manufacturers with plants in the surrounding area have been chosen for the steel components as well as the monopile. The more specialised components have been chosen via known manufacturers in the Netherlands. For the installation, it was decided to assemble to tower entirely onshore at the Damen Verolme Rotterdam shipping yard and then transport it to the Ijmuiden Ver zone using floaters or dynamically positioned vessels. In terms of the monopile, a vibro-hammer will be used in order to reduce the impact on the marine life.

One of the most important aspects concerning the design of the wind turbine is the ease of performing the maintenance work. Since both the repairing duration and downtime needed to be optimised, it was decided to place the higher failure-rated elements, in particular gearboxes, generators and converters at the bottom of the tower. In case of any malfunctions that cannot be solved in a relatively short time at the location, a spare part will be transported from the depot and immediately replaced. In this manner, the time in which the wind turbine does not work at the nominal capacity, is significantly diminished. The depot will be placed in Port of Rotterdam which will allow prompt transportation and accessibility. In the wind turbine's last stage of life, the assembly needs to be decommissioned. Similarly to the installation, the entire tower, including all components, will be transported back to shore. The removal of the monopile from the ground will be made with a lifting tool that also uses a vibro-hammer. In this fashion, the aquatic habit will be more protected. The companies that have been stated for proving such services are Heerema Marine Contractors, Cape Holland, and Boskalis.

Sustainability

One of the main pivots of this project is its sustainability aspect. To assess the sustainability of the MR-TBD turbine, a life cycle analysis was performed. The objective of this study was to assess the environmental impact of the final design throughout all the phases of its life cycle. Initially, a life cycle inventory was performed where all the elements and materials of the final structure were listed. After that, the overall emissions and energy consumption of the following design phases have been considered: extraction of materials, manufacturing, transportation, operations, decommissioning and recycling. For the analysis of each of these design stages' impact, the MaterialUniverse database of Ansys Granta was used to find all the necessary numbers. Using the EcoAudit tool present in the software, the following results were obtained. In terms of percentage, the previously mentioned life cycle phases account for 68.5%, 26.5%, 0.5%, 0.00%, 4% respectively. After the analysis of the individual phases, the energy consumed and the CO_2 kg generated per year were estimated. The turbine is going to consume 7.28e6 MJ per year and 5.55e5 kg of CO_2 per year. This leads the MR-TBD turbine to be 37% less polluting than conventional HAWT.

Technical Risk Assessment

A technical risk assessment was performed on the conceptual design. This involved identifying the technical performance, cost, scheduling, sustainability, and programmatic risks. The technical performance risks were further divided into subsystem risks. The largest identified risks included lightning strikes, harm to surrounding ecosystems in the form of pile driving noise or bird collisions, corrosion of the tower and bearings due to the saline environment, and failures of certain critical components such as the yaw bearing and shaft brakes. On the subsystem level, there were considerable risks arising from failure with WCT retraction during high wind speeds and YCT instability during windspeeds higher than the rated wind speed.

For each of these high risks, mitigation measures were identified to reduce the likelihood or consequences, resulting in a new post-mitigation risk matrix. Lightning remained a relatively high risk even after the mitigation procedures, so a contingency strategy involving unmanned inspections and maintenance after thunderstorms was proposed.

Requirements and Compliance

The compliance of the system to the user, mission, and standard requirements was examined as well. The most important requirements and their compliance are listed below. All but one of the user requirements were met. In hindsight, requirement **UR-02** was unfeasible and should have been re-negotiated.

UR-02: The system shall have energy density of at least 16 MWkm^{-2} - System energy density: a bit under 20 MWkm^{-2} ✓

UR-03: The system shall have 45 % lower LCoE - System LCoE: 29.6 % lower ✗

UR-07: The system shall have decreased rare earth metal use compared to traditional HAWTs - System uses no rare earth metals ✓

SR-03: The system shall withstand extreme wind conditions, occurring every 50 years - System withstands loading due to wind and waves at their highest values in 50 years

.

Contents

List of Symbols	xiii
1 Introduction	1
1.1 Introduction	1
1.2 Requirements.	2
2 Market analysis	4
2.1 Analysis of Competition in the Market	4
2.2 Democratising the Offshore Wind Turbine.	4
3 Site selection	6
3.1 Turbine Location	6
3.2 Wind Model.	8
3.3 Environmental Loading	12
3.4 Load models	13
4 Budgets	16
4.1 Description of the Budget Model	16
4.2 Budget of the Proposed Design	17
4.3 Conclusion and Final Budgeting	21
5 Design trade-offs	22
5.1 Rotor Orientation Trade-off	22
5.2 Yaw Control Trade-Off	22
5.3 Foundation Trade-Off	23
5.4 Drive Train Trade-Off	23
5.5 Triangle vs Rectangle based structure Trade-Off.	24
5.6 Shaft mounting position Trade-Off	25
5.7 Rotor Selection Trade-Off	26
5.8 Individual element selection Trade-Off.	27
6 Design analysis	29
6.1 TWR analysis	29
6.2 WCT Analysis	39
6.3 RTR analysis	46
6.4 YCT Analysis	51
6.5 DRT Analysis	54
6.6 FND Analysis	57
7 Final design	66
8 Production, operation and logistics	69
8.1 Production plan	69
8.2 Reliability, Availability, Maintainability, and Safety	71
8.3 Operations	78
8.4 Maintenance and logistics.	92
9 Cost analysis	95
9.1 Informing the Budget with Design Data	95
9.2 Weight Average Cost of Capital	96
9.3 Time to Break Even.	96
10 Sustainability	97
10.1 Environmental sustainability	97
10.2 Economic	102
10.3 Social	103
11 Technical Risk Assessment	104
11.1 Risk Identification	104
11.2 Risk Management	105

12	Compliance matrix	109
12.1	Compliance of the subsystems	109
12.2	System compliance matrix.	113
13	Future development	115
13.1	Project design and development logic	115
13.2	Future design Gantt chart	115
14	Conclusion	117
A	Vibration analysis	125
B	LCA detailed results	127

List of Symbols

		LIDAR	light detection and ranging
		ML	Mudline
ACFM	Alternating Current Field Measurement	MR	mission requirement
AEP	Annual Energy Production	MR-TBD	Multi-Rotor Turbine Block Design
CFD	Computation Fluid Dynamic	MRS	Multi-Rotor System
CTV	Crew Transfer Vehicle	NEWA	New European Wind Atlas project
DD-PMS	Direct drive with a permanent magnet synchronous	O&M	operations and maintenance
DD-PMSG	Direct drive with a permanent magnet synchronous generator	OWT	offshore wind turbine
DFI	double fed induction	PCB	Printed Circuit Board
DFIG	Double Fed induction generator	PMS	permanent magnet synchronous
DP	Dynamically positioned	PMSG	permanent magnet synchronous generator
DSE	Design Synthesis Exercise	RAMS	Reliability, Availability, Maintenance, and Safety
DT	digital twin	REM	Rare Earth Metal
EES	Direct drive with an electrically excited synchronous	RPM	rotations per minute
EESG	electrically excited synchronous generator	SCADA	Supervisory Control and Data Acquisition
EPS	Emergency Power Source	SKF	Svenska Kullagerfabriken
FKM	Forschungskuratorium Maschinenbau	SR	standard requirement
FR	functional requirement	SWL	Still Water Level
GHG	Greenhouse Gas	TSR	Tip Speed Ratio
HAWT	Horizontal Axis Wind Turbine	TtBE	Time to Break Even
HAWT	Horizontal axis wind turbine	UN	United Nations
HLD	high lift device	UR	user requirement
HLV	heavy lift vehicle	VAWT	Vertical Axis Wind Turbine
IEC	International Electrotechnical Commission	WACC	Weighted Average Cost of Capital
LCA	life-cycle analysis	WRF	Weather, Research and Forecasting
LCoE	Levalized Cost of Electricity	$\bar{\lambda}$	Reduced slenderness
		β_m	Moment factor

ϵ	Power density	MWkm ⁻²	C_D	Drag coefficient	-
Γ	Circulation	m ² s ⁻¹	C_L	Lift coefficient	-
κ	Flexural buckling	-	C_M	Moment coefficient	-
ω	Frequency		C_n	Inertia coefficient	-
ρ	Density	kg/m ³	C_P	Power coefficient	-
σ	Normal stress	MPa	C_T	Thrust coefficient	-
σ'	Von Mises stress	MPa	c_{diam}	Inner to outer diameter ratio	-
σ'_a	Von Mises alternating stress	MPa	c_{diam}	Inner-to-outer diameter ratio	-
σ'_m	Von Mises mean stress	MPa	C_{dyn}	Dynamic rating	-
τ	Shear stress	MPa	C_L and C_R	Foundation flexibility coefficients	-
			C_{stat}	Static rating	-
Δn	Slenderness parameter	-	D	Drag force	N
η_L and η_R and η_{LR}	Foundation stiffness parameters-	-	d_o	Outer diameter	m
		-	d_o	Outer diameter	m
\mathbf{K}	Stiffness matrix	Nm ⁻¹	D_T	Average outer diameter	m
\mathbf{M}	Mass matrix	kg	E	Elasticity modulus	GPa
τ	Torque	Nm	e	Oswald efficiency factor	-
θ_{rel}	Relative wind angle	rad	F	Force	N
\vec{d}^e	Direction vector of element e	m	f_1	Bearing load factor	-
\vec{F}	Force vector	N	f_{FB}	Natural frequency of the fixed base	Hz
\vec{r}	Position	m	f_N	Natural frequency of the fixed base-monopile system	Hz
\vec{u}	Vector of node displacements	m	g	Gravitational acceleration	m/s ²
\vec{v}	Velocity	ms ⁻¹	H_s	Significant wave height	m
A	Aspect ratio	-	H_{50yr}	50-year return period wave height	m
A	Cross-sectional area of a truss element	m ²	j_{load}	Load safety factor	-
A^*	Area per unit length	m	$j_{material}$	Material safety factor	-
c	Chord of the wing	m	k	Wave number	m ⁻¹
C_τ	Torque coefficient	-	K_{rep}	Bearing load increase factor	-

L	Length of an element	m	T_B	Breaking torque	Nm
L	Lift force	N	T_F	Friction torque	Nm
L' and L^*	Lift per unit span	Nm ⁻¹	T_J	Inertia torque	Nm
l_{loss}	Lost effective area	m	T_L	Load torque	Nm
M_p	Plastic moment resistance		u_c	Water current speed	m s ⁻¹
m_{RNA}	Mass of the rotor-nacelle assembly	kg	V	Transverse shear load	N
m_T	Mass of the tower	kg	V^*	Volume per unit length	m ²
N_e	Elastic buckling force		v_∞	Free-stream velocity	m s ⁻¹
N_p	Plastic compression resistance		v_{rated}	Rated windspeed	m s ⁻¹
S_e	Endurance strength	MPa	v_{rel}	Relative windspeed	m s ⁻¹
S_y	Yield strength	MPa	W_p	Plastic resistance capacity	
S_0	Static safety factor	-	d	Inner diameter	m
S_{ult}	Ultimate tensile strength	MPa	g	Gravitational acceleration	m/s ²
T	Torque	Nm	I	Second moment of area	m ⁴
t	Time	s	J	Polar moment of inertia	m ⁴
T_s	Significant wave period	s	m	Mass	kg
t_T	Average thickness	m	Pd	Power density	

Introduction

1.1. Introduction

In the last 20 years, the demand for sustainable energy has increased considerably. Wind energy is one of the most sustainable ways of generating electricity, as power is extracted directly by air, and no toxic emissions are produced. Furthermore, both onshore and offshore wind turbines result in being highly cost-effective for generating electricity. The main disadvantage of this technology is that the best way of increasing the amount of energy produced is by scaling up the entire structure. This raises an issue, namely that if the rotor area scales by the square of a size factor, the turbine mass scales by the cube of that very size factor. This can lead to unfeasible structural weights. Consequently, while decreasing the number of units per megawatt is beneficial for less complex infrastructure and lower maintenance costs, costs increase considerably due to the higher mass of the structure.

With this background in mind, the goal of this project was to spend ten-week to produce a conceptual design of a multi-rotor VAWT system. The following report aims to describe the final stages of the design and analysis. The mentioned paper can be seen as a continuation of the Baseline report and the Midterm report [7, 8] in which crucial elements such as subsystem requirements, preliminary design options, and initial design were presented.

The system presented in this report uses a MR-VAWT (Multi Rotor Vertical Axis Wind Turbine) design to dramatically increase the energy density of a wind farm significantly. This lowers the environmental impact of wind farms, as it reduces the amount of space needed to meet energy needs. Along with reducing the space needed for the wind farms, this allows for packing more turbines into the more energy dense areas, which allows for even greater power production. Besides improving sustainability by reducing the usage of space, the system also dramatically improves the sustainability by eliminating the need for rare earth metals used to produce permanent magnets for its generators. The system also uses steel instead of composites for its turbine blades. This allows all for them to be recycled and be produced simply by extruding them. Lastly, the system improves the social aspect of sustainability by consisting almost entirely from components which do not need a large, specialised manufacturer, thus allowing reliance on local manufacturers and suppliers instead.

The structure of the report is as follows: First the project and its scope are introduced, along with the purpose and the user requirements/constraints. This is followed by Chapter 2, which contains the market analysis performed for the design. Next is Chapter 3, which describes the site selection procedure, as well as what was the final site, which was selected for the turbine. It also presents the wind speeds and distribution at the specified site and the load cases, which arise from it. Last thing in that chapter is the wave model, which comes into play with the under-ocean part of the system.

The next chapter, Chapter 4, contains the budgets needed by the design, with primary focus on the LCoE of the system in relation with user requirements. This chapter is followed by Chapter 5, which contains some design trade-offs related to design choices which were not yet made in the midterm report [8]. This is followed by Chapter 7 and Chapter 6, the former being a brief summary of the latter. These detail the analysis and results of more detailed design of the individual subsystems of the system, as well as verification for various models used.

After the presentation of the design analysis and results, the concepts for its production, operation, and logistics are detailed in Chapter 8. This is followed by cost analysis for the design, presented in Chapter 9. Cost analysis is followed by Chapter 10, which approaches sustainability of the design, both in the quantitative way and the in the qualitative way.

The report is then continued with Chapter 11 which shows details technical risks the design faces, along with some mitigation strategies. This is followed by Chapter 12. This chapter shows compliance with the user requirements and other crucial requirements. The report is then concluded by a conclusion in Chapter 14.

1.2. Requirements

This section presents the user requirements the design was subject to. They are primary drivers of the design and have to be satisfied by the design. These are the requirements which were given by the customer, then translated into technical requirements, and lastly (re-)negotiated in for some. Compliance of the design with these requirements can be seen in Chapter 12. The requirements are:

UR-01: The system shall have a power rating of at least 30 MW

UR-02: The system shall have a power density of at least 16 MW km^{-2}

UR-03: The system shall have a 45 % lower levelized cost of energy compared to traditional horizontal axis offshore wind turbines

UR-04: The system shall have multiple rotors

UR-05: The system shall have lower lifetime emissions than traditional horizontal axis offshore wind turbines

UR-06: The system shall have increased material recyclability than traditional horizontal axis wind turbines

UR-07: The system shall have decreased rare metal use compared to traditional horizontal axis wind turbine

UR-08: The system shall be installable offshore

Subsystem definition

In the previous design phase, the system was broken down into eight subsystems, the scopes of which are presented in Table 1.1. The table has the full name of the subsystem, its identifier, which is used thorough the report. The third column has a description of the scope of each of the subsystems. Last column has the section in which it is designed.

Table 1.1: Subsystem definition and location in the report

Full name	Identifier	Scope	Design section
Tower	TWR	Structure above the foundation, which supports the rest of the system. The tower transfers loads from other subsystems to the foundation subsystem, to which it is attached on bearings. It is attached to the rotors by the means of bearings and all other components are mounted directly on it.	Section 6.1
Wake control	WCT	Downforce generating surfaces, used to generate large vortices in order to move the wake upwards and out of the way of the next turbine. Its function is to allow for higher energy density. It is integrated directly onto the TWR structure and can retract during storm to limit the loads.	Section 6.2
Rotor	RTR	Rotor blades, bearings, and breaks, which are generate lift, which in turn applies a torque on the shaft of the drivetrain to extract power from the wind into rotational energy.	Section 6.3
Yaw control	YCT	Motors and controllers responsible for yawing the tower in the desired direction. It helps the system achieve higher efficiency by helping it align with the wind better and can turn the structure away from strong winds during the storm.	Section 6.4
Drive train	DRT	Shaft, gearbox, generator, and supporting components, which focus on turning the rotational energy of the rotors into electricity.	Section 6.5
Foundation	FND	Part of the supporting structure which is attached to the ocean floor and extends up to 170 m above the surface. It attaches itself to the tower by the means of two bearings and is the access point for maintenance.	Section 6.6
Operations control	OCT	Collection of systems and components involved in supporting nominal operations and maintenance of the system. This is quite general and would be further broken down in the following phases of the design.	Section 8.4
Power control	PCT	Systems and controllers involved in controlling the power produced and regulating the loading of the system. It does so by controlling the rotor and drivetrain to maintain target shaft RPM.	Section 8.3

Market analysis

One of the most important factor of any new wind turbine design is its market feasibility. To determine if MR-TBD can become successful in the market, the market has to be evaluated. This chapter will give an overview of how the market is likely to develop up until 2050. This is presented in Section 2.1. The market of offshore wind turbines is also very concentrated. Meaning that there only a few companies that can make large OWTs. How the proposed design address this problem is shown in Section 2.2.

2.1. Analysis of Competition in the Market

"LCoE is defined as the revenue required (from whatever source) to earn a rate of return on investment equal to the discount rate (also referred to as the weighted average cost of capital or WACC) over the life of the wind farm. Tax and inflation are not modelled. In other words, it is the lifetime average cost for the energy produced, quoted in today's prices [9]." To fully capture the advantages of the proposed design, a more holistic view at the pricing is required. WindEurope has presented a plan to expand the production of electricity in the North Sea by 380 GW by 2050 [1]. An expansion of this size with a traditional solution would mean using all of the very low LCoE (under 50€/MWh), as well as all of the low LCoE (between 50€/MWh and 65€/MWh) spots available in the North Sea. There also would be the need to put some wind turbines in the medium LCoE (between 65€/MWh and 80€/MWh) zones. The plan also specifies the amount of power planned per cost bracket. For very low LCoE the projection is to install 112 GW, for low LCoE 264 GW and 4 GW at medium LCoE locations. With that information, the LCoE of the whole WindEurope project can be calculated. It comes to 54€/MWh. This will be the benchmark for the project and the requirement to lower the LCoE by 45%, meaning the proposed design should achieve an LCoE of around 30€/MWh.

Another way to measure the design performance is to look at what happens after 2050. In 2050 all low-cost areas for offshore wind turbines in the North Sea are expected to be fully developed. That means the only way to increase the power capacity of the North Sea is to develop areas that have LCoEs of 65€/MWh or higher. At the same time turbines that had been built in the 2010s and 2020s will need replacement. All of these will have been built in the very low LCoE zones available at that time. This means, that if a design has a higher power density than the wind farms being replaced, power capacity can be increased in the North Sea without the need to build in expensive areas. Therefore, increasing power capacity using conventional wind turbines in 2050 will cost at least 65€/MWh. The design being proposed can achieve a similar power increase by replacing old wind farms without increasing the LCoE. In this scenario, the benchmark LCoE will be 65€/MWh. Therefore the design would need to have an LCoE of around 36€/MWh to hit the 45% reduction target.

2.2. Democratising the Offshore Wind Turbine

One glaring issue with the current offshore wind turbine market is a de facto duopoly. Only Siemens, General Electric, and Vestas are currently producing wind turbines of 10 MW and more for the North Sea. Such a small number of manufactures limits the production throughput and the lack of competition drives prices up. This situation mainly stem from the difficulties with designing and manufacturing the blades for HAWTs. The adverse loading on the blade necessitates use of composites; the coupled vibration requires advanced computational methods to ensure safe operation and the varying linear velocity long the blades calls for continuously varying airfoils, making manufacturing almost impossible [10–12]. All these challenges makes the entry of a new company in the OWT market, unlikely, keeping the duopoly in perpetuity.

One of the goals of the MR-TBD is to enable smaller design firms and local manufactures to take part in the OWT business. The switch from a single rotor HAWT to a multi-rotor VAWT, should eliminate all the challenges mentioned before. The nature of the proposed design also lends itself to manufacturing and assembly in facilities made for the marine industry. This eliminates the logistic problems with transporting HAWT components, made in specialised plants located far from the shore. Simplifying logistics is another way the design is more approachable for smaller companies. With these changes in mind, it is clear that the proposed design significantly increases the democratisation of OWT and in theory could dethrone the duopoly.

3

Site selection

3.1. Turbine Location

Before wind turbines can be installed, a siting study must be undertaken to find the most suitable location in which the farm can be placed. Selecting the correct location for the multi-rotor VAWT considered in this project is crucial to maximising its energy production and overall performance under different conditions. This section of the report presents the results of the location study performed to select the most suitable area in the Dutch North Sea to host the wind turbine in discussion.

The main objective of the siting study is to locate the system such that the energy cost is maximised while minimising its environmental impact. The selection process involves carefully considering various factors to ensure the wind turbine operates safely and efficiently, while respecting all the regulations. Firstly, assessing wind resources is essential to determine the energy potential of a specific site. This is needed since the wind of a particular area in the sea determines the wind and wave loads the structure may be subjected to during its operation. Environmental factors, such as protected habitats, bird migration routes, and visual impact, must also be considered. It is crucial, to find an area that is the best compromise between potential harm to the environment and efficiency. Other aspects that must be considered in selecting a site are the site topography, accessibility, grid connection and economic viability.

The Dutch North Sea offers several designated areas where it is possible to build offshore wind farms ¹ according to the Dutch Offshore Wind Energy Roadmap. The objective of the Dutch government is to have 11.5 GW of offshore wind in its waters by 2030 [13]. These areas have been identified and allocated by the Dutch government for the development of offshore wind farms based on various factors. These include wind resources, technical feasibility, environmental considerations, and stakeholder engagement. Moreover, the Dutch government has implemented a tendering process to allocate these areas to developers through competitive bidding. Consequently, this has allowed to limit the location selection to a few restricted areas in the Dutch North Sea where the grid is already/partially present and all the necessary studies (environmental, geological etc.) have been performed. Figure 3.1 ³ presents all the areas that are under construction (green areas), in development (dotted areas), operational (blue areas), and available (empty areas) for future projects.

¹<https://english.rvo.nl/information/offshore-wind-energy/hollandse-kust-west-wind-farm-zone> [cited: 20 June 2023]

²<https://www.noordzeeloket.nl/en/functions-and-use/offshore-wind-energy/free-passage-shared-use/ijmuiden-ver-wind-farm-zone/> [cited: 20 June 2023]

³https://english.rvo.nl/sites/default/files/2023/05/Roadmap-Offshore-Wind-Energy-May-2023_0.pdf [cited: 20 June 2023]

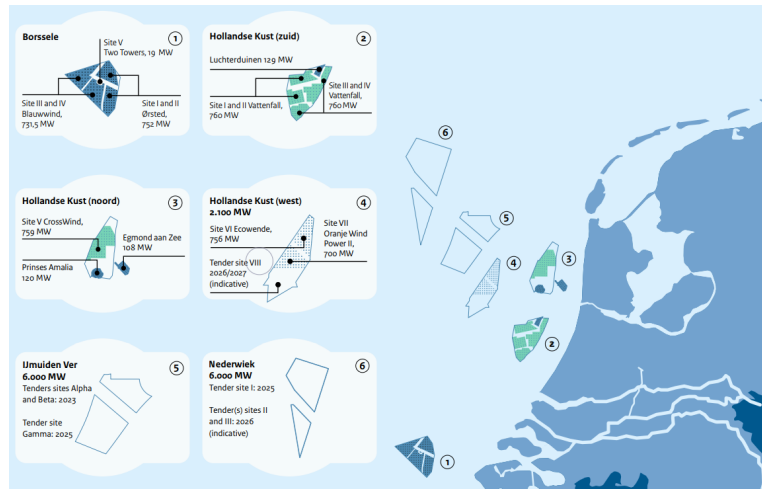


Figure 3.1: Map of the Dutch wind farm sites, comprising IJmuiden Ver Wind Farm Zone

After an availability and feasibility study of the different areas that could host the MR-TBD turbine, three wind farm zones were selected and explored in more detail. The three areas are listed as follows:

- **Hollandse Kust**: located off the coasts of Zuid-Holland and Noord-Holland provinces. It has been divided into several zones, each identified by a specific number. These zones are sequentially numbered from north to south and 18 to 38 km from the coast. While Hollandse Kust Zuid and Noord are already under construction or operational, Hollandse Kust West presents an area which could be feasible for the MR-TBD. Hollandse Kust (west) Wind Farm Zone will accommodate 1400 MW of offshore wind power capacity. Hollandse Kust (west) Wind Farm Zone will accommodate 1.4 GW of offshore wind power capacity and will become operational in 2025⁴.
- **Nederwiek**: this zone is 90 km off the west coast of the Netherlands. Three Wind Farm Sites will be designated in the Wind Farm Zone as NW Wind Farm Sites I, II and III. All these sites are 2 GW in size. The total surface area of the Wind Farm Sites within the zone is approx. 600 km². These Wind Farm Sites will accommodate 6 GW operating from 2030 onwards.⁵
- **IJmuiden Ver**: this wind farm site lies 54 kilometres from the coast to the northwest of the Hollandse Kust (west) wind farm zone. The area comprises four sites, each delivering 1GW from 2027 onwards. The IJmuiden Ver zone will comprise three offshore grid connections and corresponding transformer platforms: Alpha, Beta, and Gamma. These will connect the offshore wind farms at the I & II, III & IV, and the newly planned V & VI sites to the grid⁶. The area is 650 km² in size.⁷

After considering these three options' most important advantages and disadvantages, the IJmuiden Ver wind farm zone was selected. The motivations for this decision are multiple and depend mostly on the characteristics of the individual zones.

Starting from the Hollandse Kust, this option was discarded for three reasons. These are environmental considerations, space considerations, and time considerations. The Hollandse Kust West site is the closest option to the shore. This particularly sensitive environment for marine/flying ecosystems and coastal

⁴<https://english.rvo.nl/information/offshore-wind-energy/hollandse-kust-west-wind-farm-zone> [cited: 20 June 2023]

⁵<https://offshorewind.rvo.nl/cms/view/91063764-5eb7-428e-9c6e-e38fcf3adf22/general-information-nederwiek> [cited: 20 June 2023]

⁶<https://www.offshorewind.biz/2021/10/26/rvo-talks-6-gw-for-ijmuiden-ver-offshore-wind-zone/> [cited: 20 June 2023]

⁷<https://www.noordzeeloket.nl/en/functions-and-use/offshore-wind-energy/free-passage-shared-use/ijmuiden-ver-wind-farm-zone/> [cited: 20 June 2023]

aesthetics represents an issue that cannot be ignored. One of the most important aspects of this project is, in fact, sustainability. Installing and operating such a huge structure relatively close to the shore would be unsustainable, causing several problems for the ecosystems and local stakeholders. Additionally, the shape of the area is not favourable for ship routes compared to the other options. While the other two sites considered present a very wide shipping lane (see Figure 3.1), Hollandse Kust West does not, requiring the design of a careful coordination with existing shipping routes and maritime activities to ensure safety and minimise any conflicts or disruptions. Finally, regarding time management, this site option is the least optimal since it requires a final design by 2025. This date is too early for the MR-TBD project, which will probably not be ready at that time.

Moving to the considerations on the Nederwiek site, some issues were encountered as well. Firstly, the area is the furthest from the shore. The main benefit of this is that wind conditions are more favourable, allowing for potentially higher energy production. On the other hand, this may represent a problem since installation, operation, and maintenance procedures may become more of a challenge compared to the other sites that are more accessible. Installing the turbine in such an area will require longer transmission distances and potentially more complex logistic strategies, which can increase costs and operational complexities. This is also a problem for the sustainability of the project. Another issue is dictated by the site development being still at a very initial stage. In fact, the grid connection is not yet present, and the plan for the project still needs to be fully defined. In light of this, this option was also discarded due to the larger downsides of the area compared with the benefits of power production. However, this option may still be considered in case of delays in the MR-TBD project.

Finally, the IJmuiden Ver wind farm zone is the last option to be considered. This area represents the best compromise between all the previously discussed options. In terms of location, the site is located in a perfect area for multiple reasons. The area has excellent wind conditions because it is far from the coast. The distance from the coast is enough to not be visible to the local stakeholders and not to disturb the wildlife that is more concentrated in that area. In addition, compared to the Hollandse Kust, the IJmuiden Ver zone also offers more space for larger-scale wind farm developments due to its deep waters. This is beneficial for this project due to its extremely large scale. Moreover, as offshore wind technology continues to advance, the IJmuiden Ver area provides the opportunity to implement alternative designs to conventional wind turbines.⁸ Regarding time management, the IJmuiden Ver project results to be the most suitable option that best matches the project's expected duration. A project duration of 4 to 5 years to start operating the turbine in 2027 is reasonable for the duration estimation of the project stipulated by the team. Finally, the already existent DC grid connection and the project's readiness to be started make this option optimal for the placement of the wind turbine discussed in this project.

3.2. Wind Model

It is common knowledge that offshore winds are stronger and less turbulent than onshore ones due to the absence of obstacles that may disturb the airflows⁹. When designing a wind turbine, a wind model plays a crucial role in understanding and predicting the chaotic behaviour of the wind resource at a specific site. Consequently, it is necessary to estimate the possible wind loads as well as assess the wind resource characteristics at the site where the wind turbine will be installed. This section aims to capture the complex and dynamic nature of wind at different heights and present the results obtained by exploring the variations of wind speed, wind directions and power density as a function of time.

The method followed to achieve this uses a broad selection of wind atlas data sets provided by the New European Wind Atlas project (NEWA). The project is the result of a collaboration between multiple Euro-

⁸https://offshorewind.rvo.nl/file/download/c2ae21db-49ba-4bc0-8036-cae87fd087d8/ijv_20230512_psd-alpha-and-beta_draft-version-f.pdf [cited: 20 June 2023]

⁹https://aboutthenetherlands.com/the-reason-why-the-netherlands-is-so-windy/?utm_content=cmp_true [cited: 15 June 2023]

pean technical universities. This model aims to provide the user with atmospheric data covering the entire EU including Turkey, as well as the complete North and Baltic Seas. The data set employed is based on 30 years of mesoscale simulations around all of Europe with the Weather, Research and Forecasting (WRF) model at $3\text{ km} \times 3\text{ km} \times 30\text{ min}$ resolution [14].

Using the coordinates of the Ijmuiden Ver site, the corresponding area in Figure 3.2 was selected, and different meteorological data were collected.

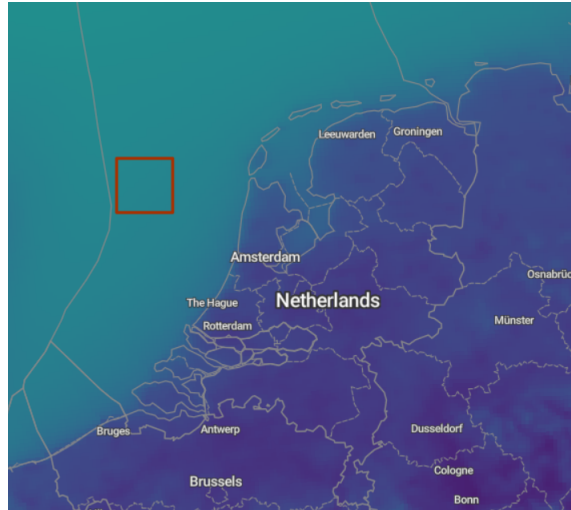


Figure 3.2: Area corresponding to the Ijmuiden Ver site selected in the Newa website

Wind speed and wind direction data for the selected area were downloaded from the provided data sets and imported into Python. This process was carried out for various heights (250m, 50m) and three-month intervals spanning a period of three years (2016, 2017, 2018). The choice of dividing the data over periods of three months was due to the larger size of the files for one entire year resulting in errors with the download. After reading the downloaded data in Python, the power density of the area was determined with the following formula:

$$Pd = \frac{1}{2} \cdot \rho \cdot v^3 \cdot \frac{1}{A} \quad (3.1)$$

Everything was then plotted as a function of time, and the following plots of wind speed and power density as a function of time were obtained. Note that for this report, only the wind speed and power density variations of 2018 at 250 m height are presented. This is done to avoid presenting similar graphs that do not add anything to the final report.

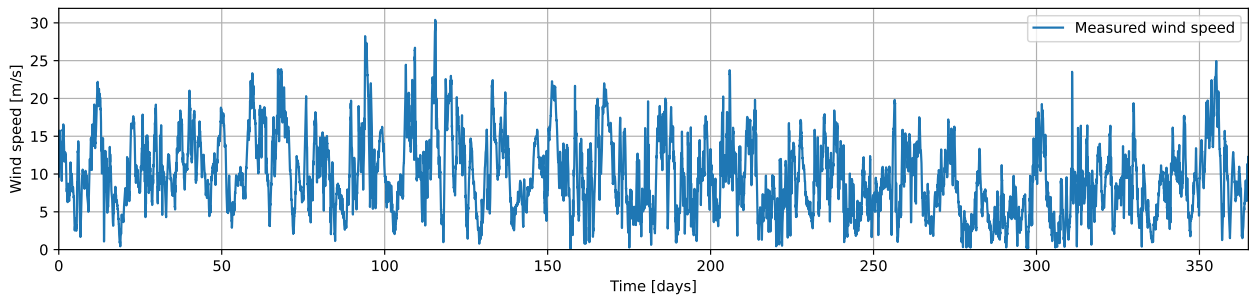


Figure 3.3: Wind speed variations of the Ijmuiden Ver site at 250m height (2018), from 1st of January to 31st of December

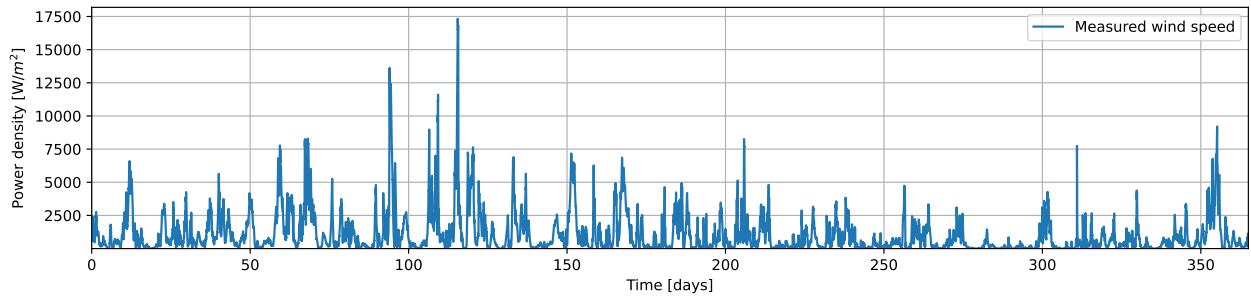


Figure 3.4: Power density variations of the Ijmuiden Ver site at 250m height (2018), from 1st of January to 31st of December

As depicted in graphs, during one year, the changes in windspeed that the MR-TBD turbine may be subjected to are a lot and, at some points, they become very sharp. From Figure 3.3, it is clear that winter is the season of the year in which the highest windspeeds are recorded. On the other hand, from July to October, the minimum windspeeds can be visualised. This is due to the following. In autumn and winter, winds are stronger on average due to the frequent passage of low-pressure systems (storm activity). In fact, in winter, the cold air passes over relatively warm water, resulting in unstable conditions. The latter leads to stronger mixing of momentum downwards. On the other hand, in summer, there is less storm activity, and warmer air passes over relatively cold water. This results in stable conditions with less vertical mixing [15]. Multiple studies have been performed on this topic that present similar trends to the ones found [16, 17]. Moving to the power density plot, it can be noticed that the location over time of the peaks corresponds to the location of the windspeed ones. This is due to the relationship between power density and windspeed.

The average, maximum and standard deviations of the different windspeed data were recorded and tabulated for all the years and heights considered for this study. These results can be found in the following table 3.1:

Table 3.1: Windspeed parameters for different heights and years in Ijmuiden Ver site

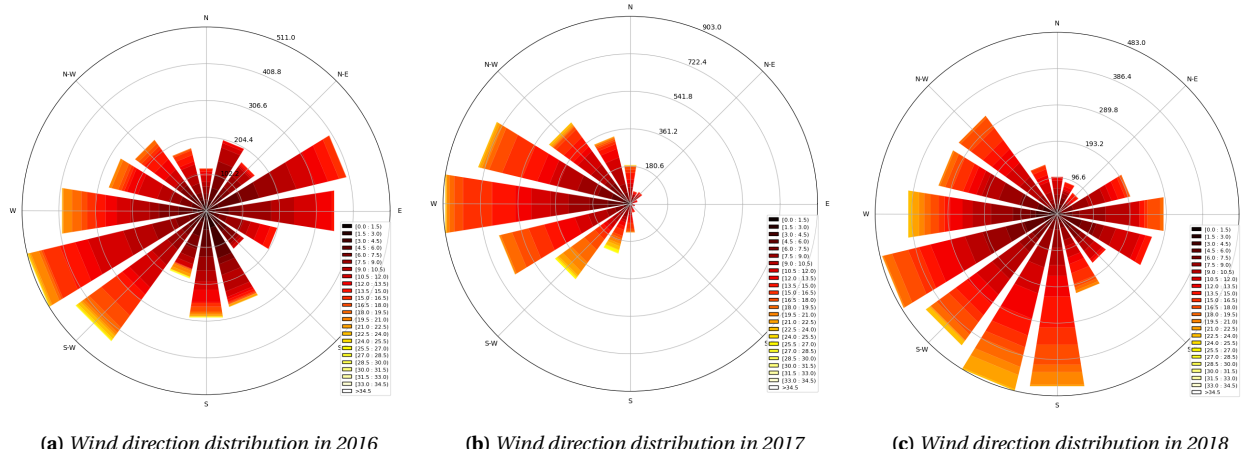
WINDSPEED	Average [m/s]	Standard deviation [m/s]	Maximum [m/s]
2016 at 50m	8.97	+/- 4.03	25.52
2017 at 50m	11.05	+/- 4.18	23.50
2018 at 50m	10.10	+/- 3.96	22.14
2016 at 250m	9.49	+/- 4.54	29.39
2017 at 250m	11.94	+/- 4.81	28.014
2018 at 250m	10.95	+/- 4.57	23.87

The same is done for the power density:

Table 3.2: Power density parameters for different heights and years in Ijmuiden Ver site

POWER DENSITY	Average [W/m2]	Standard deviation [W/m2]	Maximum [W/m2]
2016 at 50m	739	+/- 993	9870
2017 at 50m	1189	+/- 1161	7912
2018 at 50m	937	+/- 997	6622
2016 at 250m	930	+/- 1358	15070
2017 at 250m	1571	+/- 1716	13145
2018 at 250m	1247	+/- 1411	8301

Wind direction must also be considered to complete the assessment of the wind resources in the Ijmuiden Ver region. The wind direction of an area is a crucial parameter since it provides information on the optimal direction toward which the turbine can be pointed to maximise energy production. Wind direction is measured in degrees with respect to the North direction. A good way of showing the change in wind direction, highlighting the frequency of the direction the wind blows the most, is the wind rose. Wind roses are graphical charts that characterise the speed and direction of winds at a location. Presented in a circular format, the length of each "spoke" around the circle indicates the amount of time that the wind blows from a particular direction. Colours along the spokes indicate magnitudes of windspeeds ¹⁰. The wind roses for the different years considered for this study are presented in figure 3.5. Note that for the sake of brevity, only the plots at 250m height from sea level are presented. This is due to the fact that the plots at 50m have exactly the same shape as the ones shown but slightly different colours. This is mainly due to the lower windspeed closer to the sea level.

**Figure 3.5:** Wind roses showing the wind direction changes for three consecutive years at 250m height from sea level. Colours are representative for the wind speed values

From these plots, several conclusions can be identified. As it is possible to see, the wind has always blown from approximately the same direction for all three years considered. The main difference between the graphs lies in the fact that wind data have an extremely chaotic nature and will never be extremely accurate. In addition, during the years, especially recently, weather conditions have changed severally, mainly due to global warming [18]. This is also a factor to consider while reading the plots presented in this section. Besides this, the similarities in the trends that are presented by these graphs are very positive for the team, also in light of previous studies showing the same results [19]. It is clear that the wind blows the most from

¹⁰<https://english.rvo.nl/information/offshore-wind-energy/hollandse-kust-west-wind-farm-zone> [cited: 10 June 2023]

the West/South-West direction. Consequently, this is the ideal direction towards which the wind farm can be oriented to extract the most power.

3.3. Environmental Loading

The system will encounter countless load cases during its lifetime. From a load inducing perspective only, the environment in which the system operates can be described by four characteristics: wind speed and direction, wave intensity and frequency, wind gusts and wind turbulence. For the purposes of this report wind turbulence was not considered, as the correct implementation of an aerodynamic model to evaluate the dynamic turbulence loads would require the extension of the time budget of this exercise.

Wind turbines are usually divided into wind classes depending on the wind speeds under which the turbine can be loaded, based on wind historical data. The pre-defined International Electrotechnical Commission (IEC) classes are presented in Table 3.3 and are defined by four significant wind speeds. The reference wind speed is given as the 50-year return period value for 10 minute average wind speeds, while the annual average is taken as the mean of all 10 minute averaged wind speeds. Gusts, classified as having a duration of over 3 seconds, are broken down into 50-year and 1-year values. All windspeeds were taken at a height of 120 m. As the current design of the systems implies that it will be deployed offshore, with the possibility of expansion beyond the North Sea, it was chosen that the system should belong to Class I, with the highest rated wind speeds.

Table 3.3: Wind classes as defined by the IEC

	Wind classes			
	I	II	III	IV
Reference wind speed [m/s]	50	42.5	37.5	30
Annual average wind speed [m/s]	10	8.5	7.5	6
50-year gusts [m/s]	70	59.5	52.5	42
1-year gusts [m/s]	52.5	44.6	39.4	31.5

As mentioned before, the systems will need to operate in offshore conditions, which leads to the consideration of tidal loads. These loads can be mostly estimated using two defining parameters, the significant wave height and the wave period. The significant height is defined as the average of the highest 33% of registered waves ¹¹. Considering the lack of publicly available historical data regarding wave heights in the North Sea, previously determined values by Fischer et al. have been used [20]. This is a valid assumption, as these measurements were conducted within the UpWind programme, at the IJmuiden K13, a site in the dutch North Sea with a water depth of 25 m [20]. Thus, all wave calculations that would follow were conducted with the worst case scenario of having a 50-year return period value of 17.67 m. The significant wave height and period can be computed using Equation 3.2.

$$H_s = 1.1 \frac{H_{50\text{yr}}}{1.86} = 10.45 \text{ m} \quad T_s = 11.1 \sqrt{\frac{H_s}{g}} = 11.45 \text{ s} \quad (3.2)$$

It is important to note that the system will not behave in the same way for all environmental conditions. As presented in Section 6.3, the power production needs to be capped after the rated wind speed is reached. This leads to a sharp decrease in TSR, which conversely will affect the thrust and torque coefficients. As it will be presented in Figure 6.24e, maximum thrust will be reached at the rated wind speed of 11.2 ms^{-1} . Yet, the maximum torque is obtained at the wind speed of 18.2 ms^{-1} , as shown in Figure 6.24f. Furthermore, it is assumed that the HLD will impart the highest loads on the tower at this wind speed, as after

¹¹URL: <https://www.weather.gov/mfl/waves#:~:text=Significant%20wave%20height%20is%20an,most%20erosion%20on%20a%20beach>. [cited: 18 June 2023]

this peak is reached the control system will be able to decrease the aerodynamic coefficients of the wings. Lastly, the system will be strategically parked during storm conditions as to limit the loads imparted to the structure. The yaw subsystem will orient the tower along the direction of the wind, while the weathervane stability of the structural elements of the tower will help maintain this position. Furthermore, the HLD will be set to their least effective position and the rotors will be parked using the drivetrain hydraulic brakes.

Concluding, three distinct load cases were considered for the design and analysis of the system. LDC1 refers to rated power production and will yield the largest rotor thrust out of the operational envelope. LDC2 is taken as the point when the largest rotor torque and HLD performance is reached, while LDC3 represents extreme storm conditions with parked rotors. All load cases are illustrated in

Table 3.4: Load cases considered for the sizing of the system

	Wind speed [m/s]	C_T	C_t	C_L	C_D	C_M
LDC1	11.2	0.75	0.186	3	0.256	0.3
LDC2	18.1	0.43	0.431	2	0.22	0.2
LDC3	70	0.014	0.015	0.074	0.152	0.1

It is worth mentioning that the aerodynamic coefficients of the rotor were estimated based on the experimental analysis of a parked VAWT performed by [Ottermo et al.](#) at Uppsala University [21]. The coefficients were adjusted based on the dimensions of the H-rotor used and the environmental conditions, yet the difference in aspect ratio and type of airfoil makes this estimate more conservative.

3.4. Load models

In order to estimate the internal loading and thus to size the structural elements of the system, it is imperative to develop a model which can simulate the distribution of external loads acting on the system. In this section two such models are presented, namely a wind model that can estimate the wind distribution along the height of the system, and a wave model which can determine the distributed tidal load on the monopile.

Wind model

Due to wind shearing effects between various layers of air and the surface of the sea, the wind profile will not be constant along the height of the structure. This, in turn, will subject the topside structural and aerodynamic elements to a distributed and variable loading. For these purposes the wind model as presented by [Vire](#) within the course of Fundamentals of Wind Energy I [22]. This model employs the sectioning of the wind profile into two distinct parts, governed by different equations. Due to the shearing effects with the ground and the vertical turbulence created in the process, the first part of the model is modelled after the log-law presented in Equation 3.3. After the blended height is reached the model transitions to a power-law as shown in Equation 3.4.

$$V_{(h < h_{blended})} = V_{(h_{ref})} \frac{\log\left(\frac{h}{z_0}\right)}{\log\left(\frac{h_{ref}}{z_0}\right)} \quad (3.3)$$

$$V_{(h > h_{blended})} = V_{(h_{ref})} \left(\frac{h}{h_{ref}}\right)^\alpha \quad (3.4)$$

The blended height represents the height where the impact of ground surface patches on vertical wind paths become negligible and the wind is fully horizontally blended. The jump between regions is made by

calculating the wind speed at the desired height using as reference the wind speed at the blended height. The following assumptions were made in order to use this model:

WNM-ASS-01: The initial reference height and wind speed will be taken from the chosen wind class defined by the IEC and presented in Table 3.3 for the storm conditions, namely 70 m/s at 120 m.

WNM-ASS-02: The initial reference height for operation conditions will also be taken at 120 m.

WNM-ASS-03: The blended height for the profile of marine wind is considered equal to 60 m, as assumed by [Vire](#) [22].

WNM-ASS-04: The power factor α present in Equation 3.4 is taken as 0.11, as under the guidance of [Vire](#) [22].

WNM-ASS-05: The log factor z_0 present in Equation 3.3 is taken to be 0.0002 under sea-interaction conditions, as under the guidance of [Vire](#) [22].

Following these relationships, the vertical profile of the wind for LDC1 will look as shown in Figure 3.6.

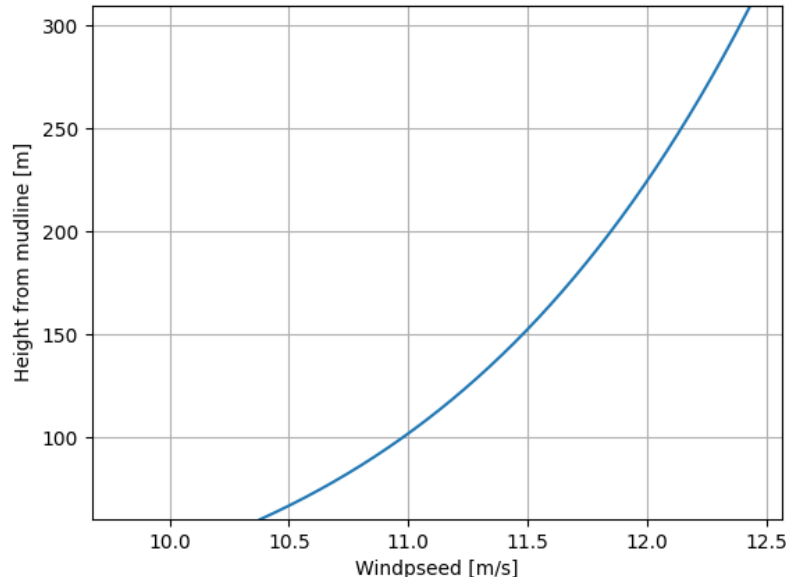


Figure 3.6: Wind profile for LDC1

Wave model

Tidal forces can greatly influence the stability and the loading of the monopile, as storm conditions can create high impact waves and high dynamic loads. For the purposes of this report, the tidal loads will be assumed to be static in order to size the foundation, after which the natural frequency of the monopile will be checked against the wave frequency. The following wave model was obtained from the sizing methodology of XL monopile as published by [K.W Hermans](#) [23]. This model employs Airy's wave theory for determining the tidal speed and acceleration, and uses Equation 3.5 and Equation 3.6, respectively.

$$u_{(z,t)} = \frac{H_s}{2} \omega \frac{\cosh(kz)}{\sinh(kh)} \sin(\omega t) + u_c(z) \quad (3.5)$$

$$\dot{u}_{(z,t)} = \frac{H_s}{2} \omega^2 \frac{\cosh(kz)}{\sinh(kh)} \cos(\omega t) \quad (3.6)$$

It is worth to mention that the wave number is found iteratively, using Equation 3.7.

$$k = \frac{\omega_n^2}{gh \tanh(k)} \quad (3.7)$$

In order to obtain the loading distribution on the foundation, K.W Hermans uses Morison's equation, which is a semi-empirical relationship to obtain the inline force acting on a body in an oscillatory flow [23]. This force can be broken down into an inertial hydrodynamic component and a drag element, as shown in Equation 3.8. This equation can be applied to the current case, using an inertia coefficient, C_n , of 2, and a water drag coefficient of a cylinder, C_D of 1. These tidal components are presented in Equation 3.9 and in Equation 3.10, respectively.

$$F_{tidal} = F_I + F_D = \rho_w C_n V^* \dot{u}_{(z,t)} + \frac{1}{2} \rho_w C_D A^* u_{(z,t)} |u_{(z,t)}| \quad (3.8)$$

$$F_{I(z,t)} = z \frac{\pi}{4} \rho_w C_n d_{o(z)}^2 \dot{u}_{(z,t)} \quad (3.9)$$

$$F_{D(z,t)} = z \frac{1}{2} \rho_w C_D d_{o(z)} u_{(z,t)} |u_{(z,t)}| \quad (3.10)$$

As mentioned before, the tidal forces will be taken into account in this design process as worst case scenario ultimate static loads. In order to do that, the forces are iterated over a period of the tidal speed and acceleration and the instance of time which gives the largest total tidal load is taken as the critical time. Thus, the foundation shall carry the tidal loads at the critical time as if it were a static load. This load profile is then considered in combination with all load cases previously mentioned in Section 3.3. The profile of such a tidal load, taken for a monopile of constant diameter of 10 m is provided as visual aid in Figure 3.7

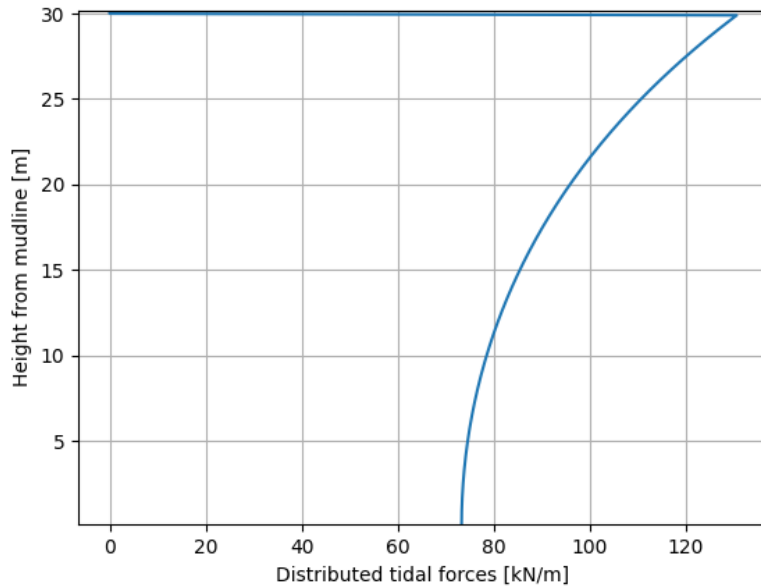


Figure 3.7: Tidal distributed load along the height of a monopile with a constant diameter of 10 m

Budgets

Budgeting is a vital part of any successful design. In a world where costs are the main differentiating factor, the financial side of a product cannot be ignored. This chapter aims to establish the budgets for most of the subsystems of the MR-TBD, informing the reader on what is crucial to consider costs-wise. The method followed to assess the wind turbine costs is explained in Section 4.1. On the other hand, the cost estimation is performed in Section 4.2. This is done to check if MR-TBD can compete in the market. Lastly, a short conclusion is presented in Section 4.3.

4.1. Description of the Budget Model

In order to estimate the system's initial budget, the average cost breakdown of a traditional HAWT wind farm from the Offshore Renewable Energy Catapult was used [9]. The individual components of the cost breakdown were then modified based on various estimations of how the designed system differs from the HAWT wind farm. These assumptions are discussed in Section 4.2. Each stage of assumptions leads to a new LCoE (see Section 4.2). The costs provided by Catapult are broken down into the cost of the turbine, the balance of the plant, development and project management, installation and commissioning, maintenance and service, and operations and decommissioning. The Catapult offshore wind farm model uses a 1 GW wind farm consisting of 100 10 MW wind turbines located 60 km from shore at a 30 m water depth. Thus, the differences between the Catapult wind farm concept and the proposed wind farm concept significantly affect the costs of individual components of the model. The costs are normalised to €/MWh allowing the costs to be compared. The annual electricity production of around 4471 GWh per year (E_t) used in the LCoE calculation has also been taken from the Catapult breakdown. The equation for LCoE, adjusted for inflation, is given in Equation 4.1 [9].

- LCoE - levelized cost of electricity
- t - time in years
- I_t - Investment expenditure in year t
- M_t - Operations maintenance and service expenditure in year t
- E_t - Net energy generation in year t
- $n = 27$ years - Lifetime of the project in years
- $r = 3\%$ - Discount rate or WACC
- WACC - weighted average cost of capital
- CapEx - The capital expenditure (including development expenditure)
- OpEx - The operational expenditure
- DecEx - The decommissioning expenditure
- O&M - Operations and Maintenance

$$\text{LCoE} = \frac{\sum_{t=-5}^{n+1} \frac{I_t + M_t}{(1+r)^t}}{\sum_{t=-5}^{n+1} \frac{E_t}{(1+r)^t}} \quad (4.1)$$

CapEx is the turbine's plant balance, installation, and decommissioning capital expenditure. These are costs that are only incurred once. In contrast, OpEx is the operational expenditure being mostly concerned with the operations and maintenance of the system. These are continuous expenses during operation. In light of this, the yearly OpEx can be multiplied by the system's lifetime to determine its effect on the final LCoE. The wind farm's lifetime was assumed to be 27 years, the same as the Catapult model. The discount rate heavily influences the LCoE. The Catapult model used a discount rate of 6%, [E.C.M. Ruijgrok](#) used 3%, and [Freeman et al.](#) didn't mention a discount rate [9, 24–26]. A dilemma arises, since the lack of a discount rate for the WindEurope study, means a direct comparison with it is problematic [1]. It has been decided

that a discount rate of 3% should be used since the study validated the "move" of the Catapult wind farm to a lower LCoE area using 3% as the discount rate [24].

4.2. Budget of the Proposed Design

Having established the model used and the performance goals (see Chapter 2), the modifications that will be applied, and the feasibility of achieving the goals will be assessed. It is important to note that, for the sake of conciseness, only changes to the original Catapult data will be shown in the tables. There are five cost-driving differences between the proposed design and the conventional option. The key differentiators are shown below and will be further explained throughout this section.

1-2 Moving to lower LCoE areas (see Table 4.1)

2-3 Increasing power density from 5 MW/km² to 16 MW/km² (see Table 4.2)

3-4 Introduction of wake losses due to the increase of power density (see Table 4.3)

4-5 Switching from a conventional HAWT to a multi-rotor VAWT (see Table 4.4)

5-6 Recovering the production lost with a wake control system (see Table 4.5)

The power density increase will allow the planned capacity of 380 GW to fit into the very low LCoE area. This area is generally cheaper due to a shorter distance to shore and shallower water depth. The cost benefits associated with this are shown in Table 4.1.

Table 4.1: Table showing the changes to the Catapult model to account for benefits of a lower LCoE location (1-2)

Name	LCoE Before	Change	LCoE After	Reason
Export cable	€ 1,91	-50,00%	€ 0,95	Closer to shore, less cable required
Foundation cost	€ 2,20	-66,00%	€ 0,75	Shallower water, smaller foundation
Offshore substation structure	€ 0,88	-33,00%	€ 0,59	Shallower water, less structure needed
Development and consenting services	€ 0,73	-33,00%	€ 0,49	Better understood regions, easier development
Offshore substation installation	€ 0,51	-50,00%	€ 0,26	Closer to shore, less rent time on equipment
Cable burial	€ 0,29	-50,00%	€ 0,15	Closer to shore
Cable pull-in	€ 0,11	-50,00%	€ 0,06	Smaller area of operation less rent time on equipment
Other (cable-laying vessel, seruvey works, route clearnace cable protection)	€ 2,73	-50,00%	€ 1,37	Closer to shore, less rent time on equipment
Turbine installation	€ 0,73	-25,00%	€ 0,55	Shallower water, easier and quicker installation
Sea-based support	€ 0,04	-40,00%	€ 0,02	Closer to shore
Maintenance of turbine	€ 8,56	-50,00%	€ 4,28	Closer to shore less time spent traveling
Maintenance of balance of plant	€ 4,67	-40,00%	€ 2,80	Closer to shore, less time spent traveling
Offshore logistics	€ 0,42	-30,00%	€ 0,29	Closer to shore
Turbine decommissioning	€ 0,27	-30,00%	€ 0,19	Closer to shore
Foundation decommissioning	€ 0,45	-33,00%	€ 0,30	Closer to shore
Cable decommissioning	€ 0,85	-50,00%	€ 0,42	Less cable to decommission
Substation decommissioning	€ 0,39	-30,00%	€ 0,27	Closer to shore
Total LCoE [EUR/MWh]	€ 56,61		€ 43,82	

Increasing the power density and therefore decreasing the turbine spacing in a wind farm has additional benefits. As turbines are closer to each other, the travel time between individual turbines shortens, and the length of the cabling connecting them is decreased. It also lessens the impact on the environment. The LCoE benefits of these changes are summarised in Table 4.2.

Table 4.2: Table showing the changes to the Catapult model to account for the benefits of a higher density wind farm (2-3)

Name	LCoE before	Change	LCoE after	Reason
Array cable	€ 0,51	-50,00%	€ 0,26	Less area covered
Electrical system	€ 0,66	-15,00%	€ 0,56	Smaller system simpler to monitor
Facilities	€ 0,29	-15,00%	€ 0,25	Smaller area requires less facilities
Environmental surveys	€ 0,06	-20,00%	€ 0,05	Less area covered
Resource and metocean assessment	€ 0,06	-20,00%	€ 0,05	Less area covered
Cable burial	€ 0,15	-20,00%	€ 0,12	Less cable to bury
Cable pull-in	€ 0,06	-20,00%	€ 0,04	Less traveling, shorter rent periods
Electrical testing and termination	€ 0,10	-20,00%	€ 0,08	Less traveling, shorter rent periods
Other (cable-laying vessel route clearance cable protection)	€ 1,37	-20,00%	€ 1,09	Less traveling, shorter rent periods
Turbine installation	€ 0,55	-15,00%	€ 0,47	Less traveling, shorter rent periods
Sea-based support	€ 0,02	-20,00%	€ 0,02	Less area covered
Onshore logistics	€ 0,12	-15,00%	€ 0,10	Less area covered
Offshore logistics	€ 0,29	-15,00%	€ 0,25	Less area covered
Turbine decommissioning	€ 0,19	-15,00%	€ 0,16	Less traveling, shorter rent periods
Foundation decommissioning	€ 0,30	-15,00%	€ 0,26	Less traveling, shorter rent periods
Cable decommissioning	€ 0,42	-20,00%	€ 0,34	Less cable
LCoE [EUR/MWh]	€ 43,82		€ 42,76	

Unfortunately, the change in the power density will also have a negative performance impact. According to analysis performed by [Ferreira](#), a traditional wind farm would lose about 30% of its electricity production due to wake losses [27]. The impact of lost production can be seen in Table 4.3

Table 4.3: Effects of the wake on energy production and their impact on LCoE for a traditional HAWT 3-4

Name	LCoE before [EUR/MWh]	Change	LCoE after [EUR/MWh]
Production lost due to wake	€ 42,76	42,00%	€ 61,03

The next step is to change the configuration of the wind farm from conventional single-rotor HAWTs to multi-rotor VAWTs. Changing the turbine design has large implications for costs. A big change stems from the multi-rotor VAWT allowing the use of components less optimised for weight. In addition to this, the design is more accommodating to maintenance, making it significantly cheaper. The design's influence on costs can be seen in Table 4.4.

Table 4.4: Table showing the changes to the Catapult model to account for benefits of a multi-rotor VAWT (4-5)

Name	LCoE before [EUR/MWh]	Change	LCoE after [EUR/MWh]
Bedplate	€ 0,42	-100,00%	€ -
Main bearing	€ 0,42	-50,00%	€ 0,21
Main shaft	€ 0,42	-33,00%	€ 0,28
Gearbox	€ 0,42	-75,00%	€ 0,37
Generator	€ 1,47	-80,00%	€ 0,42
Power take-off	€ 2,10	-10,00%	€ 1,32
Yaw system	€ 0,36	25,00%	€ 0,45
Yaw bearing	€ 0,15	25,00%	€ 0,18
Nacelle auxiliary systems	€ 0,15	-50,00%	€ 0,07
Nacelle cover	€ 0,21	-50,00%	€ 0,10
Small engineering components	€ 0,52	10,00%	€ 0,58
Structural fasteners	€ 0,15	50,00%	€ 0,22
Blades	€ 2,73	-80,00%	€ 0,55
Hub casting	€ 0,31	-75,00%	€ 0,08
Blade bearings	€ 0,42	-100,00%	€ -
Pitch system	€ 0,21	-100,00%	€ -
Fabricated steel components	€ 0,11	-33,00%	€ 0,08
Steel	€ 1,26	20,00%	€ 1,51
Tower internals	€ 0,15	20,00%	€ 0,18
Other (includes assembly, wind turbine supplier aspects of installation and commissioning profit and warranty)	€ 7,13	20,00%	€ 8,56
Array cable	€ 0,37	-25,00%	€ 0,28
Transition piece	€ 2,10	50,00%	€ 3,15
Corrosion protection	€ 0,42	25,00%	€ 0,52
Foundation cost	€ 1,07	25,00%	€ 1,34
Development and consenting services	€ 0,70	25,00%	€ 0,88
Engineering and consultancy	€ 0,08	25,00%	€ 0,10
Foundation Installation	€ 1,05	-33,00%	€ 0,70
Cable burial	€ 0,17	-15,00%	€ 0,14
Cable pull-in	€ 0,06	-30,00%	€ 0,04
Other (cable-laying vessel seruvvey works, route clearnace cable protection)	€ 1,56	-15,00%	€ 1,33
Turbine installation	€ 0,67	-20,00%	€ 0,53
LCoE [EUR/MWh]	€ 61,03		€ 51,09

The final LCoE is obtained by applying the effects of wake re-energization. The MRS-VAWT layout is conducive to placing large high-lift devices producing upwash. This should recover the energy production to levels comparable with conventional wind farms [27]. The final LCoE value can be seen in Table 4.5

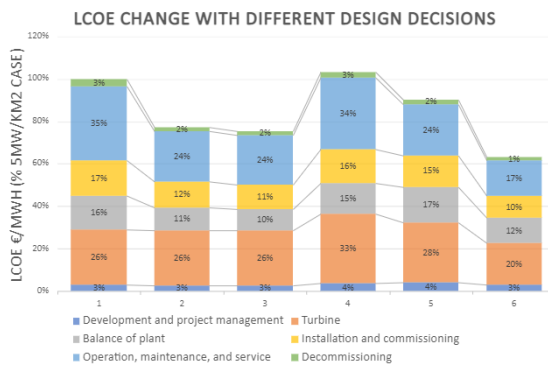
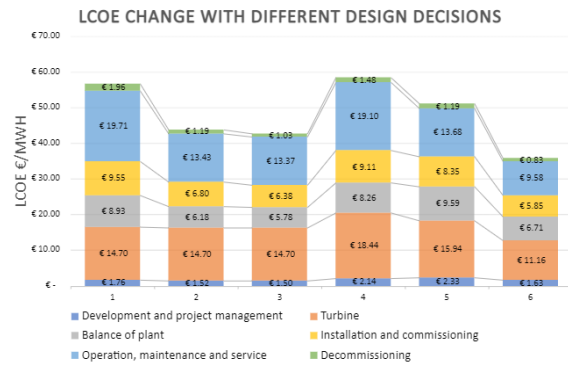
Table 4.5: Impact of wake control on LCoE in a VAWT design (5-6)

Name	LCoE before [EUR/MWh]	Change	LCoE after [EUR/MWh]
Production gained due to wake control	€ 51,09	-30,00%	€ 35,77

It is important to recognise that the cost analysis performed has some limitations. Regarding error accumulation, wake loss calculations are investigated. Wake losses influence energy generated. In step 2-4, wake losses are introduced, which is removed in steps 5-6 due to the wing on the structure. If errors were made using estimating these wake losses, they should destructively annihilate since the energy efficiency at 1 is the same as in 6. The most unreliable estimation step is thus 4-5, which concerns the design in question. To validate this result, this step will need to be revised after a more concrete design is proposed. A validation of this step can be seen in Section 9.1

4.3. Conclusion and Final Budgeting

There are a few takeaways from the cost analysis. A concise visualization of the budgeting of the wind turbine can be seen in Figure 4.1 and Figure 4.2. The most crucial takeaway from the analysis is that, depending on the target selected, building wind energy in the North Sea now or replacing old wind farms beyond 2050, the design slightly underachieves or overachieves. If the goal is to lower the LCoE by 45% for the development of the North Sea now, then the design is not economical enough. The LCoE estimate is 6€/MWh over the target value. However, [E.C.M. Ruijgrok](#) indicates that there are many locations with an LCoE under 40€/MWh, which suggests that the analysis in steps (1-2) is on the conservative side [24]. This means that an LCoE of 36€/MWh is plausible, although hard to achieve. If the goal is to provide an excellent alternative to increasing the power capacity in the North Sea beyond 2050, the design would be a great candidate. The design can achieve the goal LCoE if 36€/MWh exactly. This means the proposed design would be a good replacement for ageing turbines in the future.

**Figure 4.1:** LCoE change as a percentage of 5MW/km² case with different design changes**Figure 4.2:** LCoE change as absolute with different design changes

Design trade-offs

This chapter will cover the identified trade-offs between the available design options. Section 5.1 presents the trade-off for rotor orientation. Section 5.2 trades off the options for the yaw control. Section 5.3 compares the foundation options. Finally, Section 5.4 covers the drive train options. These sections have been shortened as the customer is more familiar with them. Section 5.5 presents different shapes for the structure cell identified. Section 5.6 trades off the main shaft attachment position. Section 5.7 compares different rotor shapes and Section 5.8 covers different individual truss element geometries.

To score the different options, a consistent colour-scoring scheme was designed. The scheme has a total of four levels presented in Table 5.1. Each criterion was assigned a weight of importance from 1 to 5 and a percentage weight was calculated based on the cumulative weight. The relative weight of importance is also represented by column width in trade-off tables.

Table 5.1: The explanation of the scoring used for the trade-off of design options

(R) Unacceptable	(O) Correctable	(L) Acceptable	(G) Exceptional
------------------	-----------------	----------------	-----------------

5.1. Rotor Orientation Trade-off

The goal of this section is to present three design options, HAWT and VAWT, both laid out in a grid with independent drive trains and VAWT grouped on the same drive train. Mass, operations and maintenance, sustainability and other cost-saving options have been evaluated in the section.

Regarding individual VAWTs, for a given power rating, the total generator mass is proportional to one over-the-tip speed ratio times the number of rotors in a row. If rotor mass is kept constant for individual VAWTs, the number of generators is $n \cdot k$. The number of generators for individual HAWTs is $n \cdot k/4$. For grouped VAWT, the number of generators is n .

The trade-off determined that grouped rotor VAWT outperform other options. To include assumptions made, HAWT are more efficient than VAWT (around +6%) [3, 28]. However, the packing ratio makes the HAWT less space efficient than VAWT (roughly -9%). Also, generator mass is not perfectly linear with torque, as some components of a generator scale with different factors. If the width of the turbine is not approximately equal to the height, then the number of generator scaling changes. More specifically, if the turbine's height is two to four times the rotor diameter, the number of generators becomes comparable between individual rotor HAWT and grouped rotor VAWT.

5.2. Yaw Control Trade-Off

Two types of yawing mechanisms can be identified: passive and active. It was evaluated that no trade-off table is needed for this selection since active yawing control is a project requirement. The active yaw system options considered are electric, hydraulic or aerodynamic. An aerodynamic yaw system stops or slows down the rotors of the structure to change the drag of the structure non-symmetrically to induce torque and yaw the structure.

The hydraulic yaw system was discounted due to maintenance reasons and cost compared to an electric yaw system. Comparing the electric yaw to the aerodynamic yaw system revealed the main difference to be added mass and the cost of an additional motor as well as the moment arm being larger for the aerodynamic yaw system. The electrical yaw system proved to be too large and expensive to provide a yaw rate of $1^\circ/s$ so an aerodynamic yaw system became the only choice for primary yaw. An additional benefit of the aerodynamic yaw system is that there is no torque in the monopile.

The aerodynamic control system requires the turbines to function. During a storm or low wind speeds a backup may be required. For this backup, an electrical yaw system was selected. With this, the system's reliability is higher allowing some additional yaw without the use of an aerodynamic yaw system.

5.3. Foundation Trade-Off

The structure can use a monopile, a jacket structure or a floating foundation. A jacket is a truss structure with similar applications as a monopile. A floating foundation is used for deeper water and consists of a pontoon, ballasts and cables attaching it to the sea floor.

Regarding the floating option, the metal mass of the floater was estimated to be 9742 t. This is significantly more than the monopile. The Jacket was found to be the lightest option with a mass estimated around 5400 t when compared to a monopile mass of 7100 t. Installation of fixed foundations is more complicated than the floaters, requiring specialised jack-up vessels. Monopiles and jackets are claimed to be feasible for usage at depths up to 70 m [29] [30]. Floating foundations have minimum depths required which is more relevant at roughly 40m. 70m depth is more than any areas with wind farms planned by the Dutch government¹.

While installation is more difficult for a fixed foundation, it is selected since the depth range better aligns with current North see plans and the mass of a fixed foundation is less.

The jacket structure is a widely underused option for wind farm design especially because of the maintenance, complexity and lifetime concerns. This caused the jacket to not be chosen. The selected option for the design is thus the monopile. In 2016 80% of all offshore wind turbines employed the monopile for their foundation [31], meaning that the trade-off was in favour of the most commonly employed option.

5.4. Drive Train Trade-Off

Within the selection of a design for the drive train, several design options were discovered.

1. Direct drive with a permanent magnet synchronous generator (DD-PMSG) and a full converter
2. Direct drive with an electrically excited synchronous generator (EESG) and a full converter
3. Drive train with a gearbox, a doubly fed induction generator (DFIG) and a partial converter
4. Drive train with a gearbox, a permanent magnet synchronous generator and full converter (PMSG)

The first two design options follow a similar design pattern, having the shaft connected to the rotor directly linked to the generator element. In order to match the frequency of the grid, either 50 Hz or 60 Hz, depending on the installation region, a full converter is included. The other two design options use a gearbox between the rotor and the generator. Usually, a planetary gearbox, comprising either two or three stages, is considered to bring the rotational velocity of the drive shaft within the operational RPM window of the generator. The doubly fed induction generator of design option 3 incorporates a partial converter, which can vary the current frequency to the generator's rotor, making it operable with variable rotational speeds [32].

[Li et al.](#) provides an overview of the average amount of rare-earth metals used for different types of generators [33]. DFIGs do not use any rare-earth metals and are, therefore, the most sustainable generator type. DD-EESGs and G-PMSGs use a moderate amount of rare-earth metals, with 30 and 52 tons/GW, respectively. DD-PMSGs are by far the most unsustainable option, with an average rare-earth metal use of 231 tons/GW [33]. According to [Pavel et al.](#), 77% of the current global wind energy capacity uses electromagnetic generators, with the remaining 23% using permanent magnet generators [34]. The direct drive generators require the generator to be matched to the specific RPM of the turbine. As the rotors in VAWT are relatively unconventional, direct-drive generators would not be widely available. The use of rare-earth metals is deemed a disadvantage, as the uneven world poses a risk to the supply chain.

¹<https://north-sea-energy.eu/en/energy-atlas/>

Two options, namely the direct drive permanent magnet and the direct drive electrically excited generator, can be easily dismissed based on their performance regarding sustainability and ease of manufacture for small and medium OEMs. Yet, considering the importance of sustainability, especially regarding rare earth metals that go into making the permanent magnets, to the client of this design exercise, it can be argued that the DFIG option is superior. Moreover, considering that 80% of the rare earth metals currently used in the wind energy industry are supplied from China, there lies a critical bottleneck in the supply chain, which can raise the potential risk of supply disruptions and spikes in prices, as seen at the beginning of the Covid-19 pandemic ² [35]. The 3G DFIG configuration has been selected as the drive train option for these reasons.

A sensitivity analysis was made to analyze if the focus would change from sustainability and democratisation of manufacturing towards better performance, either by giving more importance to availability or power efficiency. In that case, it is clear that a permanent magnet configuration would be the option to choose. If the client opts for eliminating market democratisation requirements and decides to rely on the big drive train manufacturers in the wind industry, then the best configuration would be the direct drive permanent magnet configuration, as common as it is on the market already.

5.5. Triangle vs Rectangle based structure Trade-Off

The structure base cell can be either rectangle-based or triangle based. The trade-off choice shapes are triangles in which a V- shape rotor would fit or a rectangle shape where a H-shape rotor would be mounted seen in Figure 5.1. Other rotors may also be mounted in a rectangle cell. Other shapes are not considered as there is no clear advantage to them either structurally or concerning rotor shape. This trade-off differentiates between these choices mainly by investigating generator properties for the two cases.



Figure 5.1: Trade-off choice between the structure cell shape.

CRIT-STRshape-01 (5/5 Weight - 50%): Generator count

CRIT-STRshape-02 (2/5 Weight - 20%): Structural mass

CRIT-STRshape-03 (3/5 Weight - 30%): Maintenance accessibility

CRIT-STRshape-01: The required generator count refers to the number of shafts required for a set rotor diameter. As the V-shaped rotors are staggered, there will be a shaft in between every rotor radius, while there will be a shaft spaced by diameter for the H-type rotor. This means that for the same rotor diameter a V-rotor-based turbine will have twice the generator count of an H-rotor-based turbine. If the diameter of the V-rotor is increased, such that the number of generators is the same as for an H-rotor, the torque rating of the drivetrain would have to be doubled. Higher torque drivetrains come with higher purchase prices, worse democratization and more intensive maintenance.

CRIT-STRshape-02: The required structural mass may be different for a V-rotor based compared to an H-rotor. The v-rotor-based structure allows for diagonal trusses in the front of the structure allowing a more efficient load path. The load path for the V-rotor-based structure is shorter, so the structure may be lighter.

CRIT-STRshape-03: The maintenance accessibility refers to how easily the drive train can be maintained based on the shape of the rotor. The access paths can be made in the same way thus the maintenance aspect of the rotors is the same.

²URL: <https://strategicmetalsinvest.com/5-year-prices/> [cited 17 May 2023]

Table 5.2: Rotor type trade-off

CRIT-RTRshape	01 Number of Generators	02 Mass	03 Maintenance
H-shape	(G)	(L)	(L)
V-shape	(R)	(G)	(L)

Table 5.2 shows that while the structure that accommodates V-shaped-rotors will be lighter the increase in the number of generators is detrimental and thus a rectangle is chosen. For a sensitivity analysis there is not much room for change as the number of generators and the torque in the generators are driving the design.

5.6. Shaft mounting position Trade-Off

The shaft of the rotors can be placed either in the middle of the structure cell or the edge of the structure described in Figure 5.2. The choice is mainly made due to the ease of manufacturing and replacing rotors. Additionally, the constraints imposed by the diameter on both design option depth is investigated.

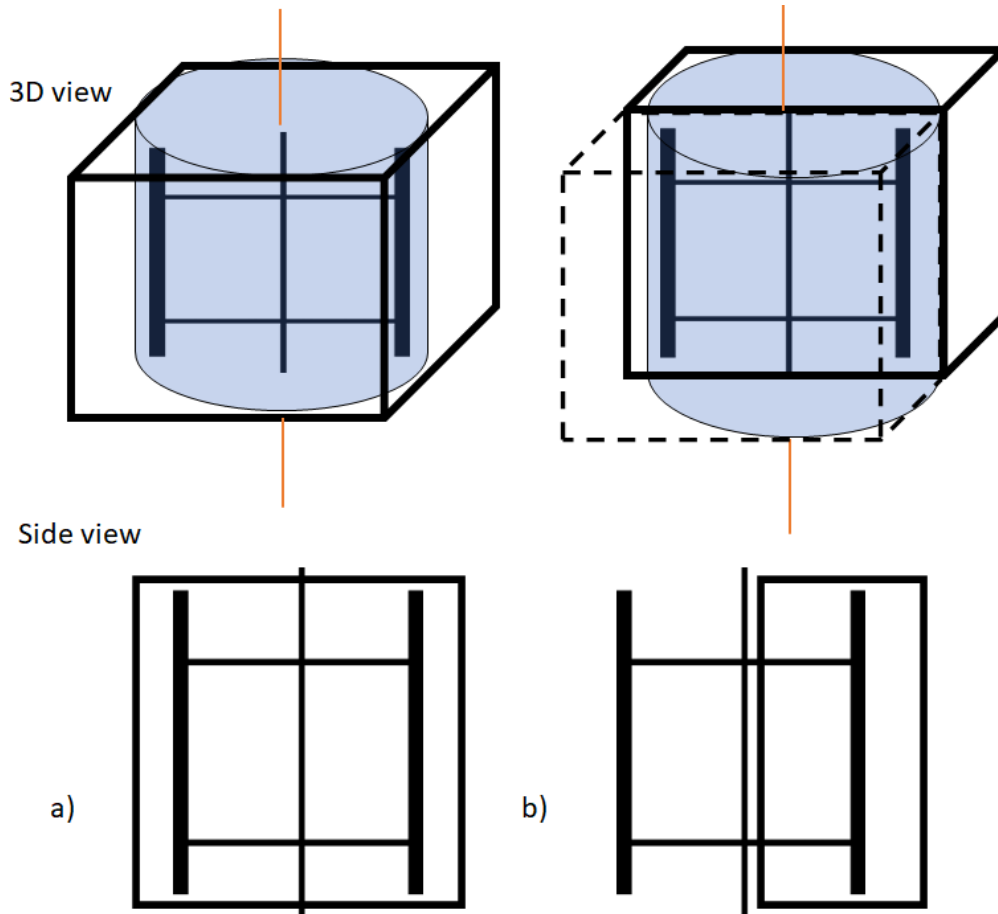


Figure 5.2: Trade-off choice between the location of the shaft. a) in the middle of the cell and b) on the side of the cell.

CRIT-AxPos-01 (3/5 Weight - 33%): Minimum structural depth

CRIT-AxPos-02 (3/5 Weight - 33%): Structural mass

CRIT-AxPos-03 (3/5 Weight - 33%): Ease to replace the rotors

CRIT-AxPos-01: The minimum structural refers to how shallow the structure can be without interfering with the rotors depending on their diameter. At this design stage, it is unclear what is the optimal structure

depth and the optimal diameter of the rotors. This makes mounting at the front advantageous since the range of possible structure and rotor sizes is bigger.

CRIT-AxPos-02: The structural mass refers to how much material is required to support all other subsystems. A comprehensive weight analysis is performed in Section 6.1. In principle, mounting the rotors at the front has benefits for carrying the thrust loads. The load path is less needing only to travel half the depth. The optimal depth of the structure might be smaller than the diameter, therefore putting the rotor at the front would make the structure lighter. Additionally, when mounting the rotor at the front of the structure, the centre of gravity is shifted forwards, partially relieving the aerodynamic bending moment, which leads to lower stress on structural members, and therefore the possibility of making the structure lighter.

CRIT-AxPos-03: The replacement of rotors may be done to extend the life of the system. Easy replacement also helps when assembling the system. It helps with maintenance time if a blade needs to be replaced. Having the rotors mounted in front of the structure makes it easily detachable and not entangled in the main structure.

Table 5.3: Rotor installation location trade-off

CRIT-AxPos	01 Minimum depth	02 Structure mass	03 Assembly
Front	(G)	(G)	(G)
Middle	(O)	(O)	(O)

From Table 5.3 it is immediately trivial which configuration is best. Mounting the rotors at the front is clearly the better option. It has the potential to be lighter, it is better for maintenance and has virtually no drawbacks. Therefore it has been decided to continue with the front-mounted option for the rest of the design.

5.7. Rotor Selection Trade-Off

This section determines the most efficient and cost effective option for the shape of the rotor. The possible options can be seen in Figure 5.3. The factors that differentiate are packing ratio and aerodynamic performance which affects structure mass. Ease of manufacturing impacts initial costs and different rotor shapes impact power consistency. Sinusoidal or constant loading on the shaft impacts the fatigue life on the drivetrain.

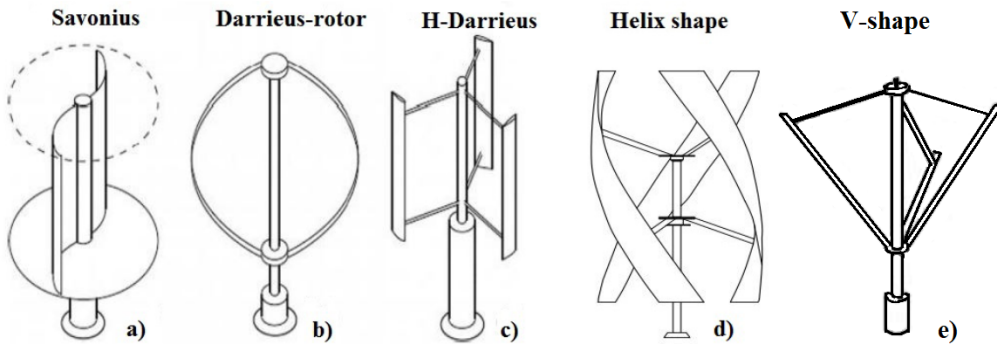


Figure 5.3: Trade-off choice of the rotor selection. Drag based Savonius (a). Possible variants of Darrieus VAWT: Troposkiens type (b), H-type (c), Gorlov (helical type, d) and V-type (e). [36, 37]

CRIT-RTRshape-01 (5/5 Weight - 38.5%): Packing ratio

CRIT-RTRshape-02 (2/5 Weight - 15.5%): Aerodynamic performance (C_P, C_T)

CRIT-RTRshape-03 (4/5 Weight - 30.5%): Manufacturability

CRIT-RTRshape-04 (2/5 Weight - 15.5%): Fatigue life

CRIT-RTRshape-01: Packing ratio refers to how well a rotor uses space that was given to it. For the comparison, a rectangle-based structure cell has been used. This makes rotor a), c) and d) perform well in this category. If a triangle based structure was used, then the V-shaped turbine would perform best. Hence the asterisk in the trade-off table. The Darrieus style rotor will always underperform since truss structures do not synergise with curved shapes.

CRIT-RTRshape-02: The aerodynamic performance is to measure how much power and thrust can be expected to be produced for a given swept area. Drag-based rotors, like the Savonius, have significantly worse parameters than lift-based ones. This makes the Savonius rotor essentially impossible to use in the design. The V-shaped and Darrieus rotors are also not optimal. The fact that different parts of the blades experience different airflow velocities, reduces their efficiency compared to the rest of the lift-based rotors.

CRIT-RTRshape-03: Manufacturability is how easy and thus how costly it is to manufacture the rotor. Complex shapes, like in the helical designs, or unfavourable loading paths, like in the V-shape, make these rotor options expensive to manufacture. From this it's clear that the H-type and Darrieus-type rotors should be the cheapest lift-based option.

CRIT-RTRshape-04: Helical rotors have a constant torque in the shaft while non-helical rotors with two blades create sinusoidal loading. This effect influences the fatigue on the generators as peak loading is higher. The uneven loading can be mitigated by placing multiple rotors out of phase on the same shaft, creating a more even loading.

Table 5.4: Rotor shape trade-off

CRIT-AxPos	01 Packing ratio	02 C_P, C_T	03 Manufacturing	04 Fa-tigue life
Savonius	(G)	(R)	(L)	(L)
Darrieus-rotor	(O)	(L)	(G)	(L)
H-shaped	(G)	(L)	(G)	(L)
Helix shaped	(G)	(L)	(R)	(G)
V-shaped	(O)*	(O)	(O)	(L)

To conclude it can be seen that the H-shaped rotor performs best as it does not have any deficiencies. There is still the question of the number of blades. [Kharade and Jagtap](#) and [Battisti et al.](#) determined that 3 blades per rotors have the best performance [36, 38]. As one shaft is likely to contain many blades the issues arising from fatigue should be mitigated.

5.8. Individual element selection Trade-Off

Before a design can be proposed, a truss element has to be chosen. There are many profiles to choose from, but it was decided that four types of elements will be considered, solid cylinders, hollow cylinders/tubes, a truss structure and I beams. The focus of the trade-off is to compare the weight performance of the different sections.



Figure 5.4: Trade-off choice of individual elements of the structure between a) solid cylinder; b) hollow cylinder; c) truss elements, d) I-beam

CRIT-IES-01 (5/5 Weight - 50%): Buckling

CRIT-IES-02 (3/5 Weight - 30%): Complexity

CRIT-IES-03 (2/5 Weight - 20%): Torsion resistance

CRIT-IES-01: The buckling performance of a profile is determined by its second moment of area per area of the cross-section. This criterion has been chosen to help minimize the mass of the structure. Since the only buckling mode taken into account is Euler buckling, the section with the highest minimum second moment of area around any axis is preferred. Therefore sections with an area distributed furthest from the centre are best. From the selection of profiles, only the solid cylinder does not move the material towards the edges, so it underperforms in this category. Analyzing the trust option is difficult since the properties will depend on the exact geometry. It has been assumed that it could be optimized for buckling, therefore it performs well. I beam usually has the best geometry to withstand buckling, however since the analysis is limited to truss structures (only Euler buckling), the lack of a radial symmetry makes the compression with hollow circular sections (tubes) unfavourable.

CRIT-IES-02: The complexity criteria ensure that the structure remains cheap to build. Making a more complex layout makes every step in the design and life of the structure more difficult, therefore more expensive. The one profile that is not 'simple' is the truss element. Building trusses from trusses is possible, but increases the count of connection points dramatically.

CRIT-IES-02: The calculations performed in Section 6.1 are limited due to the truss model used, so no torque values are obtained. However, having a profile that can handle some torque is useful, since some internal torques are to be expected.

Table 5.5: Individual element selection

CRIT-AxPos	01 Buckling	02 Complexity	03 Torsion
Solid cylinder	(R)	(G)	(O)
Hollow cylinder	(G)	(G)	(G)
Truss elements	(G)	(R)	(L)
I beam	(L)	(G)	(O)

It can be seen that the hollow cylinder outperforms other options. Not only it is highly resistant to buckling but it is easy to simulate and manufacture as well as being the most torsion resistant. For elements where bending has to be considered an I beam may perform best and if Euler buckling is very limiting then a truss structure may replace that element.

6

Design analysis

This chapter discusses detailed analysis performed for six out of eight subsystems of the turbine. Analysis of TWR is presented in Section 6.1, Section 6.2 contains analysis of WCT, followed by analysis of RTR in Section 6.3. Section 6.4 describes the design of the yaw control system, followed by design of DRT in Section 5.4. The section is concluded by FND design in Section 6.6.

6.1. TWR analysis

The tower of the MR-TBD design is a large truss structure, consisting of a repeating pattern of smaller cubical cells, stacked heightwise and widthwise. To aid the design of this subsystem, a Python program was written that analyses the internal forces in each element, selects an appropriate radius and thickness for this element, and thereby optimises the mass. This section describes the theoretical background for the model, the design decisions made based on the model, and the resulting design.

Theoretical Background

The truss model uses the theory of linear elasticity. This employs several assumptions, which are presented below:

TWR-ASS-01: Deformations are linear and obey the relation $\sigma = E\varepsilon$ (which may be rewritten as $F = \frac{EA}{L}L'$)

TWR-ASS-02: Deformations of individual elements are small, hence the change of their relative orientation from the original position is neglected.

TWR-ASS-03: The individual truss elements may only fail under yield (in tension or compression) when $\sigma \geq \sigma_y$ and when loaded with Euler's critical load

TWR-ASS-04: Individual truss elements only carry loads in the direction they are orientated in.

TWR-ASS-05: Trusses behave as if half of their masses are lumped at each of the two nodes, to which they connect.

Given these assumptions, the truss structure can be modelled as consisting of a finite number of truss elements. An individual element e is oriented in its reference frame with first node N_0^e at the origin and N_1^e at the location $\langle L, 0, 0 \rangle^T$. Suppose the vector \vec{d}^e is the vector from node N_0^e to node N_1^e in the global reference frame as $\vec{d}^e = \langle d_x^e, d_y^e, d_z^e \rangle^T$. In that case, the transformation from the global reference frame to the element's reference frame is defined as per Equation 6.1, with the angles α and β defined as per Equation 6.2 and Equation 6.3.

$$\mathbf{T}_{g \rightarrow e} = \begin{bmatrix} \cos \beta & 0 & -\sin \beta \\ 0 & 1 & 0 \\ \sin \beta & 0 & \cos \beta \end{bmatrix} \begin{bmatrix} \cos \alpha & \sin \alpha & 0 \\ \sin \alpha & \cos \alpha & 0 \\ 0 & 0 & 1 \end{bmatrix} \quad (6.1)$$

$$\tan \alpha = \frac{d_y^e}{d_x^e} \quad (6.2)$$

$$\tan \left(\frac{\pi}{2} - \beta \right) = \frac{\sqrt{(d_x^e)^2 + (d_y^e)^2}}{d_z^e} \quad (6.3)$$

By considering a local displacement vector for an element as $\vec{u}^e = \langle u_{0_x}^e, u_{0_y}^e, u_{0_z}^e, u_{1_x}^e, u_{1_y}^e, u_{1_z}^e \rangle^T$, the forces at nodes N_0^e and N_1^e can be expressed in the local reference frame as per Equation 6.4. Using the transformation $\mathbf{T}'_{g \rightarrow e}$ per Equation 6.5, this relation can be formulated in the global reference frame as per Equation 6.6 and Equation 6.7. Global stiffness matrix \mathbf{K}^g and force vector \vec{F}^g can be then assembled from the local matrices, which gives the global system as in Equation 6.8. For the global reference frame and system, the superscript g will be dropped. The system can then be reformulated in terms of external loading \vec{F}_{ext} , gravity loading \vec{F}_g , and reaction forces \vec{r} . This relation is given in Equation 6.9. The external loading \vec{F}_{ext} is given by the natural boundary conditions at each node, while the weight of each element gives the weight loading \vec{F}_g . Assuming a constant cross-section area A and material density ρ , along with constant gravitational acceleration g_0 , this gives the load of $\frac{1}{2}\rho AL$ per node, meaning each of the nodes is loaded with half of the weight. In the reference system used by the model, gravity is applied in the direction of the z-axis, downwards. The reaction forces \vec{r} occur due to numerical boundary conditions, which force the nodes to have a fixed (usually zero) displacements.

$$\vec{F}^e = \begin{bmatrix} F_{0_x}^e \\ 0 \\ 0 \\ F_{1_x}^e \\ 0 \\ 0 \end{bmatrix} = \frac{EA}{L} \begin{bmatrix} 1 & 0 & 0 & -1 & 0 & 0 \\ 0 & 0 & 0 & 0 & 0 & 0 \\ 0 & 0 & 0 & 0 & 0 & 0 \\ -1 & 0 & 0 & 1 & 0 & 0 \\ 0 & 0 & 0 & 0 & 0 & 0 \\ 0 & 0 & 0 & 0 & 0 & 0 \end{bmatrix} \begin{bmatrix} u_{0_x}^e \\ u_{0_y}^e \\ u_{0_z}^e \\ u_{1_x}^e \\ u_{1_y}^e \\ u_{1_z}^e \end{bmatrix} = \mathbf{K}^e \vec{u}^e \quad (6.4)$$

$$\mathbf{T}'_{g \rightarrow e} = \begin{bmatrix} \mathbf{T}_{g \rightarrow e} & \mathbf{0} \\ \mathbf{0} & \mathbf{T}_{g \rightarrow e} \end{bmatrix} \quad (6.5)$$

$$\mathbf{T}'_{g \rightarrow e} \vec{F}^e = \mathbf{T}'_{g \rightarrow e} \mathbf{K}^e \mathbf{T}'_{g \rightarrow e} \mathbf{T}'_{g \rightarrow e}^T \mathbf{T}'_{g \rightarrow e} \vec{u}^e \quad (6.6)$$

$$\vec{F}^{e'} = \mathbf{K}^{e'} \vec{u}^{e'} \quad (6.7)$$

$$\vec{F}^g = \mathbf{K}^g \vec{u}^g \quad (6.8)$$

$$\vec{u} = \mathbf{K}^{-1} (\vec{F}_{\text{ext}} + \vec{F}_g + \vec{r}) \quad (6.9)$$

By considering only the non-fixed degrees of freedom in Equation 6.9, the matrix \mathbf{K}_r becomes non-singular and hence invertible, provided that the system is either statically determinate or over-determinate. This will also not include reaction forces \vec{r} , as they only occur at nodes that have numerical boundary conditions and are hence not free. The system is shown in Equation 6.10. Reaction forces at fixed nodes can be recovered from Equation 6.9.

$$\vec{u}_r = \mathbf{K}_r^{-1} (\vec{F}_{\text{ext}_r} + \vec{F}_{g_r}) \quad (6.10)$$

The structure's mass matrix can be constructed from local matrices, following from **TWR-ASS-05** as per Equation 6.11. This gives a system as Equation 6.12. By applying the Fourier Transform of the system as in Equation 6.13, the solution to which becomes Equation 6.14. The solution becomes indeterminate when the determinant of the matrix $\mathbf{M}_r^{-1} \mathbf{K}_r - \omega^2 \mathbf{I}$ becomes zero, meaning that the frequency of excitation ω is one of the eigenvalues of matrix $\mathbf{M}_r^{-1} \mathbf{K}_r$. Based on that, natural frequencies of the structure can be determined by finding eigenvalues of the matrix $\mathbf{M}_r^{-1} \mathbf{K}_r$.

$$\mathbf{M}^e = \frac{\rho A L}{2} \mathbf{I} \quad (6.11)$$

$$\mathbf{M}_r \ddot{\vec{u}}_r + \mathbf{K}_r \vec{u}_r = \vec{F}_r(t) \quad (6.12)$$

$$(-\omega^2 \mathbf{M}_r + \mathbf{K}_r) \vec{u}_r = \vec{F}_r(\omega) \quad (6.13)$$

$$\vec{u}_r = \mathbf{M}_r^{-1} (\mathbf{M}_r^{-1} \mathbf{K}_r - \omega^2 \mathbf{I})^{-1} \vec{F}_r(\omega) \quad (6.14)$$

Verification of the Model

To prove that the simulation implemented the aforementioned mathematics correctly, verification of the model was performed. A statically over-determined problem was used to test if the simulation found the same result as solving the problem analytically.

The problem is illustrated in Figure 6.1, with four nodes A, B, C, and D in the same planes at positions $<0, 0, 0>^T$, $<4, 0, 0>^T$, $<0, 4, 0>^T$, and $<4, 4, 0>^T$ respectively. The fifth point E is positioned at $<1, 1, 1>^T$, with a load $P = <0, 0, -1000>^T$ applied at the centre. Points A, B, C, and D have numerical boundary conditions applied so that they may not move, meaning they experience reaction forces in all three directions.

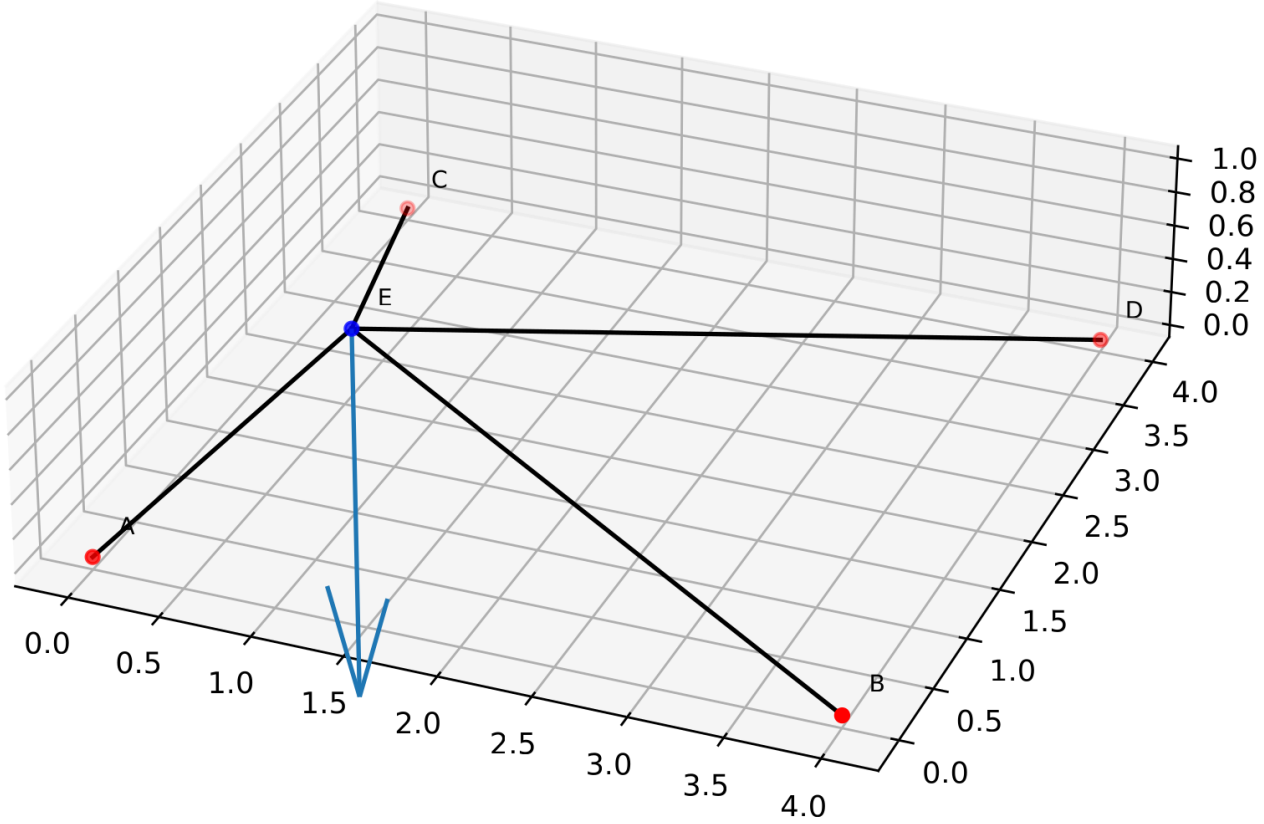


Figure 6.1: Setup used for verification calculations

The problem is statically indeterminate, as the equilibrium of forces at point E dictates that the relations Equation 6.15, Equation 6.16, and Equation 6.17 be satisfied. These equations are bound by compatibility

equations Equation 6.18, Equation 6.19, Equation 6.20, and Equation 6.21. These equations use \vec{r} to indicate the position of a point. All elements were considered to have the same profile, a hollow cylinder with an outside radius of 10 mm and a thickness of 1 mm. The used elasticity modulus was 200 GPa

$$+\swarrow \sum F_x = -\frac{1}{\sqrt{3}}F_A + \frac{3}{\sqrt{11}}F_B - \frac{1}{\sqrt{11}}F_C + \frac{3}{\sqrt{19}}F_D = 0 \quad (6.15)$$

$$+\nearrow \sum F_y = -\frac{1}{\sqrt{3}}F_A - \frac{1}{\sqrt{11}}F_B + \frac{3}{\sqrt{11}}F_C + \frac{3}{\sqrt{19}}F_D = 0 \quad (6.16)$$

$$+\uparrow \sum F_z = -\frac{1}{\sqrt{3}}F_A - \frac{1}{\sqrt{11}}F_B - \frac{1}{\sqrt{11}}F_C - \frac{1}{\sqrt{19}}F_D = -F \quad (6.17)$$

$$F_A = \frac{E_A A_A}{L_A} (||\vec{r}_E - \vec{r}_A|| - L_A) \quad (6.18)$$

$$F_B = \frac{E_B A_B}{L_B} (||\vec{r}_E - \vec{r}_B|| - L_B) \quad (6.19)$$

$$F_C = \frac{E_C A_C}{L_C} (||\vec{r}_E - \vec{r}_C|| - L_C) \quad (6.20)$$

$$F_D = \frac{E_D A_D}{L_D} (||\vec{r}_E - \vec{r}_D|| - L_D) \quad (6.21)$$

The solution to the problem was obtained analytically and compared to the values obtained from the simulation. The values and differences between the two are presented in Table 6.1. As can be seen quickly the relative difference (as in difference divided by the analytical value) is in the order between 10^{-5} and 10^{-7} , which can be attributed to errors in rounding and truncation error when computing approximations to the values of inverse square roots. Given the results from Table 6.1, the model is considered validated for solving statically over-determinate problems using linear elasticity.

Table 6.1: Analytical solution and simulation results for the verification problem along with the differences

Quantity	Analytical value	Simulation result	Relative difference	Absolute difference
u_{E_x}	2.588861-05	2.588858e-05	1.13e-06	2.92e-11
u_{E_y}	2.588861e-05	2.588858e-05	1.13e-06	2.92e-11
u_{E_z}	-1.81755e-04	-1.81740e-04	7.96e-05	-1.45e-08
F_A	-8664210.99	-8664209.17	2.11e-07	1.82
F_B	-4245768.66	-4245772.15	8.23e-07	3.49
F_C	-4245768.66	-4245772.15	8.23e-07	3.49
F_D	-3548128.79	-3548124.20	1.29e-06	4.59

In addition to the verification of these loads, the structural mass calculated by the script was verified to be correct by a hand calculation.

Validation of the model would require a laboratory test with a proper scale model, or to use another validated structural simulation software, such as Solidworks, Abaqus, or Ansys. The experimental or software results could then be compared to the outputs of the model developed for this design.

Design method

The main structural design tool was a Python implementation of the model described above in Section 6.1. This was used to generate a three-dimensional truss structure as seen in Figure 6.2. As the structure is

symmetric, only half of the structure had to be simulated. A symmetric boundary condition was applied by restricting the movement of nodes on the symmetry line in the left-to-right y-direction. These nodes are yellow in Figure 6.2. To simulate the attachment to the two bearings on the center column, the two nodes at the bottom left, and the two left nodes halfway up the structure are fully constrained. These are shown in red.

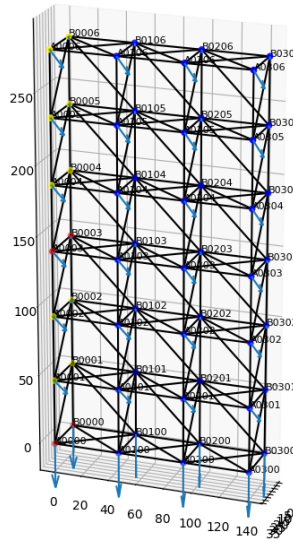


Figure 6.2: The simulated truss structure. Red nodes are fully constrained, yellow nodes are constrained from moving in the y-direction

The forces are then applied to the nodes, and the internal loads are simulated. If any element in the truss structure is then loaded above its limit load its radius and thickness are increased. The program then iterates over these cross-section profiles until all elements are as small as possible but large enough to withstand the internal loading. This way the mass of the structure is optimized. The structure is a repeating pattern made up of the same cell layout, but any element in the structure can be a different radius and thickness, from a predetermined set of radius and thickness profiles.

The failure types considered in the simulation are yield in tension, yield in compression, and Euler buckling. A safety factor of 1.3 was applied to material properties, another safety factor of 1.3 was applied to yielding in compression or tension, and a safety factor of 1.2 was applied to the buckling load. These safety factors follow international standard IEC61400-1 [39].

Applied loads

A range of loads on the structure was considered during the design. As the structure is a truss, these all had to be applied to the nodes. Firstly, the mass of the elements is lumped into the two nodes at their edges. The mass of the drivetrains is distributed over the bottom layer of nodes. The mass of the rotors and shafts is distributed over the nodes at the front face of the structure, except the bottom layer. The mass of these components is summarized in Table 7.2. The forces created by the high lift device and its mass were introduced at the back nodes on the layers where they are present as described in Subsection 6.2.3.

As the nodes at which the yaw torque would be introduced a fully constrained, the torque was modeled by applying a force to every node proportional to its mass, acceleration, and distance to the rotation axis. The acceleration of each node was calculated from the cross-product of the angular acceleration that the torque would induce in the structure and the direction vector from the rotation axis to the node. Using the mass of the node, the acceleration, and Newton's second law, the force required to induce this accelera-

tion is calculated. As this leads to a loop where the applied force on a node depends on the mass, which depends on the minimum profile for the elements connected to it, which in turn again depends on the internal forces, this problem was iterated a few times. The torque ultimately had a very low impact on the mass of the structure. The considered torque was 800 kNm as specified in Section 6.4.

Different sources of loads will have different magnitudes depending on the load cases described in Section 3.3. The rotors reach a maximum thrust at the rated wind speed, load case LDC1, while the drag on the structure is the largest during the fifty-year storm scenario, LDC3. To get a set of the most constraining loads on the structure, the worst-case scenario was picked for each individual load source. The drag on the structure and thrust of the rotors were considered as one source, as their load introduction into the structure is exactly the same in the simulation.

The drag on the structure is estimated by projecting the truss onto the plane perpendicular to the wind and multiplying the length of the projected members by the average profile radius. The length of the elements came to around 6200 m and the average radius of an element came to around 0.45 m. It is important to note that the LDC3 calculated here is larger than the used in the calculations done for the foundation sizing in Subsection 6.6.1. This was done since the increase in weight for the truss for the higher loading was only around 5%. Therefore it was decided that the truss will be sized to withstand the storm conditions with the large side facing the wind. As the drag on the structure in load case LDC3 at 19.1 MN is higher than the rotor thrust for load case LDC1 at 4.51 MN, the structure drag is considered as the limiting thrust. The downforce of the HLDs is the largest during operations at 1245 kN per wing, while the drag is largest during 70 m s^{-1} gusts at 255 kN as calculated in Subsection 6.2.6. While these can not happen at the same time, the structure is conservatively designed by superimposing these two worst-case scenarios.

Scripts were used to distribute the total loads over their respective nodes. To verify that this was done correctly, the forces on the nodes were confirmed, to sum up to the total force applied. In addition to this, every time the program is run, there is a visual check, in which the user can see at which nodes the loads are applied.

Cell type Selection

For the tower, a modular design was decided as it is both simple to analyze and simple to integrate with other systems. The tower is to be made of cuboid truss cells, which would all have the same dimensions, but with truss elements using different profiles to minimize mass. These different profiles have a range of radii, with a constant thickness-to-radius ratio.

The very first thing to be determined was the design of the cell itself. Seven different cell layouts were analyzed. Sketches of these cells are shown below in Figure 6.3 to Figure 6.9.

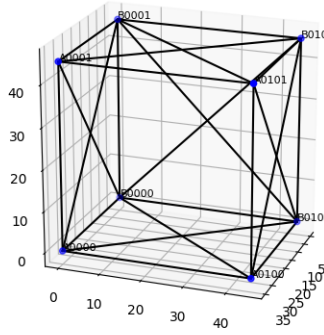


Figure 6.3: Cell type 1

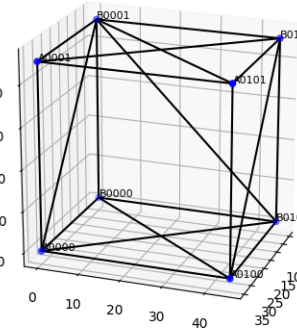


Figure 6.4: Cell type 2

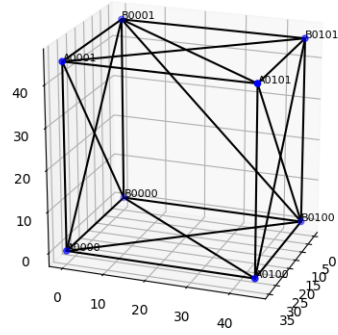


Figure 6.5: Cell type 3

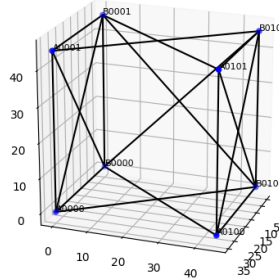


Figure 6.6: Cell type 4

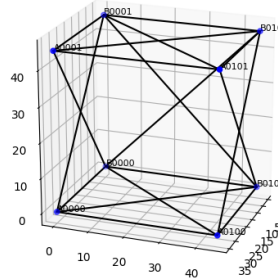


Figure 6.7: Cell type 5

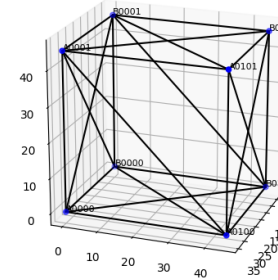


Figure 6.8: Cell type 6

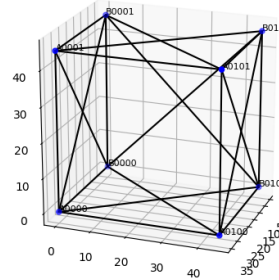


Figure 6.9: Cell type 7

A full structure based on these cell types was then generated and optimized for mass. For an accurate comparison, the same forces were applied to each structure, and the same profiles were available to all cell types. The resulting masses are shown below in Table 6.2 note that these masses are not representative of the final mass, but are only used to see how heavy they are relative to each other.

Table 6.2: A structural mass comparison between the seven cell shapes. Note that these are not representative of a final mass but only compare the relative masses of the cell types.

Cell type	Cell 1	Cell 2	Cell 3	Cell 4	Cell 5	Cell 6	Cell 7
Mass [tonnes]	5996	5377	6054	4855	6517	5764	5304

Table 6.2 shows that the lightest overall structure was cell type 4. However, this design was later discounted as without horizontal members in the front it provides no location to support the shaft bearings. The next lightest design is cell type 7, closely followed by cell type 2. While cell type 7 was slightly lighter than 2 for the load case in this comparison, it becomes a lot heavier when thrust is increased, due to the lack of horizontal braces on the back. For this reason, cell type 2 was chosen.

Cell size selection

Based on the chosen cell shape, the number of cells was then varied for the same overall dimensions of 280 x 280 m. This essentially scales the height and width of each individual cell to find the lightest design. Structure layouts of 4x4 (rows x columns), 6x4, 6x6, 6x10, 6x12, and 8x8 were tested. No layouts with an odd number of columns were considered so that an even number of rotor columns could be used, to allow canceling out the rotor torque by counter-rotating them. The resulting masses are shown in Table 6.3 below.

Table 6.3: A structural mass comparison between different cell configurations (rows x columns) for the same total structural width and height.

Cell configuration	4x4	6x4	6x6	6x10	6x12	8x8
Structural mass [tonnes]	4862	4987	4454	5472	6211	4883

Table 6.3 shows that the lightest layout is 6x6, so this was the chosen configuration. The non-square layouts also perform noticeably worse than the square layouts.

Structural depth optimization

Once the cell layout was known, the depth of the structure was optimized. To find the optimal depth, it was varied as a fraction of the structure width between 0.01-0.2. The resulting mass curve is shown in Figure 6.10 below. As the rotors are mounted on the front of the structure instead of the middle, the minimum depth of the structure is the rotor radius. This is a depth ratio of around 8% as indicated by the orange line in Figure 6.10. The mass is minimized for a depth ratio of around 12%, so this is the chosen structure depth. This leads to a depth of 33.6 m.

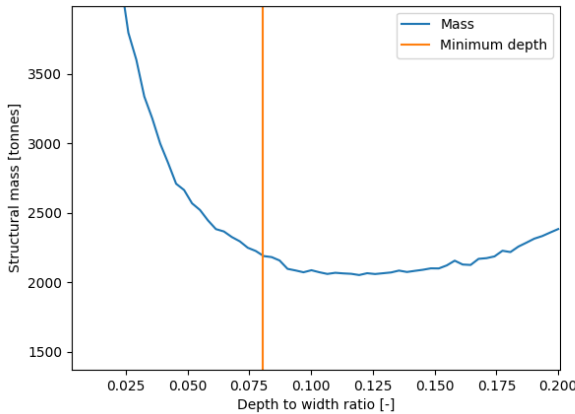


Figure 6.10: The sensitivity of the structural mass to the depth of the structure

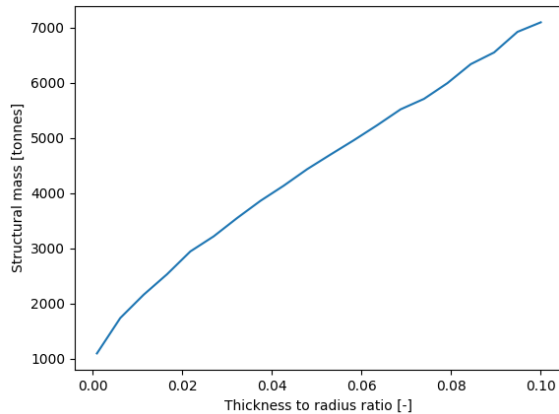


Figure 6.11: Sensitivity of the structural mass to the thickness to radius ratio

Profile selection

Finally, the specific profiles of the truss elements have to be chosen. These are a range of hollow cylinders with a constant thickness-to-radius ratio. For manufacturability, only 20 profiles between a minimum and maximum radius are used. In the specific loading case considered, some members are under very little loading and default to the smallest profile. However, they still provide stability to the structure and may be important in unexpected loading conditions. The structural members are roughly 33 m to 65 m long, and they must be stiff enough to such that they do not flex too much under their own mass. For these reasons, a minimum radius 15 cm was chosen. A maximum radius of 2 m was available, but such large members were rarely used. The selection of the thickness-to-radius ratio has a large effect on the mass of the structure, as can be seen in Figure 6.11.

Decreasing the thickness ratio increases the moment of inertia of the cross-section, which increases the resistance to column buckling. This is the failure mode for almost all of the members loaded in compression and therefore has a significant effect on the mass. Out of the total 404 structural elements, 204 are loaded in compression, out of which 180 will fail in column buckling. In addition to this, decreasing the thickness also decreases the mass of members at the minimum radius.

The downside to decreasing the thickness ratio is that the resulting radius increase leads to increased drag on the structure. This is the limiting load case as explained in Figure 6.1. Besides the fact that the total drag on the structure increases, the drag will induce a bending moment on the individual elements, which is not simulated by the truss simulation. In this aspect, using larger, thinner cylinders is undesirable. In addition to this, when the thickness ratio becomes too small, the elements may experience local sheet buckling. This is not simulated, so care must be taken not to pick too small of a ratio. Jamieson et al. uses a thickness to diameter ratio of 1:120, or a thickness to radius ratio of 0.0041 [3]. Using this ratio, 26 structural members have a diameter over 2 m, with two members reaching a diameter of 3.4 m. At a thickness-to-radius ratio of 0.01, only the four largest elements have a diameter of 2 m. To keep down the structural drag and ensure that no sheet buckling will occur but still have a low mass, a thickness ratio of 0.01 was selected.

Material selection

For the truss elements, a few different metals were considered: low-carbon steel, medium-carbon steel, high-carbon steel, low-alloy steel, and stainless steel. Material properties of these steels are shown in Table 6.4 below. To choose the optimal material, an optimized structure was generated for each. First, the raw material costs of these designs are compared. The results are shown in Table 6.5 below.

Table 6.4: Relevant material properties of the considered types of steel. The data comes from the Ansys Granta Material Universe database

Material	E [GPa]	σ_y [MPa]	ρ [kg/m3]
High-carbon steel	200	433	7800
Medium-carbon steel	200	376	7800
Low-carbon steel	200	255	7800
Low-alloy steel	200	469	7800
Stainless steel	190	252	7610

Table 6.5: The mass of the structure for various metal types, and the associated material costs.

Material	Structural mass [t]	Material cost [M€]
Low-carbon steel	2412	1.51
Medium-carbon steel	2046	1.28
High-carbon steel	1979	1.26
Low alloy steel	1922	1.48
Stainless steel	2422	6.22

Based on these results, medium-carbon steel and high-carbon steel seem like the two best options, with the high-carbon steel design being slightly cheaper than the medium-carbon steel design. However, there are other benefits of using medium-carbon steel over high-carbon steel. As medium-carbon steel is softer, it is generally easier to manufacture parts from or weld. In addition to this, although not as strong as high-carbon steel, low-carbon steel is more ductile. This is a benefit, as it allows for a more damage-tolerant design. Once damage is detected there will be a larger window of time before it has to be repaired. In addition to this, the corrosion rate of steel increases with carbon content, which also makes medium-carbon steel favorable [2]. For these reasons, medium-carbon steel will be used.

For corrosion protection, multiple layers of white organic solvent-based paint will be applied to the truss structure. This is done to protect the structure from the harsh environment and reduce its capability of absorbing heat from the sun. This process is done for all the above water elements exposed to air. To protect the turbine from lighting, a lightning protection system is installed on the structure.

Final configuration

With a 6x6 configuration, a depth of 33.6 m, and a thickness-to-radius ratio of 0.01, the optimized structural mass is 2046 t. However, this does not take into account the additional mass of connections between the truss elements. To add a contingency for this, a margin of 20 % is applied to this mass, leading to a mass of 2455 t. This still does not include the mass of the bedplates. The bedplate for the IEA 15-MW offshore windturbine is 70 t, and the IEA 10-MW offshore windturbine has a bedplate of 61 t[40][41]. Thus, without going into further loading details it is possible to roughly estimate the mass of the bedplates for the 5 MW generators to be 52 t per generator. This then leads to the final structural mass of 2767 t. This mass could be reduced by making truss elements thinner, but to safely do so, more detailed buckling analysis should be performed. The final simulated structure is shown below in Figure 6.12, with the internal stresses of the members in Figure 6.13.

Vibrations

After designing and optimizing the structure, the system's natural frequencies were analyzed according to the method described in Section 6.1. This mode assumed lumped mass at the nodes, as per **TWR-ASS-05**, which means the analysis is an estimation of the true system. While this will not be completely accurate to the real system, it still provides some insight into the approximate behaviour of the system.

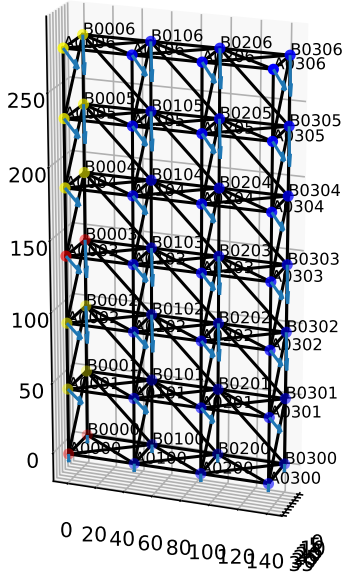


Figure 6.12: The right half of the structure in the truss simulator

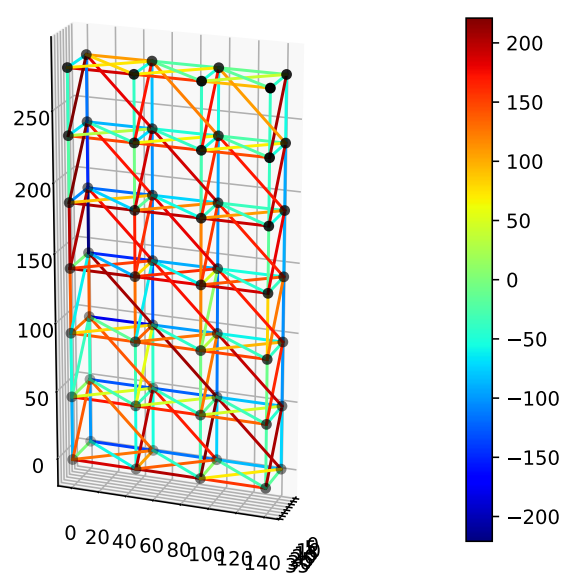


Figure 6.13: The right half of the structure in the truss simulator with stresses in MPa

There are two main excitation frequencies in the system, waves hitting the monopile, and the rotation frequency of the rotors. The highest wave frequency considered has a frequency of 0.29 Hz, as shown in Table 6.12. However the larger the period of the waves, the more energy they carry, so the most problematic waves have a lower frequency. The main cause for rotor-induced vibrations is due to the centre of mass of the rotating body not being exactly the centre of rotation. The highest rotor frequency will be obtained at the maximum TSR of 4.5, and the rated windspeed of 11.2 m s^{-1} . With the rotor diameter of 45 m, this leads to a rotation frequency of 0.357 Hz. However, the rotation frequency may reduce or completely stop with changes in wind speed. This means any frequency up to 0.357 Hz may be an excitation frequency.

Figure 6.16 shows the excitation frequencies in red, and the natural frequencies up to 1 Hz in blue. All frequencies are shown with a bar width of 10% of the frequency. As shown in Figure 6.16, the lowest natural frequency at 0.371 Hz is slightly higher than the rotor frequency. However, as the rotor frequency is very close to the rotor frequency, the excitation frequencies could slightly overlap with this lowest natural frequency, and a more detailed analysis should be performed. If the rotor frequency indeed turns out to be a problematic excitation frequency, a few measures could be taken.

The most apparent solution is to overbuild the structure and make elements larger or thicker than required. This would make the structural members stiffer, increasing the natural frequency. However, the axial stiffness of a rod is only linearly proportional to the cross-sectional area of the element. The mass of the element is also linearly proportional to the area, which reduces the natural frequency again. While there is a net gain in natural frequency, as only half of the element is lumped at each end, and there are other masses such as the drivetrain components that stay constant, this is not a very mass-efficient way of solving the problem. Another solution could be to isolate the problematic excitation frequencies. The rotor frequency is induced into the structure through the bearings that are mounted to the horizontal truss elements at the front of the structure. A damper could be integrated into the mounting bracket to isolate the vibrations. A sketch of a concept damper system is shown in Figure 6.14 below. The green layer in this sketch represents a layer of damping material. The attachment bolts are shown in red. This could then be modeled as a damper-spring system, as shown in Figure 6.15. The damping and spring coefficients of this system then have to be balanced to achieve critical damping.

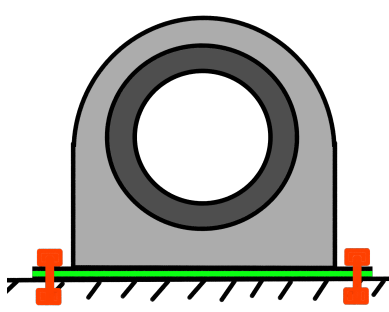


Figure 6.14: A sketch of a damping mount bracket. Green represents a damping material and the bolts are shown in red.

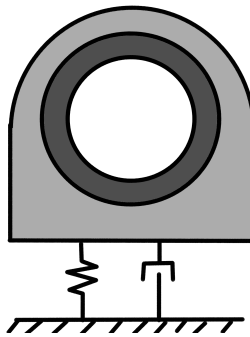


Figure 6.15: A diagram of the damping mount modeled as a parallel spring and dashpot.

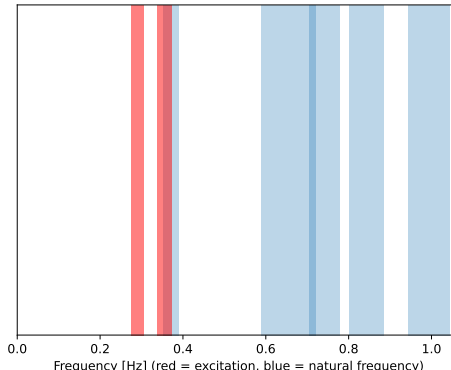


Figure 6.16: The excitation frequencies and lowest natural frequencies of the system

6.2. WCT Analysis

This section details the design and analysis of the wake control system (WCT). As the system as a whole strives to be as space efficient as possible, WCT is critical. In order to allow for turbines to be spaced more closely together, the wake must recover fast enough. The idea behind the wake control system is to use the effects of high-lift devices (HLDs) on the flow, namely the trailing tip vortices which direct the flow in the direction opposite of the lift it creates.

Since the turbine is installed close to the ground, the best place to move the wake is upwards. This means using HLD(s) to generate downforce since the lift is directed downwards. To quantify the effects of HLD on the wake, a simple potential flow model was used.

6.2.1. Theoretical Background

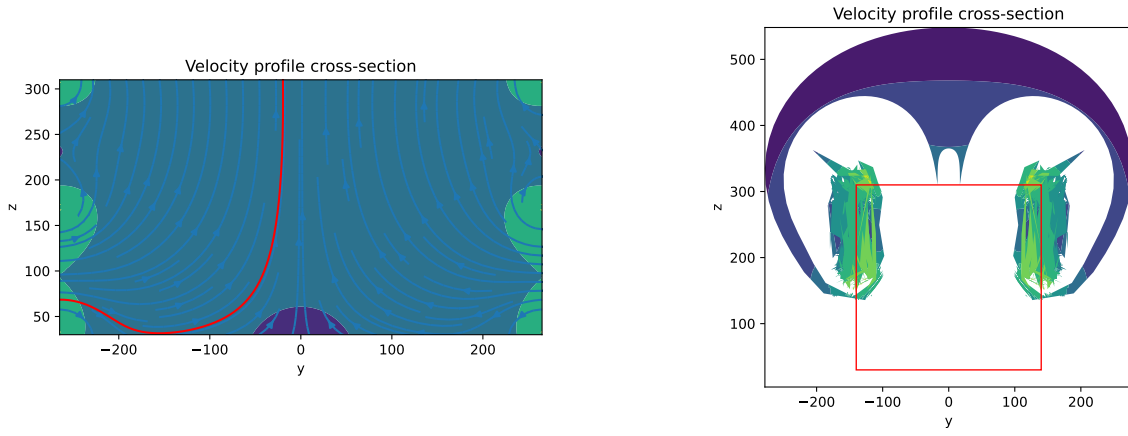
The analysis of the wake behaviour undertook the following assumptions:

- WCT-ASS-01:** Wake moves with the free-stream velocity
- WCT-ASS-02:** The effects of viscosity in the wake can be neglected
- WCT-ASS-03:** The effects of turbulence in the wake can be neglected
- WCT-ASS-04:** The effects of compressibility in the wake can be neglected
- WCT-ASS-05:** The flow within the wake is irrotational
- WCT-ASS-06:** Effects of the individual HLDs, which constitute the WCT can be accounted for by placing constant circulation vortices at the location of their wing tips
- WCT-ASS-07:** Interactions of the flow in the wake are governed primarily by the velocity components perpendicular to the free-stream velocity.

Assumptions **WCT-ASS-02**, **WCT-ASS-03**, **WCT-ASS-04**, and **WCT-ASS-05** allow for use of potential flow theory. Along with assumption **WCT-ASS-06**, this allows for modelling effect of the HLDs as simple vortices with constant circulation, the effects of which need to only be considered in two dimensions perpendicular to the free-stream velocity, as per **WCT-ASS-07**. Lastly, with **WCT-ASS-01**, the location of the wake at any point in time in the direction of the free-stream velocity can be determined.

Potential flow is a model used to describe the incompressible, inviscid, irrotational flow. A circulation source (such as a tip vortex) induces a velocity as prescribed by Equation 6.22, where the total circulation of the source is $\vec{\Gamma}$ and the relative position from it is \vec{r} .

$$\vec{v} = \frac{\vec{\Gamma}}{2\pi||\vec{r}||^2} \times \vec{r} \quad (6.22)$$



(a) An example of an initial flow field with a streamline shown in red

(b) An example of a final flow field

Figure 6.17: Example of a flow field of a simulation and end result of wake propagation

Lift produced by an HLD per unit length is related to the magnitude of circulation by equation Equation 6.23, where L' is lift per unit length, v_∞ is the free stream velocity, ρ_∞ the free stream density, C_L is the lift coefficient per unit area, and c is the chord length.

$$\|\vec{\Gamma}\| = \frac{L'}{v_\infty \rho_\infty} = \frac{1}{2} v_\infty C_L c \quad (6.23)$$

To simulate effect of multiple vortices on the wake, the domain of the wake was meshed with grid that had uniform vertical and horizontal spacing. Velocity at a point was computed as result of influence of individual vorticity contribution as given by Equation 6.24, where the index n is the index of the individual vortex and 2D flow in the y-z plane was assumed.

$$\vec{v}(\vec{r}) = \sum_{n=1}^N \left(\frac{\Gamma_n}{2\pi \|\vec{r}_n - \vec{r}\|^2} \begin{bmatrix} z - z_n \\ y_n - y \end{bmatrix} \right) \quad (6.24)$$

For each point on the mesh, the instantaneous velocity \vec{v} was computed based on Equation 6.22, which was then used to compute its position at the next time step, according to the explicit Euler method presented in Equation 6.25. This method is unstable but approaches the real solution as the time step Δt approaches zero.

$$\vec{r}(t + \Delta t) = \vec{r}(t) + \Delta t \cdot \vec{v}(\vec{r}(t)) \quad (6.25)$$

After the method was proved to converge for every point which does not start at the centre of a vortex, the method was expanded to every point in the mesh. The simulation was then tweaked to run until every point has left the initial simulated domain. The width of the domain was given a fixed width of 280 m, with a line of symmetry 30 m below the bottom boundary. The symmetry line meant that for every vortex, there was one of equal or opposite strength put on the other side of the symmetry line to simulate the ground effect and condition of tangent flow to the ground.

An initial flowfield for a setup with 6 vortices (and 6 which are placed on the other side of the symmetry plane) is shown in Figure 6.17a. An unrelated example of how a flow field looked at the moment when all points had exited the initial wake region can be seen in Figure 6.17b.

6.2.2. Verification of the Model

For verification of the model, a simple case, with a central vortex was considered. The strength of the vortex was given as $\Gamma = 100 \text{ m}^2 \text{ s}^{-1}$, positioned in the middle of simulation domain at point (3, 3). A point at

a distance of 1 m was placed next to it and the simulation was then started. Calculations were halted once the accumulated errors made the point move outside of the simulation domain of $[3, 5] \times [3, 5]$, meaning that magnitude of the distance reached at least 100%.

This simulation was repeated for time steps of size $\Delta t = 0.001\text{ s}$, 0.002 s , 0.004 s , 0.008 s , and 0.016 s . The path taken by the particle can be seen in Figure 6.18. The exact solution is drawn as a blue line, which makes a circle, and the simulated positions are shown as the red line, which quickly starts to deviate away from the exact solution. The number of steps for the deviation to reach a value of 100% is presented on a double logarithmic plot in Figure 6.19.



(a) Propagation of position error with time step of $\Delta t = 0.001\text{ s}$

(b) Propagation of position error with time step of $\Delta t = 0.016\text{ s}$

Figure 6.18: Propagation of positional error with tow different time steps (red) and exact solution (blue)

The number of time steps taken for the error to exceed 100% was found to be 126, 463, 1851, 7402, and 29609 respectively. As the time step halved, the number of steps increased by a constant factor of $10^{0.6}$. From this, it is concluded that the error approaches zero as the time step Δt approaches zero.

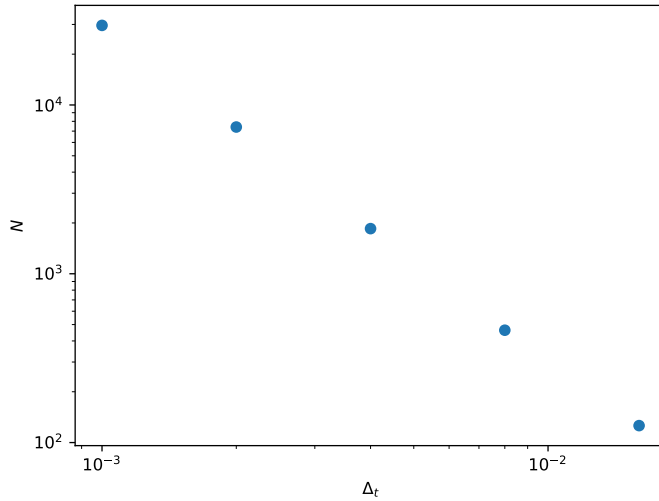


Figure 6.19: Number of steps for the error to exceed 100% plotted against the size of time step Δt

The validation plan so far is to compare the model to any test data obtained during the later stages of design, as well as to compare the results to other validated models once they become viable to use (such as ANSYS or OpenFlow).

6.2.3. Analysis of Effects on Energy Density

For the design of the WCT, there are some considerations about the system itself and some which come as a consequence of its interfacing with other subsystems. With regard to the former, the system's main purpose is the re-energization of the wake by means of using circulation produced as a result of lift force generated downwards. This follows based on Equation 6.23.

For analysis of the WCT, circulation Γ had to be determined. Based on Equation 6.23, it can be determined base on free stream velocity v_∞ , section lift coefficient C_L , and chord c . For the value of the free stream velocity v_∞ , the value of the turbine's rated wind speed of 11 ms^{-1} was used when trying to determine energy density.

After talking with an MSc student Thomas Broertjes, a value of $C_L = 5$ was taken as achievable. As justification, it was given that lift coefficients for large commercial planes come to lower values when employing HLDs mainly due to the need to retract them in a single-section airfoil. Since that is not the case for the presented HLD, a cascading airfoil with three or even four sections may be employed.

$$\Gamma = \frac{1}{2} \cdot 11 \text{ ms}^{-1} \cdot 5 \cdot c \quad (6.26)$$

For analysis, first of all, a space-filling pattern consisting of diamonds is assumed; then in order to calculate density total energy of the turbine is divided into the area covered by a single diamond. The diagonal of this diamond is assumed to be the length where the wake is fully recovered so that there is no interference between units. Described setup can be seen better in Figure 6.20.

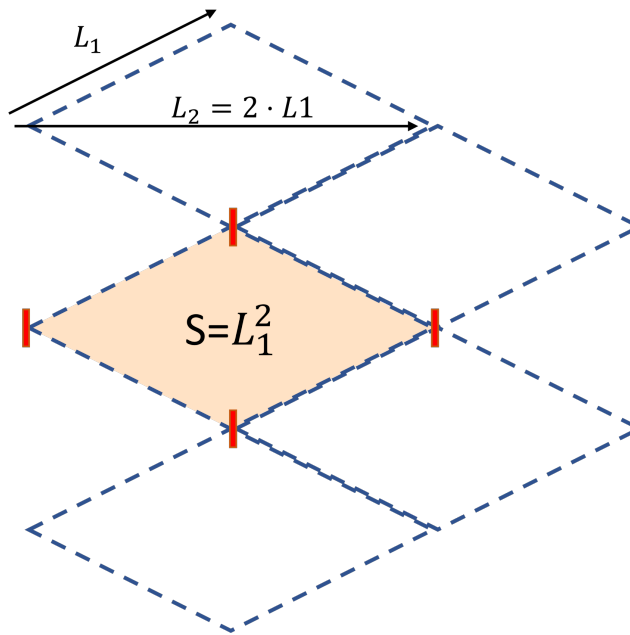


Figure 6.20: Farm Setup

Several setups were considered, using different placements of the HLDs, different system/wake widths, and different chord values. The values of chord length were taken to be scaled to 10% of the structural width up to a specified limit. Since the height of the system was kept constant, the metric considered was the maximum possible power produced by the system. Several chord and wing position configurations were considered. It must be noted that for the wake recovery calculations, extra width due to the monopile is considered, and no middle circulation is added to the frame under the assumption of no flow over the

monopile. Therefore, it acts like a part of the HLD foil. However, this extra width from the monopile is not considered in aerodynamic loads since it is not a lift-generating surface.

The results for configurations which were considered can be seen in Figure 6.21. These designs included the following configurations for the HLD:

WCT-CFG-1: 4 blades with $c_{\max} = 15$ m, with blades located at the heights of 310 m, 265 m, 170 m, and 125 m seen in Figure 6.21a

WCT-CFG-2: 4 blades with $c_{\max} = 12$ m, with blades located at the heights of 310 m, 265 m, 170 m, and 125 m seen in Figure 6.21b

WCT-CFG-3: 4 blades with $c_{\max} = 10$ m, with blades located at the heights of 310 m, 265 m, 170 m, and 125 m seen in Figure 6.21c

WCT-CFG-4: 4 blades with $c_{\max} = 10$ m, with blades located at the heights of 310 m, 265 m, 220 m, and 170 m seen in Figure 6.21d

WCT-CFG-5: 6 blades with $c_{\max} = 7.5$ m, with blades located at the heights of 310 m, 265 m, 220 m, 170 m, 125 m, and 85 m seen in Figure 6.21e

WCT-CFG-6: 7 blades with $c_{\max} = 6$ m, with blades located at the heights of 310 m, 265 m, 220 m, 170 m, 125 m, 85 m, and 30 m seen in Figure 6.21f

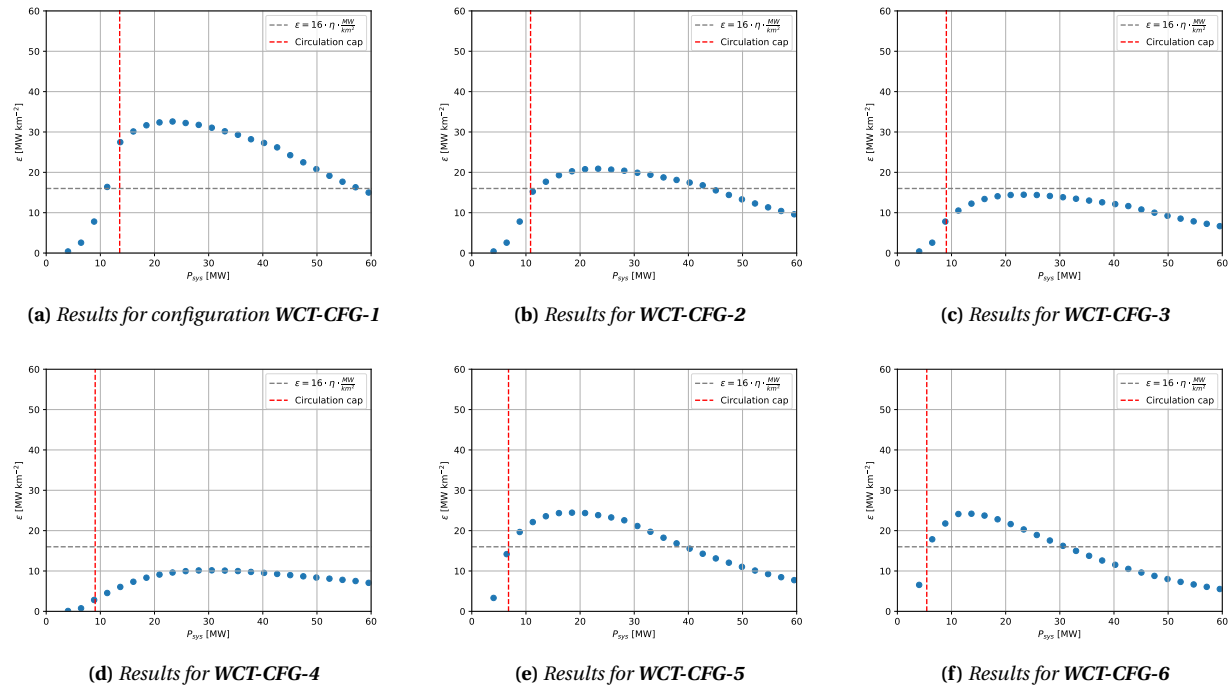


Figure 6.21: Energy density ϵ versus system's maximum available power P_{sys} for several configurations tested with the required minimum power density of $\epsilon_c = 16 \text{ MW km}^{-2}$ as a horizontal grey dashed line and point where the chord limit indicated as a vertical red line

Based on results in Figure 6.21, along with the results of the structural and operational maintenance. The structural analysis determined it would be favorable to have a width-to-height ratio of 1:1, which corresponds to the maximum available power of around 31.7 MW in plots shown Figure 6.21. Since a bigger HLD would mean larger loads on the structure and more difficult assembly, the design **WCT-CFG-2** was chosen as the best choice given the constraints.

Considering that analysis results depend only on circulation produced by the WCT, this means that given the current assumptions, it would be possible to change both C_L and c , as long as their product is con-

stant.

6.2.4. Analysis Assumptions, Limitations, and Errors

This section briefly touches on the assumptions made by the rest of the section, and the subsequent limitations and errors which are present in the results and conclusions presented in Subsection 6.2.3.

Assumptions made for the HLDs performance were made for the value of $C_L = 3$, which was made based on the recommendation by T. Broertjes. The choice for maximum chord of $c = 20\text{ m}$ due to the fact that this is not too far off from the root chord of an Airbus A380. Since a multi-section airfoil would be required for desired performance, it was deemed a feasible length for the HLDs chord, however, a much larger value would likely be infeasible to make.

A major assumption on which the wake analysis stems is that when all of the air originally in the area of the original wake is dispersed, a wind turbine placed at that point could operate at or at least very close to full efficiency. This is an assumption which would need to be verified either using CFD simulations or scale models.

The next assumption is that the effects of an airfoil can be modelled well with a pair of stationary vortices of a set circulation. This is tied to the assumption of potential flow, which is deemed acceptable, considering that low speeds allow for compressibility to be neglected. Viscous effects in the wake should also be rather mild due to the large physical dimensions and consequently low-velocity gradients. On the other hand, the analysis did not take into effect the turbulence of the flow itself and the consequent Reynolds stresses. The effect of these may be significant, however hard to predict, as a very detailed model of wind at the installed location would be required.

Next, since the model used assumes potential flow, This neglects the contribution of viscous forces and dissipative effects. Some of these effects would lower the effectiveness of the WCT, as they would dissipate the energy of the vortices as they travel forward. On the other hand, there would be a positive contribution from the dissipation of momentum into the wake. This would aid re-energization by providing another mechanism of momentum transfer, other than just outside flow coming into the wake.

It is also assumed that the time in which the wake should be removed in, is the time it takes air to travel the distance between two turbines in a staggered grid, while at the rated wind speed. This assumption is a conservative one, as air in the wake which needs to be replaced would travel at a lower speed.

Lastly, the way in which the effect of tip vortices is modelled also does not include the contribution of the other nearby turbines, which would aid in wake mixing, since the effect of vortices produced by HLDs of other turbines would also generate a contribution to flow upwash.

6.2.5. Design of WCT

Based on the analysis, using **WCT-CFG-2** would allow having the fewest number of HLDs with the lowest amount of circulation required to still meet the requirement **UR-01**. As such, the WCT was determined to use a design with a total circulation $\Gamma = 330\text{ m}^2\text{ s}^{-1}$ per blade. As an alternative to the combination of the chord length of $c = 12\text{ m}$ and lift coefficient of $C_L = 5$, the same circulation may be provided by having a longer chord with $c = 20\text{ m}$ and lift coefficient of $C_L = 3$.

Based on considerations for the structure in Section 6.1, individual cells have a depth of a bit over 30 m, it would be possible to have the HLDs integrated in the structure. With the larger chord and lower lift coefficient, WCT elements would be less demanding to design and provide additional structural stiffness. As such, the proposed design for WCT is to use four HLDs with maximum values of lift coefficient $C_L = 3$ and chord lengths of $c = 20\text{ m}$.

Since the value of lift coefficient $C_L = 3$ is still rather high, this could be achieved using a two or three-element airfoil, which would be augmented using slats and flaps in order to increase its lift coefficient C_L

to the desired amount.

6.2.6. Integration of WCT

The main effects of WCT on the structure are the loads it will exert on it. With the selected chord of $c = 20\text{ m}$, operating lift coefficient $C_L = 3$, and rated wind speed of $v = 11\text{ m s}^{-1}$, the operational loads are the downforce L per blade as per Equation 6.27, or a total downforce of about 4.98 MN. For the drag, the force is given by Equation 6.29, resulting in a total structural drag of 425 kN.

$$L = \frac{1}{2} \cdot 1.225 \text{ kg m}^{-3} \cdot 280 \text{ m} \cdot 20 \text{ m} \cdot (11 \text{ m s}^{-1})^2 \cdot 3 = 1245.09 \text{ kN} \quad (6.27)$$

$$C_D \approx \frac{C_L^2}{Ae\pi} + C_{D_0} \approx \frac{3^2}{\frac{280}{20}0.8\pi} + 0.015 = 0.256 \quad (6.28)$$

$$D = \frac{1}{2} \cdot 1.225 \text{ kg m}^{-3} \cdot 280 \text{ m} \cdot 20 \text{ m} \cdot (11 \text{ m s}^{-1})^2 \cdot 0.256 = 106.25 \text{ kN} \quad (6.29)$$

While the forces during operation are very significant, the more important case to consider is storm safety. During the last 50 years, the worst wind conditions had wind gusts with speeds of up to 70 m s^{-1} as per Section 3.3. In order to reduce loading on the structure, the lift would have to be reduced, leading to a consequent reduction in drag. Without this intervention, the total experienced loads would increase by a factor of 40.

Since the proposed design of WCT is to use a multi-element airfoil integrated into the structure, along with some integrated high-lift devices (like slats and flaps), the main idea for reducing loads is to use retraction mechanism to retract HLDs into the individual airfoils, and to move the non-fixed airfoil elements into the same plane as the airflow. This would effectively reduce the lift coefficient to almost zero and the drag coefficient to only a bit more than its profile drag. The required value for the maximum allowed lift coefficient during such a storm would be $C_L = 0.074$ as per Equation 6.30. The drag caused by this would be given as Equation 6.32, meaning that the total loading during the storm would result in 1.02 MN of drag force. This is an optimistic plan, but considering that the forces here are rather small compared to the weight of shafts, rotors, and generators, an increase in the actual values for lift and drag should not be critical.

$$C_L = 3 \left(\frac{11 \text{ m s}^{-1}}{70 \text{ m s}^{-1}} \right)^2 = 0.074 \quad (6.30)$$

$$C_D \approx \frac{C_L^2}{Ae\pi} + C_{D_0} \approx \frac{0.074^2}{\frac{280}{20}0.8\pi} + 0.015 = 0.0152 \quad (6.31)$$

$$D = \frac{1}{2} \cdot 1.225 \text{ kg m}^{-3} \cdot 280 \text{ m} \cdot 20 \text{ m} \cdot (70 \text{ m s}^{-1})^2 \cdot 0.0152 = 255.45 \text{ kN} \quad (6.32)$$

Since the tower structure would be made six cells wide, as shown in Section 6.1, this offers an opportunity to split each HLD blade into six individual pieces. This would allow for smaller systems which would help in terms of maintenance as well as construction. With the airfoil's chord being 20m, it would likely be thick enough to allow for the housing of some important components within the airfoil itself. It is decided to have HLD at the bottom of the rotor at each cell; since it has 20 m chord length, it can be considered a structural element this way.

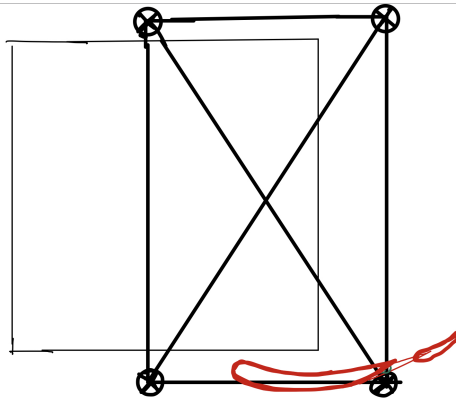


Figure 6.22: Installation of HLD

6.2.7. Mass of the WCT

The wings of the WCT subsystem need to withstand the aerodynamic loads while transferring them to the truss structure to which it is connected. This adds another functionality apart from the aerodynamic wake performance, namely structural capabilities. With this in mind, it is important to analyse the possible failure modes of the wing and design accordingly. For the purposes of this report, the airfoil thickness will be evaluated against failure by yielding. The following assumptions were taken into consideration:

WCT-ASS-08: The wing is connected to the truss structure at the edges of each truss cell through pin connections

WCT-ASS-09: The loads will be carried exclusively by 2 spars, located at 25% and 75% of the chord

WCT-ASS-10: Both spars are considered to have a web height equal to half of the airfoil thickness, namely the spars are 1.5 m high, denoted by the symbol H .

Considering the geometry of the airfoil, the bending stress introduced by the distributed drag is negligible, making the bending stress produced by lift in storm conditions the limiting case factor. Using the wind profile previously described in Section 3.4, it was determined that the maximum loading of the wing is equal to 5.5 kN/m. The maximum stress will be found at the midway point of each truss cell and will be given by Equation 6.33, where t is the thickness of the spars.

$$\sigma = \frac{M j_{\text{safety}} \cdot y}{I} = \frac{1.7 \frac{L^* w_{\text{cell}}^2}{8} \cdot \frac{H}{2}}{\frac{1}{6} t H^3} = \frac{51}{80} \frac{L^* w_{\text{cell}}^2}{t H^2} \quad (6.33)$$

The spars were considered to be made out of the same material as the truss elements of the tower. Applying the condition that the spars should not yield leads to the spars having a minimum thickness of 12.31 mm and a total spar weight of 81 t. Of course, the WCT subsystem comprises more than the structural spars, as it includes the skin of the airfoil and the HLD assembly. With this in mind, a margin of 100% was applied to the mass of the subsystem, leading to 162 t for each one out of the four wings.

6.3. RTR analysis

The goal of this section is to analyze the performance of the rotors. This will include a closer look at the relations between C_P , C_T and the tip speed ratio, creating power and shaft torque curves and calculating the expected power production. These calculations will provide necessary data for sizing the drivetrain as well as determining the attainable yaw rate.

6.3.1. Obtaining the Thrust and Power Coefficients

The analysis starts with establishing the relation of the power and thrust coefficients with the tip speed ratio (TSR). As a base, the data from a paper by Jamieson et al. is used [3]. In the process of creating power curves, it was discovered that the data does not cover a sufficiently wide TSR range. To maintain a production of 30 MW, with wind speeds exceeding 15 ms^{-1} , the TSR has to drop below 2. The data set only contains C_P and C_T information for TSR values between 2 and 6.5. Therefore, a parabola was fitted to the data. Whenever C_P or C_T information from outside the 2 to 6.5 TSR window is required, the fitted parabola is used to calculate the coefficients. The results of the fusion of the data and the fitted parabola can be seen in Figure 6.23.

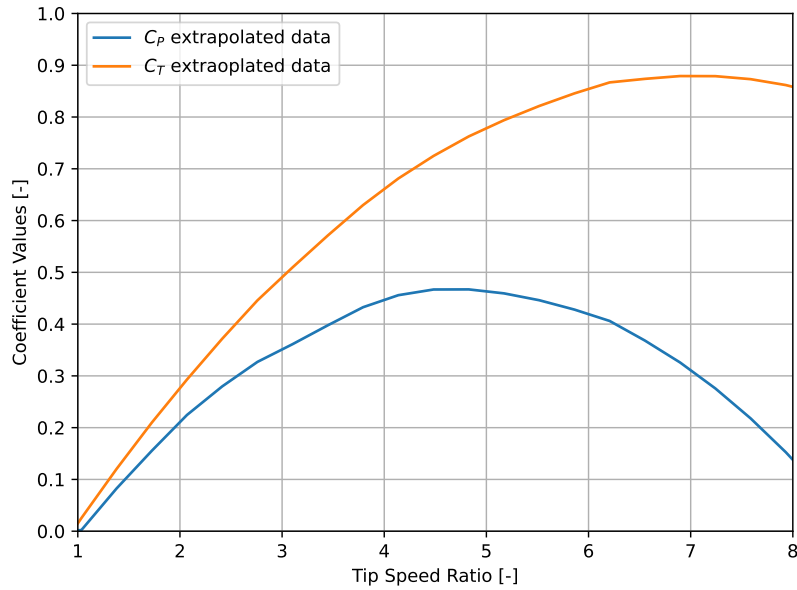


Figure 6.23: Extrapolated power and thrust coefficients over the tip speed ratio

6.3.2. Power and Shaft Torque Curves

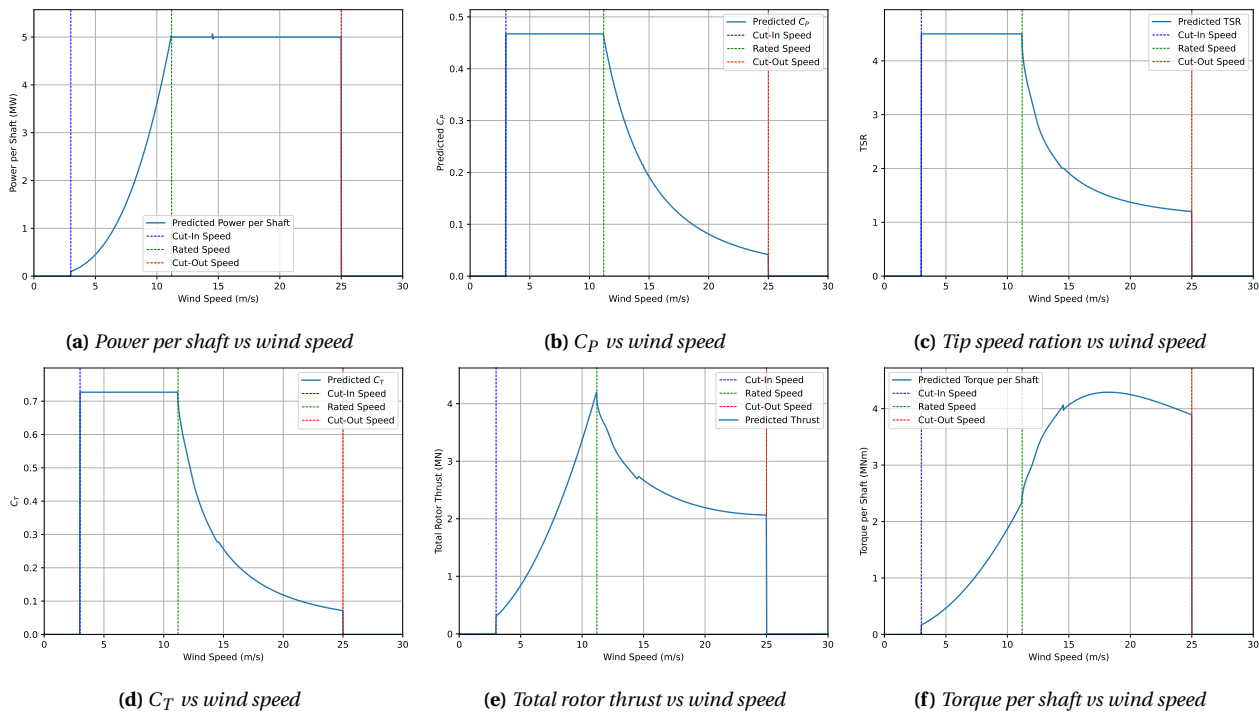
With access to C_P and C_T data at all the necessary TSR values available, a closer look at the turbine operation is possible. The most pertinent information pertaining to operation is the power produced, the torque on the rotor shaft and the thrust of the rotors at a given wind speed. These are the properties that will influence the rest of the design and therefore need to be controlled.

In theory, the optimal design would balance out the three values. Creating such a design is beyond the scope of the project, therefore, a simpler approach was taken. The plan of action is to produce as much power as possible while under the rated speed and make the rated power above the rated speed. This is not the optimal strategy. It causes quite high torques in the rotor shaft and misses out on potential energy production. However, it is also the easiest case to analyse and should provide an underestimate of energy production and an overestimate of shaft torque, leading to conservative performance numbers for the design.

To calculate all of the curves, the following procedure was implemented. First, for a given wind speed, check if the C_P at TSR equal 4.5 produces more than the 30 MW rated power. If yes, then the TSR is reduced until rated power is achieved. With the established TSR value, C_T and thrust is calculated. Lastly, the power produced per shaft is divided by the rotational speed of the rotor to get the torque on the shaft.

The power and C_P curves can be seen in Figure 6.24a and Figure 6.24b. It is worth noting that C_P has to drop cubically with wind speed to maintain the rated power production. Such an aggressive change in

C_P has a correspondingly quick change of TSR, leading to unforeseen results. The most intriguing of the outcomes is the fact that the thrust produced by the rotors peaks at the rated wind speed and falls from there. The change of TSR, C_T and thrust with wind speed can be seen in Figure 6.24c, Figure 6.24d and Figure 6.24e. The last value that important to the design is the torque on the shaft. The torque curve can be seen in Figure 6.24f. There is an important observation to be made, namely, the torque in the shaft doesn't max out at the rated wind speed, but at a wind speed of around 18.2 m s^{-1} . Using the previously mentioned wind profile as depicted in Figure 3.6, the rated power production of the system is evaluated as 31.3 MW. This margin was chosen as contingency considering mechanical and electrical efficiency losses of up to 96%. This evaluation was made assuming that the top 12 m are occupied by the wake control and do not contribute to electricity production. Considering that this top region has the highest winds, this makes the estimate conservative.



6.3.3. Shaft design

The main shaft to which the blades are attached will be connected to the tower using seven equidistant locating bearings, taken as deep groove ball bearings. Through this type of bearing, the shaft will be able to transfer axial and radial loads to the truss structure, effectively fixing and unloading the shaft in the process. A sketch of the shaft, along with the dimensions of the final design, are presented in Figure 6.25a. The shafts are hollow cylinders with a diameter of 1618mm, a thickness of 24.3mm and a length of 270m. All bearings are modelled as pin supports, restricting translation but allowing for rotation. The shaft will experience aerodynamic lateral loads and torsional loads created by the blades, while also carrying the blades and struts weight. All external and reaction forces and moments considered are presented in Figure 6.25b. The following simplifying assumptions were used:

RTR-ASS-01: All bearings carry the same axial reaction force along the z-axis

RTR-ASS-02: The bearings at the extremities of the shaft carry the same radial reaction force along the x-axis

RTR-ASS-03: The bearings between the first and last bearings carry the same radial reaction force along the x-axis

RTR-ASS-04: All rotors are loaded by the same wind speed

RTR-ASS-05: All rotors are assumed to transfer their entire loads to the shaft through the middle point between consecutive bearings

RTR-ASS-06: The arrangement of the equally phased displaced rotors lead to a constant torque along a full rotation

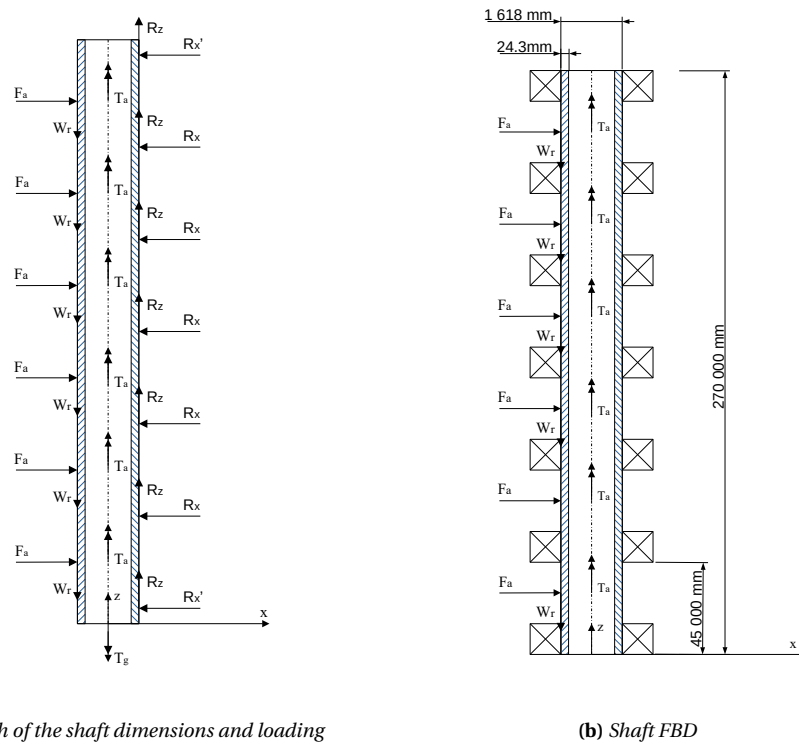


Figure 6.25: Shaft relevant drawings

During the sizing of the shaft it was determined that the most restrictive load case is LDC2. This was no surprise, as this load case leads to the highest torque the system will experience. By imposing equilibrium of forces and moments it is possible to determine that the vertical loading of the bearings is equal to 317 kN, while the radial loadings are 63.9 kN and 31.9 kN, respectively. These values will be used further for the sizing of the bearings. The aforementioned loads will determine the internal loading of the shaft as described in Figure 6.26.

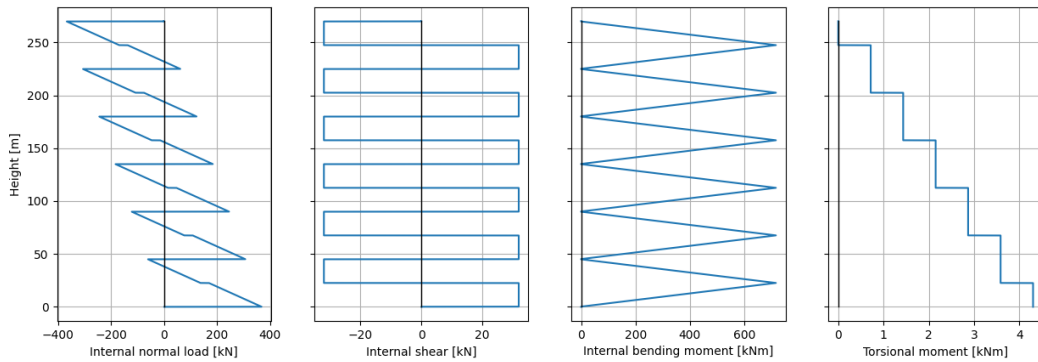


Figure 6.26: Internal loading of the main shaft

As the length of the shaft is set by the necessary rotor swept area, the only dimensions yet to be defined are the diameter and the shaft thickness. These will be accounted for in the following derivation by using the outer diameter, d_o , and the inner-to-outer diameter ratio, c_{diam} . Equation 6.34 and Equation 6.35 were used in order to calculate the normal and shear stresses within the hollow shaft. Note that the transverse shear stress given in Equation 6.35 is given for the maximum found along the shaft's cross-section.

$$\sigma_{axial} = \frac{4P}{\pi d_o^2 (1 - c_{diam}^2)} \quad \sigma_{bending} = \frac{32M_{bending}}{\pi d_o^3 (1 - c_{diam}^4)} \quad (6.34)$$

$$\tau_{transverse,max} = \frac{8V_{transverse}}{\pi d_o^2 (1 - c_{diam}^2)} \quad \tau_{torsion} = \frac{16M_{torsion}}{\pi d_o^3 * (1 - c_{diam}^4)} \quad (6.35)$$

Two distinct failure modes were considered for the shaft, namely failure through yielding and failure through fatigue. In both cases a safety factor of 1.3 was considered for both the loads and the performance of the material, yielding a cumulative safety factor of 1.7. For this initial calculations, the material considered was low carbon steel, with a yield strength of 255 MPa, an ultimate tensile strength of 400 MPa, and an ideal endurance limit of 203 MPa.

Firstly, the yield strength of the material was compared to the von Mises stress of the shaft, as obtained using Equation 6.36. As long as the von Mises stress, multiplied by both safety factors, is lower than the yield stress, the shaft is considered correctly sized

$$\sigma' = \frac{1}{\sqrt{2}} \left[(\sigma_x - \sigma_y)^2 + (\sigma_y - \sigma_z)^2 + (\sigma_z - \sigma_x)^2 + 6(\tau_{xy}^2 + \tau_{yz}^2 + \tau_{xz}^2) \right]^{1/2} \quad (6.36)$$

Secondly, the fatigue life of the shaft must be considered, as the rotor will impart a rotation from 6 RPM to 22 RPM for a lifetime of at least 25 years. In order to account for fatigue, the modified Goodman criterion was employed, which takes into account the impacts of both mean stress and alternating stress on the life of the component. The criterion is presented in Equation 6.37. Note that if this criterion is passed, then the shaft is designed for infinite life.

$$\frac{\sigma'_a}{S_e} + \frac{\sigma'_m}{S_{ult}} \leq \frac{1}{j_{material} * j_{load}} \quad (6.37)$$

Investigating the loading of the rotating shaft, it is easy to come to the conclusion that the mean normal and shear stresses are driven only by the axial and torsional shear, respectively, as these stresses are constant across the cross-sectional area of the shaft. In the case of alternating stresses, given that the shaft rotates, each given point on the circumference of the shaft will go from experiencing positive to negative bending and transverse shear stresses. Thus, the expressions of the mean and alternating von Mises stresses are given by Equation 6.38

$$\sigma'_m = \frac{1}{\sqrt{2}} [2\sigma_{axial}^2 + \tau_{torsion}^2]^{1/2} \quad \sigma'_a = \frac{1}{\sqrt{2}} [2\sigma_{bending}^2 + \tau_{transverse}^2]^{1/2} \quad (6.38)$$

It is worth mentioning that the actual endurance limit of the shaft can greatly differ from the endurance limit of its constituent material, depending on a myriad of factors. In this analysis the following effects were considered:

Surface finish: The roughness of the outer layer of the product will affect the propagation of surface cracks, while other finishing processes can introduce residual stresses. Considering rolled steel, the correction factor for surface finish can be considered to be equal to 0.65, as instructed by the guidelines of the FKM¹.

Size: It has been observed that the endurance limit varies with size, possibly due to higher chances of flaws in bigger components. Yet, for thin hollow cylinders made out of steel, with a thickness lower than 40 mm, this factor can be assumed to be equal to 1 [42].

Loading: Loading a member in reverse shear or axial stress has been proven to reduce the endurance limit as more of the cross-section is subjected to full reversed stress, as compared to bending where only the outer layers are fully loaded and the loading factor is equal to 1. As the shaft is under partially reversed shear loading, it was assumed that a load factor of 0.8 would suffice².

Reliability: Considering that all S-N curves after which the endurance limit is empirically determined are statistical in nature, this factor accounts for the reliability of the performed fatigue tests. Thus, statistical theory using 8% standard deviation in stress and strength informs us that in order to have a reliability of 0.9999, a reliability factor of 0.702 is needed³.

Thus, the final fatigue correction factor will be equal to around 0.36. Now, both criteria can be combined while optimizing for the lowest mass, with the constraints of having a shaft with an outer diameter smaller than 2 m for ease of manufacturing and a minimum diameter ratio of 0.97 to avoid small thicknesses which can lead to buckling. During the optimisation, it was determined that the critical failure mode is fatigue. The optimised shaft has the dimensions as presented in Figure 6.25b and yielded a single shaft weight of 260 t. Using these dimensions, it was evaluated that the maximum deflection that the shaft will experience will be around 3.84 mm, located in the middle of each shaft section between bearings. This deflection is equivalent to a rotation of 0.01° at the bearings, small enough to not cause additional bearing compatibility issues. Using the SKF bearing catalogues, it is possible to further estimate the mass of each bearing to about 1 tonne per bearing, as inspired by the 618/1700 MB model⁴.

6.4. YCT Analysis

This section is concerned with the design of the yaw subsystem of the turbine. This consists of sizing the yaw bearings to withstand static and dynamic loads during the lifetime of the system.

Since the turbine will have a monopile of diameter larger than 10 meters, there is need for a yaw bearing that can fit into this arrangement and, similarly to the monopile, be able to withstand both the static loads imparted on it by the external forces and moments from the turbine. Additionally, the service life of the bearing must be sufficiently high to ensure that the yaw motion does not wear out the bearing during the lifetime of the system.

A unique problem that this turbine faces is the relatively large moment arm from the centre of thrust to the base of the tower, z_{c_T} . This induces a very large tilting moment on a bearing placed at the base of the tower compared to traditional single HAWTs, where the centre of thrust moment arm to the base of the nacelle is only a few meters at most. For this reason, it is difficult to find slew bearings suitable for this application. Thus, two bearings are used so that the axial and radial loads can be reduced for each bearing, while counteracting the thrust force at the centre of thrust to reduce the tilting moment on the lower yaw bearing. Additionally, some load bearing capability is maintained if one of the bearings fails. The presence

¹ URL: <https://www.quadco.engineering/en/know-how/material-fatigue-surface-roughness-factor.htm> [cited on 18 June 2023]

² URL: https://roymech.org/Useful_Tables/Fatigue/FAT_Mod_factors.html [cited on 18 June 2023]

³ URL: https://roymech.org/Useful_Tables/Fatigue/FAT_Mod_factors.html [cited on 18 June 2023]

⁴ URL: <https://www.skf.com.sg/products/rolling-bearings/ball-bearings/deep-groove-ball-bearings/productid-618%2F1700%20MB> [cited on 18 June 2023]

of two bearings rather than one also gives more room to add larger yaw drive pinions, which would allow for a higher torque capacity when electrical yaw is used. The bottom bearing will be located at the base of the tower, while the top bearing will be on the top of the monopile, 140 m above the bottom bearing.

The static loads considered are the axial force F_a , the radial force F_r and the tilting moment M_k . For this design, F_a is the compression force resulting from the weight of the structure and the downwards facing lift induced by the WCT. F_r mostly consists of the thrust force resulting from the turbine, while M_k mainly consists of the moment due to this force. The structural truss solver provides loads as seen in Figure 6.27 for the right hand side of each yaw bearing. Loads on the left hand side are equivalent in the x and z direction but mirrored in the y direction due to symmetry.

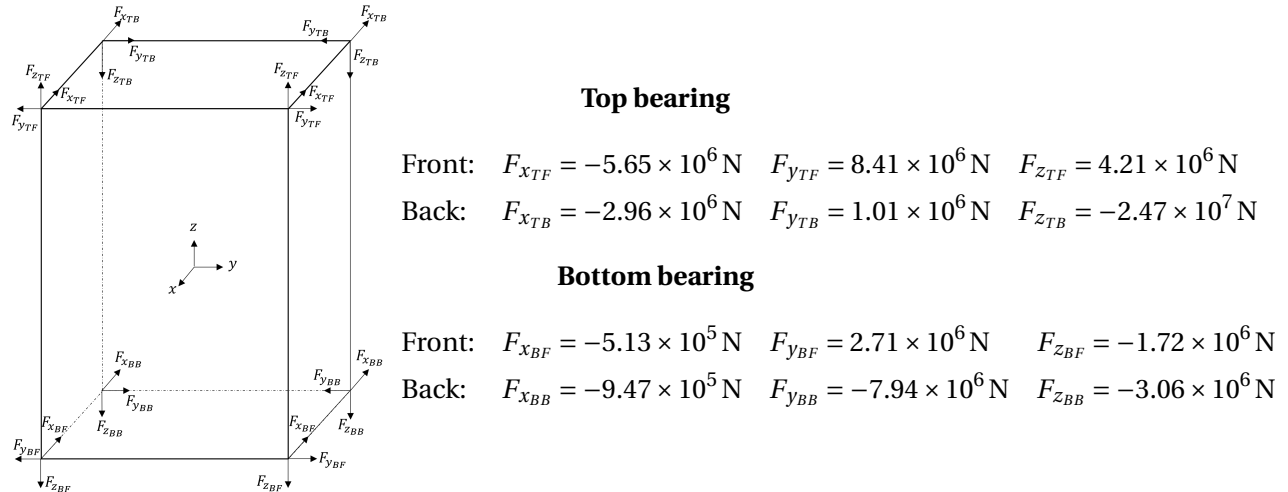


Figure 6.27: Loads transmitted from tower to top and bottom bearings

Summing these forces results in the following static loads on the top and bottom bearings. It is assumed that the upper bearing lies at the centre of thrust and so tilting moments due to thrust are negligible as they are taken by the upper bearing as radial loads.

Top bearing

$$F_a = 2 \cdot F_{zTF} + 2 \cdot F_{zTB} = -4.01 \times 10^4 \text{ kN} \quad F_r = 2 \cdot F_{xTF} + 2 \cdot F_{xTB} = -1.72 \times 10^4 \text{ kN}$$

Bottom bearing

$$F_a = 2 \cdot F_{zBF} + 2 \cdot F_{zBB} = -9.56 \times 10^3 \text{ kN} \quad F_r = 2 \cdot F_{xBF} + 2 \cdot F_{xBB} = -2.92 \times 10^3 \text{ kN}$$

Liebherr⁵ provides a flowchart for determining the static suitability of a bearing to the loads. This begins with the use of a limiting load diagram which outlines the maximum combination of F_a and M_k that can be withstood. If the loading point fits within the diagram, the loading ratio F_a/F_r is checked to ensure it is above 4 for a four-point contact ball bearing. In both bearings, it can be seen that F_a is less than 4 times larger than F_r , so the bearings will have to be oversized to withstand $F_a = 4 \cdot F_r$. This is $F_a = -6.88 \times 10^4 \text{ kN}$ for the top bearing and $F_a = -1.17 \times 10^4 \text{ kN}$ for the bottom bearing.

After this step, the static load stability is checked using Equation 6.39 which compares the equivalent axial load P_0 to the static load rating C_{stat} .

⁵URL: <https://www.liebherr.com/shared/media/components/documents/grosswaelzlager/liebherr-slewing-bearings-product-catalogue-en-metric-web.pdf> [cited: 05 June 2023]

$$S_0 = \frac{C_{\text{stat}}}{P_0} \quad P_0 = K_{\text{rep}} \cdot f_1 \left(F_A + 1.93 \cdot F_R + \frac{4 \cdot M_k}{D_L} \right) \quad (6.39)$$

Where K_{rep} is the load increase factor, equal to 1.2 for wind turbine yaw bearings, f_1 is the load factor, 1.0 for a single row bearing and 1.4 for a double-row ball bearing. For these calculations the bearing will be assumed to be double row as they can handle more loads. The static safety factor S_0 for slew bearings must be higher than 1.0. If all of these conditions are met, the bearing can be considered suitable for the static loads.

The bearing must also be ensured to have a sufficient dynamic life. This is especially true for the yaw bearings as they cannot be easily replaced during the service life of the turbine, since they transmit all the tower forces to the monopile. Therefore it must be ensured that their longevity exceeds that of the lifetime of the turbine. The dynamic analysis, also provided by Liebherr⁶, is performed through the use of the Miner rule to calculate the estimated 10% probability of failure bearing service life L_{10} . For this, load levels need to be established. This specifies the number of rotations that will need to be done by the system at each load situation. For this turbine, different wind speeds result in different F_r values. F_a and M_k will remain constant in all cases. To come up with a conservative estimate, it can be assumed that the wind turbine consistently generates the largest thrust possible and therefore largest F_r which happens at the rated wind speed. Making this assumption allows the use of only one load level.

After determining the load cases, the dynamic equivalent axial loads can be calculated, assuming the use of ball bearings, using Equation 6.40.

$$P_a = K_{\text{rep}}^{0.66} \cdot \left(F_A + 0.63 \cdot F_r + \frac{2 \cdot M_k}{D_L} \right) \quad (6.40)$$

Since there is only one load level considered, the equivalent dynamic bearing load is simply the dynamic equivalent axial load. Lastly, to calculate the bearing service life, expressed in number of rotations, Equation 6.41 is used.

$$L_{10} = 10^6 \cdot \left(\frac{C_{\text{dyn}}}{P_a} \right)^p \quad (6.41)$$

Where p is the service life exponent, $p = 3$ for ball bearings. Wind changes direction by a few degrees every 30 minutes. Using a conservative assumption that the bearings will have to make a 180° rotation to align with the wind every 30 minutes implies 219000 full rotations over the lifetime, which can comfortably assure that the bearing has sufficient life.

Performing the static and dynamic loading analysis leads to the following specifications for each bearing as seen in Table 6.6. Due to the large diameter of the bearings, they will probably have to be segmented bearings. These are usually custom made per request and therefore static and dynamic load ratings are not provided for them. The equations for calculating the equivalent loads might also differ for larger diameter bearings. Therefore, a consultation with the bearing manufacturer and an analysis performed by them for the suitability of the bearings is required. Due to insufficient data about the masses of yaw bearings with such diameters and specifications, a preliminary mass estimation was made by extrapolating the mass to outer diameter relation of the Liebherr ROD-50-DA bearing lineup⁷. This leads to a combined mass of 54

⁶URL: <https://www.liebherr.com/shared/media/components/documents/grosswaelzlager/liebherr-slewing-bearings-product-catalogue-en-metric-web.pdf> [cited: 05 June 2023]

⁷URL: <https://www.liebherr.com/shared/media/components/documents/grosswaelzlager/liebherr-slewing-bearings-product-catalogue-en-metric-web.pdf> [cited: 05 June 2023]

tonnes for both bearings. To account for other smaller components of the yaw system, such as brakes, yaw drives, etc. a mass of 100 tonnes is budgeted for the yaw system.

Table 6.6: Top and bottom bearing specifications

Parameter	Top bearing	Bottom bearing
Inner diameter [m]	10	15
F_a [kN]	68800	11700
F_r [kN]	17200	2920
C_{stat} [kN]	171353.3	29123.8
Lifetime revolution req.	219000	219000
C_{dyn} [kN]	54139.9	9204.8
Estimated mass [kg]	19000	35000

Furthermore, the bearings will need to include outward facing gears in order to be driven by the electrical yaw drives. They will also need corrosion protection to level C5-M (level of corrosion protection required for offshore environments)⁸ to prevent the salinity of the water from reducing their service life.

6.5. DRT Analysis

This chapter aims to present the wind turbine's drive train design. The drive train is the mechanical system responsible for transferring power from the rotor blades to the generator. The generator transforms the mechanical power into an electrical one. The most important components of the assembly that will be presented are the brake, gearbox and generator.

Generators

The starting point in choosing the most appropriate generators was the conclusion drawn in the Midterm Report. It has been decided that a drive train with a gearbox, a doubly fed induction generator (DFIG), and a partial converter will be used.

The power required for each generator depends on several design considerations. The most important one was the reduction of the power produced from the 60 MW to 30 MW. Secondly, since it was assumed that having a generator per shaft would be the most optimal solution in terms of simplicity and maintenance. It is important to keep in mind how many segments will produce the total power required for the wind turbine in order to comply with the imposed requirement. As six shafts have been selected in Subsection 6.3.3, the wind turbine will be equipped with six generators, each being able to deliver roughly 5 MW each.

Brushless DFIGs can be considered the best terms of sustainability and ease of maintenance. They have three two-phase windings which are used for handling the electrical power. The current frequency to the generator's rotor can be varied and thus, making it operable for variable rotational speeds. Brushless generators do not have sliding rings or brush arrangements. They include a separate exciter. Such devices use magnetic induction between the exciter stator, exciter rotor winding, and the rectifier assembly to supply the current to the main rotor winding⁹. Multiple advantages of using such generators can be identified. The first one is that they necessitate less maintenance. Since there are no moving parts, in particular, sliding rings and carbon brushes, there is no wear or tear. Additionally, they are less noisy due to the lack of friction. However, noise pollution was not considered an issue as the wind turbine is offshore and TSR is lower than the conventional horizontal ones. Aside from that, they are more expensive as a result of higher

⁸URL: https://www.liebherr.com/shared/media/components/documents/grosswaelzlager_liebherr-slewing-bearings-product-catalogue-en-metric-web.pdf [cited: 18 June 2023]

⁹URL: https://www.promsnab.info/catalogues/rotheerde/rothe_erde_gwl_en_13.08_v05w.pdf [cited: 04 June 2023]

reliability. Moreover, they do weigh more and take more space as they have a primary rotor and an exciter rotor.¹⁰

The closest version of the required generator was found in the paper of the American Society of Mechanical Engineers (ASME) [43]. It has a rated power of around 5.56 MW However, it is a direct drive one that is directly connected to the turbine shaft, which is not the case for the designed wind turbine. After further consideration, the decision is to have a generator that is part of the AMK series, provided by ABB.¹¹. As a consequence of having an unique product, the wind turbine should have customised components according to the desired specifications. Nevertheless, they should be reasonably in accordance with what is available on the market. The most important characteristics of the generator are presented in Table 6.7.

Table 6.7: DFIG characteristics [44]

Power [MW]	5.56
Rated Speed [rpm]	1750
Voltage [V]	690-1000
Locked rotor voltage [V]	1800
Total mass [t]	16



Figure 6.28: Double fed induction generator model

As previously stated, six generators will be needed, one for each shaft. Each will be placed underneath the vertical structure of the turbine. They will be mounted horizontally in order to avoid any uncontrolled movement by virtue of the rotation of the shafts. This arrangement will further facilitate the maintenance work since the generators will be easily disconnected from the assembly and then transported for the onshore maintenance service. They will also be accessible via catwalks, tower stairways, or even elevators.

Brake system

The brake system is another essential element of the drive train. The main use of this system is for safety, over-speed protection, and maintenance during extreme weather conditions or emergencies. This is usually the case when the wind speed exceeds safe levels and the wind turbine should be slowed down to operate within the specified range of wind speed. Furthermore, the brakes can also completely stop the rotors and keep them in a stationary position while proceeding with maintenance and service activities. The torque needed for stopping a single shaft can be calculated with Equation 6.42¹²:

$$T_B = T_J + T_L - T_F \quad (6.42)$$

where T_B represents the total breaking torque, T_J - inertia torque, T_L - load torque and T_F - friction torque. T_J describes the dynamic braking, which depends on the polar moment of inertia of the entire shaft, $J = \pi \cdot p \cdot l \cdot \frac{d_0^4 - d^4}{32}$ and the angular acceleration of both shaft and blades. Additionally, T_L is the torque produced by each shaft. The braking system needs to overcome this load before it can start to slow down the structure.

¹⁰ URL: <https://yourpowerguide.com/brushless-generator/> [cited: 04 June 2023]

¹¹ URL: <https://new.abb.com/docs/default-source/ewea-doc/generators-for-wind-turbines-standard-slip-ring-generator-pdf.pdf> [cited: 04 June 2023]

¹² https://www.altraliterature.com/-/media/Files/Literature/Brand/twiflex-limited/Catalogs/p-1648-tf-a4-sections/p-1648-tf-a4_braking_calculations.ashx?fbclid=IwAR3s8CZGSesCItDDjXGUXM_PUGm7ocSEBrmm9pUMfoneN2prGVJnVh7FgBw [cited: 13 June 2023]

For a conservative estimation, a safety factor of 1.3 will be assumed for this load. Friction torque stands for the friction between the breaking mechanism in the shaft. This can be assumed to be 0 since it is significantly lower than the other two terms. In order to calculate the angular acceleration of the shaft a breaking time of 10 min was considered to be reasonable ¹³, while the ω was taken as an input from the shaft sizing section Subsection 6.3.3. In order to calculate the polar moment of inertia of one shaft together with the blades Equation 6.43 was used.

$$J = \pi \cdot \rho \cdot l \cdot \frac{d_0^4 - d^4}{32} + m \frac{d_0^2}{4} \quad (6.43)$$

where $l=280$ m- total length of the shaft, $d_0=1.57$ m- outer diameter of the shaft, $d=1.47$ m- inner diameter of the shaft, $m=1$ t- mass of a single blade. Moreover, for simplifying the calculations, it was considered that all blades are point masses at a distance $\frac{d_0}{2}$ from the rotational axis. All necessary values for picking a model for the brake are showcased in Table 6.8.

Table 6.8: Brake system characteristics

Mass [kg]	610
Reaction time [s]	0.2
Breaking time [s]	600
T_J [kNm]	33.24
T_L [kNm]	5577
T_F [kNm]	0
T_B [kNm]	5610.24
Rated torque [kNm]	207

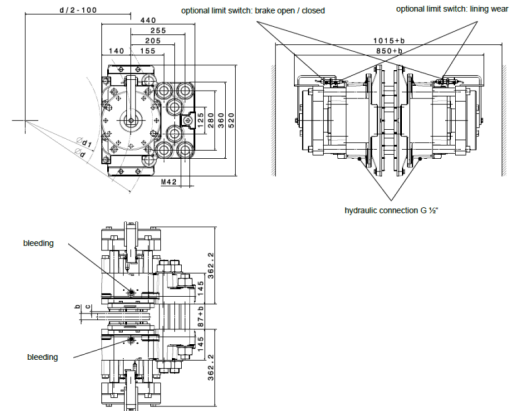


Table 6.9: Brake system model

As displayed in Table 6.8, the total moment for breaking is roughly 6.61 MNm. This value is beyond the capacity of any brake on the market and for this reason, it was decided to place the brake after the gearbox as the gearbox can reduce the torque required for stopping the mechanism. In this matter, the breaking assembly will act on the high-speed shaft of the transmission and not on the low-speed one.

Gearbox

The gearbox is the element of the wind turbine that transmits and converts the power between the driving source and the driven load. Usually, gearboxes are used for speed conversion, load distribution, mechanical isolation, and torque or directional changes. There are three main reasons for choosing to equip the wind turbine with a gearbox. The first one is that it is not realistic to halt the main shafts considering the current technology of the braking systems. Since the torque experienced by each shaft is about 4.29 MNm and the total moment needed for stopping each sub-assembly is roughly 5.61 MNm, those values should be lowered in order to be able to be dealt with. Secondly, as the designed product is a vertical wind turbine, the rotational axis of the rotors is vertical and the generators are placed horizontally. The consequence of this is that the rotational axis should be altered by 90 deg which can only be achieved by a bevel gear. Lastly, this type of transmission is well-developed and is almost at its maximum efficiency point. ¹⁴ Even if the failure of a gearbox for a wind turbine is more probable than other's components, removing it improves

¹³<https://www.bbc.com/news/blogs-magazine-monitor-24706238> [cited: 17 June 2023]

¹⁴<https://www.engineering.com/story/the-future-of-wind-turbines-comparing-direct-drive-and-gearbox> [cited: 18 June 2023]

the reliability of the entire turbine. However, the lack of such a device is reflected in a direct drive and thus, a direct drive generator which is costly and heavier than a DFIG.

As stated, each shaft will be connected with a right-angle gear which will include multiple planetary stage bearings and a bevel. The bearings are used for reducing the torque and increasing the angular velocity of the shaft, respectively. The assembly is rated to have an efficiency between 93% and 97%. ¹⁵. Since the shafts spin at a rated speed of 28 RPM and the rated at 120 RPM, a gearbox ratio of about 43 will be needed. A single-stage planetary bearing can have a ratio that ranges from 3 : 1 to 10 : 1, but it is considered that the best combination of pinion and planet-gear size leads to ratios between 4 : 1 and 8 : 1. ¹⁶ In this matter, it was decided to include a double-stage gearbox for aiming to a ratio of 43. A reasonable product that has been found available is the ABXU 535 or ABXU 555 right-angle gearbox models provided by Rexton. Table 6.29 depicts the technical drawing of them. ¹⁷

Table 6.10: Gearbox characteristics

Low-speed shaft velocity [RPM]	28
High-speed shaft velocity [RPM]	1200
Low-speed shaft torque [kNm]	5611
High-speed shaft torque [KNm]	131
Gear ratio [-]	43
Mass [t]	4

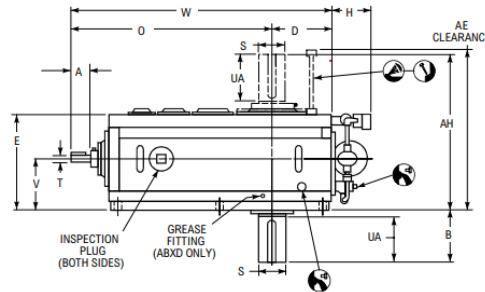


Figure 6.29: Gearbox model

As illustrated in Table 6.10, the gearbox should have a ratio of about 43. The component has not been found in the Rexton catalog and that is why an existing model was updated with the required specifications which were also dependent on other elements of the drive train. In addition, with regard to the gearbox's ratio, the torque the braking system needs to counteract was lowered from 5611 kNm to only 131 kNm. In this context, the SHI 251 1750 mm brake model, provided by Hindon, was chosen for the designed wind turbine. It is a hydraulic disc brake, used for holding and emergency stop applications, which is installed and developed for breaking on the output shaft of the right-angle transmission. A technical drawing of it is pictured in Table 6.9. ¹⁸ If necessary, the connection between several parts of the drive train will be made via couplings.

6.6. FND Analysis

The foundation of the system has the function of carrying all gravitational, aerodynamic, and tidal loads experienced by the system and transferring them into the sea bed. In previous reports, it has been decided that the best design option for the foundation is an XXL monopile. Currently, extra-large monopiles are used in water depths exceeding 30 m, having diameters that can reach 11 m at mudline and wall thicknesses of around 150 mm ¹⁹. As of the date of this report, the heaviest ever installed monopiles lay in the Baltic Sea at Parkwind's Arcadis Ost 1, and weigh more than 2000 t. In this section, the sizing of such a monopile is performed, using the design guidelines and methodology laid out in [23].

¹⁵<https://www.meadinfo.org/2008/11/gear-efficiency-spur-helical-bevel-worm.html> [cited: 18 June 2023]

¹⁶<https://www.machinedesign.com/motors-drives/article/21834575/planetary-gears-a-review-of-basic-design-criteria-and-practices> [cited: 18 June 2023]

¹⁷<https://www.rexnord.com> [cited: 18 June 2023]

¹⁸<https://www.hindon.com/product/industrial-brakes/disc/shi-251-1750-mm/> [cited: 18 June 2023]

¹⁹URL: <https://www.offshorewind.biz/2020/05/11/beyond-xxl-slim-monopiles-for-deep-water-wind-farms/> [cited on 19 June 2023]

6.6.1. Monopile sizing

The monopile is supposed to carry all loads experienced by the tower. These loads are introduced through the yawing bearings, and they are of three types: transverse loads, normal loads and bending moments. Additionally, the foundation will experience a loading driven by waves, for the submerged section, and driven by wind, for the afloat section. The models described in Section 3.4 will be used for these purposes. For the current design sizing process, the monopile will be considered to be capped at the mudline, so that the driving length of the monopile can be evaluated independently. One unusual characteristic of the monopile to be designed is the height. Due to the large overturning moment of the turbines, a second yaw bearing has to be placed halfway up the truss structure at a height of 170 m above the water. To achieve this, a central tower will be located on top of the monopile, that supports this bearing, analogous to the tower of a conventional wind turbine. This central tower is considered part of the foundation. The following assumptions have been used:

FND-ASS-01: Half of the weight of the topside mass is introduced through each bearing

FND-ASS-02: The monopile is assumed to be clamped to the seabed

FND-ASS-03: The drag coefficient under wind loading of the afloat portion of the monopile is equal to 1.2

FND-ASS-04: The drag coefficient under wave loading of the submerged portion of the monopile is equal to 1

FND-ASS-05: The inertial coefficient under wave loading of the submerged portion of the monopile is equal to 2

FND-ASS-06: The tidal loading is assumed to be applied between the SWL and the ML

FND-ASS-07: The torque created by one pair of counter-rotating rotors is assumed to be zero, leading to no torque loading of the monopile

The bearing loading can be further broken down into its constituent elements as shown in Equation 6.44 to Equation 6.49.

$$V_{B1} = D_{HLD,top} + D_{HLD,top-middle} + T_{upper-tower} \quad (6.44)$$

$$V_{B2} = D_{HLD,bottom} + D_{HLD,bottom-middle} + T_{lower-tower} \quad (6.45)$$

$$N_{B1} = L_{HLD,top} + L_{HLD,top-middle} + \frac{1}{2} mass_{topside} * g \quad (6.46)$$

$$N_{B2} = L_{HLD,bottom} + L_{HLD,bottom-middle} + \frac{1}{2} mass_{topside} * g \quad (6.47)$$

$$M_{B1} = D_{HLD,top} * (z_{HLD,top} - z_{B1}) + D_{HLD,top-middle} * \\ (z_{HLD,top-middle} - z_{B1}) + M_{HLD,top} + M_{HLD,top-middle} + \int_{z_{B1}}^{z_{top}} T_{(z)}^* * z dz \quad (6.48)$$

$$M_{B2} = D_{HLD,bottom} * (z_{HLD,bottom} - z_{B1}) + D_{HLD,bottom-middle} * \\ (z_{HLD,bottom-middle} - z_{B1}) + M_{HLD,top} + M_{HLD,bottom-middle} + \int_{z_{B1}}^{z_{bottom}} T_{(z)}^* * z dz \quad (6.49)$$

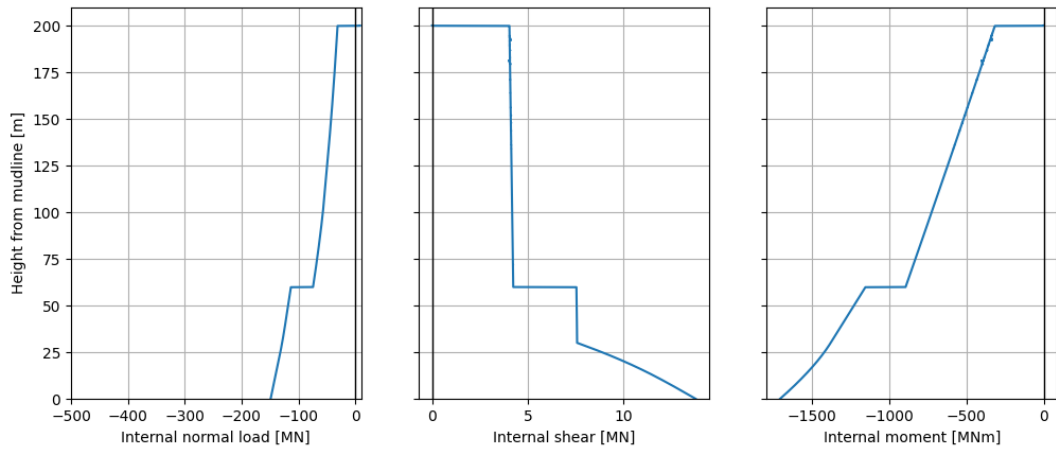


Figure 6.31: NVM loading diagram of the monopile under LDC1

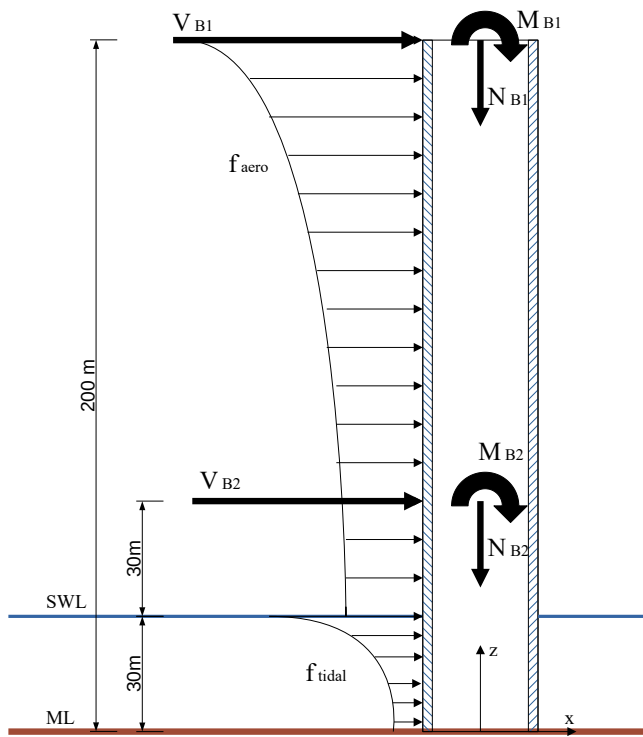


Figure 6.30: Drawing of the loading of the monopile

Using the previous loading it is possible to solve for the reaction forces on the seabed and determine the loading diagram for the monopile. The loading diagram for rated operation, namely LDC1, is provided in

The stresses throughout the monopile can be calculated using the above mentioned loading together with

the stress equations described by Equation 6.34, and Equation 6.35. Moreover, Equation 6.36 can be used in order to obtain the von Mises stress.

The foundation was tested against three failure modes, namely failure by yielding, by local buckling, and by global buckling. The yielding criterion is applied in the same way it was used in Section 6.3, again using the von Mises stress with a cumulative safety factor of 1.7. The two buckling failure modes were investigated using the methodology described by K.W Hermans [23]. The local buckling criterion is described by Equation 6.50.

$$\frac{N j_{\text{load}} j_{\text{material}}}{N_e} \leq 1 \quad N_e = \frac{\pi^2 EI}{4.8 L^2} \quad (6.50)$$

The global buckling criterion, also called the DNVGL standard, was developed by Det Norske Veritas and the Germanischer Lloyd [45]. This standard is a global buckling check and takes into account both normal and bending moment loading. The unity check follows Equation 6.51.

$$\frac{N j_{\text{load}}}{\kappa N_p} + \frac{\beta_m M j_{\text{load}}}{M_p} + \Delta n \leq 1 \quad (6.51)$$

The plastic resistances present in Equation 6.51 are determined using Equation 6.52

$$N_p = \frac{A_{\text{cross}} S_{\text{yield}}}{j_{\text{material}}} \quad M_p = \frac{1}{6} d_o^3 \left[1 - \left(1 - \frac{2t}{d_o} \right)^3 \right] \frac{S_{\text{yield}}}{j_{\text{material}}} \quad (6.52)$$

In addition to these elements a third term evaluates the impact on global buckling of the slenderness of the structure. First, the reduced slenderness is calculated using the following equations:

$$\bar{\lambda} = \sqrt{\frac{N_p j_{\text{material}}}{N_e}} \quad \phi = \frac{1}{2} [1 + 0.2(\bar{\lambda} - 0.2) + \bar{\lambda}^2] \quad \kappa = \begin{cases} \frac{1}{\phi + \sqrt{\phi^2 - \bar{\lambda}^2}} & \text{if } \bar{\lambda} > 0.2 \\ 1 & \text{if } \bar{\lambda} \leq 0.2 \end{cases}$$

Lastly, the slenderness parameter can be calculated using

$$\Delta n = \min(0.25\kappa\bar{\lambda}, 0.1) \quad (6.53)$$

Using all three structural integrity check, it is possible to size the monopile. As with the design of the main shaft, two design parameters are considered: the outer diameter, d_o , and the inner-to-outer diameter ratio c_{diam} . The sizing of the monopile was performed with the goal of optimizing for lowest mass, keeping in mind that the yield strength of the element would depend on the wall thickness, as shown in Table 6.11²⁰. Note that the low carbon manganese alloy steel S355J was chosen for the monopile as it is graded for use in marine conditions and it is highly common among current monopile materials.

During the sizing of the monopile it was discovered that the drag of the tower in storm conditions would create too high of a bending moment, leading to early global buckling. This would happen only if the tower was oriented perpendicular to the direction of the wind. In order to mitigate this, the yaw subsystem was

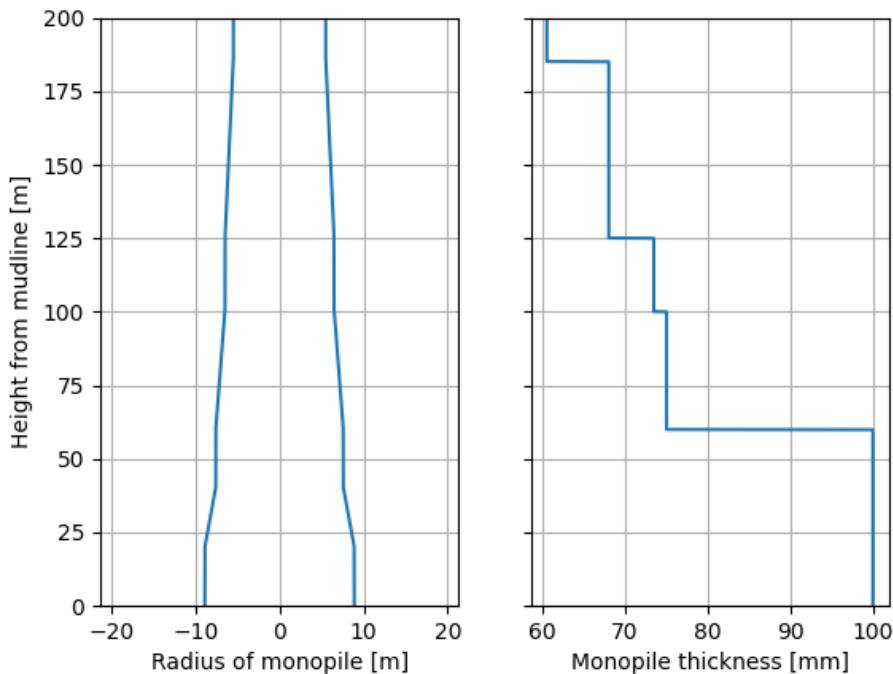
²⁰URL: https://www.joostdevree.nl/bouwkunde2/jpgs/staal_23_standaarden_s355_european_standard_steel.pdf [cited on 18 June 2023]

Table 6.11: Mechanical properties of S355J alloy steel based on nominal thickness

Thickness [mm]	3-15	16-40	40-63	63-80	80-100	100-150	150-200	200-250
Yield strength [MPa]	355	345	335	325	315	295	285	275
Tensile strength [MPa]	550	550	550	550	550	525	525	—

given the additional function to yaw the structure parallel to the direction of the wind during extreme storm conditions.

During the hand optimisation procedure, it was also noticed that the best geometry for the monopile would be a cone with a varying slope and thickness. Due to manufacturing reasons though, this was deemed unfeasible, so only three steps in diameter between 11 m to 17.8 m were considered. This optimisation resulted in the following geometry, as shown in Figure 6.32. The final design will weigh 6200 t.

**Figure 6.32:** Profile of the chosen design of the monopile

The buckling and yielding criteria for all load cases of the chosen monopile design are presented in Figure 6.33.

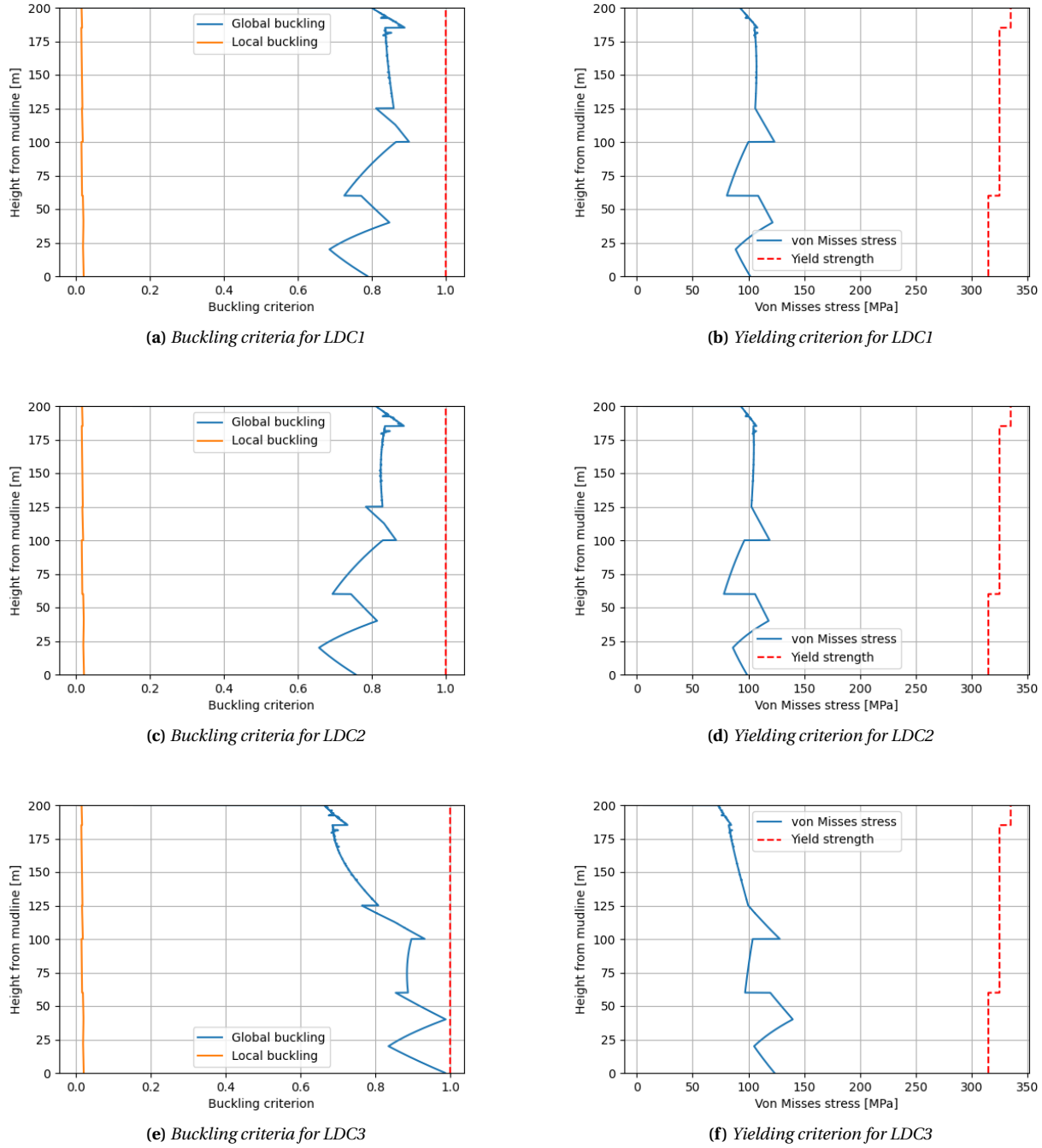


Figure 6.33: Failure modes criteria of the final monopile design

It is important to note here that the design of the driving section of the monopile, which lies under the mudline and it transfers the loads into the sea bed, was not sized in this design phase. This is because using historical data and interpolating about these points will not yield a valid value for the driving length, as the only available data was addressing small monopiles, with base diameters lower than 7, most definitely yielding inaccurate results [31]. After consultations with an external expert on the topic on underground monopile foundations, Ir. Jeroen Donkers of Huisman Equipment B.V., it was determined that more information on the sea bed composition and a more advanced FEM model which can analyse dynamic loading would be required to correctly size the driving portion of the monopile. Thus, it was decided that the sizing of the driving length of the monopile will be conducted during post-DSE activities.

6.6.2. Vibrations analysis for the monopile

As predicted, the foundation of the wind turbine experiences vibrations that could lead to catastrophic failures. Even though it was assumed that the vibrations from the tower are fully damped, the monopile is exposed to several loading conditions, the most important one considered being the vibrations from the tidal loads. In this subsection, the frequencies of the waves and foundation will be analysed and afterward compared. To avoid the failure of the structure, the resonance should not be achieved which happens when the natural frequencies of the two are equal.

Firstly, the natural frequency of the foundation will be calculated. [Bakhti et al.](#) propose a finite element investigation of offshore wind turbine's harmonics with a monopile base [46]. It particularly studies the interaction of the geometry of the basis with the soil. However, this analysis is beyond the scope of this design exercise. The core formulas will be used to obtain the desired data. The paper uses f_{FB} to define the first eigenfrequency of the fixed base, which can be calculated based on geometric characteristics. Equation 6.54 presents how the f_{FB} can be calculated [46].

$$f_{FB} = \frac{1}{2\pi} \cdot \sqrt{\frac{3 \cdot E \cdot I}{L^3 \cdot (m_{RNA} + \frac{33}{144} m_T)}} \quad (6.54)$$

where E - Young Modulus of the material from which the monopile is made of, L -total monopile length, I -second moment of inertia of a hollow cylinder, which can be calculated in terms of the diameter and thickness of the body by $I = \frac{1}{8} \cdot (D_T - t_T)^3 \cdot t_T \cdot \pi$. As presented in Subsection 6.6.1, the pile has both varying thickness and diameter and not necessarily the same D/t ratio along its length. Since the diameter changes reasonably in a linear manner, D_T can be estimated by $D_T = \frac{D_{top} + D_{base}}{2}$ while t_T can be approximated by averaging the values for the different thickness by taking in account the right proportions. In addition, m_{RNA} is the total mass of the rotor-nacelle assembly which can be assumed to be equal to the mass of the entire structure above the foundation, whereas the m_T represents the mass of the monopile.

The next step in the analysis is to investigate how the sea bed interacts with the steel structure of the foundation. Apart from the length which is above the mud line, the base should be mounted into the ground in such a way that it does not deflect due to the several loading scenarios. The first natural frequency of the system which includes the pile and the soil can be computed with Equation 6.6.2 [46].

$$f_N = C_L \cdot C_R \cdot f_{FB} \quad (6.55)$$

where C_R and C_L stand for the foundation flexibility coefficients. They are dependent on mainly the soil's characteristics and possibly the metocean conditions, in particular winds and rains that can slightly influence the submarine land. They can be expressed by Equation 6.57 and Equation 6.56 [47].

$$C_R = 1 - \frac{1}{1 + 0.6 \cdot (\eta_R - \frac{\eta_{LR}^2}{\eta_L})} \quad (6.56)$$

$$C_L = 1 - \frac{1}{1 + 0.5 \cdot (\eta_L - \frac{\eta_{LR}^2}{\eta_R})} \quad (6.57)$$

η_L , η_R and η_{LR} can be further determined with formulas for stiffness of monopiles exhibiting rigid behaviour. For these calculations, it was assumed that the solid stiffness profile is a parabolic one since it is the most regular one according to Figure A.1. They can be computed with the formulas displayed in Table A.1 which can be found in Appendix A. E constitutes the Young Modules of the soil which was approximated with 147.65 MPa considering the values and ratios from Figure A.2. Furthermore, the f_{vs} suggests

the effect of the water movement on the sea bed which regardless does not have a major influence on the frequency of the system combining the soil and foundation. Assuming that the diameter of the monopile ranges from 17.8 m to 11 m and thickness is between 0.1 m and 0.06 m, $f_N = 0.148\text{Hz}$.

Lastly, the natural frequencies of the tides need to be estimated. Since waves' propagation is principally dependent on the wind speed which acts as an exciting force, it can be accepted that waves have a periodic motion which can be defined by amplitude, periodicity, frequency, wavelength, and phase. [Schlöer et al.](#) proposed a method in which the significant wave height can be related with respect to the wind speed [48]. The approach is particularly advantageous due to the fact that a reference wind turbine of 10 MW, suggested by the Technical University of Denmark, was chosen. Presumably, it is located in the North Sea. Two different scenarios were investigated. The first one implies normal weather conditions, when all load cases are within the normal parameters, while the second one entails the ultimate limit state when extreme weather conditions are assumed. Table A.2 and Table A.3, which can be presented in Appendix A, indicate the values of wind speed and the corresponding wave height for both cases. Two expressions have been found by interpolating the values where v is the wind speed. Both Equation 6.59 and Equation 6.58 have a coefficient of determination for the regression of 0.99.

$$H_S = 0.0032v^2 + 0.0227v + 0.9242 \quad (6.58)$$

$$H_S = 0.0071v^2 - 0.1074v + 6.1445 \quad (6.59)$$

Based on the wind speed from Section 3.2, the probability of occurrence of each wind velocity has been computed. The most recent information, from 2018, has been used for a level of 50 m above sea level since it could reproduce the conditions at water level better than the data from a height of 250 m. Equation 6.60 was used in order to compute the period tides starting from their significant height [48].

$$T_S = 11.1 \cdot \sqrt{\frac{H_S}{g}} \quad (6.60)$$

where g - gravitational acceleration. Table 6.12 showcases the recorded wind speeds together with their calculated probabilities of occurrence. The speeds are rounded to the nearest integer for simplifying the calculations. The period, height, and first natural frequency of waves are presented for the normal and extreme weather scenarios which have been calculated starting from Equation 6.59 and 6.58.

Table 6.12: Recorded and probability of occurrence of each wind speed, and the height, period, first natural frequency of the waves in IJmuiden Ver zone

Wind speed[m/s]	Probability[%]	H_{normal} [m]	T_{normal} [s]	f_{normal} [Hz]	$H_{extreme}$ [m]	$T_{extreme}$ [s]	$f_{extreme}$ [Hz]
1	1.85	0.95	3.45	0.29	6.04	8.71	0.11
2	3.22	0.98	3.51	0.28	5.96	8.65	0.12
3	5.14	1.02	3.58	0.28	5.89	8.60	0.12
4	5.61	1.07	3.66	0.27	5.83	8.56	0.12
5	6.90	1.12	3.75	0.27	5.79	8.52	0.12
6	7.19	1.18	3.84	0.26	5.76	8.50	0.12
7	9.17	1.24	3.95	0.25	5.74	8.49	0.12
8	9.54	1.31	4.06	0.25	5.74	8.49	0.12
9	9.89	1.39	4.17	0.24	5.75	8.50	0.12
10	8.32	1.47	4.30	0.23	5.78	8.52	0.12
11	8.07	1.56	4.43	0.23	5.82	8.55	0.12
12	5.77	1.66	4.56	0.22	5.88	8.59	0.12
13	4.73	1.76	4.70	0.21	5.95	8.64	0.12
14	4.10	1.87	4.85	0.21	6.03	8.70	0.11
15	3.29	1.98	4.99	0.20	6.13	8.78	0.11
16	2.48	2.11	5.14	0.19	6.24	8.86	0.11
17	1.50	2.23	5.30	0.19	6.37	8.94	0.11
18	1.15	2.37	5.46	0.18	6.51	9.04	0.11
19	0.78	2.51	5.62	0.18	6.67	9.15	0.11
20	0.65	2.66	5.78	0.17	6.84	9.27	0.11
21	0.35	2.81	5.94	0.17	7.02	9.39	0.11
22	0.17	2.97	6.11	0.16	7.22	9.52	0.11
23	0.10	3.14	6.28	0.16	7.43	9.66	0.10
24	0.03	3.31	6.45	0.16	7.66	9.81	0.10
25	0.02	3.49	6.62	0.15	7.90	9.96	0.10

As depicted in Table 6.12, the fundamental frequencies of the waves created for each wind velocity are presented. For the ordinary case, the natural frequencies vary from 0.29 Hz, when the wind speed is roughly 1 m/s, to 0.15 Hz when a wind of 25 m/s is experienced. Furthermore, frequencies oscillate between 0.10 Hz and 0.12 Hz in the ultimate limit case. Since the first harmonic of the fixed foundation and soil is nearly 0.148 Hz, it can be accepted that it is not likely for the system including the base and waves to achieve the resonance below 24 m/s wind speed in terms of the first eigenfrequencies. There are no data recording a higher wind speed than 24 m/s according to Section 3.2. However, the resonance is plausible only if $f_{monopile} = f_{waves} = f_{N_{nat}}$, where $f_{N_{nat}}$ is the N^{th} eigenfrequency of waves.

To conclude, the possibility of failure as a consequence of vibrations due to tidal loads is small, but not impossible. Results show that resonance is not expected during storms or normal conditions when the wind speed varies from 1 m/s to 25 m/s. The more problematic scenario is when the wind exceeds this upper limit. In general, there was no recorded value in this sense in the reference year, 2018, although in case of very exceptional conditions such as, hurricanes, cyclones, typhoons or tornadoes, the collapse of the foundation is likely. Nevertheless, the foundation of the wind turbine was not designed with the primary scope of resisting against vibrations, but withstanding the loads. One solution that was already introduced in this design exercise for the tower of the entire assembly was to equip the wind turbine with several dampers that will reduce vibrations. In this manner, they will be damped out and not further propagated to the foundation of the structure. Therefore, various dampers will be placed along the monopile to minimise the risk of failure due to the oscillation of the water.

Final design

This chapter presents the results of previous chapters, calculations and trade-offs. It gives an overview of relevant numbers and dimensions. The design consists of multiple rectangular parallelepiped cells. The cells are supported by a monopile. Inside the cell are vertical-axis wind turbines with H-shaped rotors. The shafts of the rotors are attached in front of the structure. The Drive train has a gearbox with a doubly fed induction generator (DFIG) and a partial converter. The yaw system uses differential thrust or aerodynamic effects to yaw. An electrical yaw system is used as a backup. A scaled drawing can be seen in Figure 7.1. Design parameters are summarised in Table 7.1 and Table 7.2

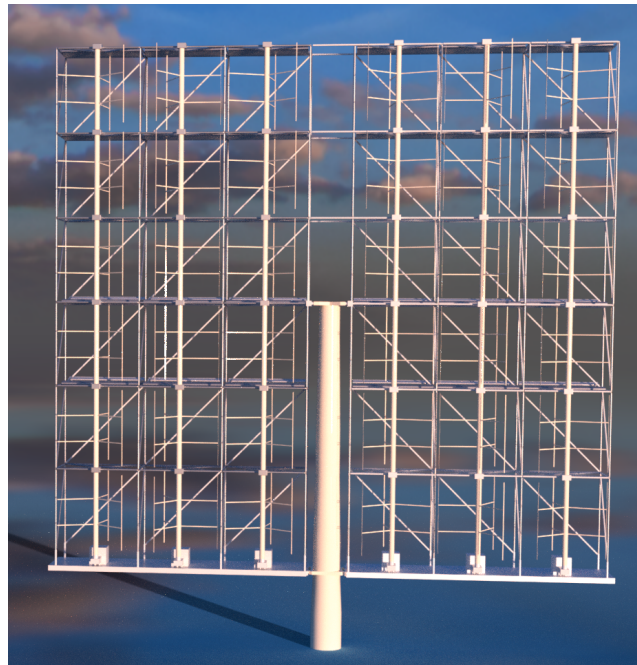


Figure 7.1: Render of Final Design

TWR Design

The tower is a large truss structure, consisting of repeating cubes. The truss structure is 140 m wide on each side of the central monopile, leading to a total width of 290 m. The height and depth of the truss are 280 m and 33.6 m respectively. The mass of the truss structure, including bedplates for the generator is 2767 t. The truss elements are made out of medium-carbon steel, and optimized for structural mass. The elements are all between 0.3 m to 2 m in diameter. To protect the structure from corrosion, multiple layers of white organic solvent-based paint will be applied to the truss structure. This is done to protect the structure from the harsh environment and reduce its capability of absorbing heat from the sun. To protect the turbine from lightning, a lightning protection system is installed on the structure.

WCT Design

The wake control system consists of four wing blades, which are each split into six equal sections, integrated into individual tower cells. Individual sections are two-element airfoils, which can move the second segment in order to drop their lift coefficient below $C_L \leq 0.074$ in case of storms but can reach a lift coefficient of up to $C_L = 3$ when fully deployed during operation. When operating, their drag coefficient is almost $C_D = 0.256$, which drops to $C_D = 0.0152$ when retracted. To allow for large changes in C_L and C_D ,

Kruger slats and triple-slotted flaps would be installed in one or both airfoil elements.

Wake control systems can fully recover the wake of a turbine over 2.5 km. On a staggered grid, this gives a power density of almost 20 MWkm^{-2} . WCTs of subsequent turbines are expected to interfere in a constructive way and improve wake recovery even further. Most parts of the WCT are to be made of medium-carbon steel.

RTR Design

The rotor subsystem consists of six vertically oriented shafts of 270 m connected to the drivetrain at the lower extremity. The profile of the low carbon steel shaft is of a hollow cylinder with a diameter of 1.6 m and a wall thickness of 24.3 m. All shafts are supported by the tower through seven equidistant deep groove ball bearings. Attached to each shaft are six H-type rotors of height 45 m and a diameter of 46.7 m. All rotors attached to the same shaft are equally phased displaced in order to smooth the torque fluctuations. The blades are supported by simple circular profile struts. All blades have the airfoil profile of the DU17DBD25.

YCT Design

The yaw control subsystem consists of two slewing bearings of diameter 10 and 15 meters attached to the monopile and tower at 170 m and 30 m above sea level respectively. The yawing mechanism uses an on-off differential thrust controller to yaw during operational conditions. Yaw breaks are included to fix the tower during non-yawing time. Additionally, the subsystem includes an electrical yawing system with yaw drives at a rated torque of 800 kNm for yawing during storms, wind speeds below cut-in speed and for cable disentanglement.

DRT Design

The drive train is a standard one including a generator, gearbox, brake, and several couplings. Since there will be six shafts in total and the power requirement is set to 30 MW, each segment needs to produce 5 MW. The chosen brushless generator is part of the AMK series, provided by ABB. It should have a rated power of around 5.56 MW and a total mass of 16 t. The gearbox, manufactured by Rexton, is right-angled. It should have a conversion ratio of 43 weighting roughly 4 t. The 610 kg break is placed after the gearbox. It is produced by Hindon and produces a break torque of 207 kNm.

FND Design

The foundation consists of a variable diameter and thickness monopile that spans to 170 m above sea level and is 200 m long from the mud line. Due to corrosion risks, the monopile has been manufactured using S355J marine-grade steel and primed with anti-corrosive paint. The tower is connected to the monopile using two slewed bearings, through which all topside loads are transferred. Due to this reason, the monopile starts from a diameter of 11 m and thickness of 60 mm and gets to a diameter of 17.8 m and a thickness of 100 mm.

OCT Design

Fifteen different sensors are installed on the structure to collect data to develop models and synchronize the digital twin of the structure for predictive maintenance. The most prominent of these sensors are an anemometer, wind vane, and wind gust sensor to measure wind characteristics during the operations, which will be placed per cell (midpoint of edges) of the structure to provide enough spatial resolution. Accelerometers and strain gauges are utilized mostly to pair the data from the wind and system response to improve the prediction algorithm and pair weather conditions with possible failures. This way, shortly after operations start, exact loadings of the truss elements due to extreme weather conditions will be determined. They have been placed on the connectors of the HLD and truss structure. Also, they have been installed on the other moving systems, such as RTR, to detect any misalignments of the shafts from the

frequency spectrum change. Also, sensors such as acoustic sensors and ACFM will be utilised for error detection due to the working principle of these sensors as they can detect surface-level cracks in structures. Additionally, oil sensors will be placed on the bearings and generators to detect oil conditions such that the condition of these parts will be monitored. All the data generated by these sensors will be collected by SCADA.

PCT Design

The rotor airfoil was chosen so that the turbine will be stall regulated, meaning that the maximum rotation rate can be enforced through dynamic stall at a certain wind speed. This assures that the rotor does not go over its rotation limit and that the power electronics are not overcharged by the excess produced power. Torque control is used in order to obtain maximum efficiency before reaching the rated wind speed. This is done by varying the synchronous speed of the generator through the interface of the DC-DC bus within the partial converter. An Optimum Torque Controller was chosen together with a Maximum Power Point Tracking algorithm. Hydraulic brakes were employed in case of sudden power halting during operations.

Table 7.1: Key parameters for the MR-TBD design

Parameter	Unit	Value
Power rating	MW	31.3
Power density	Wm^{-2}	20
Turbine class	—	IEC class I
Control		Variable speed
Cut-in wind speed	ms^{-1}	3
Rated wind speed	ms^{-1}	11.2
Cut-out wind speed	ms^{-1}	25
Design TSR	—	4.5
Rotor diameter	m	46.7
Rotor height	m	45
Airfoil series	—	DU17DBD25
Number of rotors	—	36
Number of shafts	—	6
Turbine height	m	310
Turbine width	m	290
Cell dimensions	m	46.67 X 46.67 X 33.6
truss thickness ratio	-	0.01
Drivetrain	—	Geared
Gearbox	—	Angular & Planetary
Generator	—	Brushless DFIG
Wake control	—	Adjustable HLD
Wing chord	m	20
Wing span	m	280

Table 7.2: Weights of all sized subsystems

Element	Mass [tn]
Rotor	1717
Main shaft	260 X6
Blades	3.2 X6
Bearings	1 X42
Tower	2767
Truss	2455
Bedplate	52 X6
Yaw control	100
Bearings	54
Drivetrain	46
Wake control	648
Wing	81 X4
HLD	81 X4
Drivetrain	150
Gearbox	4 X6
Break	0.6 X6
Generator	16 X6
Converter	4 X6
Miscellaneous	0.4 X6
Monopile	6200
Total	11582

Production, operation and logistics

8.1. Production plan

Now that the design has been chosen and the materials for the various components have been decided, the production can take shape. As the project will be deployed in the North Sea next to the Netherlands, the location of where components are manufactured is an important parameter to keep in mind. This section is divided into a description of the production and manufacturing of all the components of MR-TBD, followed by a description of the assembly process.

Monopile

The monopile consists of 3 main structures: a large hollow cylinder made of low carbon steel, the yaw bearings/transition pieces through which loads are transferred to the monopile and an underground foundation made from concrete. It is broken up by the lowest yaw bearing; and the bearings themselves as part of the yaw control subsystem (YCT).

The monopile itself must thus be manufactured as two separate cylinders of varying thickness and diameter, following Figure 6.32. As described by [Anandavijayan and Brennan](#), monopiles in the offshore wind industry are constructed by bending metal sheets into cylindrical 'cans', usually by three-point or roll bending, followed by welding them into place before tack welding and circumferential welding the cans together [49]. This same process will be used to create the monopiles for the MR TBD design, as it is a mature and trusted technology in the industry. The processing time depends on the size of the monopile (as well as the production interval decided by the manufacturer).

Monopiles require large factories to be manufactured. However, the Netherlands is home to various companies that have the capabilities to produce them. Of particular interest is Sif offshore foundations, who possess a monopile manufacturing plant in Roermond and are also building a site in Rotterdam¹. This is beneficial for the construction as Rotterdam possesses large dry docks and is near the proposed implementation site of the project.

The bearings in the monopile must allow for free yaw rotation, support and transport the complete loading from the rest of the tower into the monopile, and be connected to the electrical yawing system. For this, the bearings must be manufactured accurately, as any imperfections or decrease in quality may cause significant load transfer or vibration issues. The bearings will be mainly made from low alloy steel for their casing in combination with various other materials and lubricants as they are complex parts. They will also be sensitive to corrosion, so corrosion prevention methods (mainly to reach c5m protection level Section 6.4) will be used to keep them clean, as well as keeping them as far from the saltwater environment as possible i.e. protective outer layers.

Due to how crucial the bearings are to load transfer and how they will constantly be under gravitational loading of the rest of the tower, the maintenance required must be minimal, as the replacement of the bearings would require the entire tower section to be removed or propped up in order to operate on it. The production will be handed off to wind turbine and crane bearing manufacturing companies in order to assure the quality of the product. Of particular interest of these are Liebherr², SKF³, and Huisman⁴ as they produce products of similar size and strength to those required for the project.

¹ URL: <https://windpowernl.com/2023/02/14/sif-gives-green-light-for-worlds-largest-monopile-manufacturing-plant/> [cited on 19 June 2023]

² URL: <https://home.liebherr.com/nl/nld/home/homepage.html> [cited: 20 June 2023]

³ URL: <https://www.skf.com/nl> [cited: 20 June 2023]

⁴ URL: <https://www.huismanequipment.com/en/> [cited: 20 June 2023]

Rotor and wake control system

Both the rotors of the turbines and the wake control system mainly feature long airfoils that do not vary in profile along their lengths. However, the differences in size for both require different methods of production.

Given that the rotor blade chord and thickness are smaller than a meter, and that they are made purely from steel, they are small enough to be produced via extrusion. This method can produce constant profiles of metal but becomes more difficult for larger parts, requiring larger machinery. Thus the HLD airfoils will instead be made by metal forming processes. Similar to the monopile, the forming of the HLD profiles can be done by bending and rolling large metal sheets and welding them into the right shapes.

It is necessary for both these processes to find companies that have the correct machinery and experience for metal forming. For steel components, there are various manufacturers in the Netherlands that have manufacturing plants capable of creating the airfoils necessary. The most advantageous of these are ThyssenKrupp⁵ and Tata Steel⁶ for their manufacturing plant locations near Rotterdam.

Finally, the rotors also require bearings and shafts as part of the turbines. The shafts will be planned for in the subsection discussing the truss structure while the bearings are a more complex design. As mentioned in Figure 6.1, there may be vibration issues in the truss structure. One of the potential solutions is integrating dampers into the mounting brackets and combining these with the bearings of each rotor shaft. This would result in a more complex design that would require more development and more complex manufacturing. However, for basic bearings there are various companies that specialise in their production, in particular SKF and Huisman and Liebherr.

Drivetrain

The drivetrain has been analyzed and broken down into a series of components. The following table summarises the most likely manufacturers based on their manufacturing abilities and specialisations for each of the component categories (except for the rotor shafts which will be explained in the truss section)

Table 8.1: Drivetrain manufacturing

Component	Possible Manufacturers
Generator	ABB ltd
Gearbox	Rexnord
Brake	Hindon

Complex components

Given that the project encompasses a large and complex system, there are many parts that have complex sub-components and require specialized knowledge and tools to produce, beyond the processes listed earlier. Of particular importance are the electrical connections, electrical yaw motor, and specialized sensors that cover the structure. Each of these components is complex enough that describing their manufacturing is not relevant to this project. Instead, the relevant manufacturers are listed in Table 8.2 below.

Table 8.2: Component manufacturing

Component	Possible Manufacturers
Electrical connections/cabling	Tennet (also handles connection to electrical grid)
Electrical yaw motor	Liebherr
Sensors	Industry specialists

⁵URL: <https://www.thyssenkrupp-steel.com/en/> [cited: 20 June 2023]

⁶URL: <https://www.tatasteeurope.com/nl/home> [cited: 20 June 2023]

It must be noted that there are various types of sensors so no single manufacturer was chosen.

Truss and tower structure

The truss structure as well as the rotor shafts are made from medium alloy carbon steel specifically AISI 1040 and are both series of metal hollow cylinders that are sized for the loading that they must withstand. They comprise a variety of thicknesses and radii. The truss beams all have radii between 150mm and 1m, thicknesses ranging from 15mm to 100mm, and a length between 34m and 70m while the shafts all have a radius of 809mm thickness of 24.3mm and a length of 270m. Given that all of these components have simple circular cross sections and are structural components, hot rolling the components is the chosen method of manufacturing.

The tower contains one final structural component: the base plate on which the drivetrain rests. This is a large plate that must transfer the loads to the appropriate beams and the tower. Due to its multiple points of loading, as well as the differences in geometry, it has different material requirements. High-carbon steel is used as its material.

Due to the large size of the members, the cylinders and the baseplate will all be manufactured from multiple smaller members joined together during assembly. This benefits the shafts by making them easier and cheaper to replace in case of faults. The same effect applies to the beams and the baseplate, although more care must be taken due to their structural importance. The manufacturing of such large shafts requires the machinery and experience of large steel manufacturers. Again, the most advantageous of these are ThyssenKrupp and Tata Steel.

Assembly

Traditional wind turbines are tall with a small base. Transporting them upright in one piece is difficult. In contrast, the truss structure of the MR-TBD design has a wide and deep base, which is capable of carrying all exerted loads. It is therefore well suited to be transported in a single piece, which then only has to be lifted and installed onto the monopile. This saves money by avoiding the high cost of assembling the turbine at sea with little infrastructure, and unstable and dangerous conditions. It also minimizes the amount of time at sea as well as the vessels needed for the process since the structure can simply be towed and connected to the foundation.

Thus the assembly of the structure should be completed onshore. The most suitable location to assemble it is a shipyard or drydock.

The shipyard must be large enough to fit the whole structure, so it must be at least 280m long and 40m wide. In addition to this, it must be near the IJmuiden installation site and must provide easy access to it without obstructions along the way to the site. Also, the transportation of materials and components must be facilitated and the travel distance minimized for both time and emissions from transport.

Thus the Damen Verolme Rotterdam shipping yard was chosen. It possesses multiple berths and a drydock more than 300m long that can be utilized to construct the turbine and is less than 10km from the city of Rotterdam itself as well as most of the manufacturing plants in the area. The Yard is also under 100km from the installation leading to rapid transport of the construction to be possible. Finally, it has multiple berths that can be used for assembly, meaning that multiple structures can be built at once, hastening the installation time of wind farms as a whole as well as individual systems.

8.2. Reliability, Availability, Maintainability, and Safety

This section discusses the reliability, availability, maintainability, and safety of the system. This analysis is mainly based on data collected in reports by [Carroll et al. \[5\]](#). The data in these reports concern traditional HAWTs. This data is then modified based on the changes made by the system's design. Data on offshore wind turbines are seldom available and often onshore wind turbine data must be adapted for use in these

data sets.

Reliability

The reliability of the system is first examined on a subsystem and component level. The failure rates for different components with regard to unscheduled maintenance are presented in Table 8.3. The failure rates are based on data for events requiring a major replacement, major repair, minor repair, or cases where no cost data was available. The adjusted rates are presented in Table 8.4, which includes changes explained in the following paragraphs.

Major replacement means that a heavy lift vessel (HLV) was needed to carry out the repair. Using HLVs means large expenses and they are not always available immediately, meaning more downtime. For both major and minor repairs, a crew transfer vessel (CTV) was considered. These vessels nowadays have a carrying capacity of between 1 t and up to 30 t⁷.

Table 8.3: Base failure rates from [5]

Component	Major Replacement	Major Repair	Minor Repair	Unknown	Total
Pitch/Hydraulic	0.001	0.179	0.824	0.072	1.076
Others	0.001	0.042	0.812	0.150	1.005
Generator	0.095	0.321	0.485	0.098	0.999
Gearbox	0.154	0.038	0.395	0.046	0.633
Blades	0.001	0.010	0.456	0.053	0.520
Oil and Coolant	0.000	0.006	0.407	0.058	0.471
Electrical components	0.002	0.016	0.358	0.059	0.435
Circuit breaker	0.002	0.054	0.326	0.048	0.430
Control	0.001	0.054	0.355	0.018	0.428
Safety	0.000	0.004	0.373	0.015	0.392
Sensors	0.000	0.070	0.247	0.029	0.346
Pumps and motors	0.000	0.043	0.278	0.025	0.346
Shaft hub	0.001	0.038	0.182	0.014	0.235
Heaters/coolers	0.000	0.007	0.190	0.016	0.213
Yaw system	0.001	0.006	0.162	0.020	0.189
Tower and foundation	0.000	0.089	0.092	0.004	0.185
Power supply and converter	0.005	0.081	0.076	0.018	0.180
Service items	0.000	0.001	0.108	0.016	0.125
Transformer	0.001	0.003	0.052	0.009	0.065
Total	0.265	1.062	6.178	0.768	8.273

The system aims to reduce maintenance by reducing both the rate at which components fail, as well as the material and transport costs of maintenance. The system uses DFIGs with 3-stage gearboxes. These two components commonly become the main sources of downtime [6].

In the case of unscheduled maintenance, the most common cause of failure of DFIGs is the failure of the slip ring, which is responsible in 31.1 % of cases [5]. Because the MR-TBD system proposes the use of a brushless DFIG, this source of failure would be eliminated due to the lack of slip rings. In brushed generators, the repair of the slip rings is a very labor-intensive process due to their location, and the general size of the generator. For this reason, it is assumed that the aforementioned 31.1 % failure rate reduction

⁷<https://www.4coffshore.com/support/an-introduction-to-crew-transfer-vessels-aid2.html> [cited: 20 June 2023]

affects the major replacement and major repair categories. The failure rate for these categories is reduced such that the total failure rate of the generator is reduced by 31.1 %.

For the case of the gearbox, one of the main reasons for the need for unscheduled maintenance requiring HLVs rather than CTVs is the fact that in traditional HAWTs the gearboxes are heavy and located at the top of the tower. The design of the proposed system avoids this by having a strong base plate at the height of 30 m above sea level with a built-in crane, meaning that HLVs would not be needed and CTVs could carry out these replacements. This results in quicker response times and lower transport costs.

Another thing to consider for the gearboxes used by the system is that they would experience loads that would cause much less fatigue. With six rotors per shaft, with three blades each, the torque loading would be almost constant, barring gusts. This would mean that the lifetime of gearboxes would be much longer, and the probability of mechanical failure would be much lower compared to the traditional turbines. With that in mind, the assumed reduction in overall unscheduled maintenance for gearboxes is 10 %, in the categories of major replacements and major repairs.

Another major difference between a traditional OWT and the proposed system design is the size of the tower structure. With a large truss, it can be assumed that the number of repairs and unscheduled maintenance events will be greater. To account for this, the occurrence of maintenance events was set to 200 % for the tower. The same goes for the number of sensors and consequently their failure/repair rate.

For turbine blades, the main cause for blade repair comes from corrosion of the blades due to leading edge erosion, which occurs on HAWTs when blades are moving close to the sea surface, where they hit droplets with high relative velocity. For the proposed design, this will not happen at comparable impact velocity. The main reason for this, is that the tip speed ratio of the VAWTs is 4.5, compared to typical ratios around 9.0. Since the velocity is halved, the kinetic energy of droplets hitting the blades is one-fourth the kinetic energy for an impact on a traditional HAWT. In addition to this, the blades always move parallel to the water surface. The blades stay at the same level, meaning that the higher the blades are placed, the less they will suffer from leading-edge erosion. As such, it is asserted that the number of replacements and unscheduled maintenance events will be reduced by 50 %.

Other failures in Table 8.3 come mainly from failures of hatches and doors, as well as covers and lifts. Issues with hatches and doors typically aren't a problem and do not have an impact on actual performance. Still, by not requiring a compact design of subsystems compared to traditional ones which must fit into a tight nacelle, it is asserted that the number of maintenance events in this category will be reduced by 25 %.

Since the yaw system primarily uses aerodynamic forces during its normal operation and seldom employs the use of its electric motor, it is expected that less stress will be placed on the electric motor. Combined with the large and bulky design, this means that the system would likely fail less often. As such, it is asserted that the number of failures will reduce by 30 %.

Since the system's rotors are stall-regulated machines, they will not be using a pitch system. As such, the failure rates in the Pitch/Hydraulics category are expected to decrease. The reduction in major repair rate and minor repair rate of 20 % and 10 % respectively are asserted.

Table 8.4: Adjusted failure rates

Component	Major Replacement	Major Repair	Minor Repair	Unknown	Total
Pitch/Hydraulic	0.001	0.179	0.824	0.072	1.076
Others	0.001	0.042	0.812	0.150	1.005
Generator	0.047	0.158	0.485	0.098	0.788
Gearbox	0.091	0.038	0.395	0.046	0.570
Blades	0.001	0.010	0.456	0.053	0.520
Oil and Coolant	0.000	0.006	0.407	0.058	0.471
Electrical components	0.002	0.016	0.358	0.059	0.435
Circuit breaker	0.002	0.054	0.326	0.048	0.430
Control	0.001	0.054	0.355	0.018	0.428
Safety	0.000	0.004	0.373	0.015	0.392
Sensors	0.000	0.140	0.494	0.029	0.663
Pumps and motors	0.000	0.043	0.278	0.025	0.346
Shaft hub	0.001	0.038	0.182	0.014	0.235
Heaters/coolers	0.000	0.007	0.190	0.016	0.213
Yaw system	0.000	0.002	0.054	0.020	0.076
Tower and foundation	0.000	0.178	0.184	0.004	0.366
Power supply and converter	0.005	0.081	0.076	0.018	0.180
Service items	0.000	0.001	0.108	0.016	0.125
Transformer	0.001	0.003	0.052	0.009	0.065
Total	0.153	1.054	6.409	0.768	8.384

Availability

For unscheduled repairs, the time required per component was computed using the scaling factors from Table 8.5, Table 8.6, Table 8.7 and repair times presented by [Carroll et al.](#) along with failure rates from Table 8.3 and Table 8.4 [5]. The results for that are presented in Table 8.8 and Table 8.9 respectively.

Table 8.5: Weight factors to account for size and number of subsystems (first table)

Component	Pitch/Hydraulic	Others	Generator	Gearbox	Blades	Oil and Coolant	Electrical components
Relative to VAWT	0.3	1	6	6	36	6	6

Table 8.6: Weight factors to account for size and number of subsystems (second table)

Component	Circuit breaker	Control	Safety	Sensors	Pumps and motors	Shaft hub	Heaters/coolers	Yaw system
Relative to VAWT	1	3	1	10	1	6	2	5

Table 8.7: Weight factors to account for size and number of subsystems (third table)

Component	Tower and foundation	Power supply and converter	Service items	Transformer
Relative to VAWT	4	3	1	1

Table 8.8: Base component repair times

Component	Major Replacement	Major Repair	Minor Repair	Unknown	Total
Pitch/Hydraulic	0.025	3.401	7.416	1.224	12.066
Others	0.036	0.882	4.060	1.200	6.178
Generator	7.695	7.704	3.395	1.274	20.068
Gearbox	35.574	0.836	3.160	0.322	39.892
Blades	0.288	0.210	4.104	1.484	6.086
Oil and Coolant	0.000	0.108	1.628	0.174	1.910
Electrical components	0.036	0.224	1.790	0.413	2.463
Circuit breaker	0.300	1.026	1.304	0.240	2.870
Control	0.012	0.756	2.840	0.306	3.914
Safety	0.000	0.028	0.746	0.030	0.804
Sensors	0.000	0.420	1.976	0.232	2.628
Pumps and motors	0.000	0.430	1.112	0.175	1.717
Shaft hub	0.298	1.520	1.820	0.112	3.750
Heaters/coolers	0.000	0.126	0.760	0.048	0.934
Yaw system	0.049	0.120	0.810	0.180	1.159
Tower and foundation	0.000	0.178	0.460	0.024	0.662
Power supply and converter	0.285	1.134	0.532	0.180	2.131
Service items	0.000	0.000	0.756	0.144	0.900
Transformer	0.001	0.078	0.364	0.171	0.614
Total	44.599	19.181	39.033	7.933	110.746

Table 8.9: Adjusted repair times

Component	Major Replacement	Major Repair	Minor Repair	Unknown	Total
Pitch/Hydraulic	0.025	3.401	7.416	1.224	12.066
Others	0.036	0.882	4.060	1.200	6.178
Generator	3.807	3.792	3.395	1.274	12.268
Gearbox	21.021	0.836	3.160	0.322	25.339
Blades	0.288	0.210	4.104	1.484	6.086
Oil and Coolant	0.000	0.108	1.628	0.174	1.910
Electrical components	0.036	0.224	1.790	0.413	2.463
Circuit breaker	0.300	1.026	1.304	0.240	2.870
Control	0.012	0.756	2.840	0.306	3.914
Safety	0.000	0.028	0.746	0.030	0.804
Sensors	0.000	0.840	3.952	0.232	5.024
Pumps and motors	0.000	0.430	1.112	0.175	1.717
Shaft hub	0.298	1.520	1.820	0.112	3.750
Heaters/coolers	0.000	0.126	0.760	0.048	0.934
Yaw system	0.000	0.040	0.270	0.180	0.490
Tower and foundation	0.000	0.356	0.920	0.024	1.300
Power supply and converter	0.285	1.134	0.532	0.180	2.131
Service items	0.000	0.000	0.756	0.144	0.900
Transformer	0.001	0.078	0.364	0.171	0.614
Total	26.109	15.787	40.929	7.933	90.758

As a result of all the aforementioned modifications, the total repair time per year is reduced by 20.00 hours or 18.0 % per year. Assuming the same would follow for the scheduled maintenance, this would imply a significant increase in availability. This is not considering the fact that a failure on a single shaft would cause a 33 % reduction in power, rather than 100 % of a traditional HAWT.

Based on an article by [Carroll et al.](#), for a wind farm which is 50 km to 60 km from shore, the expected availability of a system with a DFIG would be at about 90 %. Considering the reduction in unscheduled maintenance time and assuming it carries over to scheduled as well, this would give an estimate of wind farm availability of 91.8 %.

Maintenance

Material costs were derived based on failure rates and component costs. Costs for individual component materials and transport from an article by [Carroll et al.](#) were adjusted in a manner similar to the failure rates [5]. Outcomes of this are presented in Table 8.10. The changes included:

- Generator material cost for major replacement was reduced by 30 % on account of it being a less complicated machine, as it does not need to be as compact as possible
- Gearbox material costs for all cases were reduced by 50 % on account of not requiring an external crane and not needing to be as compact as possible
- Blade costs were reduced by 70 % since the production and material costs would be lower due to the use of steel instead of composites, as well as being installable with smaller machinery.
- Yaw system costs were raised by 200 % due to the larger system scale

Table 8.10: Adjusted component cost adapted from [5]

Component	Major Replacement	Major Repair	Minor Repair
Pitch/Hydraulic	€ 14 000.00	€ 1 900.00	€ 210.00
Others	€ 10 000.00	€ 2 400.00	€ 110.00
Generator	€ 42 000.00	€ 3 500.00	€ 160.00
Gearbox	€ 115 000.00	€ 1 250.00	€ 62.50
Blades	€ 27 000.00	€ 450.00	€ 51.00
Oil and Coolant	€ -	€ 2 000.00	€ 160.00
Electrical components	€ 12 000.00	€ 2 000.00	€ 100.00
Circuit breaker	€ 13 500.00	€ 2 300.00	€ 260.00
Control	€ 13 000.00	€ 2 000.00	€ 200.00
Safety	€ -	€ -	€ -
Sensors	€ -	€ 2 500.00	€ 150.00
Pumps and motors	€ -	€ 2 000.00	€ 330.00
Shaft hub	€ 95 000.00	€ 1 500.00	€ 160.00
Heaters/coolers	€ -	€ 1 300.00	€ 465.00
Yaw system	€ 37 500.00	€ 9 000.00	€ 420.00
Tower and foundation	€ 1 100.00	€ 140.00	€ -
Power supply and converter	€ 13 000.00	€ 5 300.00	€ 240.00
Service items	€ -	€ 1 200.00	€ 80.00
Transformer	€ 70 000.00	€ 2 300.00	€ 95.00

Based on costs in an article by [Carroll et al.](#), costs expected due to materials are presented in Table 8.11 [5]. These are sorted from the most expensive base costs (not based on values adjusted for the proposed design). The costs of transport were not changed from the reference article by [Carroll et al.](#) [5]. Since not

all systems are the same size or are installed the same number of times per turbine, scaling factors from Table 8.5, Table 8.6, and Table 8.7 were used.

Table 8.11: Unscheduled Maintenance Costs

Component	Base	Adjusted Faults	Adjusted Costs	Adjusted Both
Pitch/Hydraulic	€ 158.14	€ 158.14	€ 158.14	€ 158.14
Others	€ 200.12	€ 200.12	€ 200.12	€ 200.12
Generator	€ 41 406.60	€ 20 703.60	€ 31 146.60	€ 15 627.60
Gearbox	€ 213 386.25	€ 126 446.25	€ 106 693.13	€ 63 223.13
Blades	€ 6 570.72	€ 6 570.72	€ 1 971.22	€ 1 971.22
Oil and Coolant	€ 462.72	€ 462.72	€ 462.72	€ 462.72
Electrical components	€ 550.80	€ 550.80	€ 550.80	€ 550.80
Circuit breaker	€ 235.96	€ 235.96	€ 235.96	€ 235.96
Control	€ 576.00	€ 576.00	€ 576.00	€ 576.00
Safety	€ -	€ -	€ -	€ -
Sensors	€ 2 120.50	€ 4 241.00	€ 2 120.50	€ 4 241.00
Pumps and motors	€ 177.74	€ 177.74	€ 177.74	€ 177.74
Shaft hub	€ 1 086.72	€ 1 086.72	€ 1 086.72	€ 1 086.72
Heaters/coolers	€ 194.90	€ 194.90	€ 194.90	€ 194.90
Yaw system	€ 265.90	€ 67.80	€ 797.70	€ 203.40
Tower and foundation	€ 49.84	€ 99.68	€ 49.84	€ 99.68
Power supply and converter	€ 1 537.62	€ 1 537.62	€ 1 537.62	€ 1 537.62
Service items	€ 9.84	€ 9.84	€ 9.84	€ 9.84
Transformer	€ 81.84	€ 81.84	€ 81.84	€ 81.84
Total Materials	€ 269 072.21	€ 163 401.45	€ 148 051.38	€ 90 638.42
Total Transport	€ 77 229.11	€ 50 203.01	€ 77 229.11	€ 50 203.01
Total	€ 346 301.32	€ 213 604.47	€ 225 280.50	€ 140 841.44
LCoE	€ 2.32	€ 1.43	€ 1.51	€ 0.95
Change	100.00%	61.68%	65.05%	40.67%

Based on effects on LCoE in Table 8.11 the reduction in maintenance costs is between 35 % and 60 %, depending on what assumptions hold. Assuming that actual maintenance costs scale the same way as the unscheduled maintenance costs, the expected reductions show results reflective of changes to the previously used cost model, where the maintenance cost reduction for the LCoE was estimated between 40 % and 50 %.

In offshore wind turbines, a key issue for maintenance is that a site may not be accessible at all times, which may lead to long downtimes. Combined with the need for specialized maintenance vessels, this leads to lower availability than their onshore counterparts. Combined with the harsh marine operating conditions, and consequently higher failure rates, O&M becomes even more critical.

The simplest maintenance strategy would be corrective maintenance for components with longer lifetimes, such as generators, gearboxes, and shaft hubs. For other components with shorter lifetimes, such as dampers, and converters, a preventative maintenance strategy with a fixed schedule based on weather and site accessibility would be sufficient. However, with the use of sensors and a novel maintenance strategy, availability and maintenance costs could be improved.

Based on research by [Xia et al.](#), wind turbine blade maintenance costs may be reduced by as much as 18 % by employing a condition-based maintenance strategy [50]. Condition-based maintenance may also be applied to other subsystems using the Digital Twin technique as [Zhong et al.](#) [51]. This technique is

based on creating a digital simulation of the system which is continuously updated using sensor data and then used to predict the remaining useful life of individual components. This technique necessitates the use of appropriate sensors to ensure that the digital twin is actually representative of the real system. The approach to maintenance for the overall system and subsystems is further discussed in Section 8.3.

Safety

The system itself is not manned but still needs to be safe to operate and safe to fail. It also has to be safe for and during maintenance. The most safety-critical components are:

- The shaft brakes, which must prevent shafts from rotating. These may be deployed due to failure on the related systems, maintenance, or the need to park the system during storms
- Yaw system brake, which should hold the system in place during maintenance to allow safe operation and prevent the system motion during storms
- The monopile, because it supports the entire turbine.
- The lightning protection system, which is essential for a large steel structure. Without a proper lightning protection system, there is a large risk of damage to components due to lightning strikes, which can not be avoided.

For the case of shaft brakes, it would be wise to include one or more additional redundant systems, since maintenance of shaft bearings is expected to be among the most common types of maintenance which will be needed. In addition, their performance should be monitored by the use of strain gauges and hydraulic oil sensors.

For the yaw system brake, the bearing and the brake should be monitored with strain gauges, cameras, and potentially accelerometers to check for abnormal vibrations. There may also be a need for an additional emergency brake, which should be fail-safe and lock the system in place with respect to the monopile in case of failure.

The monopile itself can not be fail-safe or redundant and as such requires constant monitoring, which could be done visually via remote underwater drones and mounted cameras. Additionally, the status of the ocean floor would also need to be monitored.

For the lightning protection system, redundancy seems like the best option, as a failure of this system could lead to the failure of other critical components. The system is also easily replaceable and does not incur a large cost for installation.

8.3. Operations

Control strategy

Controlling and operating the wind turbine was another aspect that needed to be analyzed in this design stage. The wind turbine can only operate in a set range of wind speeds. It was assumed that the cut-in and cut-out wind velocities are 3 to 4 m/s and 25 m/s, respectively⁸. Within this interval, the wind turbine should be able to produce usable power and safely run. Three control techniques will be implemented in order to ensure that the maintenance required is minimized and the energy produced is maximized. According to [Mwaniki et al.](#), the designed product should have a supervisory, control and safety system.

The supervisory system aims to continuously monitor the entire assembly to facilitate preventive maintenance and planned system service. It is also capable of shutting down the system in case of extreme wind scenarios and other catastrophic failures.

⁸<https://theroundup.org/wind-turbine-power-curve/> [cited: 20 June 2023]

Secondly, a control system will be needed to control the actuators and adjust the rates of individual elements for producing the required power in different conditions. This system will deal with regulating the torque on the drivetrain through the DFIG settings, provide the proper orientation for the high lift device, command generator inputs, for converting the power mechanical into electrical power and vice-versa, and turn on the yawing system when the structure needs to orientate itself with the wind direction.

Lastly, the wind turbine should have a second redundant control system for safety. This should be independent of the main control system. In case of serious issues, it should halt the required operations and engage brakes. Usually, it aims to halt any activity in order to prevent additional damage.

Control of WCT

The wake control system should be controlled to provide the required wake recovery, but not produce loads of unacceptable magnitude. The control system concept is outlined in Figure 8.1. The main idea behind it is that the target value of circulation Γ_{ref} would be given as input, which would change the deflection of slats, flaps, and other sections of the airfoil in order to produce this desired circulation. The lift and drag produced would in turn have an effect on the structure, which should be integrated into another, bigger control loop.

At this stage, it is not possible to give a more detailed control block diagram, as many more details about the actual implementation of the WCT concept would be required. As more information becomes available at later design stages, the control block diagram in Figure 8.1 should be updated.

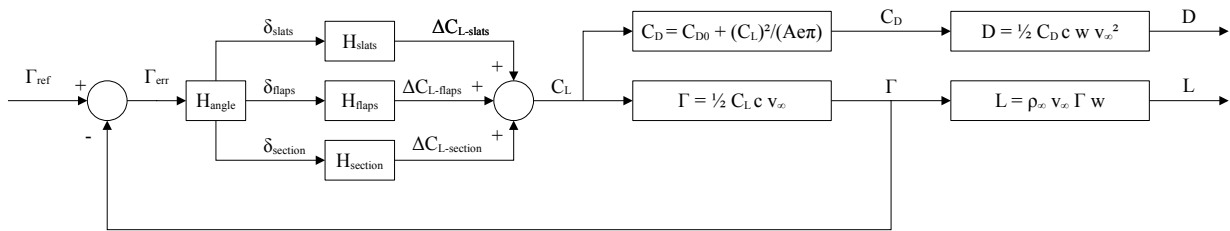


Figure 8.1: Concept for control of WCT

Torque control

In order to obtain maximum power production in the operating regime limited by the cut-in and rated wind speeds, it is required to regulate the TSR of the rotors. As the introduction of a pitching system will introduce costly maintenance aspects in this purposely low-maintenance design, it was decided that the appropriate method for rotor control is through the generator. As discussed in the previous report, the DFIG requires a feeding connection from a power source in order to generate the variable magnetic field used in electricity production. By connecting a PI controller to the inverter and DC bus within the rotor-side converter, both the voltage and phase slip of the rotor can be modified. Changing these parameters leads to different values of generator synchronous speed, allowing the controller to set the slip setting of the DFIG. The slip of the generator is defined as the percentage difference between the rotor speed and the synchronous speed. For a DFIG the synchronous speed depends on the voltage fed into the generator rotor and the number of magnetic poles within.

The relationship between the slip of the generator and the produced torque is presented in Figure 8.2

9.

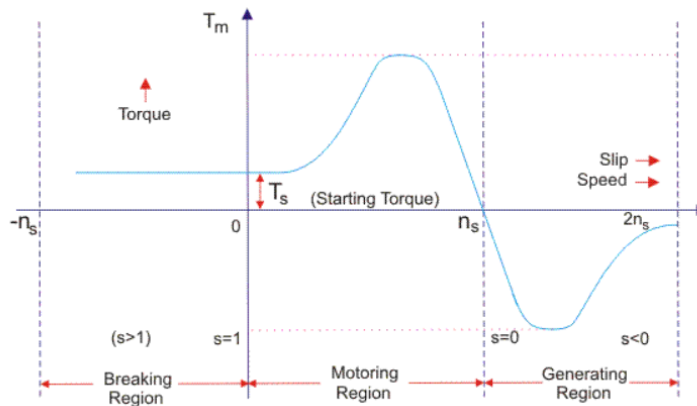


Figure 8.2: Relationship between generator slip and torque for a generic induction generator, with positive torque relating to torque delivered by the generator.

By either increasing or decreasing the synchronous speed of the generator it is possible to influence the shaft torque, and thus the speed of the rotors. By doing so, the turbine TSR can be modified to approach the optimum value for the given airfoil, thus maximizing the total power production. Multiple controller designs can be considered to regulate the TSR of the system, such as Tip Speed Ratio Control (TSRC), Optimal Torque Control (OTC), Power Signal Feedback Control (PSFC), and Perturbation and Observation Control (POC). From literature, it was determined that OTC is able to deliver maximum power while maintaining low response and recovery times compared to the other three [53]. Moreover, using OTC would also be beneficial when encountering turbulent gusts, as the low response time would make the controller more adaptable to these changes in windspeeds. This method can be combined with the implementation of a Maximum Power Point Tracking controller for the DC-to-DC converter connected to the DFIG in order to keep power transfer at maximum efficiency.

Control of YCT

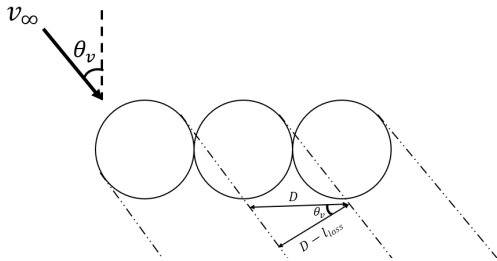
Next, the yaw control system is designed. This consists of yaw control during operating conditions with differential thrust and yaw control using electric motors during low wind and storms. Finally, verification and validation are performed for the simulations developed.

Unforced yaw system response

Firstly, a wind velocity vector that is incident at an angle θ_v would cause the thrust generated by the left-most rotor as seen in Figure 8.3 to have a larger effective area, and thereby a higher thrust, than the other rotors. This is because part of the wake of each rotor, presented as the dotted lines in Figure 8.3, overlaps with the next rotor, causing it to lose efficiency. Assuming that there is no space between the rotors, the lost effective width of each rotor, l_{loss} , can be calculated by $l_{loss} = D(1 - \cos\theta_v)$ where D is the diameter of the rotor. The only rotor which does not experience this effect is the first rotor and therefore provides a slightly higher thrust which exerts a torque on the system. The wind velocity in the wake of each rotor can be found using the c_t relation to the induction coefficient in Equation 8.1 [54].

Using a c_t of 0.75 results in an induction coefficient of 0.25 which leads to a wind velocity that is 75% of the freestream velocity, thus the shading effect can be assumed to lead to a 75% of freestream speed at the wake.

⁹URL: <https://www.elprocus.com/what-is-slip-in-an-induction-motor-importance-its-formula/> [cited: 16 June 2023]



$$c_t = 4a(1-a) \quad a = 1 - \frac{v_{wake}}{v_\infty} \quad (8.1)$$

Figure 8.3: Shielding effect

The resultant torque (anticlockwise positive) induced by this effect is described by Equation 8.2.

$$\tau_{shield} = \frac{1}{2} \rho c_t (0.25 l_{loss}) H \left(v_\infty^2 + 2 \frac{W-D}{2} \omega v_\infty \cos(\theta_v - \theta_{sys}) + \omega^2 \left(\frac{W-D}{2} \right)^2 \right) \cos \theta_{rel} \cdot \frac{W-D}{2} \quad (8.2)$$

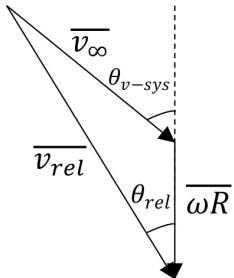
In the case where windspeeds are below the rated windspeed v_{rated} , if a torque is applied that causes the structure to rotate at an angular velocity ω , a dampening torque is induced. This is due to the increase in relative windspeed, and thereby thrust, in the rotors moving into the wind, and a complementary decrease in those moving away from the wind. This is because the thrust to windspeed gradient is positive below v_{rated} .

Simulating this, the natural response of the system due to a change in the angle of wind velocity θ_v is to re-align to be perpendicular to the wind velocity, therefore the system is stable with regards to wind direction changes. However, this motion is overdamped, leading to a correction time of hours. Thus, an additional torque needs to be applied to decrease the time of angle correction.

Yaw control with differential thrust

The use of differential thrust to yaw the turbine relies on reducing the thrust generated by one or more rotors which in turn reduces the torque generated on that side of the turbine, causing it to yaw in the desired direction. This method is able to achieve high torques, and therefore a faster correction rate, without having to use large motors.

A Python script simulates the application of this by setting an initial angular displacement, velocity, and acceleration of zero for the system, with a wind velocity vector aligned at θ_v counterclockwise. The simulation follows a turbine-fixed frame of reference and so the wind speed vector changes relative to the rotor as it moves. Thus the effective windspeed angle is $\theta_v - \theta_{sys}$. The relative velocity V_{rel} and angle of relative velocity θ_{rel} experienced by each rotor are calculated iteratively as ω changes.



$$v_{rel} = \sqrt{v_\infty^2 + 2 v_\infty \omega R \cos(\theta_v - \theta_{sys}) + \omega^2 R^2} \quad (8.3)$$

$$\theta_{rel} = \arctan2 \left(\frac{v_\infty \cdot \sin(\theta_v - \theta_{sys})}{v_\infty \cdot \cos(\theta_v - \theta_{sys}) + \omega R} \right) \quad (8.4)$$

Figure 8.4: Relative velocity for a rotor moving into the wind

The relative velocity is used in the calculation of the thrust vector in the direction of relative velocity for each rotor. The perpendicular component of each thrust vector is calculated and multiplied by its moment arm to calculate the torque induced by each rotor. Finally, the torques are added, resulting in the total applied torque on the turbine system. This iteratively leads to a new α through $\alpha = \tau/I$, and thereby ω and θ are updated.

The controller used for differential thrust is a simple on-off switch to turn the outermost rotors depending on the sign of the angle error. The controller accounts for overshooting the target angle by reversing the side on which the rotors are switched off, until the system angle θ_{sys} is within 10% of the desired angle θ_v , where all rotors are switched back on and the system is allowed to self-stabilize. A block diagram of the controller can be seen in Figure 8.5. The on-off controls are displayed as Heaviside step functions denoted by U.

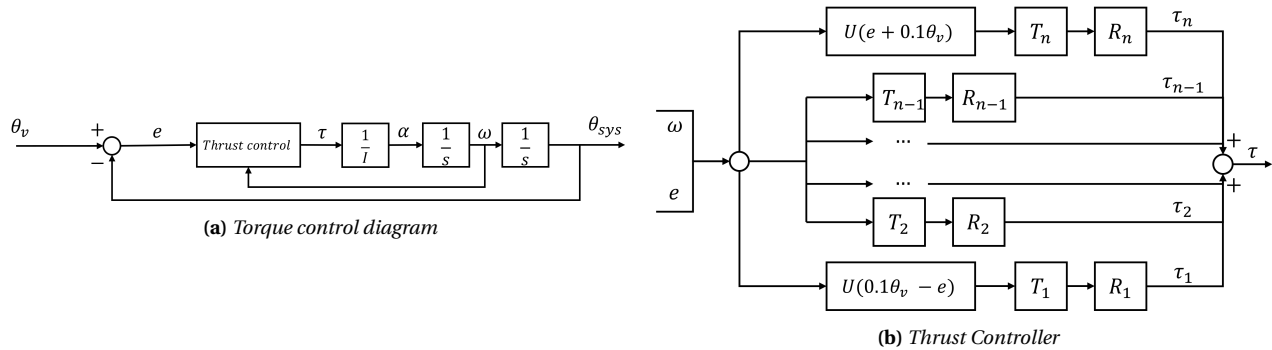


Figure 8.5: Block diagram of yaw control

Simulating system response to the thrust controller results in yaw error correction times as shown in Figure 8.6 for a mass moment of inertia $2.75 \times 10^{10} \text{ kg m}^2$, and a windspeed of 10 ms^{-1} .

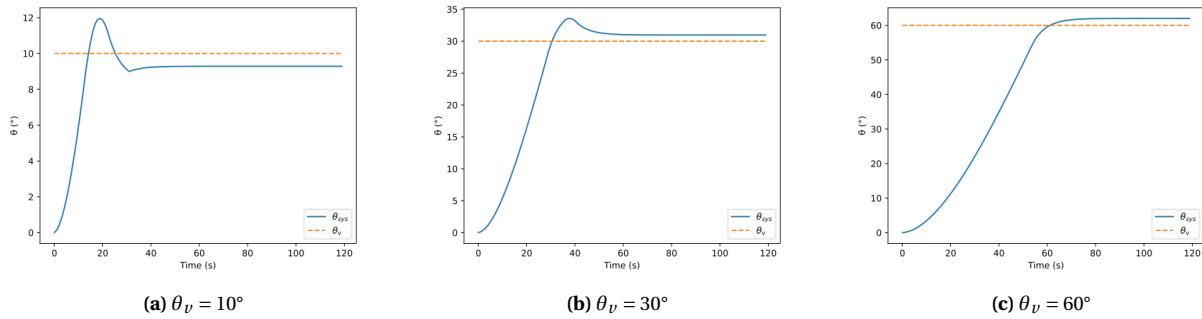


Figure 8.6: System response to varying changes in θ_v at 10 ms^{-1}

Limitations

One of the limitations of this yaw control mechanism is that it does not optimize for power production while yawing. Rather it serves as a simple mechanism that can perform yaw quickly, and therefore allow for more non-yawing time where all the rotors can give maximum performance. The use of other more complex yaw controllers can be designed to minimize power loss while yawing as well.

Additionally, the simulation assumes a windspeed below v_{rated} , so c_t remains 0.75, this is the case most of the time. In reality, the system will also need to yaw at or above v_{rated} . Above v_{rated} , thrust decreases with

windspeed, which causes the system to become unstable with changes in θ_v as the direction of the damping torque reverses. This can be overcome by applying yaw brakes when the windspeed approaches v_{rated} to avoid an unstable free movement. When disengaging the brakes and yawing the system, the thrust generated by the rotors can be artificially lowered to keep a positive thrust to windspeed gradient, keeping the system yaw stable even during $v_\infty > v_{rated}$.

Using differential thrust is slightly less effective during lower wind speeds, as it takes longer to yaw. However, the time to yaw is still very small compared to changes in wind direction, so it could still be used. When there is virtually no wind, the use of an electrical yaw system becomes more effective.

Yaw control with electric motor

The use of electric motor drives connected by a set of planetary gearboxes to the yaw slewing bearings to induce a torque and therefore yaw the system is also possible. This can be useful for example during storms, when the differential thrust cannot be used as all rotors are put on standby. Another use case would be below cut-in speed when the wind speed is too low to use differential trust.

This section will size the electric yaw system based dampening torque that is induced by the rotational speed. The main assumptions will be that there is no shielding effect and that the system inertia is small and reaches terminal velocity quickly. The calculations boil down to the trust force of the structure times the moment arm integrated over the domain. The critical case will be in 70 m s^{-1} storm conditions rotating at $90^\circ/30\text{min}$.

Previous simulations showed that the system is highly damped so damping dominates over inertia. It is assumed the system will spend most of the time at terminal velocity while yawing. During this time the Torque produced by the electric motors will be equal to this damping torque. Damping torque is due to different relative wind speed on opposite sides of the structure due to rotation of the structure. Assuming the worst-case scenario when the structure is 90° to the wind the relative wind speed distribution will be linear to the distance along the width of the structure $v_{rel} = v_\infty + \omega R$ Equation 8.5. Figure 8.7 and the following equations help to understand the reasoning. Drag force is proportional to v^2 so the Drag force distribution will be a parabola. The combined drag force comes from the drag of the rotors described in Equation 8.7 and from the wings described in Equation 8.8. The drag of the wings has to be multiplied by the number of wings. The derivation assumes one wing. To get the torque distribution acting on the structure the force distribution needs to be multiplied by the distance from the rotational axis described in Equation 8.6. Torque distribution will be a 3rd-order polynomial and which needs to be integrated over the domain of the structure to get the total torque. So the torque has up to fourth-order dependencies on the radius. To do this in integral form it is advantageous to notice that these variables are not dependent on the height of the structure so it is possible to only integrate along one dimension along the width to get the resultant torque. This integration is performed in Equation 8.9, Equation 8.10 and Equation 8.11. Since the structure is symmetric and the integration is carried from $-R$ to $+R$ even order terms cancel out and we are left to only consider odd-numbered terms. The equation is valid for $v > 3 \text{ m/s}$.

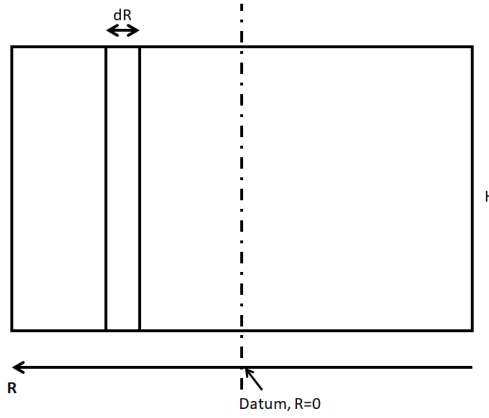


Figure 8.7: Drawing for the derivation

- $\rho = 1.225 \text{ kg/m}^3$ - air density
- $C_T = 0.014$ - thrust coefficient when stationary
- $C_D = 0.0152$ - drag coefficient when stationary
- $H = 280 \text{ m}$ - height of the structure without clearance

$$v_{rel} = v_\infty + \omega R \quad (8.5)$$

$$\tau = (F_{flow} + F_{wing}) \cdot R \quad (8.6)$$

- $c = 20 \text{ m}$ - cord of the wing
- $R = 145 \text{ m}$ - halve of the width of the structure
- v - free stream velocity velocity
- ω - rotational velocity of the system
- τ - Torque

$$F_{flow} = C_T \frac{1}{2} \rho v^2 H dR \quad (8.7)$$

$$F_{wing} = C_D \frac{1}{2} \rho v^2 c dR \quad (8.8)$$

$$\tau_{storm} = \int_{-R}^R C_T \frac{1}{2} \rho (v + \omega R)^2 HR + C_D \frac{1}{2} \rho (v + \omega R)^2 c R dR = \frac{1}{2} \rho (C_T H + C_D c) \int_{-R}^R (v + \omega R)^2 R dR \quad (8.9)$$

$$\int_{-R}^R (v + \omega R)^2 R dR = \int_{-R}^R v^2 R + 2vR^2\omega + R^3\omega^2 dR = \frac{1}{2}v^2 R^2 + \frac{2}{3}vR^3\omega + \frac{1}{4}R^4\omega^2 \Big|_{-R}^R = \frac{4}{3}vR^3\omega \quad (8.10)$$

$$\tau_{storm} = \frac{1}{2} \rho (C_T H + C_D c) \frac{4}{3} v R^3 \omega \quad (8.11)$$

It can be seen that Equation 8.11 requires zero torque to yaw the structure at any rotational speed which is not true. This is because it was assumed that the relative speed always acts in one direction. When in Equation 8.7 and Equation 8.8 the velocity is squared the direction of the wind is lost. This is a good assumption as long as $v > \omega R$ however at $v = 0 \text{ m/s}$ the sign changes direction in the middle of the structure. Therefore Equation 8.12 accounts for this change in direction. Another inaccuracy is that this equation assumes only one wing to get the result for 4 wings $C_d c$ should be multiplied by 4. The results Table 8.12 are with 4 wings.

$$\begin{aligned} \tau_{v=0} &= \int_{-R}^0 (F_{flow} + F_{wing}) \cdot R dR - \int_0^R (F_{flow} + F_{wing}) \cdot R dR = \frac{1}{2} \rho (C_T H + C_D c) \left(\frac{1}{4} R^4 \omega^2 \Big|_{-R}^0 - \frac{1}{4} R^4 \omega^2 \Big|_0^R \right) = \\ &= \frac{1}{2} \rho (C_T H + C_D c) \left(-\frac{1}{4} R^4 \omega^2 - \frac{1}{4} R^4 \omega^2 \right) = \frac{1}{4} \rho (C_T H + C_D c) (-R^4 \omega^2) \end{aligned} \quad (8.12)$$

For a torque rating wind speed and yaw rate are needed. To size the electrical yaw system yaw rate requirement should be found. Several conditions will be considered. Wind speed calculations will be presented for 70m/s, 50m/s 30m/s and 0m/s. These speeds are between 50 year maximum and 0m/s while not taking into account operating conditions. To determine the yaw rate required during storm conditions and during low wind speed conditions, historical wind data is considered. Wind data presents wind speed and wind direction in 2016, 2017 and 2018 for every 30 minutes [14]. Wind data indicated that within 30 minutes the wind can change the direction by 180° however this change was rare [14]. The 75 percentile is a change of 4.5° and the 95 percentile is a change of 11.5°. To compare, for a typical yaw system for operating conditions, the yaw rate is 1°/s [55]. The results are presented in Table 8.12

Table 8.12: Torque in MNm required to yaw the system depending on wind speed and rotational speed.

	0 m/s	30 m/s	50 m/s	70 m/s
4.5° / 30 min	<0.01	0.02	0.03	0.04
11.5°/30 min	<0.01	0.04	0.07	0.10
90° / 30 min	<0.01	0.33	0.56	0.78
180°/30 min	<0.01	0.67	1.12	1.56
1°/s	0.21	6.70	11.16	15.62

Table 8.13: Time required to accelerate the structure

	t[s]	t[min]
4.5° / 30 min	2	0.1
11.5°/30 min	6	0.1
90° / 30 min	49	0.8
180°/30 min	98	1.6
1°/s	980	16.3

Based on the table we can see that the limiting case is yaw during storm conditions. It is very unlikely that a rare storm event will happen at the same time as a rare wind change happens so the red cells ($> 1.2\text{MNm}$) of Table 8.12 are not a design requirements. Considering this an electric yaw system capable of providing 800 kNm is selected. To check if the assumption of damping dominated system was correct it is required to calculate the time it would take to accelerate the system to the given yaw rate calculated in Table 8.13. It can be seen that for anything less than 180°/ 30min acceleration time is at least 20 times smaller than 30 minutes.

Verification of yaw simulation

The yaw simulation is verified to ensure that it performs the calculations correctly. For this, the simulation is restricted to only the $0 < \theta < \frac{\pi}{2}$ quadrant of the wind directions, as the reaction of the system to wind vectors from any of the other quadrants is symmetric.

The verification consists of checking that the program performs as expected for each step of the analysis by comparing output from the program to calculations done manually. This is performed for an iteration for the leftmost rotor where $v_\infty = 10\text{ms}^{-1}$, $\theta_v = 30^\circ$, $\Delta t = 1\text{s}$, $t = 4\text{s}$, $\alpha = 0.001\ 660\ 506\ 869\ 86\text{rad s}^{-2}$, $\omega = 0.007\ 749\ 071\ 214\ 34\text{rad s}^{-1}$, $\theta_{sys} = 0.020\ 453\ 453\ 970\ 14\text{rad}$, and Total torque = 45 675 014 Nm.

Table 8.14: Verification using hand calculation at $t = 4$ iteration for a single rotor

Step	Output from code	Hand Calculation	Absolute Error	Relative Error
R	-116.66666667	-116.66666667	0	0
ωR	-0.90405831	-0.904058308	1.63E-09	-1.8E-09
v_{rel}	9.21829427	9.218294267	-3E-09	-3.3E-10
θ_{rel}	0.55045175	0.55045175	3.66E-10	6.65E-10
T	510074.1375302	510074.1375	-2.4E-06	-4.8E-12
T_\perp	434730.22512485	434730.2251	-2.5E-06	-5.7E-12
τ	50718526.26456571	50718526.27	0.001161	2.29E-11

The results show that the code performs as expected based on the given equations. The maximum relative error found in this case is in the order of 1×10^{-9} , which can be considered negligible. Furthermore, the

simulation is convergent with a reduction in time step.

Validation of yaw simulation

The physical equations used in the simulation must be validated to ensure that they accurately reflect the dynamics that would occur in real-life. The assumptions made in the initial simulation need to be validated to be true. This can be done either through the comparison of results with literature or by building a prototype and collecting real-life data and comparing results. Since this is a novel concept, it would be difficult to find literature in which such type of system is addressed. [MacMahon et al.](#) provides such a simulation for yaw with differential thrust for an MRS, however, this is provided for an MRS of HAWTs so cannot be directly used to validate this model [56]. Therefore it is better to collect real-life data from a prototype instead.

Sensors

Sensors are devices that detect and respond to physical input or changes in the environment. It is imperative for the designed wind turbine to be equipped with several sensors in order to detect potential issues and prevent the failure of the structure. Multiple types of sensors have been identified that will be installed on the wind turbine. They are presented and briefly described below:

1. Anemometer. The anemometer measures the wind speed and it will be placed in various locations.
2. Wind vane. It measures the wind direction and it will be placed in multiple locations.
3. Wind gust sensor. The wind gust sensors detect the sudden changes in wind speed. It will be located on the top of the structure.
4. Torque sensor. The torque sensor measures the magnitude of the torque exerted on the shaft. It should be located on each rotor and generator.
5. Accelerometer. This device is used for monitoring the vibrations inside the wind turbine. Vibrations could constitute an issue, especially for the tower while operating and in extreme weather conditions.
6. Thermometers. They will be placed in several locations in order to check the temperature of multiple components. Typically, the elements that experience the most overheating are the power electronics, generator windings, gearboxes, and bearings.¹⁰
7. Yaw position sensor. Since the wind turbine is equipped with two bearings that will facilitate the yawing movement, such devices will be presumably placed near the motors.
8. Generator voltage and current sensors. Each generator will include this type of equipment.
9. Rotor speed sensors. Six instruments will be needed in total, one for each shaft.
10. Ice detection sensors. Since the wind turbine is located in the Ijmuiden Ver zone, a harsh climate can be experienced during winter. Having the blades covered with ice can damage their structure of them and also affect the power production efficiency.
11. Rain sensors and Light Detection and Ranging (LIDAR) scanner. LIDAR scanners are capable of mapping the wind's and rain's characteristics in advance. They sent laser pulses into the atmosphere which are further reflected by particles from the air.¹¹

¹⁰<https://www.ediweekly.com/overheated-bearings-gearboxes-among-causes-wind-turbine-fires/> [cited: 13 June 2023]

¹¹<https://www.vaisala.com/sites/default/files/documents/WEA-LEO-ScanningLidar-eBook-B212128EN-A.pdf> 18 June 2023

12. Cameras. Cameras will be used mostly for monitoring the external cracks and damage to the wind turbine. Since there is a lot of free space in the truss structure, they can be mounted in several locations on the struts and transmit up-to-date information consciously.
13. Strain gauges. This equipment is meant to measure the strain in different turbine members. They will be located in different spots.
14. Oil condition sensors. Six such sensors will be needed for each gearbox.
15. Humidity and pressure sensor. These instruments will be used to measure the atmospheric conditions.
16. GPS. The GPS is particularly important in the case of maintenance work when a specific wind turbine is damaged inside a wind farm.
17. Lighting sensors. They should be located in several parts of the structure.
18. Acoustic sensors and microphones, which will be used for noise monitoring. Noise pollution should not be an issue as a lower TSR, except for the installation phase of the wind turbine, but they should be present to detect, when possible, to detect different types of mechanical malfunctions.
19. ACFM sensors, is a probe sensor to detect surface level cracks on the conductive surfaces of the structure. It is mainly utilized for the truss structure and blades of the rotor, as they are hollow metal cylinders.

The most important data to be collected by SCADA for predictive maintenance were decided. They are presented for the individual subsystems level (FND, TWR, YCT, PCT, WCT, DRT, RTR). The list is not exhaustive, only including the most relevant sensors.

FND: Foundation health would require sensors to determine the progress of corrosion and any structural damage. FND will be installed with strain gauges to measure the strain induced on the monopile as a function of the wind speed. In addition, it will have acoustic sensors to inspect the interference pattern of sent signals and analyze crack formations.

TWR: Since it has a significant number of truss elements, TWR system will be the closest inspected. Furthermore, every load induced in the system goes through the truss structure to the monopile. Therefore, analysis of the vibrational characteristics of this structure is essential for cutting operational expenses. The TWR will be equipped with multiple accelerometers and strain gauges to send the frequency spectrum and amplitude of vibrations due to wind characteristic changes to the SCADA. These devices will also be used to detect rotor-induced vibrations and to determine interference between aerodynamic loads induced by the HLD and rotors. To inspect partial failures and cracks of the truss structures, both acoustic and ACFM (Alternating current field measurement) sensors will be used. Moreover, the cameras and microphones will be placed on this structure for visual and noise inspection of both itself and the rotors.

RTR: The RTR structure will also be monitored, given relatively high and fluctuating loading. Both ACFM(since blades are entirely metallic) and acoustic sensors will be used for operational and non-operational inspections, respectively, for crack formations. Also, RTR RPM will be measured with the vibrations on the RTR.

DRT: DRT failures are catastrophic for the operations. Oil sensors for the gearboxes will be installed for oil pressure, temperature, granularity, and leakage. Also, vibrations on the gearboxes and shafts will be collected as functions of generator RPM and capacity to predict failures before they happen.

YCT: Attitude and yaw rate of the structure during the yaw movements will be collected as well as the vibrations with yaw position sensor and accelerometers on the truss structure, respectively.

WCT: WCT induces high loads on the structure that supports it and itself. These loadings are heavily influenced by wind characteristics and are unstable. Therefore, accelerometers and strain gauges will be utilized.

Interrelations between the collected data and sensors can be observed better in Figure 8.8.

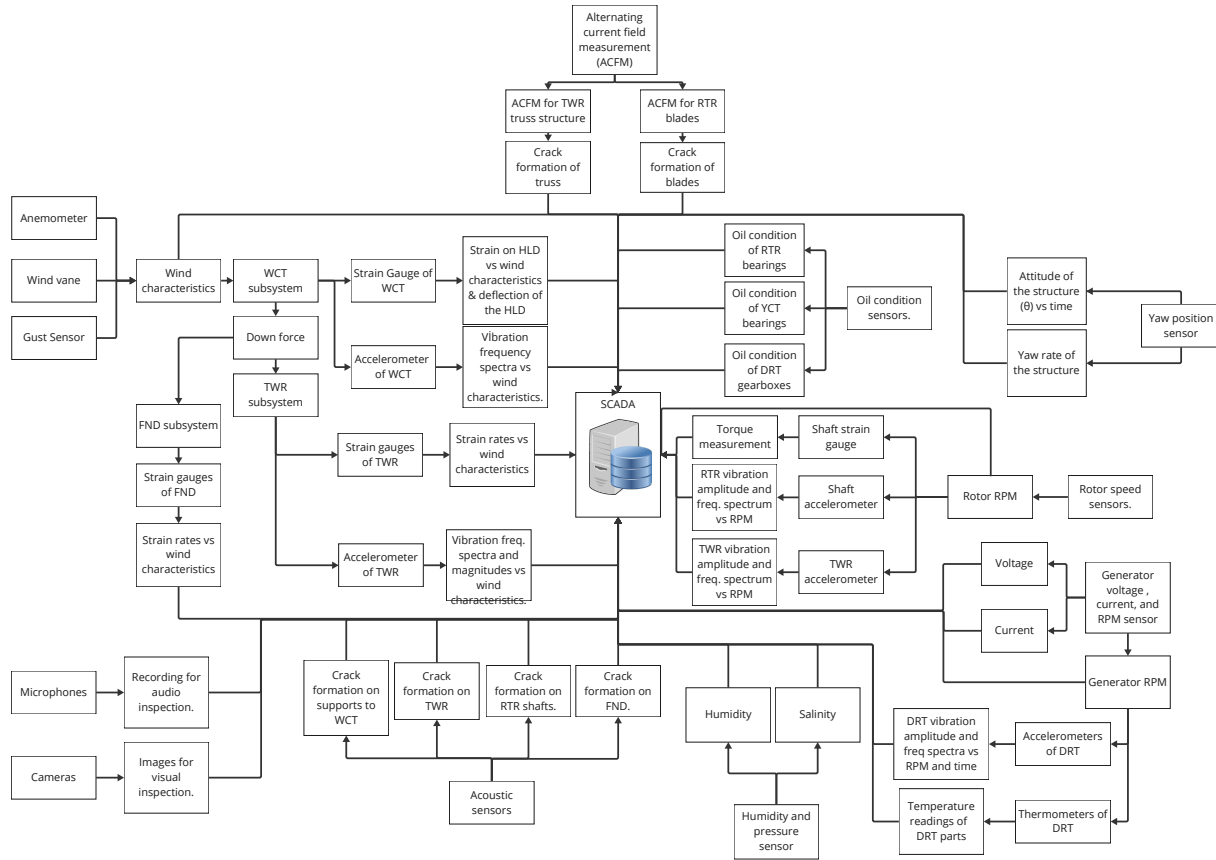


Figure 8.8: SCADA data acquisition diagram

Electrical layout

It is important to evaluate, at least at the conceptual level, the components of the electrical department that enable the system to send and receive power to and from the grid. Usually, offshore wind parks are connected to the grid through a transformer platform that converts the AC current from the wind turbines to HVDC current. This is done in order to minimize cable losses over the tens of kilometers between the wind park and the landing point. As the scope of the MR-TBD project did not include the transformer platform, it was assumed that will be covered by Tennet, the Dutch national grid operator.

The main electrical elements that can be found on the turbine are the generator, the partial converter that provides a load to the generator's induction rotor, and various filters that prevent the overloading of other components. Due to safety reasons, the system also includes an Emergency Power Source (EPS) that can operate independently of the generator and the grid connection. This EPS is designed to power both the hydraulic brake and the yaw drive to operate in emergency conditions. The sizing of this additional power bank will be considered in the next design iterations post-DSE. A conceptual diagram is provided in Figure 8.9.

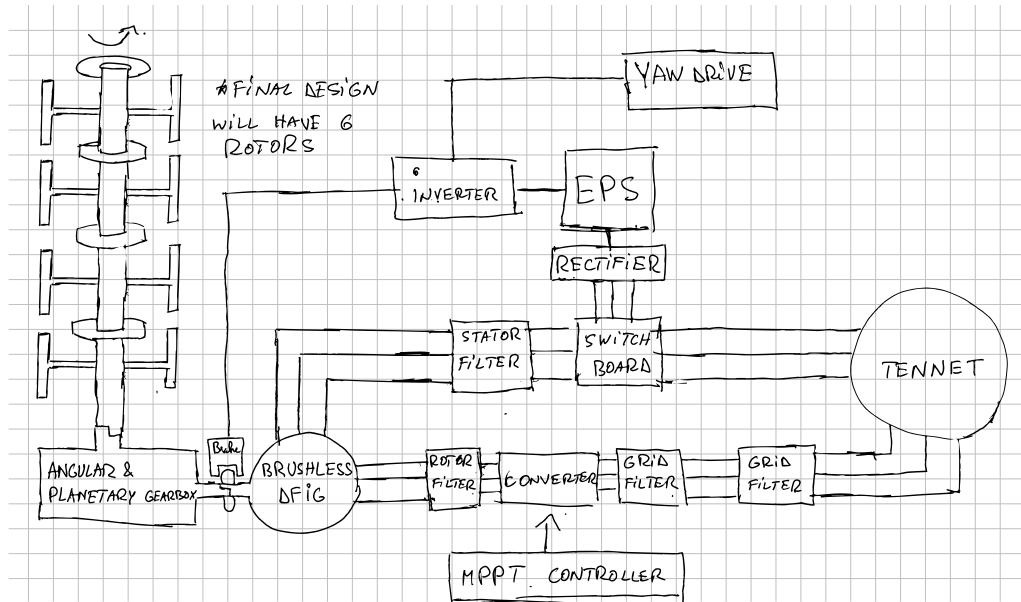


Figure 8.9: Conceptual electrical diagram

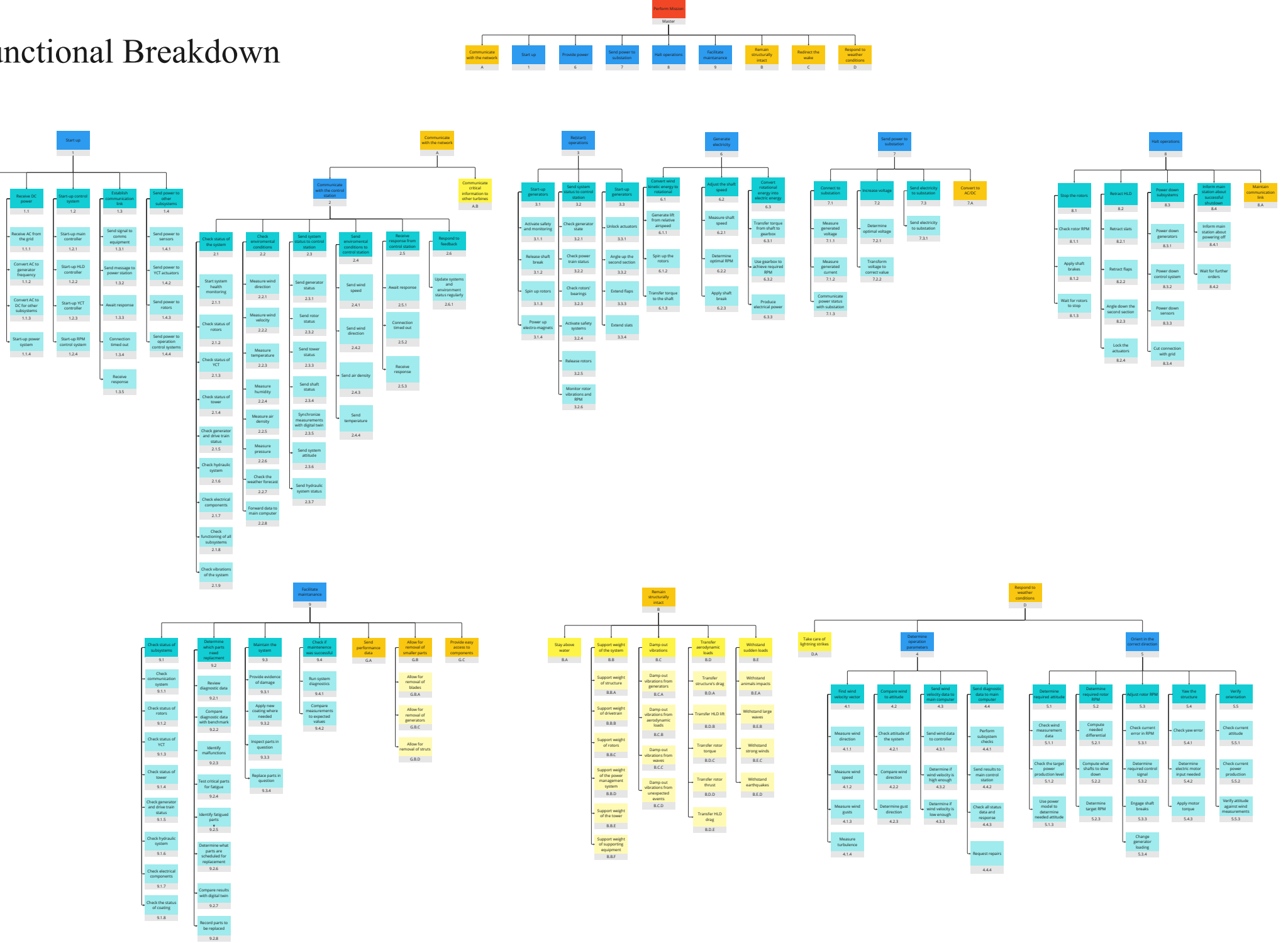
System Operation

The system's function flow diagram (FFD) and function breakdown structure (FBS) have been updated from their initial version presented in the baseline report [7]. Some functions in both have been changed, namely, all the functions related to the pitching of the blades. Functions were also made more specific and all but one were now broken down into three levels.

For the FFD, the diagram was remade to show the nesting of the tasks within each other more clearly. The previous version of the diagram did not show the hierarchy quite as clearly.



Functional Breakdown



Expected Annual Energy Production

The main goal of any wind turbine is to produce electrical energy. With all the data presented before it is possible to estimate the energy production of the design. The calculation was straightforward, the power production for a given wind speed was given in Section 6.3 and the wind speed data was given in Section 3.2. To obtain the yearly energy production, for every data point in the wind model, the power produced is calculated. Since the wind data points are spaced 30 minutes apart, it is assumed that the wind conditions are stable, so the power produced can be multiplied with time separation of the data points to get the energy produced. Using this approach, the annual energy production (AEP) was calculated to be around 149 GWh. This is roughly in line with the values predicted by the Catapult data, which were 134 GWh [9]. The energy production calculated here is most likely an overestimation, since stops for maintenance or other disruption are not taken into account. However, it still shows that the proposed design has an energy production close to expectations.

8.4. Maintenance and logistics

This section describes the operations plan the designed wind turbine. It focuses on the installation, decommissioning and maintenance of the system. Its operations are not expected to be much different from the offshore ones of the current wind turbines. This would mean that an onshore control center is used for most of the operations, with a small support crew on the wind farm site to allow for quick repair.

Installation and offshore transportation

A few aspects of the installation and decommissioning of the wind turbine will closely follow the procedures currently in place for traditional designs. For example, the installation of the foundation and connection to the grid will remain the same, just on a larger scale. What will be different is the transportation of the structure to the IJmuiden Ver zone and the installation of the structure.

The design of the tower will be built onshore, then towed to the location where it should be placed. The monopile will be installed on the ocean floor up to a few meters below the surface of the ocean. The structural frame will be built and equipped with all components inland. There are multiple ways in which the tower, including all elements, and the monopile can be transported to the desired location. The most common methods are to use a crane that will ferry the assembly, pile drive the foundation and afterward mount the tower. An alternative would be to employ dynamically positioned (DP)/anchor handling/floating vessels in combination with floaters to transport and connect the two components of the wind turbine. With regard to big floaters nominated, they would be filled with more water to sink further down, allowing for the monopile to be joined to the structure. For inserting the monopile into the ground, the classical hydraulic hammering could be adequate. The big disadvantage of the impact driving method is the generation of underwater noise that can affect the marine life [57]. However, there is an additional technique that uses hammering by vibrations. Simulations and calculations prove that this will save up to 40 % reduction in installation time and installation cost.¹² Installation and transportation services are provided by several companies from the Netherlands, namely, Heerema Marine Contractors, Cape Holland and Boskalis, respectively.

Before proceeding with the installation of the foundation, there are preliminary measures and preparations that need to be taken into account. The most important ones are protecting the seabed and preventing it from further deepening while driving the foundation and parking the necessary vessels.¹³ Furthermore, seabed rock installation is required to establish the connection with the onshore grid. The three companies mentioned above do have facilities for performing all preparatory operations.

¹²<https://ocean-energyresources.com/2021/07/30/introduction-of-safe-installation-process-for-ultra-long-xxl-monopiles/> [cited: 20 June 2023]

¹³<https://boskalis.com/activities/offshore-energy/offshore-wind-farm-installation/seabed-preparation-and-scour-protection/> [cited: 20 June 2023]

Storing and Repairing Parts

There are four different maintenance strategies that can be adopted to ensure that the wind turbine operates within the normal parameters: corrective maintenance, preventive, condition-based and predictive maintenance. From previous work, it has been decided that predictive maintenance allows for both the lowest operational costs and downtime. However, in practice, a combination of all four needs to be employed. The product proposed in this report was designed for several purposes, in particular, higher energy production, be more sustainable and cheaper than the competitors and, allow easier maintenance work. All of them should be reflected in a lower LCOE.

An essential advantage of the design is the ease of pursuing the maintenance work. Since the wind turbine has six shafts, when a component from one of the shafts is ruined, the repair can be done, by only turning off the shaft from the opposite side. For this scenario, the yawing movement will be avoided and power will still be produced, but at a lower capacity. As presented in Table 8.3, elements from the electrical/power sector and drive train are more likely to fail, in particular, the gearbox, generator, power supply and converters. For this reason, it was decided to place them at the bottom part of the tower. They will be accessible via stairs, catwalks and elevators. The maintenance of the damaged parts will be done relatively fast and efficiently. For instance, if a gearbox or a generator is broken, it will be immediately changed in an effective way. After disconnecting it from the entire assembly, it will be transferred to the underneath vessel and thereafter fixed at the onshore depot. The affected unit will be changed with newer one right away after it is disjointed. In this fashion, the downtime is minimised since the maintenance work is not performed offshore and the replacement is effective. The only period when the wind turbine will experience a loss in energy production will be while travelling to the location and shifting the parts. Table 8.8 and Table 8.9 showcase a replacement time for the generator of about eight and four hours, respectively, which is reasonable. The gearbox replacement times can be assumed to be almost the same since the procedure of fixing it is similar.

In order to have an efficient and safe maintenance service, personnel performing maintenance to the wind turbines needs to have easy access to spare parts. If possible, spare parts are often stored in specific warehouses close to the wind turbine site, known as depots [58]. For the design presented in this paper, only one depot will be considered due to the potentially limited extent of the wind farm and the limitations in the project's cost. Inside this facility, both repairable and discardable parts may be stored, and the quantity of each item will be normally known as the stock level of the storage [58]. Warehouses make up the entire skeleton of the support aspect of the project, assembly components, and can also allow for repairs of certain components. Apart from not severe repairs done at the depot, most broken items are sent to a workshop/provider for repair. Most of the time, workshops are in small designated areas close to the depot, where each turbine component's repair facilities are provided. Especially for advanced equipment, the workshop can often be the property of the part manufacturer. In some cases, operators get a new item from the manufacturer in exchange for sending a broken item obtaining a deduction on the component's price. The time it takes for an item to be repaired and returned to the depot is called turn-around time (TAT). This is a very important parameter when optimising stocks for repairable items [58]. Finally, every item needs to be properly collected inside the depot and an inventory of all the elements needs to be performed. This is done to keep track of and identify all the stored items.

Onshore Transportation

Onshore transportation is one of the biggest challenges in designing and building a wind farm. The large size and weight of most components make the design extremely hard to transport, even for small distances. Due to the increased number of elements, the logistics cost is expected to be high for regular wind turbines. However, this will not be the case for the designed product since most of the manufacturers and providers are located close to the Port of Rotterdam, where the central depot of the wind turbine will be situated, as stated in Section 8.1. They will be able to transport all the components via ships and when necessary,

via trucks. The only elements that might not be available on the domestic market are the elements from the drive train and sensors. In this sense, one option would be to be delivered by freighters to Amsterdam Schiphol Airport and then further transported by vessels or trucks to the final destination. The second option would be to directly deliver them by cargo ships to Rotterdam.

The onshore transportation cannot be considered an issue on account of the location chosen for the depot of the wind turbine. It will facilitate a reliable method of ferrying goods with a low risk of delay.

Decommissioning

Although life extension is a valuable tool for increasing the EROI of the asset and making the system more sustainable, it is only a prolonging of the inevitable decommissioning. According to decision 98/3 of the OSPAR convention, ratified by all Western European countries, all offshore structures above 4000 t are required to be disassembled by parts once they reach the end of their useful lives ¹⁴. Thus, it is important to prepare for this event from the inception of the project. Otherwise, future wind farms will have to deal with the left-behind structures and develop their own decommissioning plan. Moreover, planning and designing for the decommissioning phase would make the disposal of the asset go smoother and would mitigate the costs, emissions, and impact on the environment.

Nevertheless the decision from the OSPAR convention, the plan for decommissioning is similar to the one for the installation. The tower, including all elements, will be placed on a floater or dynamically positioned (DP)/anchor handling/floating vessels and transported back to the shore. The companies that have been stated for installing the designed wind turbine, Heerema Marine Contractors, Cape Holland, and Boskalis are able to provide such services.

The only potential issue with the wind turbine's last stage of life that can be encountered while disassembling the structure is the removal of the foundation. Since the monopile has a massive size and a large embedded length, it will be difficult to extract all of it. Any excavation work should be avoided as much as possible due to the marine environment created around its underwater part [57]. Besides the standard procedure of digging below the mud line, there are two other methods for decommissioning the foundation of a wind turbine. According to Cape Holland, it is proposed to apply pressure on the inside of the monopile which pushes the cylinder upwards in the same manner as with the extraction of the suction bucket. Secondly, a lifting tool and a vibro-hammer in one can be used in order to minimise the impact on the aquatic habitat. Moreover, especially using a hammer that can also provide small vibrations will contribute to significant costs savings. ¹⁵

¹⁴ URL: <https://www.ospar.org/news/scm-21> [cited 06 June 2023]

¹⁵ <https://www.offshorewind.biz/2016/12/07/cape-holland-tests-decommissioning-tool/> [cited: 20 June 2023]

Cost analysis

To ensure the success of the MR-TBD, it is of paramount importance that the design is financially viable. To check whether the design meets expectations of investors, a few economic indicators need to be checked. Namely, the expected return on investment and the time to break even. With all the information from Chapter 8, Chapter 6 and previous financial estimations from Chapter 2, a better informed budget evaluation. The chapter will begin with updating the budgets with design data in Section 9.1. Using the updated values a return on investment will be calculated in Section 9.2. Lastly, the time to break even will be computed in Section 9.3.

9.1. Informing the Budget with Design Data

The initial cost estimations shown in Chapter 2 had to be estimated in a rather crude way. Little was known about the individual sizes of the subsystems at the time of the analysis, requiring educated guesses to be taken often. With the design finalised, it is possible to correct some of the estimated values.

The main idea behind reevaluating the budgets is to see how much a given component has grown compared to a reference 10MW wind turbine. The results are normalised by dividing by the rated power of each of the turbines. The values being compared are different for each subsystem, which reflects that subsystems scale according to different values. The actual percentage changes and the previously predicted changes can be seen in Table 9.1 ^{1 2}.

Table 9.1: A data driven cost analysis based on the approximate sizing

Component	Reference data	MR-TBD data	% change of cost	Previous % change of cost
Bedplate	8.24 t/MW [59]	10.40 t/MW	26%	-100%
Main shaft	5.9 t/MW [60] (3.2 EUR/kg)	48.6 t/MW (0.5 EUR/kg)	28%	-50%
Yaw system	30kNm/MW	26.7kNm/MW	-11%	25%
Yaw bearing	0.3 t/MW	1.8 t/MW	500%	25%
Blades	4770 EUR/MW [61]	3.8 EUR/MW	-99%	-80%
Steel for the Tower (including HLDs)	62.9 t/MW [61]	111 t/MW	76%	20%
Foundation cost	207 t/MW [61]	205 t/MW	-1%	25%
Turbine maintenance	Analysis in Chapter 8	Analysis in Chapter 8	-60%	-75%
Gearbox	198m diameter TSR 9[61]	45m diameter TSR 4.5	-55%	-75%
Generators	198m diameter TSR 9[61]	45m diameter TSR 4.5	-55%	-80%

After analysis of the newly available data, it was discovered that most the past predictions were on the optimistic side. Most the cost changes grow with comparison to the previous estimates, some of them

¹URL:https://www.bonfiglioli.com/Product-Range-Wind_ENG_R04_0.pdf [cited: 21 June 2023]

²URL:<https://www.liebherr.com/shared/media/documents/grosswaelzlager/liebherr-slewing-bearings-product-catalogue-en-metric-web.pdf> [cited: 21 June 2023]

quite substantially. These changes caused the LCoE to grow from 35.77 €/MWh to 37.89 €/MWh.

9.2. Weight Average Cost of Capital

The return on investment (ROI) is an important metric for any investment. It dictates which projects are built and which are never considered. The easiest way to see if the MR-TBD is a better investment than traditional HAWTs is to see what WACC can be achieved for both configurations. There were two targets set up in Chapter 2. One for expanding the production in the North Sea up until 2050 and one for expanding production past 2050. The first assumes that wind turbines can still be placed in relatively cost-attractive areas, while the other assumes these spots were already used, so the MR-TBD is used to increase the energy density in already existing or just decommissioned farms. Both targets assumed that the traditional designs achieve WACCs of around 3%. In Table 9.2 the WACCs achievable by the MR-TBD are shown.

Table 9.2: *Return of investment*

Sale price of energy	54€/MWh	65€/MWh
Traditional design return on investment	3%	3%
MR TBD	6.7%	8.7%

From the analysis, it is clear that the MR-TBD can achieve ROIs far greater than conventional HAWT designs and could remain profitable for longer, despite adverse market forces.

9.3. Time to Break Even

The last financial factor to calculate is the time to break even (TtBE). This metric shows how much time needs to pass for an investment to recoup the up front costs. With a lower initial cost to install and with lower maintenance costs, it is easy to foresee that the proposed design should have a shorter TtBE. This is confirmed with calculations, the results of which can be seen in Table 9.3.

Table 9.3: *Years of operation to break even*

Sale price of energy	54€ /MWH	65€ /MWH
Traditional design return on investment	13.4 years	11 years
MR TBD	9 years	7.3 years

Sustainability

In this chapter, the sustainability strategy is presented. The scope of this chapter addresses both the way sustainability is taken into account in the design and the way the product or system contributes to sustainability. Impacts have been broken down into environmental, economic and social sustainability aspects.

10.1. Environmental sustainability

One of the main pivots of this project is its sustainability aspect. The project's mission objective itself states that to have a successful design, it is crucial to improve the system's sustainability under different factors, including materials, energy and emissions. To achieve this, a life cycle study needs to be performed, and the environmental impact of the final design needs to be assessed. This is what this section is going to focus on.

A life cycle analysis (LCA) is a systematic study used to assess the environmental impacts of a product, process, or service throughout its entire life cycle. For this project, this study aims to evaluate the ecological impact of the MR-TBD turbine throughout its whole life cycle phases, from the extraction of materials to decommissioning. This analysis helps identify areas where improvements can be made to minimise environmental harm and promote sustainable practices.

Multiple LCAs were performed in recent years about different conventional wind turbines [62, 63]. Depending on the level of detail of the study, various factors can be considered, including resource consumption, energy use, emissions to air, water, and soil and potential impacts on human health and ecosystems. Since the MR-TBD is still in the early phase of the design, the only two factors that are considered in this study are the energy consumed and the CO_2 emissions generated during its life cycle.

To perform a complete LCA, it is crucial to define all the life cycle phases of the turbine as well as define all the components that make up the structure with their respective materials. The MR-TBD consists of many components with different electrical and mechanical parts; hence, gathering information on all the parts composing it is challenging. Consequently, the team has used the Ansys Granta MaterialUniverse database to collect all the necessary information about materials and production methods and to perform the detailed LCA analysis. Ansys Granta aims to provide the user with an easy-to-use database of materials properties as well as analysis tools for environmental, production and cost estimations. After obtaining the necessary information on the weight and the materials of all the individual subsystems, the following life cycle inventory was defined:

Table 10.1: Final design inventory table

Subsystem	Elements	Percentage of total [%]	Weight [ton]	Material	Manufacturing process
Truss structure	Structure (x 404 elements)	58.11	2455.00	Medium carbon steel (Aisi1040 normalized)	Welding
	Shafts (x6)	34.51	1458.00	Medium carbon steel	Fine, coarse machining
	Base plate	7.38	312.00	High carbon steel	Rolling
	Total		4225.00		
Rotors	Blades (x108)	73.25	115.00	Low carbon steel	Forming, welding (extrusion)
	Bearings (x42)	26.75	42.00	AISI5046 (low alloy steel)	Fine machining, grinding
	Total		157.00		
Foundation	Monopile		6140.00	S355 (low carbon steel)	Welding, rolling
Wake management	HLD (x4)		1088.00	Medium carbon steel	Forming, welding
Yaw system	Bearings (x2)		100.00	AISI5046 (low alloy steel), silicon nitride	Coarse machining, grinding
Electrical subsystem	Generator (x6)	54.69	84.00	Copper, cast iron, low carbon steel	Assembly components
	Cables	11.72	18.00	Copper	Wire drawing
	Gear box (x6)	15.63	24.00	Low alloy steel/medium carbon steel	Fine machining, grinding OR low pressure die casting
	Converters (x6)	15.63	24.00	Resin, copper, fibre glass	Outsourcing
	Brake (x6)	2.34	3.60	Low alloy steel	Casting
	Total		153.60		
	TOTAL WEIGHT		11863.60		

In addition to showing the number of elements per subsystem, Table 10.1 presents all their respective ma-

terials as well as their manufacturing processes. These last have been described in detail in Section 8.1. For simplicity, only the main elements of the overall design that account for the most environmental impact have been considered. It is important to notice that some structure elements have not been included in this analysis, although their environmental impact is considerable. An example of this is the concrete used to fix the foundation underwater. This choice has been made due to the fact that in the entire design process the sizing of this part of the foundation has never been considered. Taking it into account is one of the Post DSE activities Section 13.1 .

The overall emissions and energy consumption of the following design phases have been considered:

- Extraction of materials
- Production and assembly of components
- Transportation
- Installation
- Operations
- Decommissioning and recycling

10.1.1. Extraction of materials impact

Materials are made from naturally occurring ores or feedstocks. Making them requires energy and releases emissions on a very large scale. The main parameter considered for this section of the LCA is the so-called embodied energy of the material. This is a crucial parameter since it represents the energy required to create 1kg of usable stock. As the MR-TBD is almost entirely steel-made, multiple aspects about this material must be considered to assess the environmental impact of its extraction and processing. Extracting steel often involves large-scale mining operations, which can have an adverse environmental footprint. Its extraction and processing for wind turbine applications require high energy inputs due to high energy-intensive processes like mining and refining. These contribute to greenhouse gas emissions and the consumption of non-renewable energy sources. Supply chains for wind turbines are also very complex, leading to high transportation emissions. For this project, the material extraction and processing accounts for almost 70% of the overall emissions. Specifically, the energy consumed amounts to 68.5% of the overall energy consumed, while the CO_2 footprint account for 69.4%. Consequently, the total energy consumed for this phase of the MR-TBD's life cycle is 120 TJ. On the other hand, the t of CO_2 generated are 9600. This is a very reasonable result, also considering the amount of materials the MR-TBD will need to produce. A more detailed table of this life cycle phase is shown in Appendix A.

10.1.2. Production and assembly of components impact

The manufacturing of the MR-TBD is also a critical stage of its life cycle. This phase, in fact, can be considered the second most polluting aspect of the design, accounting for 25% of the overall emissions. The variable characterising it is the processing energy, the total energy used to shape, join and finish 1kg of material to create a component or product. The overall CO_2 emissions and energy consumption of this life cycle phase are caused by multiple things and are highly dependent on the material and manufacturing process. Manufacturing wind turbine components requires a significant amount of energy, mainly sourced from power plants. These rely on fossil fuels and emit greenhouse gases and other pollutants during electricity generation. Secondly, manufacturing processes involved in producing the MR-TBD, such as steel fabrication, casting, forging, machining, and assembly, generate a considerable amount of CO_2 . In addition to this, especially for some specific material processing, chemicals may be used. Inadequate handling, storage, or disposal of these chemicals can lead to environmental pollution, including soil and water contamination. For this phase of the LCA, the material processes considered in Section 8.1 are considered. As can be seen in Appendix B in Table B.2, some manufacturing processes slightly differ from the ones considered in Section 8.1. This is due to the fact that a few processes data were not present in the Ansys database. To fix this, similar manufacturing processes, both in terms of emissions and final products, have been selected for the LCA. In light of this, the emissions related to this life cycle phase are presented: 48 TJ

of energy consumed and 3600 t of CO_2 .

10.1.3. Transportation impact

For transportation, the environmental impact has been assessed according to the logistics plan presented in Section 8.3. The impact on the environment of this design phase mainly comes from the routes that the MR-TBD elements need to follow before finalising the construction at the wind farm site. It is important to note that the transportation related to raw materials extraction and processing is not considered. Instead, they are considered in the extraction of materials subsection. Specifically, the ecological impact of two main routes have been evaluated. Assuming that all the steel needed to build the structure is already in the Netherlands, it will need to be transported from the different steel companies to the Damen Verolme drydock in Rotterdam. These companies are a few and spread over the Netherlands. Consequently, an indicative route of 113km by train is considered due to the small size of the country and the efficient transportation network. The second transportation route consists of moving the assembled structure from the drydock to the Ijmuiden Ver site. This will be performed by medium size coastal freights that will tug the entire structure for 115 km. This being said, the overall transportation ecological impact results to be extremely small compared to the other phases (0.5%). This is mainly due to the fact that the entire structure will be manufactured in the Netherlands and will use accessible materials. The energy consumed for transportation is 828 GJ, while the CO_2 footprint is 59.6 t.

10.1.4. Operations impact

The impact of wind turbine operations is mainly related to maintenance. During most of its life, the MR-TBD will not produce a lot of emissions. Most of them come from the transportation of crew members and repairing materials. Since the complete maintenance strategy has not yet been defined at this stage of the design process, assumptions were made regarding the most likely route. As a consequence, an average of 5 visits per year per 25 years has been assumed to assess the environmental impact of this design phase. This number is based on the results obtained in the RAMS Section 8.2. The vehicles used to maintain the structure are small-size coastal freights operating at maximum power. The route's starting point is assumed to be 65km far from the wind turbine site, which is the average distance of the turbine from the coast. In light of this, 130km routes need to be followed to perform maintenance 5 times a year per 25 years. This being said the operation phase of the MR-TBD turbine accounts for less than 1% of the overall emissions for both energy consumed and CO_2 emissions. Therefore, this contribution to the system's ecological impact can be neglected.

10.1.5. Decommissioning and recycling impact

The last two phases of the life cycle of the MR-TBD wind turbine to be assessed consist of decommissioning and recycling. The decommissioning and recycling phases of the MR-TBD turbine involve its removal from the site location at the end of its operational life and the subsequent recycling or disposal of its components. Due to the fact that the time to decommission a wind turbine is pretty low, compared to the installation one, this phase of the design will have an almost negligible impact on the overall emissions of the turbine itself. This, in fact, contributes to 4.25% of the total environmental impact. On the other hand, the recycling aspect of the turbine life cycle cannot be ignored. This is, in fact, one of the most important aspects that designers need to consider in order to have a final product being as sustainable as possible. Being mostly made of different types of steel, the recyclability potential of the turbine is pretty high. The main reason is that there is a strong and consistent demand for recycled steel in various industries. The market for it is well-established and economically viable and could represent an additional source of income for the project. Based on the percentage of steel reused, it is possible to reduce the overall impact of the wind turbine up to 10/15%. For the MR-TBD turbine, the percentage of recycled material has been chosen to be 90%. This leads to the following result: a reduction of -27 TJ of energy and -2000 t of CO_2 emissions reduction to the overall project's environmental impact. This is an incredible result since it corresponds to a reduction of 15% of the consumed energy and CO_2 emissions for recycling 90% of the entire

structure

10.1.6. Summary of the results

In light of all these results obtained previously, Figure 10.1, Table 10.2, Figure 10.2, and Figure 10.3 presents a summary of the overall environmental impact of the turbine:

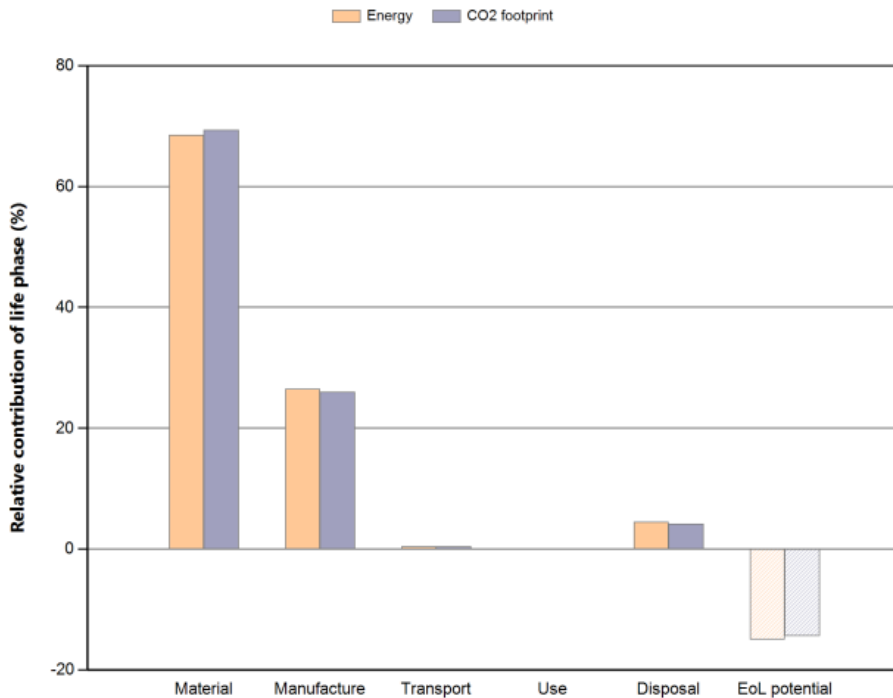


Figure 10.1: Summary of the contributions of each life cycle phase to the overall environmental impact

Table 10.2: Summary table of the contributions of each life cycle phase to the overall environmental impact

Phase	Energy [{}]	Energy [%]	CO2 mass [{}]	CO2 mass [%]
Material	1.20E+08	68.5	9.64E+06	69.4
Manufacture	4.82E+07	26.5	3.61E+06	26.0
Transport	8.28E+05	0.5	5.69E+04	0.4
Use	7.91E+04	0.0	5.70E+03	0.0
Disposal	8.21E+06	4.5	5.75E+05	4.1
Total (for first life)	1.82E+08	100.0	1.39E+07	100.0
End of life potential	-2.72E+07		-1.99E+06	

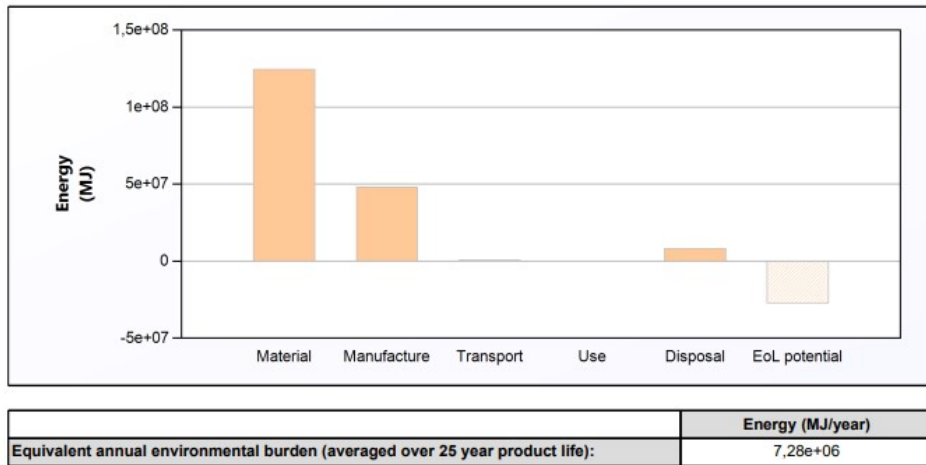


Figure 10.2: Summary of energy consumption of each life cycle phase of the design

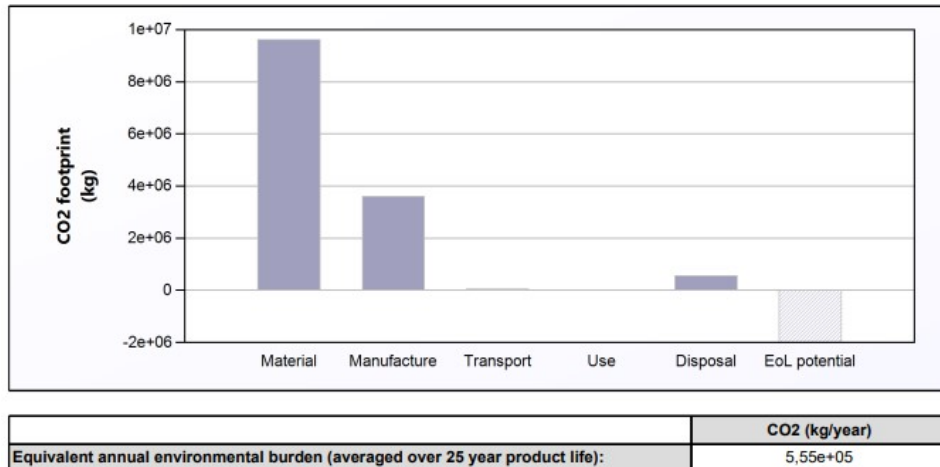


Figure 10.3: Summary of CO₂ of each life cycle phase of the design

All the numbers that are presented in this chapter come from multiple estimations. The most important one is that the concrete needed to set up the foundations has been neglected. In addition, the routes of the materials and components are also an estimation approximated by Ansys Granta. Finally, smaller complex elements of the structure, such as sensors, PCBs, lubricants, non-steel metals, have been neglected too to simplify the study. This introduces uncertainties that can only be evaluated, increasing the level of detail of the study. Being a design synthesis, the scope of this LCA section is not to give precise values, but give the reader an idea of the ecological impact of the project, compared to conventional wind turbines. Based on the results found in Section 8.3 about the annual energy production of the MR-TBD, the total amount of grams of CO₂ per kwh produced by the turbine is 3.73. There are currently several LCA studies in existence which analyse offshore wind turbines ecological impacts. [Raadal et al., Wang and Sun](#) tried to evaluate the potential for wind energy to mitigate the effects of climate change by reducing CO₂ [64, 65]. They did this performing a comparison between different types of wind turbines, both onshore and offshore. What it is possible to get from this, is that the MR-TBD wind turbine results to be the least polluting one due to its very accessible materials and improved life cycle performance. In detail, the MR-TBD results to be 37% less polluting than conventional offshore wind turbines in terms of CO₂.

10.2. Economic

Economic sustainability refers to the strategy and practices of a business to prioritise long-term economic development over short-term profits. The management of resources, labour protection and safety, encouragement of investments in renewable energy, growth of micro-, small- and medium-sized enterprises, and eliminating waste are all key concepts relating to economic sustainability. As sustainability is a core concept of the proposed system, the engineering team has been making several design choices in order to appeal to the economic sustainability targets established by the UN. By doing so, a number of decisive actions have been formulated to encompass the used economic sustainability strategy:

Restrict the use of REM: A majority of rare Earth metals used in drivetrains in current wind turbine designs are mined in China, with 70% market share of all REM in 2022 according to the U.S. Geological Survey ¹. With rising political and ideological apathy between the western world and China, it is important to consider the origin of all resources through the lens of possible embargos. Moreover, as the trade restriction imposed by the UE and the US towards Russia, it is becoming apparent that allocation of resources can become at least a deterrent, or at most an economical weapon. In this spirit, the proposed design has focused on eliminating REM and moving towards locally and readily available materials such as copper and steel alloys. Through this strategy, it is believed that the proposed design can contribute to investment and energy safety.

Promote effective use of natural resources: Perhaps the most used and the most essential natural resource in the wind energy department is the wind itself. Yet, current wind farms output, on average, between 35% and 45% capacity factors for the last decade, according to Statista ². The proposed design was evaluated to have a capacity factor of 56.7%, as given by the total energy production calculated in Section 8.3 and divided by the annual rated energy production. With the implementation of the wake control subsystem, the capacity factor will not decrease with the size of the wind park. Moreover, by improving on the power density of conventional wind turbines, the proposed design can utilise prime offshore parcels rated for low LCOE more efficiently and effectively. Thus, the energy needs of the country could be met through more sustainable and ecological means without having the negative impact of restricting sea space now allocated for other economic uses.

Minimize waste: All structural materials have been chosen so that they can be recycled upwards to 90% percent. Additionally, the rotor blades, which are conventionally made out of fiberglass composites and are difficult if not impossible to recycle, have been manufactured out of structural steel. This was possible through the innovation in the rotor concept of using the vertical axis configuration coupled together with low rotor RPM operations. Yet, not only material waste was considered, but also time waste during energy production. Through design decisions concerning the drivetrain, rotor and tower, the accessibility, maintainability and repairability were improved when compared to a conventional WT. Moreover, the capability to replace important assemblies, such as gearboxes, and make repairs onshore without having prolonged downtime further minimises wasted time, and in turn, wasted energy

Promote affordable and cheap energy: Investing in the green energy sector through novel and high performing designs improves the detachment from conventional GHG emissive energy sources. Through the development of this system the engineering team is facilitating the dutch governmental plan of expanding wind energy production in the North Sea to 380 GW by 2030. This will assure that electricity is not subjected to high volatility caused by external or malicious factors, such as how the price of oil driven by the invasion of Ukraine by Russia caused an increased in spot price of up to 1000% ³.

¹ URL: <https://pubs.usgs.gov/periodicals/mcs2023/mcs2023-rare-earths.pdf> [cited on 20 June 2023]

² URL: <https://www.statista.com/statistics/1368679/global-offshore-wind-capacity-factor/#:~:text=Between%202010%20and%202021%2C%20the,wind%20stood%20at%2039%20percent.> [cited on 20 June]

³ URL: <https://www.statista.com/statistics/1314549/netherlands-monthly-wholesale-electricity-price/> [cited on 20 June 2023]

Moreover, as the wind is a free resource, the design towards long life and high maintainability will reduce the cost of electricity, leading to more affordable energy to the consumer.

10.3. Social

Social sustainability concerns the management of the impact imposed by businesses on people, communities and society in large. The cornerstone of social sustainability is covered by the first six UN Global Compact principles and focuses on labour rights and equity, protecting the future generations from avoidable concerns, help and empower communities at risk and promote human rights. The proposed design has been engineered with social sustainability in mind from its inception, as a good relationship with stakeholders can increase the social acceptance of large-scale projects such as this one, facilitating development in the process. In this sense, the further social sustainability aspects were considered:

Improving labour safety: Forbes estimated that in 2011 wind turbines contributed to 163 accidents leading to 14 deaths in England alone ⁴. The engineering team was aware of the great health hazard imposed by maintenance procedures and made an objective to create better and safer work conditions for repairs crew. Firstly, all electrical and mechanical drivetrain components have been moved to a much lower height compared to traditional wind turbines to avoid accident risks. Furthermore, these components, which usually have amongst the highest failure rates and down times, have been placed on a spacious platform in order to avoid cramped working conditions. Lastly, multiple sensors and a pre-emptive maintenance strategy was employed in order to minimise the number of visits to the turbine altogether.

Avoiding REM: As mentioned in the previous section, a majority of rare Earth metals come from China. This increasing demand in RRM has sparked a multitude of illegal, toxic and unsafe mining sites all around the resource rich regions of China. The Yale School of the Environment has conducted an investigation into the illegal RRM mining operations in southern Jiangxi and reported on the great environmental impact on the hillside of the region ⁵. The two main mining methods include the use of harmful chemicals and acids, and the removing of layers of topsoil, both having a destructive and long-term effect on the region. By not using RRM in the design, the MR-TBD team takes a stance against these practices and acknowledges the vicious cycle of a green future dependant on the hazardous mining of natural resources.

Improving equity in OEM distribution: In the current wind energy market only a handful of business are able to manufacture large off-shore wind turbines, such as GE, Gamesa, and Vestas. By employing ordinary available materials and common manufacturing practices, the MR-TBD team encourages small to medium OEMs to tackle the production of wind turbines parts and assemblies. It is believed that through a bigger manufacturing pool the smaller and local business can thrive and compete against the established manufacturers, leading to more prosperity and innovation.

Protect fisheries and fishermen: The MR-TBD design was specifically conceived in order to yield a higher energy density compared to traditional HAWTs. Through this, the team takes affirmative action to protect the North Sea fishing grounds and the people dependent on them from the ever expanding plans of installation of wind energy. By having higher energy density systems, it is possible to obtain more electricity without infringing on fishing and protected grounds, maintaining the health of the natural habitats that reside in the North Sea and protecting the livelihood of the people who depend on them.

⁴ URL <https://www.forbes.com/sites/jamesconca/2013/09/29/forget-eagle-deaths-wind-turbines-kill-humans/?sh=252f59215467> [cited on 20 June 2023]

⁵ URL: <https://e360.yale.edu/features/china-wrestles-with-the-toxic-aftermath-of-rare-earth-mining> [cited on 20 June 2023]

Technical Risk Assessment

In this chapter, the technical risk assessment of the project mission is performed. This consists of identifying the technical risks that affect the success of the project mission. The risks are quantified according to their perceived probability of occurrence and seriousness of impact. Next, a mitigation plan is devised for the risks that pose the highest impact on the project mission to bring them down to an acceptable level, including contingency for the risks that remain at a high level.

11.1. Risk Identification

Risk categorisation

To identify the technical risks affecting the designed system, risk categories were first identified to break down the aspects of the project where risks might arise. This is broken down into:

Technical performance risks These affect the system during operation, causing it to perform to a lower performance level than required. These risks can be broken down for each subsystem at this design stage.

Cost risks These are risks that can increase the project's costs beyond the allocated cost budget.

Scheduling risks These are risks that can cause a delay in the scheduling of the project mission. This includes the system's design, production, transportation, operation, and decommissioning.

Sustainability risks Since sustainability is a driving factor in the design of this mission, risks related to not meeting the sustainability goals of the system or inadvertently becoming unsustainable are included in this category.

Programmatic risks These are risks that result from events out of the control of the project management. This can include events arising from higher management or international or national directives. This can also include natural disasters and other events that pose a risk to the mission's success.

The likelihood of the risks is categorised into: very unlikely with a chance of occurrence less than five percent (<5%), unlikely (<25%), plausible (<50%), likely (<95%) and very likely (>95%). Furthermore, the consequences were divided into negligible, marginal, critical and catastrophic implications for the project. Negligible risks incur no reductions in technical performance; marginal risks incur a slight reduction in technical performance; critical risks reduce technical performance significantly to a point where system success is questionable; catastrophic risks cause some of the mission requirements not to be achieved, leading to mission failure ¹.

A few subsystem risks were added from literature. [Hou et al.](#) discuss several risks related to the monopile subsystem [66]. During installation, these include pile sliding due to soil properties, hammer refusal if the monopile is allowed to set while installing, and damage due to crane accidents. The operational risks include scouring and corrosion due to the sea environment, fatigue failure and collisions with ships [66]. For the generators and gearbox, [Shafiee and Dinmohammadi](#) present a fault tree diagram that outlines the standard failure modes, including wear of gearbox teeth, over-warming and abnormal vibrations [67]. Additionally, a fault tree diagram describes a few potential modes of failure for rotor blades [67]. Thermal cycling has been described to cause 55% of converter failures, followed by vibration-induced failures at 20% by [Sepulveda et al.](#), considering that the power converter shows high failure rates [68].

In the final stage of design, each subsystem's weaknesses presented risks that became more clear while getting further into the design and some previous risks were no longer considered as it became clear that they would not present a threat to the project. For example, as shown in Figure 11.1, the WCT faced some

¹URL: <https://brightspace.tudelft.nl/d2l/le/content/498709/viewContent/2937470/View> [cited 19 June 2023]

risks of retraction during higher wind speeds, as it generates much more forces on a structure in these conditions. The YCT subsystem showed to be unstable during wind speeds higher than the rated wind speed, this also posed a risk that was only discovered during the final design.

Some risks are present under two different subsystems. For example, the YCT and RTR subsystems have bearings and the same risks under different codes. This is because despite the risks being the same, yaw-bearing risks present more considerable consequences as only one yaw-bearing system supports the whole structure. In contrast, the rotor bearings only support the rotor, making their failure consequence less critical. Due to dividing the risk into multiple smaller subsystems, the rotor and drivetrain subsystems present mostly marginal risks as they only heavily affected the performance of only one rotor assembly. Taking all the above into account, the identified technical risks of the project are laid out in Figure 11.1.

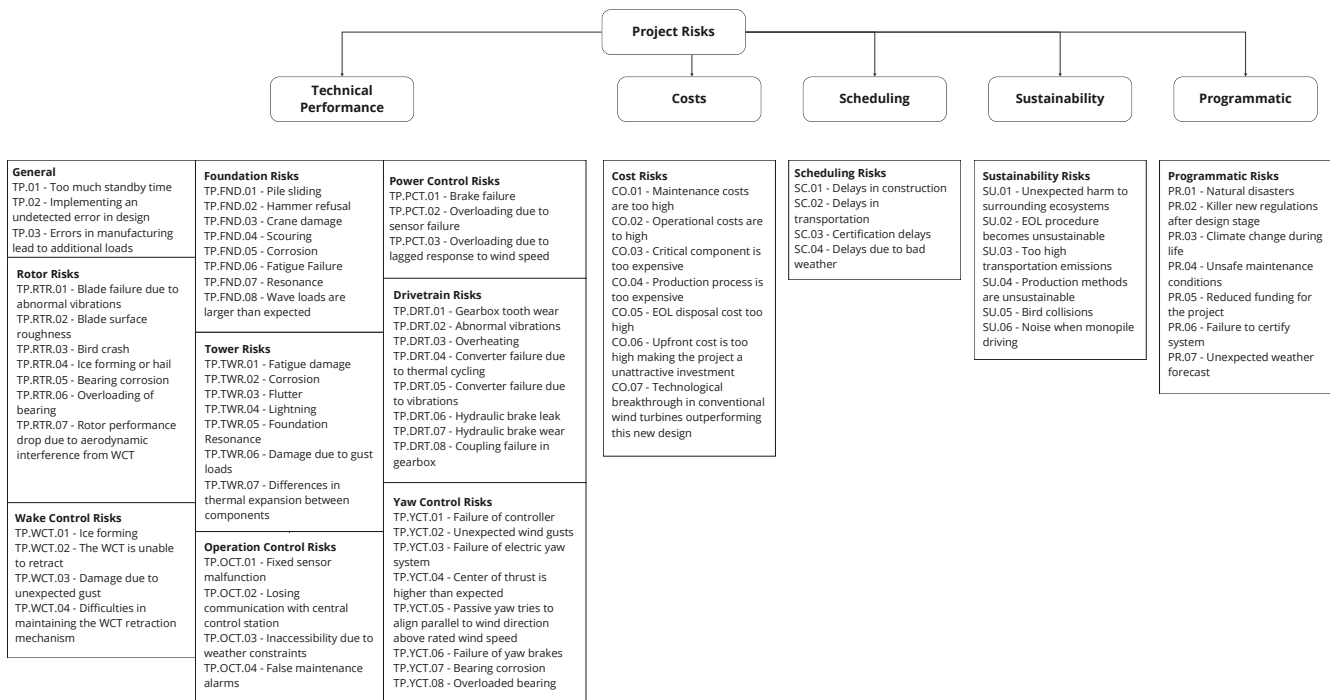


Figure 11.1: Project Risks

For each of these risks, the likelihood and consequence are predicted and added to the risk matrix in Figure 11.2. Risks that have been mitigated are highlighted in bold.

11.2. Risk Management

In this section risk mitigation measures are determined for the risks with the highest combination of likelihood and consequence (risks in the top right corner of Figure 11.2).

Table 11.1: Reasoning and mitigation for highest risks

Risk	Reasoning	Mitigation
TPTWR.05 - The truss structure resonates with the rotor frequency	Structural members may be damaged due to resonance with the rotor frequency.	A more detailed natural frequency analysis should be performed. If natural frequencies are still close to the rotor frequency, dampeners can be installed in the mounting brackets of the shaft bearings.
TPTWR.07 - Differences in thermal expansion between components	Can cause high additional stresses in structural members leading to buckling, especially in interfaces between different materials.	Thermal expansion should be modelled, and the design should be modified to withstand these loads.
SU.01 - Unexpected harm to surrounding ecosystems	The wind farm may have a serious impact on the surrounding ecosystems. This would have catastrophic consequences leading to mission failure since institutions will never allow the building of the farm.	Study site ecology. Avoid fragile areas. Minimise system size. Minimise noise emissions
PR.04 - Unsafe maintenance conditions	Maintenance is a crucial element of a wind turbine design. It is a critical risk therefore to not have safe maintenance procedures.	Apply a strict safety procedure for operators. Design for facilitated maintenance. Automate maintenance as much as possible. Minimise maintenance
PR.07 - Unexpected weather forecast	Unexpected weather conditions might lead to the structure having to withstand higher wind speeds than it is ready for or not standby on time.	Implement emergency procedures to prevent damage. Design for unexpected weather conditions.
SU.05 - Bird collisions	Bird populations can be reduced by wind turbine collisions. This is a big risk on the sustainability of the project.	Minimise size of wind turbine for power produced. Include sensors/deterrents for bird migrations. Turn off turbine if bird migrations are detected.
TPTWR.02 - Corrosion	Corrosion of the tower structure is very likely to occur due to high salinity in offshore conditions. This can negatively affect the material properties of the tower.	Use corrosion resistant coating. Monitor corrosion of vulnerable components.
TPYCT.07 - Bearing corrosion	Corrosion of bearings is very likely to occur due to high salinity in offshore conditions. A corroded bearing has lower load capabilities and is more likely to fail. Since the yaw bearing holds the whole tower, this is a critical risk.	Use corrosion resistant materials or paints. Monitor corrosion of vulnerable components.
TPYCT.08 - Overloading of bearing	Overloading the bearing can lead to bearing failure, which not only leads to failure of the YCT but also reduces the bearing capability of withstanding tower loads, leading possibly to catastrophic failure	Oversize the yaw bearing. Add supporting elements to support bearing

TPOCT.03 - Inaccessibility due to weather constraints	During extreme weather conditions accessing the turbine might be impossible, this is often the time where unscheduled maintenance is most likely to be needed, so a lot of damage can occur due to this risk	Add automatic shutdown algorithms to turbine. Increase health monitoring cameras/sensors to reduce need for manual inspections.
TP.TWR.04 - Lightning	Lightning is certain to strike the tower during its lifetime. Lightning can cause damage to material and electrical components of the turbine and is the leading cause of unplanned downtime in wind turbines, leading to a much higher maintenance cost [69].	Include wind turbine grounding system. Construct blades with conductive material to avoid lightning arcs. Add surge protectors to electrical systems [69].
SU.04 - Production methods are unsustainable	Production methods will always have at least a small amount of emissions produced. Therefore production methods will never be 100% green. As a consequence this it is very likely to be present but at the same time marginal.	Optimise logistics. Use manufacturing methods that minimise waste. Employ lean production. Recycle waste
SU.06 - Noise when monopile driving	Monopile driving emits large amounts of noise, capable of killing marine life in the vicinity [70]. Since the monopile used is large, the noise level will be even greater and have a devastating effect on the sustainability of the project.	Use bubble curtains while monopile driving. Pile driving with vibratory hammers [70].
TP.RTR.04, TP.WCT.01 - Ice forming or hail	Ice forming is almost certain due to the cold of the north sea, it can negatively affect the aerodynamics of the rotor and WCT and cause damage.	employ de-icing systems.
TP.DRT.04 - Converter failure due to thermal cycling	This is a likely failure mode for converters due to the different expansion coefficients of different materials in the converter [68].	Model thermal cycling and predict failure date for scheduled maintenance [68].
TP.YCT.05 - Passive yaw aligns the structure with wind direction above rated windspeed	Might cause significant acceleration on the system. When the system becomes parallel to windspeed no power can be generated.	Apply brakes when approaching rated windspeed. Control thrusts so that thrust to windspeed gradient is positive and system is stable.
TP.FND.07 - Foundation Resonance	The natural frequencies of the foundation are below the rotor frequency, and in the realm of wave frequencies.	The natural frequency should be further investigated including potential damping from water inside the monopile. If it turns out to be a problem further damping should be installed.

This mitigation leads to the post-mitigation risk matrix as seen in Figure 11.3:

Catastrophic		SU.03 PR.01 PR.02 PR.06 CO.07	SU.01	TP.TWR.05 TP.FND.07	
Critical	CO.03 TP.FND.03	TP.02 CO.02 PR.05 CO.05 TP.FND.01 TP.FND.02 TP.TWR.01 TP.WCT.02 TP.PCT.02 CO.06 TP.YCT.01	TP.01 TP.03 CO.01 SU.02 PR.03 TP.FND.06 TP.FND.08 TP.TWR.03 TP.DRT.03 TP.WCT.07 TP.PCT.07 TP.YCT.08	PR.04 TP.YCT.07 TP.OCT.03 TP.TWR.07 PR.07 TP.YCT.08	TP.TWR.04 SU.06
Marginal		TP.RTR.02 TP.WCT.03 TP.TWR.06 TP.PCT.03	CO.04 TP.DRT.02 TP.DRT.05 TP.OCT.02 TP.OCT.04 TP.RTR.07	SC.01 TP.FND.04 TP.FND.05 TP.RTR.01 TP.RTR.03 TP.RTR.05 TP.DRT.01 TP.WCT.04 TP.DRT.06 TP.DRT.08 SC.03 TP.YCT.04 TP.YCT.01	SU.04 TP.RTR.04 TP.RTR.06 TP.DRT.01 TP.DRT.04 TP.YCT.05
Negligible	SC.04			SC.02 TP.YCT.02	TP.OCT.01 TP.DRT.07

Figure 11.2: Pre mitigation risk matrix

Catastrophic		SU.03 PR.01 PR.02 PR.06 CO.07 TP.PCT.01			
Critical	CO.03 TP.FND.03	TP.02 CO.02 PR.05 CO.05 TP.FND.01 TP.FND.02 TP.TWR.01 TP.WCT.02 TP.PCT.02 CO.06 TP.YCT.01	SU.01 TP.TWR.05 TP.FND.07 CO.03 SU.01 PR.04 TP.FND.06 TP.RTR.06 TP.TWR.03 TP.DRT.03 TP.FND.08 TP.YCT.01	TP.01 TP.03 CO.01 SU.02 PR.03 TP.FND.06 TP.RTR.06 TP.TWR.03 TP.DRT.03 TP.FND.08 TP.YCT.01	
Marginal		TP.RTR.02 TP.WCT.03 TP.TWR.06 TP.PCT.03	CO.04 TP.DRT.02 TP.DRT.05 TP.OCT.02 TP.OCT.04 TP.RTR.07	SC.01 TP.FND.04 TP.FND.05 TP.RTR.01 TP.RTR.03 TP.RTR.05 TP.DRT.04 TP.PCT.03 TP.RTR.07	TP.TWR.04
Negligible	SC.04		SC.02 TP.YCT.02	SC.02 TP.YCT.05 TP.DRT.04	TP.OCT.01 TP.DRT.07 SU.06 TP.YCT.05 TP.DRT.04

Figure 11.3: Post mitigation risk matrix

One risk remains in the high-risk region, **TP.TWR.04**. This is the risk due to lightning. It is very difficult to avoid damage due to lightning in the lifetime of the system. Therefore, a contingency plan was devised in the midterm and implemented in the final design in order to limit the damage caused by this risk. To reduce the maintenance cost needed for this, unmanned inspections and health monitoring sensors can be used to monitor damage caused by lightning strikes since there will be a lot of space to mount these sensors in the wind turbine. Furthermore, manned inspections and repairs can be added into planned maintenance visits to reduce the cost of unplanned maintenance. Since lightning has the potential to cause a surge that prevents the turbine from operating, damaged electrical components need to be replaced promptly to reduce costly downtime.

Compliance matrix

This chapter details compliance of individual subsystem with user, mission, functional, and standard requirements. First all subsystems are presented, then the compliance for the entire system is.

12.1. Compliance of the subsystems

This section presents the compliance of the eight separate subsystems which were defined in the baseline report. Only the requirements deemed as most important and indicative of the design were presented for brevity's sake.

12.1.1. Compliance of TWR

Compliance of the tower to the most important requirements defined in the preliminary report is listed in Table 12.1. The value for requirement **MR-30-TWR-01** is not finalized yet, because the use of composites was not even considered during the design process, so it was not used at all. With regard to other subsystems, the tower has the most requirements which could be checked against due to the design having the most detailed models. For this subsystem, most requirements did not need to be changed themselves.

Table 12.1: *Compliance matrix for the tower subsystem*

ID	Requirement	Value	Status
MR-28-TWR-01	The tower height shall not exceed 315 m	Height is 315 m	✓
MR-30-TWR-01	The mass of composites used for the tower shall not exceed <TBD> tonnes	No composites are used	✓
MR-32-TWR-01	The tower shall consist of at least 90% of recyclable metals by mass	Tower is 100 % made of steel	✓
MR-34-TWR-01	The tower shall withstand loads due to maximum wind speed of at least 70 ms^{-1}	Tower is sized to take winds of 70 ms^{-1}	✓
FR-20-TWR-01	The tower shall stay above water	The tower is on the monopile	✓
FR-20-TWR-02	The tower shall transfer all loads to the foundation	The tower transfers all loads to the monopile	✓
FR-27-TWR-01	The tower shall be able to be yawed	The tower is attached to the monopile with a double bearing	✓
SR-01-TWR-01	The tower shall withstand normal wind condition for its installed location	The tower can withstand load case LDC1, which corresponds to its normal operating condition	✓
SR-02-TWR-01	The tower shall withstand extreme wind condition for its installed location, occurring every 50 years	The tower can withstand load case LDC3, which corresponds to that condition	✓
SR-12-TWR-01	The tower shall include safety guards and railing to facilitate maintenance	The tower includes safety guards	✓
SR-16-TWR-01	The tower shall have its platform outside of the splash zone	The platform of the tower is 30 m above the surface of ocean, well out of the splash zone	✓

12.1.2. Compliance of YCT

Compliance of YCT can be presented in Table 12.2. The requirement **MR-28-YCT-01** was updated when analysis in Figure 8.3 was performed. The control system components themselves were designed mostly on conceptual level, so the requirements presented refer to the functions and operations of the system, rather than the specific implementations.

Table 12.2: *Compliance matrix for the yaw control subsystem*

ID	Requirement	Value	Status
MR-08-YCT-01	YCT shall allow to lock the turbine's yaw and prevent it from turning	YCT has a break and emergency break, both of which prevent the structure from turning	✓
MR-28-YCT-01	The yaw control subsystem shall be able to yaw at a rate of $0.2 \text{ }^{\circ} \text{s}^{-1}$ during normal operating conditions	The yaw control subsystem can yaw at a rate of $1 \text{ }^{\circ} \text{s}^{-1}$ during normal operation conditions	✓
SR-12-YCT-01	The yaw control subsystem shall be accessible to inspection and/or maintenance	The yaw control subsystem is designed to be accessible to inspection and maintenance	✓

12.1.3. Compliance of PCT

Table 12.3 shows compliance of the power control system. Requirement **MR-33-PCT-01** was updated based on the rated wind speed and **MR-28-PCT-01** was updated based on preliminary design presented in the midterm report.

Table 12.3: *Compliance matrix for the power control subsystem*

ID	Requirement	Value	Status
MR-07-PCT-01	The PCT shall allow predictive (condition-based) maintenance	PCT is designed to include sensors, which in combination with DT technology allow for condition-based maintenance strategy	✓
MR-08-PCT-01	The PCT shall be maintained without total operation halt	The modular design allows for maintenance of PCT with only two turbines needing to shut down at once	✓
MR-13-PCT-01	The PCT shall have an energy production density of at least 16 MWkm^{-2}	Energy density of PCT is close to 20 MWkm^{-2}	✓
MR-28-PCT-01	PCT shall not exceed the height of 315 m	PCT reaches until 312 m high	✓
MR-30-PCT-01	PCT shall use less than <TBD> % of total mass as composites	PCT does not use composites	✓
MR-33-PCT-01	PCT shall operate with rated wind speed of 11.2 ms^{-1}	PCT has a rated wind speed of 11.2 ms^{-1}	✓
FR-10-PCT-01	The system shall be able to adjust the amount of power it produces	The system is stall regulated, in combination with a shaft break and variable loading generator	✓
FR-13-PCT-01	The normal operation of the PCT shall be possible at the platform level	PCT can be operated at platform level	✓

12.1.4. Compliance of DRT

For the compliance of DRT, presented in Table 12.4, most of the requirements presented focus on maintainability and option to replace it. This is because one of the key parts of the design is modularity and redundancy.

Table 12.4: *Compliance matrix for the power control subsystem*

ID	Requirement	Value	Status
MR-02-DRT-01	The drivetrain shall be produced from common easily sourced metals, limited to non-rare earth metals	drivetrain uses DFIG, which needs no rare earth metals	✓
MR-05-DRT-01	The drive train shall be replaceable	The drive train can be replaced due to modular design	✓
MR-07-DRT-01	The shaft shall be maintainable by predictive maintenance	The shaft incorporates sensors which facilitate predictive maintenance	✓
MR-07-DRT-02	The gearbox shall be maintainable by predictive maintenance	The gearbox incorporates sensors which facilitate predictive maintenance	✓
MR-07-DRT-03	The generators shall be maintainable by predictive maintenance	The generators incorporate sensors which facilitate predictive maintenance	✓
MR-07-DRT-04	The bearings shall be maintainable by predictive maintenance	The bearings incorporate sensors which facilitate predictive maintenance	✓
MR-23-DRT-01	The drive train technology shall be lab tested	Brushless DFIGs have been tested in labs[4]	✓

12.1.5. Compliance of WCT

Wake control system requirements presented are few because the design of the WCT was done mostly on its effects and not much was done for the analysis of the structure and mechanisms. As such, the requirements presented are the few ones which refer to things considered so far. Requirement **MR-38-WCT-01** was changed from wetted area to circulation, since that was a more relevant quantity at this stage of design.

Table 12.5: *Compliance matrix for the wake control subsystem*

ID	Requirement	Value	Status
MR-38-WCT-01	The wake control system shall have circulation of $330 \text{ m}^2 \text{s}^{-1}$ at rated wind speed	The wake control system has the circulation of $330 \text{ m}^2 \text{s}^{-1}$ at rated wind speed	✓
SR-01-WCT-01	The wake control system shall successfully transfer aerodynamic loads during normal wind conditions to the tower subsystem	WCT transfers all loads to tower structure at all times	✓
SR-03-WCT-01	The wake control subsystem shall successfully transfer aerodynamic loads during extreme wind conditions to the tower substructure	WCT transfers all loads to tower structure at all times	✓

12.1.6. Compliance of OCT

Operations control system compliance matrix Table 12.6 presents requirements related to sensors which the system has to facilitate maintenance. Since other things related to it were not given much consideration at this stage of the design, they were not discussed.

Table 12.6: *Compliance matrix for the wake control subsystem*

ID	Requirement	Value	Status
MR-07-OCT-01	The operation control subsystem shall monitor the vibration of the tower subsystem	The operation control subsystem has sensors to monitor the vibration of the tower subsystem	✓
MR-07-OCT-02	The operation control subsystem shall monitor the vibration of the drive train subsystem	The operation control subsystem has sensors to monitor the vibration of the drive train subsystem	✓
MR-07-OCT-03	The operation control subsystem shall monitor the vibration of the rotor subsystem	The operation control subsystem has sensors to monitor the vibration of the rotor subsystem	✓
MR-07-OCT-04	The operation control subsystem shall monitor the strains of the tower subsystem	The operation control subsystem has sensors to monitor the strains of the tower subsystem	✓
MR-07-OCT-05	The operation control subsystem shall monitor the strains of the drive train subsystem	The operation control subsystem has sensors to monitor the strains of the drive train subsystem	✓
MR-07-OCT-06	The operation control subsystem shall monitor the strains of the rotor subsystem	The operation control subsystem has sensors to monitor the strains of the rotor subsystem	✓
FR-18-OCT-01	The OCT shall be able to alert the maintenance department if a failure occurs	The OCT is designed to be able to request maintenance if a failure occurs	✓

12.1.7. Compliance of RTR

Since RTR and DRT share many requirements, only three were presented in Table 12.7. These focus on operations and logistics of the rotor itself.

Table 12.7: *Compliance matrix for the rotor subsystem*

ID	Requirement	Value	Status
MR-02-RTR-01	The rotor shall be produced from common, easily sourced materials, limited to metals	The rotors are made of steel	✓
MR-05-RTR-01	The rotor shall be replaceable	Rotors and blades can both be replaced separately from the shaft sections	✓
SR-19-RTR-01	The rotor shall be able to stop and be parked	The rotor is designed to be able to stop and be parked	✓

12.1.8. Compliance of FND

Last subsystem compliance matrix Table 12.8, which shows the compliance of the foundation subsystem focuses on its operation and production. These were deemed most indicative of what the focus for the design was, which makes it unique.

Table 12.8: Compliance matrix for the foundation subsystem

ID	Requirement	Value	Status
MR-02-FND-01	The foundation shall be produced from common, easily sourced metals, limited to metals and concrete	The monopile is made of marine steel and ocean floor part is encased in concrete	✓
MR-23-FND-01	The foundation technology used shall be lab tested	The monopile technology is in use commonly	✓
FR-21-FND-01	The foundation shall keep all other subsystems above water	Monopile is sized to keep the rest of the turbine above water for load cases LDC1, LDC2, and LDC3	✓
FR-22-FND-01	The foundation shall support a mass of 6628 t	The foundation shall support a mass of 6628 t and environmental loads	✓
SR-20-FND-02	The foundation shall be protected against corrosion	The foundation uses coating and sacrificial plating to prevent corrosion	✓

12.2. System compliance matrix

After subsystem compliance matrices, the overall system compliance matrix is shown in Table 12.9. This is the most important compliance matrix contained in the section. It contains the most important requirements. With requirement **UR-02**, which was deemed the most important of the all user requirements, the system is able to meet the needed value and exceeds it by almost 25 %. This is a good margin which allows for a nice safety margin. On the other hand, the second most important of the user requirements **UR-03** was not satisfied. The system can not achieve the full 45 % required for the LCoE. Based on the cost model used in this report and the midterm, this value can not be achieved by the system.

Another important user requirement **UR-06** is satisfied. This one addresses the sustainability of the system, which aim at limiting its environmental impact. At the same time, the system is also more space efficient, since it provides much higher energy density, at 20 MWkm^{-2} . Combined with **MR-01**, this makes the system sustainable from both the environmental and social perspective.

Requirements **MR-07**, **MR-37**, **FR-21**, **SR-03**, and **SR-19** were shown to highlight the operational aspects of the entire system. These show the main capabilities which were given most consideration during these stages of the design. The last requirement **MR-29** was included in order to show that the system is economically feasible.

Table 12.9: Compliance matrix for the system

ID	Requirement	Value	Status
UR-01	The system shall have a power rating of at least 30 MW	The system has power rating of 31.3 MW, as stated in Chapter 7	✓
UR-02	The system shall have an energy density of at least 16 MWkm^{-2}	The system has an energy density close to 20 MWkm^{-2}	✓
UR-03	The system shall have a 45 % lower levelised cost of energy compared to traditional HAWT	System has 29.6 % reduced LCoE compared to traditional HAWT Section 2.1	✗
UR-04	The system shall have multiple rotors	System has 36 rotors	✓
UR-05	The system shall have lower lifetime emissions than traditional horizontal axis offshore wind turbines offshore wind turbines	Based on LCA, the lifetime emissions are 37 % less polluting Section 10.1	✓
UR-06	The system shall have increased material recyclability than traditional horizontal axis wind turbines	90 % of the structure will be recycled directly as per Subsection 10.1.5	✓
UR-07	The system shall have decreased rare metal use compared to traditional HAWT	System does not use rare earth metals	✓
UR-08	The system shall be installable offshore	the system can be installed offshore	✓
MR-01	The system shall be able to be produced by small Original Equipment Manufacturer(s)	System does need highly complex or specialised components, allowing them all to be produced by small OEM(s)	✓
MR-07	The system shall allow predictive (condition-based) maintenance	System has sensors which allow for use of DT system to implement conditions-based maintenance	✓
MR-29	The system shall be profitable without the intervention of governmental subsidies	Based on return-on-investment analysis, the system is profitable, with return on investment of between 6.7 and 8.7 %, as per Section 9.2	✓
MR-37	The system shall be able to align to a specified direction	The system has YCT, which allows it to align in any direction	✓
FR-21	The system shall stay above water	The system is on a monopile foundation, which keeps it above the ocean surface	✓
SR-03	The system shall withstand the extreme wind conditions, occurring every 50 years for its installation location	The system is sized to withstand LDC3, which corresponds to worst wind condition in 50 years	✓
SR-19	The system shall allow for parking of the wind turbine	System can park all its rotors and stop operating	✓

Future development

This section includes the future development stages for the MR-TBD project, starting from the end of the DSE design stage to the end of the life of the wind farm. Section 13.1 shows the future tasks and Section 13.2 includes a Gantt chart for the tasks to be done.

13.1. Project design and development logic

Figure 13.1 Includes both a flow chart and a breakdown of tasks to be completed after the DSE stage is finished. Blocks that are parallel or staggered in the flow diagram, are performed at the same time.

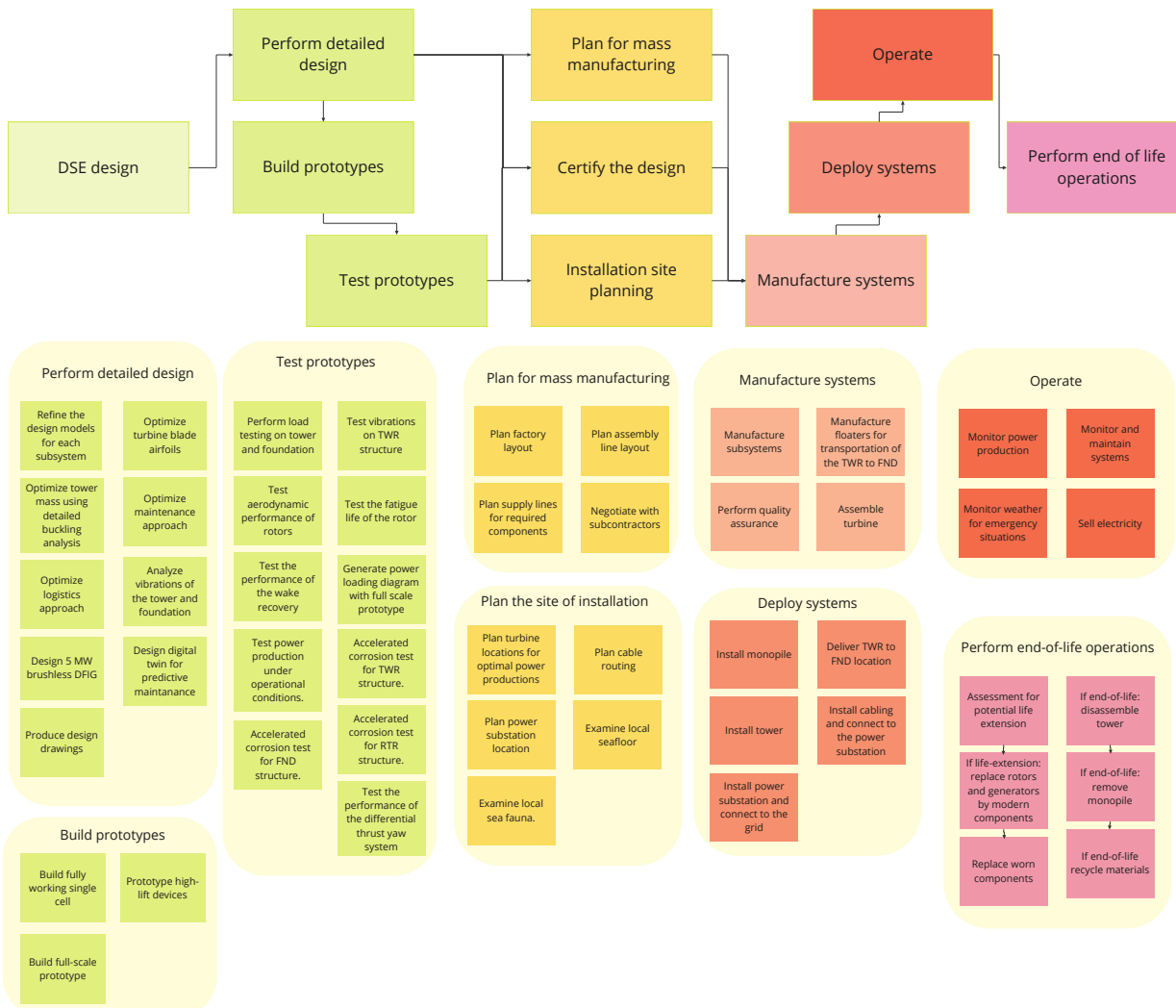
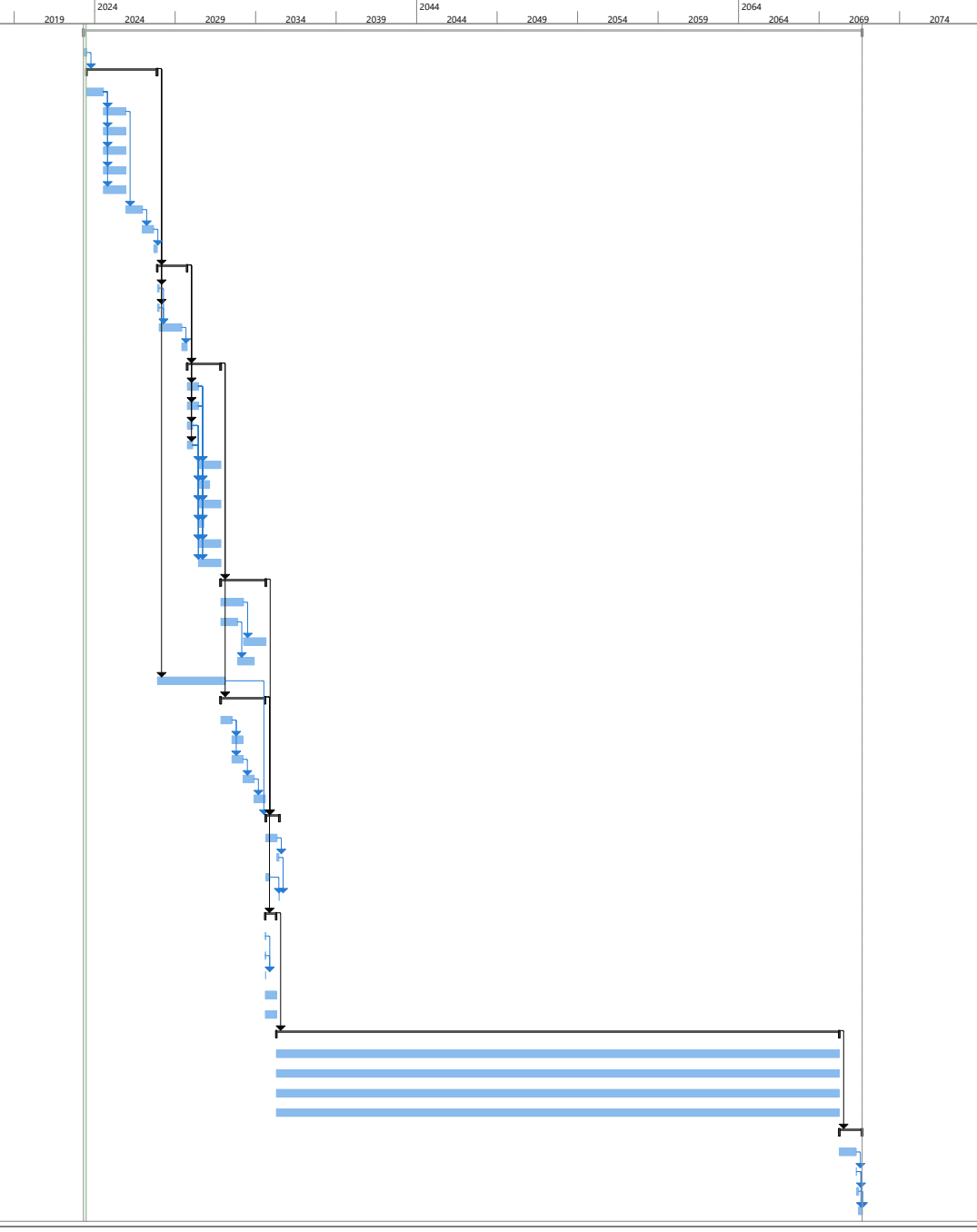


Figure 13.1: An overview of activities to be performed post-DSE

13.2. Future design Gantt chart

ID	Unique ID	Task Mode	Task Name	Duration	Start	Finish	Predecessors
0	0	MR-TBD		12620 days	Mon 4/24/23	Fri 9/4/71	
1	227	DSE design		50 days	Mon 4/24/23	Fri 5/30/23	
2	228	Perform detailed design		1145 days	Mon 7/3/23	Fri 11/19/27	1
3	229	Refine the design models for each subsystem		270 days	Mon 7/3/23	Fri 1/12/24	
4	230	Optimize tower mass using detailed buckling analysis		365 days	Mon 7/15/24	Fri 12/5/25	3
5	231	Optimize logistics approach		365 days	Mon 7/15/24	Fri 12/5/25	3
6	232	Optimize turbine blade airfoils		365 days	Mon 7/15/24	Fri 12/5/25	3
7	233	Design 5 MW brushless DFIG		365 days	Mon 7/15/24	Fri 12/5/25	3
8	234	Optimize Optimise maintenance approach		365 days	Mon 7/15/24	Fri 12/5/25	3
9	235	Analyse vibrations of the tower and foundation		270 days	Mon 12/8/25	Fri 12/18/26	4
10	236	Design digital twin for predictive maintenance		180 days	Mon 12/21/26	Fri 8/27/27	9
11	237	Produce design drawings		60 days	Mon 8/30/27	Fri 11/19/27	10
12	238	Build prototypes		485 days	Mon 11/22/27	Fri 9/28/29	2
13	239	Build fully working single cell		30 days	Mon 11/22/27	Fri 12/31/27	2
14	240	Prototype high-lift devices		30 days	Mon 11/22/27	Fri 12/31/27	2
15	241	Build full-scale prototype		365 days	Mon 1/3/28	Fri 5/29/29	13,14
16	242	Validate the wake recovery		90 days	Mon 5/28/29	Fri 9/28/29	15
17	243	Test prototypes		545 days	Mon 10/1/29	Fri 10/31/31	12
18	244	Perform load testing on tower and foundation		180 days	Mon 10/1/29	Fri 6/7/30	12
19	245	Test aerodynamic performance of rotors		180 days	Mon 10/1/29	Fri 6/7/30	12
20	246	Test the performance of the wake recovery		90 days	Mon 10/1/29	Fri 2/1/30	12
21	247	Test power production under operational conditions		90 days	Mon 10/1/29	Fri 2/1/30	12
22	248	Accelerated corrosion test for FND		365 days	Mon 6/10/30	Fri 10/31/31	18,19,20,21
23	249	Test vibrations on TWR structure		180 days	Mon 6/10/30	Fri 1/14/31	18,19,20,21
24	250	Test the fatigue life of the rotor		365 days	Mon 6/10/30	Fri 10/31/31	18,19,20,21
25	251	Generate power loading diagram		90 days	Mon 6/10/30	Fri 10/11/30	18,19,20,21
26	252	Accelerated corrosion test for TWR		365 days	Mon 6/10/30	Fri 10/31/31	18,19,20,21
27	253	Accelerated corrosion test for RTR		365 days	Mon 6/10/30	Fri 10/31/31	18,19,20,21
28	254	Plan for mass manufacturing		730 days	Mon 11/3/31	Fri 8/18/34	17
29	255	Plan factory		365 days	Mon 11/3/31	Fri 3/25/33	
30	256	Plan supply lines for required components		270 days	Mon 11/3/31	Fri 11/12/32	
31	257	Plan assembly line layout		365 days	Mon 3/28/33	Fri 8/18/34	29
32	258	Negotiate with subcontractors		270 days	Mon 11/15/32	Fri 11/25/33	30
33	259	Certify the design		1100 days	Mon 11/22/27	Fri 2/6/32	2
34	260	Installation site planning		720 days	Mon 11/3/31	Fri 8/4/34	17
35	261	Plan turbine locations for optimal power location		180 days	Mon 11/3/31	Fri 7/9/32	
36	262	Examine local sea fauna		180 days	Mon 7/12/32	Fri 3/18/33	35
37	263	Examine local seafloor		180 days	Mon 7/12/32	Fri 3/18/33	35
38	264	Plan cable routing		180 days	Mon 3/21/33	Fri 11/25/33	37
39	265	Plan power substation location		180 days	Mon 11/28/33	Fri 8/4/34	38
40	266	Manufacture systems		220 days	Mon 8/21/34	Fri 6/22/35	33,28,34
41	267	Manufacture subsystems		180 days	Mon 8/21/34	Fri 4/27/35	
42	268	Perform quality assurance		30 days	Mon 4/30/35	Fri 6/8/35	41
43	269	Manufacture floaters for transportation of the TWR to FND		60 days	Mon 8/21/34	Fri 11/10/34	
44	270	Assemble turbine		10 days	Mon 6/11/35	Fri 6/22/35	42,43
45	271	Deploy systems		180 days	Mon 8/7/34	Fri 4/13/35	34
46	272	Install monopile		2 days	Mon 8/7/34	Tue 8/8/34	
47	273	Deliver TWR to FND location		1 day	Mon 8/7/34	Mon 8/7/34	
48	274	Install tower		5 days	Wed 8/9/34	Tue 8/15/34	46,47
49	275	Install power substation and connect to the grid		180 days	Mon 8/7/34	Fri 4/13/35	
50	276	Install cabling and connect to the power substation		180 days	Mon 8/7/34	Fri 4/13/35	
51	277	Operate		9125 days	Mon 4/16/35	Fri 4/4/70	45
52	278	Monitor power production		9125 days	Mon 4/16/35	Fri 4/4/70	
53	279	Monitor weather for emergency situations		9125 days	Mon 4/16/35	Fri 4/4/70	
54	280	Monitor and maintain systems		9125 days	Mon 4/16/35	Fri 4/4/70	
55	281	Sell electricity		9125 days	Mon 4/16/35	Fri 4/4/70	
56	282	Perform end-of-life operations		370 days	Mon 4/7/70	Fri 9/4/71	51
57	283	Assessment for potential life extension and potential repowering		270 days	Mon 4/7/70	Fri 4/17/71	
58	284	Disassemble tower		10 days	Mon 4/20/71	Fri 5/1/71	57
59	285	Remove monopile		30 days	Mon 5/4/71	Fri 6/12/71	58
60	286	Recycle materials		60 days	Mon 6/15/71	Fri 9/4/71	59,58



Project: MR-TBD
Date: Wed 6/21/23



Conclusion

The main objective of the project was to design a multi-rotor VAWT system that has increased power density, is more democratically producible, has better material and emission sustainability, and decreases the cost of energy compared to conventional wind turbines. The Ijmuiden Ver wind farm zone was selected as a reference location to design the system.

The system was designed to the user requirements shown below:

- UR-01:** The system shall have a power rating of at least 30 MW
- UR-02:** The system shall have a power density of at least 16 MWkm^{-2}
- UR-03:** The system shall have a 45 % lower levelized cost of energy compared to traditional horizontal axis offshore wind turbines
- UR-04:** The system shall have multiple rotors
- UR-05:** The system shall have lower lifetime emissions than traditional horizontal axis offshore wind turbines
- UR-06:** The system shall have increased material recyclability than traditional horizontal axis wind turbines
- UR-07:** The system shall have decreased rare metal use compared to traditional horizontal axis wind turbine
- UR-08:** The system shall be installable offshore

The final design is a large truss structure consisting of repeating cubical cells. Inside each cell is a vertical-axis turbine with a triple H-blade rotor. Six rotors are vertically connected to a single shaft, which is connected to the front of the structure. Each shaft is connected to a gearbox with a doubly fed induction generator (DFIG) and a partial converter. The yaw system alters the rotational speed of rotors to generate differential thrust in order to yaw. An electrical yaw system is used as a backup. To increase the power density, The system uses a high lift device (HLD) to recover the wake domain. The critical parameters of the design and resulting masses of components are shown in Table 14.1 and Table 14.2 below.

As shown in Table 14.1, the rated power is 31.3 MW, and the power density is 20 MWkm^{-2} , so **UR-01** and **UR-02** are satisfied. In addition, the turbine was designed as an offshore multi-rotor system, so **UR-04** and **UR-08** are also satisfied. The system uses DFIGs, which do not use rare-earth metals. This means **UR-07** is also satisfied.

To investigate **UR-03**, a cost analysis was performed. After analysis of the current predictions for the wind turbine market, it has been established that MR-TBD is significantly cheaper than current turbines on the market. Using a cost analysis based on modifying the cost for a reference 10 MW wind turbine, it was calculated that the LCoE should drop by 30%. This does not satisfy user requirements, which were to drop the LCoE by 45%, but it is still an attractive investment opportunity. The design also showed a 30% shorter time to break even and profitability at doubled the weighted average cost of capital. The largest cost reductions were obtained on the cost of the generators, gearboxes, and rotors, and the cost of maintenance.

To make the system more sustainable, metal rotors are used instead of composite ones. This accounts for the major majority of non-recyclable components in regular wind turbines. This satisfies **UR-06**.

To investigate the emissions for **UR-05**, a life cycle analysis was performed. The analysis aims to evaluate the environmental impact (energy consumed and CO_2 emissions of the turbine's design throughout its entire life cycle. The analysis considers various phases, including material extraction, manufacturing, transportation, operations, decommissioning, and recycling. The MaterialUniverse database of Ansys Granta

Table 14.1: Key parameters for the MR-TBD design

Parameter	Unit	Value
Power rating	MW	31.3
Power density	MWkm ⁻²	20
Turbine class	—	IEC class I
Control		Variable speed
Cut-in wind speed	m/s	3
Rated wind speed	m/s	11.2
Cut-out wind speed	m/s	25
Design TSR	—	4.5
Rotor diameter	m	46.7
Rotor height	m	45
Airfoil series	—	DU17DBD25
Number of rotors	—	36
Number of shafts	—	6
Turbine height	m	310
Turbine width	m	290
Cell dimensions	m	46.67 X 46.67 X 33.6
truss thickness ratio	-	0.01
Drivetrain	—	Geared
Gearbox	—	Angular & Planetary
Generator	—	Brushless DFIG
Wake control	—	Adjustable HLD
Wing chord	m	20
Wing span	m	280

Table 14.2: Weights of all sized subsystems

Element	Mass [tn]
Rotor	1717
Main shaft	260 X6
Blades	3.2 X6
Bearings	1 X42
Tower	2767
Truss	2455
Bedplate	52 X6
Yaw control	100
Bearings	54
Drivetrain	46
Wake control	648
Wing	81 X4
HLD	81 X4
Drivetrain	150
Gearbox	4 X6
Break	0.6 X6
Generator	16 X6
Converter	4 X6
Miscellaneous	0.4 X6
Monopile	6200
Total	11582

and the EcoAudit function was used to obtain the necessary data for assessing the impact of each phase. The results indicate that the life cycle phases account for 68.5%, 26.5%, 0.5%, 0.00%, and 4% of the overall emissions of the project (energy consumed and CO₂ footprint), respectively. After evaluating the individual phases, the estimated energy consumption is 7.28 TJ per annum and the CO₂ emissions amount to 555 t per annum. Comparing this to conventional wind turbines, the MR-TBD turbine is found to be 37% less polluting. This means that the final user requirement **UR-05** is also satisfied.

Recommendations

A few aspects of the structural design should be further considered. More detailed vibration analysis is required for both the tower and foundation. Based on the results of this, vibration damping of the shafts and waves should be considered and further researched. In addition to this, the weight of the truss structure may be further reduced by making the elements thinner. To do so safely, a more detailed sheet buckling analysis should be performed. Truss or cable components similar to suspension bridges may be added. It should be investigated whether it would result in cost savings. Another aspect of the structural design that requires further attention is thermal expansion. Part of the structure is in the water, which could lead to a thermal gradient in the structure, inducing forces in the members due to shrinking and expansion.

As the design allows relatively easy switching of generators and rotors, fatigue life analysis should be made.

The potential to extend the service life of the structure cell indefinitely and change out the generators and rotors to save on costs and increase sustainability. Rotor cycle life should also be investigated as an individual airfoil on a rotor experiences many cycles with a large difference between minimums and maximums.

Another critical thing to consider would be the integration of the HLD into the structure, as it has the potential to improve the performance of the design, if its effects on the rotors can be minimized. There is also potential to use it to assist with yawing of the structure using differential drag. Another interesting area for future analysis would be examining the effects of how HLDs of several turbines interact with each other since it is expected that they would aid wake recovery with their upwash. A detailed CFD analysis using actuator cylinder theory can be done to better understand interference between two turbines since previous work shows this increases the pressure coefficient. Also, scaled models or industry-level software can be utilized to inspect wind farm behavior since the model used assumes potential flow with only effects from circulations due to HLDs.

Lastly, for the yaw control with differential thrust, a simple on-off controller was used, which resulted in a fast correction rate. However, it was not investigated whether this was the most power-efficient method of yawing. Investigation of other types of control, such as partial power control for each rotor or the use of a PID (proportional integral derivative) controller, is recommended to optimize the system's reaction to wind direction changes. Furthermore, the yaw control of the system should be subjected to a simulation of the usual wind direction behavior in the region to determine the average power loss due to yaw response time.

Bibliography

- [1] Freeman, K., Frost, C., Hundleby, G., Roberts, A., Valpy, B., Holttinen, H., Ramírez, L., and Pineda, I., “Our energy, our future. How offshore wind will help Europe go carbon-neutral.” , 2019.
- [2] Pleshivtsev, V. G., Filippov, G. A., Pak, Y. A., and Livanova, O. V., “EFFECT OF CARBON CONTENT AND STRESSED STATE ON THE CORROSION RATE OF PIPE STEEL IN HEATING SYSTEMS,” *Metallurgist*, Vol. 53, 2009, pp. 62–64.
- [3] Jamieson, P., Ferreira, C. S., Dalhoff, P., Störtenbecker, S., Collu, M., Salo, E., McMillan, D., McMorland, J., Morgan, L., and Buck, A., “Development of a multi rotor floating offshore system based on vertical axis wind turbines,” *Journal of Physics: Conference Series*, Vol. 2257, No. 1, 2022. doi:[10.1088/1742-6596/2257/1/012002](https://doi.org/10.1088/1742-6596/2257/1/012002).
- [4] Abdi, E., McMahon, R., Malliband, P., Shao, S., Mathekga, M. E., Tavner, P., Abdi, S., Oraee, A., Long, T., and Tatlow, M., “Performance analysis and testing of a 250 kW medium-speed brushless doubly-fed induction generator,” *IET Renewable Power Generation*, Vol. 7, No. 6, 2013, pp. 631–638. doi:<https://doi.org/10.1049/iet-rpg.2012.0234>.
- [5] Carroll, J., McDonald, A., and McMillan, D., “Failure rate, repair time and unscheduled O&M cost analysis of offshore wind turbines,” *Wind Energy*, Vol. 19, No. 6, 2016, pp. 1107–1119. doi:<https://doi.org/10.1002/we.1887>.
- [6] Carroll, J., McDonald, A., Dinwoodie, I., McMillan, D., Revie, M., and Lazakis, I., “Availability, operation and maintenance costs of offshore wind turbines with different drive train configurations,” *Wind Energy*, Vol. 20, No. 2, 2017, pp. 361–378. doi:<https://doi.org/10.1002/we.2011>.
- [7] Distelbrink, L., Fetecau, M., Gonzalez, L., Jemioł, B., Rizk, M. K., Peralta Tapia, M., Porcescu, I., Pudāns, J., Roth, J., and Tuğtekin, M., “60MW Multi-Rotor Vertical Axis Wind Turbine Baseline techreport,” , 2023.
- [8] Distelbrink, L., Fetecau, M., Gonzalez, L., Jemioł, B., Rizk, M. K., Peralta Tapia, M., Porcescu, I., Pudāns, J., Roth, J., and Tuğtekin, M., “60MW Multi-Rotor Vertical Axis Wind Turbine Midterm techreport,” , 2023.
- [9] “Guide to an offshore wind farm,” , January 2019.
- [10] Cox, K., and Echtermeyer, A., “Structural Design and Analysis of a 10MW Wind Turbine Blade,” *Energy Procedia*, Vol. 24, 2012, pp. 194–201. doi:<https://doi.org/10.1016/j.egypro.2012.06.101>, selected papers from Deep Sea Offshore Wind R&D Conference, Trondheim, Norway, 19-20 January 2012.
- [11] Bayati, I., Belloli, M., Bernini, L., Mikkelsen, R., and Zasso, A., “On the aero-elastic design of the DTU 10MW wind turbine blade for the LIFES50+ wind tunnel scale model,” *Journal of Physics: Conference Series*, Vol. 753, No. 2, 2016, p. 022028. doi:[10.1088/1742-6596/753/2/022028](https://doi.org/10.1088/1742-6596/753/2/022028).
- [12] Tüfekci, M., Genel, E., Tatar, A., and Tüfekci, E., “Dynamic Analysis of Composite Wind Turbine Blades as Beams: An Analytical and Numerical Study,” *Vibration*, Vol. 4, No. 1, 2021, pp. 1–15. doi:[10.3390/vibration4010001](https://doi.org/10.3390/vibration4010001).
- [13] Macquart, T., Kucukbahar, D., and Prinsen, B., “Dutch Offshore Wind Market techreport 2023,” , April 2023.
- [14] Witha, B., Hahmann, A., Sile, T., Dörenkämper, M., Ezber, Y., García-Bustamante, E., González-Rouco, J. F., Leroy, G., and Navarro, J., “WRF model sensitivity studies and specifications for the NEWA mesoscale wind atlas production runs,” Tech. rep., NEWA, May 2019. doi:[10.5281/zenodo.2682604](https://doi.org/10.5281/zenodo.2682604).
- [15] Coelingh, J., van Wijk, A., and Holtslag, A., “Analysis of wind speed observations over the North Sea,” *Journal of Wind Engineering and Industrial Aerodynamics*, Vol. 61, No. 1, 1996, pp. 51–69. doi:[https://doi.org/10.1016/0167-6105\(96\)00043-8](https://doi.org/10.1016/0167-6105(96)00043-8).
- [16] Coelingh, J., van Wijk, A., and Holtslag, A., “Analysis of wind speed observations over the North Sea,” *Journal of Wind Engineering and Industrial Aerodynamics*, Vol. 61, No. 1, 1996, pp. 51–69. doi:[https://doi.org/10.1016/0167-6105\(96\)00043-8](https://doi.org/10.1016/0167-6105(96)00043-8).

- [17] Hasager, C. B., Barthelmie, R. J., Christiansen, M. B., Nielsen, M., and Pryor, S. C., "Quantifying offshore wind resources from satellite wind maps: study area the North Sea," *Wind Energy*, Vol. 9, No. 1-2, 2006, pp. 63–74. doi:<https://doi.org/10.1002/we.190>.
- [18] Pryor, S., and Barthelmie, R., "Climate change impacts on wind energy: A review," *Renewable and Sustainable Energy Reviews*, Vol. 14, No. 1, 2010, pp. 430–437. doi:<https://doi.org/10.1016/j.rser.2009.07.028>.
- [19] Siegismund, F., and Schrum, C., "Decadal changes in the wind forcing over the North Sea," , October 2018.
- [20] Fischer, T., De Vries, W. E., and Schmidt, B., "Upwind design basis (WP4: Offshore foundations and support structures)," Tech. rep., TU Delft, 2010.
- [21] Ottermo, F., Eriksson, S., and Bernhoff, H., "Parking strategies for vertical axis wind turbines," *ISRN Renewable Energy*, Vol. 2012, 2012, p. 1–5. doi:<10.5402/2012/904269>.
- [22] Vire, A., "Fundamentals of Wind Energy I - Lecture 2," , 2023.
- [23] K.W Hermans, J. W. P., "Future XL monopile foundation design for a 10 MW wind turbine in deep water," Tech. Rep. ECN-E-16-069, Energieonderzoek Centrum Nederland, Den Haag, NL, Dec 2016.
- [24] E.C.M. Ruijgrok, B. B., E.J. van Druten, "Cost Evaluation of North Sea Offshore Wind Post 2030," Tech. rep., North Sea Wind Power Hub Consortium, 2019.
- [25] B.H. Bulder, E. B., and Bedon, G., "Optimal wind farm power density analysis for future offshore wind farms," *ECN*, 2018.
- [26] Stehly, T., and Duffy, P., "Cost of Wind Energy Review," *NREL Transforming energy*, 2022.
- [27] Ferreira, C. S., "60 MW VAWT MultiRotor Wind Energy System," , 2023.
- [28] Çetin, N., Yurdusev, M., Ata, R., and Özdamar, A., "ASSESSMENT OF OPTIMUM TIP SPEED RATIO OF WIND TURBINES," *Mathematical and Computational Applications*, Vol. 10, No. 1, 2005, pp. 147–154.
- [29] Kallehave, D., Byrne, B. W., LeBlanc Thilsted, C., and Mikkelsen, K. K., "Optimization of monopiles for offshore wind turbines," *Philosophical Transactions of the Royal Society A: Mathematical, Physical and Engineering Sciences*, Vol. 373, No. 2035, 2015, p. 20140100. doi:<10.1098/rsta.2014.0100>.
- [30] Sánchez, S., López-Gutiérrez, J.-S., Negro, V., and Esteban, M. D., "Foundations in Offshore Wind Farms: Evolution, Characteristics and Range of Use. Analysis of Main Dimensional Parameters in Monopile Foundations," *Journal of Marine science and Engineering*, 2019. doi:<10.3390/jmse7120441>.
- [31] Negro, V., López-Gutiérrez, J.-S., Esteban, M. D., Alberdi, P., Imaz, M., and Serraclará, J.-M., "Monopiles in offshore wind: Preliminary estimate of main dimensions," *Ocean Engineering*, Vol. 133, 2017, pp. 253–261. doi:<doi.org/10.1016/j.oceaneng.2017.02.011>.
- [32] Carroll, J., McDonald, A., Dinwoodie, I., McMillan, D., Revie, M., and Lazakis, I., "Availability, operation and maintenance costs of offshore wind turbines with different drive train configurations," *Wind Energy*, Vol. 20, No. 2, 2016, p. 361–378. doi:<10.1002/we.2011>.
- [33] Li, C., Mogollón, J. M., Tukker, A., Dong, J., von Terzi, D., Zhang, C., and Steubing, B., "Future material requirements for global sustainable offshore wind energy development," *Renewable and Sustainable Energy Reviews*, Vol. 164, 2022. doi:<10.1016/j.rser.2022.112603>.
- [34] Pavel, C. C., Lacal-Arántegui, R., Marmier, A., Schüler, D., Tzimas, E., Buchert, M., Jenseit, W., and Blagoeva, D., "Substitution strategies for reducing the use of rare earths in wind turbines," *Resources Policy*, Vol. 52, 2017, pp. 349–357. doi:<10.1016/j.resourpol.2017.04.010>.
- [35] Balaram, V., "Rare Earth Element Deposits: Sources, and Exploration Strategies," *Journal of the Geological Society of India*, Vol. 98, 2022, pp. 1210–1216. doi:<10.1007/s12594-022-2154-3>.
- [36] Kharade, V., and Jagtap, K., "A Review Study on Vertical axis Wind Turbines (lift and drag type) for Optimizing the Aerodynamic and Structural Performance," *Recent Developments in Mechanical En-*

- gineering, 2019, pp. 61–65.
- [37] Castellani, F., Astolfi, D., Peppoloni, M., Natili, F., Buttà, D., and Hirschl, A., “Experimental Vibration Analysis of a Small Scale Vertical Wind Energy System for Residential Use,” *Machines*, Vol. 7, No. 2, 2019. doi:[10.3390/machines7020035](https://doi.org/10.3390/machines7020035).
- [38] Battisti, L., Brighenti, A., Benini, E., and Castelli, M. R., “Analysis of Different Blade Architectures on small VAWT Performance,” *Journal of Physics*, Vol. 753, No. 6, 2016. doi:[10.1088/1742-6596/753/6/062009](https://doi.org/10.1088/1742-6596/753/6/062009).
- [39] International Electrotechnical Commission, “IEC 61400-1: Wind turbine generator systems Part 1: Design requirements,” Tech. rep., IEC, 2005. IEC 61400-1:2005(E).
- [40] Gaertner, E., Rinker, J., Sethuraman, L., Zahle, F., Anderson, B., Barter, G., Abbas, N., Meng, F., Bortolotti, P., Skrzypinski, W., Scott, G., Feil, R., Bredmose, H., Dykes, K., Shields, M., Allen, C., and Viselli, A., “Definition of the IEA Wind 15-Megawatt Offshore Reference Wind Turbine,” Tech. rep., NREL, 2020. NREL/TP-5000-75698.
- [41] Bortolli, P., Tarres, H. C., Dykes, K., Merz, K., Sethuraman, L., Verelst, D., and Zahle, F., “Systems Engineering in Wind Energy - WP2.1 Reference Wind Turbines,” Tech. rep., NREL, May 2019.
- [42] Lee, Y.-L., and Barkey, M. E., “Chapter 4 - Stress-Based Uniaxial Fatigue Analysis,” *Metal Fatigue Analysis Handbook*, edited by Y.-L. Lee, M. E. Barkey, and H.-T. Kang, Butterworth-Heinemann, Boston, 2012, pp. 115–160. doi:<https://doi.org/10.1016/B978-0-12-385204-5.00004-5>.
- [43] Li, S., Lamei, A., Wong, C., and Hayatdavoodi, M., “Concept design and analysis of wind-tracing floating offshore wind turbines,” *ASME 2019 2nd International Offshore Wind Technical Conference*, American Society of Mechanical Engineers (ASME), 2019, pp. 1–9. doi:[10.1115/IOWTC2019-7580](https://doi.org/10.1115/IOWTC2019-7580).
- [44] Sethuraman, L., Xing, Y., Gao, Z., Venugopal, V., Mueller, M., and Moan, T., “A 5MW direct-drive generator for floating spar-buoy wind turbine: Development and analysis of a fully coupled Mechanical model,” *Proceedings of the Institution of Mechanical Engineers, Part A: Journal of Power and Energy*, Vol. 228, 2014, pp. 718–741. doi:[10.1177/0957650914537262](https://doi.org/10.1177/0957650914537262).
- [45] de Haan, T., “Buckling monopiles: Stability of a monopile based offshore wind turbine,” Master’s thesis, TU Delft, Delft, NL, Jan 2020.
- [46] Bakhti, R., Benahmed, B., and Laib, A., “Finite Element Investigation of Offshore Wind Turbines Natural Frequency with Monopile Foundations System,” *Journal of Vibration Engineering and Technologies*, 2023. doi:[10.1007/s42417-023-00989-3](https://doi.org/10.1007/s42417-023-00989-3).
- [47] Jalbi, S., Shadlou, M., and Bhattacharya, S., “Chapter 16 - Practical Method to Estimate Foundation Stiffness for Design of Offshore Wind Turbines,” *Wind Energy Engineering*, edited by T. M. Letcher, Academic Press, 2017, pp. 329–352. doi:<https://doi.org/10.1016/B978-0-12-809451-8.00016-3>.
- [48] Schløer, S., Castillo, L. G., Fejerskov, M., Stroescu, E., and Bredmose, H., “A model for Quick Load Analysis for monopile-type offshore wind turbine substructures,” *Journal of Physics: Conference Series*, Vol. 753, No. 9, 2016, p. 092008. doi:[10.1088/1742-6596/753/9/092008](https://doi.org/10.1088/1742-6596/753/9/092008), URL <https://dx.doi.org/10.1088/1742-6596/753/9/092008>.
- [49] Anandavijayan, S., and Brennan, A. M. F., “A numerical analysis of the effects of manufacturing processes on material pre-strain in offshore wind monopiles,” *Procedia Structural Integrity*, Vol. 13, 2018, pp. 953–958. doi:<https://doi.org/10.1016/j.prostr.2018.12.178>.
- [50] Xia, T., Ding, Y., Dong, Y., Chen, Z., Zheng, M., Pan, E., and Xi, L., “Collaborative production and predictive maintenance scheduling for flexible flow shop with stochastic interruptions and monitoring data,” *Journal of Manufacturing Systems*, Vol. 65, 2022, pp. 640–652. doi:<https://doi.org/10.1016/j.jmsy.2022.10.016>.
- [51] Zhong, D., Xia, Z., Zhu, Y., and Duan, J., “Overview of predictive maintenance based on digital twin technology,” *Heliyon*, Vol. 9, No. 4, 2023, p. e14534.

doi:<https://doi.org/10.1016/j.heliyon.2023.e14534>.

- [52] Mwaniki, J., Lin, H., and Dai, Z., "A Condensed Introduction to the Doubly Fed Induction Generator Wind Energy Conversion Systems," *Journal of Engineering (United Kingdom)*, Vol. 2017, 2017. doi:[10.1155/2017/2918281](https://doi.org/10.1155/2017/2918281).
- [53] Abdullah, M., Yatim, A. H., and Tan, C. W., "A study of maximum power point tracking algorithms for wind energy system," *2011 IEEE 1st Conference on Clean Energy and Technology, CET 2011*, 2011. doi:[10.1109/CET.2011.6041484](https://doi.org/10.1109/CET.2011.6041484).
- [54] De Tavernier, D., Ferreira, C., and Goude, A., "Vertical-axis wind turbine aerodynamics," *Handbook of Wind Energy Aerodynamics*, Springer, 2022, pp. 1317–1361.
- [55] T. Harris, C. B., J.H. Rumbarger, "Wind Turbine Design Guideline DG03: Yaw and Pitch Rolling Bearing Life," *Innovation for our energy future*, 2009.
- [56] MacMahon, E. N., Stock, A., Leithead, W., and Jamieson, P., "Yaw control for 20MW offshore multi rotor system," *European Wind Energy Association Annual Event (EWEA 2015)*, 2015.
- [57] Teunis, M., Collier, M. P., Bakker, E. G. R., Didderen, K., Gyimesi, A., and Lengkeek, W., "Ecological impact of decommissioning offshore wind farms Overview of potential impacts and their importance," Tech. rep., Bureau Waardenburg Ecology Landscape, 1 2020.
- [58] Lindqvist, M., and Lundin, J., "Spare Part Logistics and Optimization for Wind Turbines-Methods for Cost-Effective Supply and Storage," , 2010.
- [59] Smith, E. B., "Design of Nacelle for a 10 MW Wind turbine," Tech. rep., NTNU, 2012.
- [60] Wang, S., Nejad, A. R., and Moan, T., "On design, modelling, and analysis of a 10-MW medium-speed drivetrain for offshore wind turbines," *Wind Energy*, Vol. 23, 2020, pp. 1099–1117. doi:[10.1002/we.2476](https://doi.org/10.1002/we.2476).
- [61] Bortolotti, P., Tarres, H. C., K. Dykes, K. M., Sethuraman, L., Verelst, D., and Zahle, F., "IEA Wind Task 37 on Systems Engineering in Wind Energy WP2.1 Reference Wind Turbines," Tech. rep., IEA, May 2019.
- [62] Ozoemena, M., Cheung, W., and Hasan, R., "Comparative LCA of technology improvement opportunities for a 1.5 MW wind turbine in the context of an onshore wind farm," *Clean Technologies and Environmental Policy*, Vol. 20, 2018, p. 173–190. doi:[10.1007/s10098-017-1466-2](https://doi.org/10.1007/s10098-017-1466-2).
- [63] Schleisner, L., "Life cycle assessment of a wind farm and related externalities," *Renewable Energy*, Vol. 20, No. 3, 2000, pp. 279–288. doi:[https://doi.org/10.1016/S0960-1481\(99\)00123-8](https://doi.org/10.1016/S0960-1481(99)00123-8).
- [64] Raadal, H. L., Vold, B. I., Myhr, A., and Nygaard, T. A., "GHG emissions and energy performance of offshore wind power," *Renewable Energy*, Vol. 66, 2014, pp. 314–324. doi:<https://doi.org/10.1016/j.renene.2013.11.075>.
- [65] Wang, Y., and Sun, T., "Life cycle assessment of CO₂ emissions from wind power plants: Methodology and case studies," *Renewable Energy*, Vol. 43, 2012, pp. 30–36. doi:<https://doi.org/10.1016/j.renene.2011.12.017>.
- [66] Hou, G., Xu, K., and Lian, J., "A review on recent risk assessment methodologies of offshore wind turbine foundations," *Ocean Engineering*, Vol. 264, 2022, p. 112469. doi:<https://doi.org/10.1016/j.oceaneng.2022.112469>.
- [67] Shafiee, M., and Dinmohammadi, F., "An FMEA-based risk assessment approach for wind turbine systems: a comparative study of onshore and offshore," *Energies*, Vol. 7, No. 2, 2014, pp. 619–642. doi:<https://doi.org/10.3390/en7020619>.
- [68] Sepulveda, M., Davies, P., Spring, M., Shek, J., Thies, P., and Oterkus, E., "Risk assessment of an offshore wind turbine and remaining useful life estimation of the power converter. Improving availability by prioritising failures with higher risk to operation," *Open Research Exeter*, 2016.
- [69] Glushakow, B., "Effective lightning protection for wind turbine generators," *IEEE Transactions on En-*

ergy Conversion, Vol. 22, No. 1, 2007, pp. 214–222. doi:doi.org/10.1109/TEC.2006.889622.

- [70] Saleem, Z., “Alternatives and modifications of Monopile foundation or its installation technique for noise mitigation,” Tech. rep., Technical University of Delft, 2011.

A

Vibration analysis

In this section, several tables and figures have been used in order to calculate the natural frequency of the system combining the foundation of the wind turbine and soil. Soil characteristics have been computed based on its profile, flexibility and stiffness coefficients.

Table A.1: Formulas for stiffness of monopiles exhibiting rigid behavior [47]

Ground Profile (See Fig. 16.4)	K_L	K_{LR}	K_R
Homogeneous	$3.2 \left(\frac{L}{D_p} \right)^{0.62} f_{(vs)} E_{SO} D_p$	$-1.8 \left(\frac{L}{D_p} \right)^{1.56} f_{(vs)} E_{SO} D_p^2$	$1.65 \left(\frac{L}{D_p} \right)^{2.5} f_{(vs)} E_{SO} D_p^3$
Parabolic	$2.65 \left(\frac{L}{D_p} \right)^{1.07} f_{(vs)} E_{SO} D_p$	$-1.8 \left(\frac{L}{D_p} \right)^2 f_{(vs)} E_{SO} D_p^2$	$1.63 \left(\frac{L}{D_p} \right)^3 f_{(vs)} E_{SO} D_p^3$
Linear	$2.35 \left(\frac{L}{D_p} \right)^{1.53} f_{(vs)} E_{SO} D_p$	$-1.8 \left(\frac{L}{D_p} \right)^{2.5} f_{(vs)} E_{SO} D_p^2$	$1.59 \left(\frac{L}{D_p} \right)^{3.45} f_{(vs)} E_{SO} D_p^3$

* $f_{(vs)} = 1 + 0.6|v_s - 0.25|$

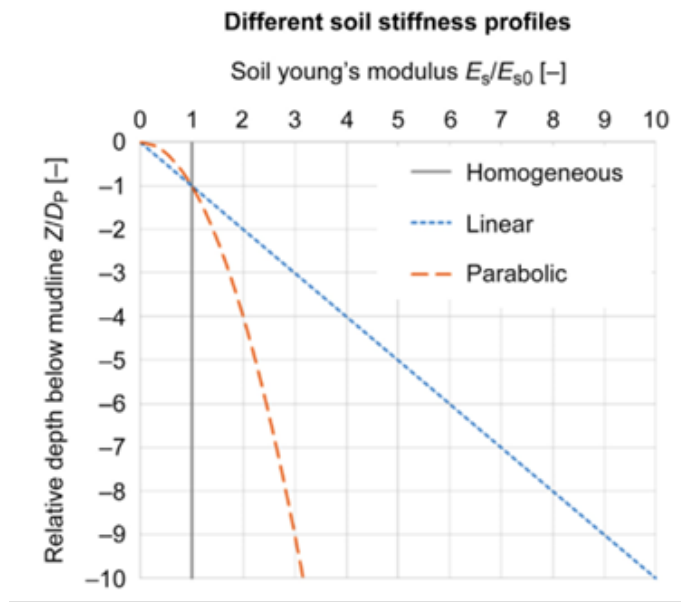


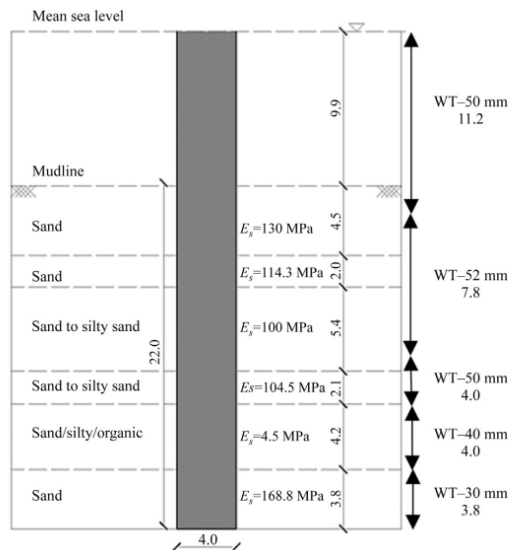
Figure A.1: Homogeneous, linear, and parabolic soil stiffness profiles [47]

Table A.2: The wind speeds(W) and H_S for normal weather scenario [48]

W (m/s)	P_{rel} (-)	I (-)	H_S (m)	T_p (s)
4.16	0.11	0.29	1.10	5.88
6.23	0.14	0.23	1.18	5.76
8.31	0.16	0.20	1.31	5.67
10.39	0.15	0.18	1.48	5.74
12.47	0.13	0.17	1.70	5.88
14.55	0.11	0.16	1.91	6.07
16.62	0.08	0.15	2.19	6.37
18.70	0.05	0.15	2.47	6.71
20.78	0.03	0.14	2.76	6.99
22.56	0.02	0.14	3.09	7.40
24.94	0.01	0.14	3.42	7.80

Table A.3: The wind speeds(W) and H_S for extreme weather conditions [48]

W (m/s)	I (-)	H_S (m)	$T_{p,min}$ (s)	$T_{p,max}$ (s)	T_p for $f_1 = 1/T_p$ (s)	T_p for $f_1 = 2/T_p$ (s)
4.16	0.82	5.88	4	11	+	+
6.23	0.90	5.76	4	11.5	+	+
8.31	1.05	5.67	4	11.5	+	+
10.39	1.23	5.74	4	11.	+	+
12.47	1.46	5.88	5	9	-	-
14.55	1.72	6.07	5	8	-	-
16.62	2.07	6.37	5	9	-	-
18.70	2.38	6.71	5	10	-	+
20.78	2.80	6.90	5	8	-	-
22.56	3.13	7.40	7	9	-	-
24.94	3.58	7.80	7	10	-	+

**Figure A.2:** Young Modulus of the soil depending on the depth [47]

LCA detailed results

Table B.1: Material extraction detailed analysis

Component	Material	Recycled content* (%)	Part mass (kg)	Qty.	Total mass (kg)	Energy (MJ)	CO2 footprint (kg)
Structure	Medium carbon steel	90,0%	6e+03	404	2,4e+06	2,6e+07	2e+06
Shafts	Medium carbon steel	90,0%	2,4e+05	6	1,5e+06	1,6e+07	1,2e+06
Base plate	High carbon steel	90,0%	3,1e+05	1	3,1e+05	3,4e+06	2,6e+05
Blades	Low carbon steel	90,0%	1,1e+03	108	1,1e+05	1,2e+06	9,3e+04
Bearings	Low alloy steel	90,0%	1e+03	42	4,2e+04	4,7e+05	3,5e+04
Monopile	Low carbon steel	90,0%	6,1e+06	1	6,1e+06	6,4e+07	4,9e+06
HLD	Medium carbon steel	90,0%	2,7e+05	4	1,1e+06	1,2e+07	9,1e+05
Bearings	Low alloy steel	90,0%	5e+04	2	1e+05	1,1e+06	8,3e+04
Cables	Copper	90,0%	1,8e+04	1	1,8e+04	3,2e+05	2,4e+04
Gearbox	Medium carbon steel	90,0%	4e+03	6	2,4e+04	2,6e+05	2e+04
Brakes	Low alloy steel	90,0%	6e+02	6	3,6e+03	4e+04	3e+03
Total				581	1,2e+07	1,2e+08	9,6e+06

Table B.2: Manufacturing process detailed analysis

Component	Process	Amount processed	Energy (MJ)	CO2 footprint (kg)
Structure	Roll forming	2,4e+06 kg	1,3e+07	9,5e+05
Shafts	Roll forming	1,5e+06 kg	7,6e+06	5,7e+05
Base plate	Roll forming	3,1e+05 kg	2e+06	1,5e+05
Blades	Extrusion, foil rolling	1,1e+05 kg	6,3e+05	4,7e+04
Bearings	Casting	4,2e+04 kg	4,7e+05	3,5e+04
Monopile	Roll forming	6,1e+06 kg	1,8e+07	1,3e+06
HLD	Roll forming	1,1e+06 kg	5,7e+06	4,2e+05
Bearings	Casting	1e+05 kg	1,1e+06	8,3e+04
Cables	Wire drawing	1,8e+04 kg	9e+04	6,7e+03
Gearbox	Casting	2,4e+04 kg	2,7e+05	2e+04
Brakes	Casting	3,6e+03 kg	4e+04	3e+03
Total			4,8e+07	3,6e+06

Table B.3: Transportation detailed analysis

Stage name	Transport type	Distance (km)	Energy (MJ)	CO2 footprint (kg)
Factory - Drydock	Rail freight	1,1e+02	4,6e+05	3,3e+04
Drydock - Wind site	Coastal freight	1,2e+02	3,6e+05	2,6e+04
Total		2,3e+02	8,3e+05	6e+04

Table B.4: Decommissioning detailed analysis

Component	End of life option	Energy (MJ)	CO2 footprint (kg)
Structure	Recycle	1,7e+06	1,2e+05
Shafts	Recycle	1e+06	7,1e+04
Base plate	Recycle	2,2e+05	1,5e+04
Blades	Recycle	8e+04	5,6e+03
Bearings	Recycle	2,9e+04	2,1e+03
Monopile	Recycle	4,3e+06	3e+05
HLD	Recycle	7,6e+05	5,3e+04
Bearings	Recycle	7e+04	4,9e+03
Cables	Recycle	1,3e+04	8,8e+02
Gearbox	Recycle	1,7e+04	1,2e+03
Brakes	Recycle	2,5e+03	1,8e+02
Total		8,2e+06	5,7e+05

Table B.5: Recycling detailed analysis

Component	End of life option	Energy (MJ)	CO2 footprint (kg)
Structure	Recycle	-5,8e+06	-4,1e+05
Shafts	Recycle	-3,5e+06	-2,5e+05
Base plate	Recycle	-7,4e+05	-5,3e+04
Blades	Recycle	-2,6e+05	-1,9e+04
Bearings	Recycle	-9,3e+04	-7,7e+03
Monopile	Recycle	-1,4e+07	-1e+06
HLD	Recycle	-2,6e+06	-1,9e+05
Bearings	Recycle	-2,2e+05	-1,8e+04
Cables	Recycle	-8,2e+04	-4,6e+03
Gearbox	Recycle	-5,7e+04	-4,1e+03
Brakes	Recycle	-7,9e+03	-6,6e+02
Total		-2,7e+07	-2e+06